

# Radial Diffusion Models of Earth's Outer Radiation Belt using Stochastic Parameterizations

Rhys Thompson

A thesis presented for the degree of  
*Doctor of Philosophy*



**University of  
Reading**

University of Reading  
Department of Mathematics and Statistics  
United Kingdom  
September 2021



DECLARATION

I confirm that this is my own work and the use of all material from other sources has been properly and fully acknowledged.



Rhys Thompson

Earth's outer radiation belt is very dynamic and contains high-energy particles which are hazardous to spacecraft. Radial diffusion is the process by which energetic electrons undergo bulk transport and energization, driven by interactions with ultralow frequency (ULF) waves. Modelled by a Fokker-Planck equation, all of the physics to describe the strength of radial diffusion is contained in the radial diffusion coefficient,  $D_{LL}$ , typically modelled proportionally to ULF wave power as a function of electron drift-shell ( $L^*$ ) and geomagnetic activity. A number of parameterizations for  $D_{LL}$  exist but can vary by orders of magnitude. State of the art radial diffusion coefficient models therefore carry great uncertainty.

All modern  $D_{LL}$  parameterizations are deterministic and based on median ULF wave power spectral density. In this Thesis we investigate the impact on radial diffusion when  $D_{LL}$  is modelled as an ensemble which encompasses the probabilistic distribution of ULF wave power. The underlying factors which contribute to variability in ULF wave power distributions are extensive and we concentrate on three of the largest: the variability of  $L^*$  with an observation's location when mapping ULF wave power to adiabatic space, the shape of ULF wave power distributions as measured on board spacecraft as a function of  $L^*$ , local time and ULF wave frequency, and finally the mapping of ground-based magnetic wave power to space-based electric field power to infer a key component of  $D_{LL}$ .

We find that  $L^*$  varies in physical space significantly as a function of magnetic field model and geomagnetic activity, with uncertainties between magnetic field models unable to be completely mitigated. Further, shapes of space-based power approximations are either log-symmetric or log-skewed when separated into  $L^*$  and wave frequency, although there are characteristic differences across local time. Finally, we find that while mapping ground-based power with a stochastic ULF wave resonance width better aligns with space-based power distributions compared to the state-of-the-art analytic mapping, stochastic parameterizations of other key wave parameters are necessary to recover the full distribution.

Combining the sources of variability which quantify the ULF wave power distributions into a stochastically parameterized  $D_{LL}$ , we model an ensemble of radial diffusion and compare with a number of deterministic radial diffusion coefficients. In most cases a stochastic  $D_{LL}$  results in more diffusion, with the spread of resulting phase space densities in the ensemble rarely enclosing those from the deterministic parameterizations. In addition, ensembles are collectively more diffusive when  $D_{LL}$  is sampled more frequently in time and on shorter scale-lengths in  $L^*$ . Overall, this thesis demonstrates the importance of variability for impacting rates of radial transport. Future work could extend the stochastic approaches used to here to account for yet to be determined spatio-temporal ULF wave power variability.

---

## ACKNOWLEDGEMENTS

All of the work in this thesis represents four years of my life for which I will be forever grateful, especially to those who have supported me along the way. First and foremost I am grateful for my supervisor Clare Watt who has consistently encouraged and inspired me to pursue the projects I'm most excited about, and for making me feel validated as a developing researcher. I honestly feel like I could not have done any better in the supervisor department and am honoured to have worked with you over these past few years. I would also like to thank my second supervisor Paul Williams for the valuable experience and advice to help the motivations of this project take hold - specifically helping me to see the value in multi-disciplinary research. Both of you have kept me grounded and thinking of the bigger picture, and I am thankful for the time you have committed to meeting with me and providing feedback on the numerous paper and thesis drafts.

My journey to this point would also not exist without the support of friends and family. Specifically I want to thank my mother Sharon for introducing the love of learning to me from as early as I can remember, and instilling in me the belief that I am as worthy of achieving my goals as anybody else regardless of my background. To my partner Corey, I want to thank you for lifting me up through those times when imposter syndrome kicked in, reassuring a very frustrated me that I always manage to fix my code in the end (I always did!), and for making me laugh and smile through it all. To the rest of my family

and friends, both those who knew me before and those I've met along the way, you know who you are and I hope you know how much I appreciate you.

To end, this thesis could not have come to fruition without the help of my fellow researchers. My thanks in particular go to Dr Sarah Bentley and Dr Jasmine Sandhu for providing the in-situ ULF databases used in Chapters 6 and 5, respectively. To everyone else, please know that I'm very appreciative for your support.

---

## RELATED PUBLICATIONS

The work in this thesis has produced two publications. The first, which represents the entirety of Chapter 3, was published in the *Journal of Geophysical Research: Space Physics*. The full reference for this publication can be found in the bibliography under Thompson et al. [2020b].

The second, which can be found in Chapter 4 Section 1, was published in *Space Weather*. The full reference for this publication can be found in the bibliography under Thompson et al. [2020a].

One final unpublished manuscript, which has been prepared for submission in *Geophysical Research Letters*, can be found in Chapter 6 Section 7 (with the associated Supporting Information in Chapter 6 Section 7.1).

---

---

## CONTENTS

Declaration . . . . .	i
Abstract . . . . .	ii
Acknowledgements . . . . .	iv
Related publications . . . . .	vi
<b>1 Introduction</b>	<b>1</b>
1.1 The Sun-Earth system . . . . .	4
1.1.1 The Sun and Solar Wind . . . . .	5
1.1.2 The Earth's magnetosphere . . . . .	6
1.1.3 Van Allen radiation belts . . . . .	8
1.2 Plasma physics . . . . .	9
1.2.1 Single particle motion in a plasma and adiabatic invariants . . . . .	12
1.2.1.1 Gyromotion and magnetic moment . . . . .	12

1.2.1.2	Bounce motion and the second adiabatic invariant . . . . .	15
1.2.2	Drift motion and the third adiabatic invariant . . . . .	16
1.3	Radiation belt modelling . . . . .	17
1.3.1	Fokker-Planck equation . . . . .	18
<b>2</b>	<b>Radial Diffusion</b>	<b>26</b>
2.1	Theoretical frameworks for radial diffusion . . . . .	29
2.1.1	Beyond Fälthammer and Fei . . . . .	32
2.2	Modern parameterizations of the radial diffusion coefficient . . . . .	34
2.2.1	Brautigam and Albert [2000] . . . . .	35
2.2.2	Brautigam et al. [2005] . . . . .	36
2.2.3	Ozeke et al. [2012, 2014] . . . . .	37
2.2.4	Ali et al. [2015, 2016]; Ali [2016] . . . . .	40
2.2.5	Liu et al. [2016] . . . . .	42
2.3	Assumptions and uncertainties . . . . .	42
<b>3</b>	<b>Pilot study: Accounting for Variability in ULF Wave Radial Diffusion Models</b>	<b>47</b>
<b>4</b>	<b>Variability of <math>L^*</math> with observation location</b>	<b>64</b>
4.1	Pro- $L^*$ - A Probabilistic $L^*$ Mapping Tool for Ground Observations . . . . .	66
4.2	Physical variability of $L^*$ during geomagnetic storms . . . . .	90
4.2.1	Quiet→Initial phase . . . . .	98

4.2.2	Initial→Main phase . . . . .	99
4.2.3	Main→Recovery phase . . . . .	100
4.3	Chapter summary . . . . .	100
4.4	Future work . . . . .	102
<b>5</b>	<b>Variability of space-based ULF wave power spectral density</b>	<b>104</b>
5.1	Magnetospheric ULF waves . . . . .	106
5.2	Data, instrumentation and power spectral density approximation . . . . .	107
5.2.1	Global distribution of ULF wave power . . . . .	109
5.2.2	Correlations of $\mathcal{P}$ in time, space and frequency . . . . .	116
5.2.3	Variability of $\mathcal{P}$ with geomagnetic activity . . . . .	117
5.2.4	Drift-averaged ULF wave power . . . . .	122
5.3	Chapter Summary . . . . .	128
<b>6</b>	<b>Mapping ULF wave power from the ground into space</b>	<b>131</b>
6.1	MHD Waves . . . . .	133
6.1.1	Alfvén Waves . . . . .	135
6.1.2	Magnetosonic waves . . . . .	136
6.2	Field line resonances (FLRs) in a simple magnetic field box model . . . . .	136
6.3	FLRs in an arbitrary magnetic field . . . . .	139
6.4	FLRs observed at the ground . . . . .	140
6.5	Analytic mapping . . . . .	142

6.5.1	Mapping $b^g$ to $b^i$ . . . . .	145
6.5.2	Coupling $b_i$ to $E_i$ . . . . .	145
6.5.3	Mapping $E^i$ to $E^{eq}$ . . . . .	146
6.5.4	Mapping $b^g$ to $E^{eq}$ . . . . .	146
6.6	Uncertainty and limitations . . . . .	147
6.7	Global frequency distribution of field line resonances in the inner magnetosphere . . . . .	152
6.7.1	Supporting Information . . . . .	170
6.8	Towards a probabilistic mapping . . . . .	195
6.8.1	Global distribution of resonance widths . . . . .	195
6.8.2	Inclusion of resonance widths in the Ozeke et al. [2009] mapping . . . . .	198
6.9	Chapter summary . . . . .	207
6.10	Future work . . . . .	208
<b>7</b>	<b>Probabilistic radial diffusion with stochastic parameterization of <math>D_{LL}</math></b> . . . . .	<b>211</b>
7.1	Experiment set-up . . . . .	212
7.1.1	Modelling the radial diffusion equation . . . . .	213
7.1.2	Formalism for $D_{LL}$ . . . . .	214
7.1.3	Energy dependence . . . . .	214
7.1.4	Construction of probabilistic $D_{LL}$ . . . . .	216
7.1.5	Ensemble modelling of $D_{LL}$ . . . . .	217
7.2	Numerical experiment results . . . . .	219

7.3	Chapter summary and Future work . . . . .	222
<b>8</b>	<b>Conclusion</b>	<b>228</b>
<b>A</b>	<b>Appendix A</b>	<b>232</b>
A.1	Fälthammar's description of radial diffusion . . . . .	232
A.1.1	Magnetic disturbances and electromagnetic radial diffusion . . . . .	232
A.1.2	Electric potential disturbances and electrostatic radial diffusion . . . . .	241
A.2	Fei's description of radial diffusion . . . . .	245
A.2.1	Magnetic disturbances and magnetic diffusion . . . . .	247
A.2.2	Electric disturbances and electric diffusion . . . . .	249

# CHAPTER 1

## INTRODUCTION

Earth's magnetosphere, the near-Earth region of space dominated by the Earth's magnetic field, is home to the Van Allen radiation belts, two concentric torus shaped regions containing magnetically trapped energetic particles (Van Allen and Frank [1959]). The outer belt, which consists mostly of energetic electrons with energies ranging 0.1-10MeV (where the electron-Volt (eV) =  $1.6022\text{e-}19$  J), is highly spatially and temporally variable in response to changing geomagnetic activity levels (Shprits et al. [2008b]). A large number of commercial satellites which support many modern technologies operate in the outer belt, and are constantly under threat of degradation by these radiative electrons (Baker and Lanzerotti [2016]). In fact, this threat features as one of the space weather risks in the UK Government's National Risk Register (<https://www.gov.uk/government/publications/national-risk-register-2020>). It is therefore imperative to be able to understand and model outer belt dynamics and variability.

The motion of a charged particle in a plasma is controlled by electromagnetic fields, and under steady-state or slowly varying conditions follows three periodic motions each with an associated *adiabatic invariant* - a quantity that stays approximately constant when changes to the magnetic field occur slowly relative to the respective periodic motion. In real-life, the Earth's magnetic field is constantly distorted by interaction with the solar wind from the Sun. Under some conditions, the solar-terrestrial interaction leads to magnetic

field changes or wave-particle interactions that violate the adiabatic invariants and alter plasma motion which can be modelled by a Fokker-Planck diffusion equation in adiabatic phase-space (Roederer and Zhang [2014]). This thesis concerns violation of a particle's third adiabatic invariant, the conservation of flux through a particle's azimuthal drift trajectory around the Earth (drift shell), which results in the radial diffusion of the particle distribution closer to or further away from the Earth. Radial diffusion is considered to be an important and effective mechanism to accelerate and transport relativistic electrons in the outer radiation belt (Elkington et al. [2003]; Mann et al. [2013, 2016]; Ozeke et al. [2017, 2018]; Shprits et al. [2008b]). All of the physics to describe the strength of radial diffusion is contained in the radial diffusion coefficient,  $D_{LL}$ , which is driven by and proportional to ultralow frequency (ULF) wave power in the 1-20mHz range (Elkington et al. [1999, 2003]; Fälthammar [1965]; Roederer and Zhang [2014]).

A number of models for  $D_{LL}$  exist, based on a number of theoretical formalisms (Fälthammar [1965]; Fei et al. [2006]; Lejosne [2019]), but almost always constructed empirically from ULF wave power observations (e.g. Ali et al. [2015, 2016]; Brautigam and Albert [2000]; Brautigam et al. [2005]; Huang et al. [2010a]; Liu et al. [2016]; Ozeke et al. [2012, 2014]). In all instances the empirical  $D_{LL}$  are deterministic, that is, for a given drift shell and level of geomagnetic activity we expect a certain amount of diffusion. Due to the highly variable nature of the outer radiation belt, as well as the underlying ULF wave power (Bentley et al. [2019]; Sandhu et al. [2021]), much information might be lost by not accounting for the natural variability in radial diffusion models. Indeed, the different approaches to collapse ULF wave power distributions into simplified deterministic models has led to significant disagreement between existing  $D_{LL}$  descriptions, by up to several orders of magnitude (Huang et al. [2010a]).

In this thesis we explore probabilistic descriptions of  $D_{LL}$  for use in radial diffusion models, also known as *stochastic parameterizations*, which aim to capture the natural variability of the diffusion coefficient excluded from current descriptions. We show that the inclusion of said variability can have significant impact on the levels of radial diffusion observed (Thompson et al. [2020b] and Chapter 3). The variability to account for, however, is not solely due to the probability distribution of ULF wave power. There are uncertainties

in the radial diffusion formalisms we adopt, the instruments and techniques that we use to measure relevant variables, the mapping of observation locations to adiabatic invariant space, and the outer belt boundary conditions, to name a few. Here we address some of the largest sources of variability, quantifying their uncertainties, which can either be used directly in full constructions of  $D_{LL}$  or to supplement existing models.

The accuracy of the radial diffusion coefficient depends on valid portrayals of diffusion across drift shells, which we describe by the adiabatic  $L^*$  parameter (Roederer [1970]).  $L^*$  can be understood as the equatorial radius of the electron drift contour (in Earth radii  $R_E$ ) subject to the 'switching off' of magnetospheric drivers and relaxation of magnetic field lines back to an axi-symmetric dipole (Roederer and Lejosne [2018a]). The  $L^*$  representation is important to assign a ULF power value to a particular *location* in adiabatic invariant space, but there are clear discrepancies between magnetic field model assignments for the same observation location. In Thompson et al. [2020a]/Chapter 4 we quantify the uncertainty of magnetic field models in the assignment of ULF wave power to drift shells for  $D_{LL}$  parameterization by creating Pro- $L^*$ , a probabilistic  $L^*$  mapping tool for ground-observations to the magnetic equator. Using Pro- $L^*$  we are able to investigate the variability of  $L^*$  between magnetic field models, across fixed locations of ground and space-based observations, and with changes in geomagnetic activity.

With an understanding and quantification of  $L^*$  variability, it is necessary to reanalyse the distribution of ULF wave power across drift-shells. This is to assess the conflation of information in deterministic  $D_{LL}$  models due to magnetic field model inaccuracies, or through the use of average ULF wave power to infer  $D_{LL}$ . Using multiple years of ULF wave power data measured on board spacecraft, in Chapter 5 we are able to describe the power distributions in multiple dimensions and activity levels in closed form, which can be easily implemented into probabilistic radial diffusion models (see Thompson et al. [2020b]). We also address some of the pitfalls of using average wave power for  $D_{LL}$  descriptions, when techniques across studies have been inconsistent which can result in notable differences in the resulting radial diffusion equation (e.g. see Watt et al. [2021]).

While satellite data is useful to explore ULF wave power distributions in particular regions (or *bins*), the sparsity of any *in situ* measurements forgoes any information about

radial, local time and spectral covariance which are key for any probabilistic representation of  $D_{LL}$ . An alternative is to use ULF wave power approximated using ground magnetometers which remote sense the magnetosphere. In Chapter 6 we study the mapping of ground-based magnetic power to space-based electric power to infer one component of  $D_{LL}$  (Fei et al. [2006]). Performing this mapping rests on a relationship between the ground-based compressional magnetic field and the equatorial azimuthal electric field (Ozeke et al. [2009]), assuming the occurrence of a field line resonance (FLR). An FLR occurs when the discrete frequency of a propagating ULF wave matches that of the local magnetic field eigenfrequency, causing irreversible energy exchange along the magnetic field line (Chen and Hasegawa [1974]; Southwood [1974]; Radoski [1971]). Previous parameterizations of  $D_{LL}$  have mapped ground power assuming that particular resonant wave properties remain constant. To quantify the variability of numerous resonant wave variables, we design an automated FLR detection algorithm across a latitudinal array of ground magnetometers and apply on 7 years of data. We use our results to investigate the probabilistic nature of FLRs, and discuss whether the inclusion of realistic resonant wave variables helps reproduce the ULF wave power distributions on board spacecraft.

We end with a return to the radial diffusion equation in Chapter 7. Performing a number of ensemble experiments, with a probabilistic  $D_{LL}$  reflecting the quantified uncertainties considered throughout this thesis, we discern the impact on radial diffusion and compare to existing deterministic models. A number of uncertainties remain, however, and we discuss some how some can be tackled in future work. The outer radiation belt is a highly variable and exciting region of space, and a lot of progress can be made in our diffusion models by becoming more certain about its uncertainty.

## 1.1 The Sun-Earth system

In following sections we will introduce the notion of charged particles in a plasma that are trapped in the Earth's geomagnetic field. This thesis concerns the motion of these trapped particles, specifically, the radial motion closer to or further away from the Earth. The trapped particle populations can have either solar or terrestrial origin and are temporally

driven by Sun-Earth interactions.

### 1.1.1 The Sun and Solar Wind

The Sun releases a flow of charged particles from the corona (the Sun's upper atmosphere) which travels radially outward from the Sun known as the *solar wind*. Since plasmas (see Section 1.2) in both the corona and solar wind are highly electrically conductive, their flows can be considered *frozen together* (Roberts [2007]), and the superposed solar magnetic field (Owens and Forsyth [2013]) travelling with the solar wind flow is known as the *interplanetary (or heliospheric) magnetic field (IMF)*.

Typically the solar wind exists in two fundamental states, *fast* and *slow*, which have different source regions on the Sun. Both reach supersonic speeds at several solar radii away from the Sun, meaning that they travel faster than the speed of fast magnetosonic waves. The fast solar wind has typical speeds of  $\sim 750 \text{ km s}^{-1}$  and a composition nearly that of the Sun's photosphere (Geiss et al. [1995]), the Sun's outer shell from which light is radiated. The sources of the fast solar wind are coronal holes (Zirker [1977]), regions of open field lines in the corona with a lower plasma-density and pressure, which act like a funnel where particles can escape at greater speeds than surrounding areas. The slow solar wind has typical speeds of  $\sim 300 - 500 \text{ km s}^{-1}$  and a composition nearly that of the corona (Geiss et al. [1995]). While the slow solar wind typically originates near the Sun's equatorial region, the structures that drive its formation are not widely agreed upon (Abbo et al. [2016]).

When fast flows ejected from coronal holes overtake slow flows originating westward of them a turbulent region is formed, known as the *co-rotating interaction region (CIR)*, which accelerates particles and creates IMF structure that can cause geomagnetic storms (induced large scale electric currents felt globally) when they reach the Earth's magnetosphere (see Section 1.1.2). Sometimes, large-scale fast-moving coronal plasma is ejected into space following instabilities in coronal structures, known as *coronal mass ejections (CMEs)*. Occasionally CMEs produce *solar energetic particle (SEP)* events, which are high-energy particles coming from the Sun which can endanger life in space. When CMEs

reach Earth they temporarily deform the magnetosphere, causing geomagnetic storms.

Solar magnetic activity has a characteristic periodicity of roughly 11 years relative to the number of sunspots (phenomena on the photosphere that appear darker than surrounding areas) on its surface. Sunspots have been drawn as early as 1128 by English monk John of Worcester (Stephenson and Willis [1999]) and the solar cycle was discovered in 1843 by Schwabe [1843]. Geomagnetic activity is correlated with the solar cycle, with more activity during *solar maximum* (sunspot number peak during a solar cycle) and the declining phase (post solar maximum) (Chapman [1962]).

### 1.1.2 The Earth's magnetosphere

The Earth's magnetosphere is the region of space dominated by the Earth's magnetic field and acts as a barrier to the incoming solar wind. Deep convective motion of conductors in the Earth's interior are the primary source of the Earth's magnetic field, which is dipole-like in shape with an axis slightly offset to that of the Earth's rotation axis. The dipole shape is distorted upon interactions with the solar wind, however. When the solar wind transitions from supersonic to subsonic when approaching upstream of the nose of the magnetosphere, a *bow shock* forms. The *magnetosheath* is the region that contains this shocked plasma, which is turbulently diverted along the magnetospheric flanks and facilitates coupling of the solar wind and magnetosphere. The *magnetopause* then forms the boundary between the magnetospheric and solar wind plasma and encloses the magnetosphere. When these dynamics hold in a *frozen in* (Roberts [2007]) steady state there is no mixing between the solar wind and magnetospheric plasmas, with the magnetosphere acting as an electromagnetic cavity (container of electromagnetic fields) and topology of a compressed dipole with stretched tail.

However, there is further deformation of the field by a process known as magnetic reconnection. When the IMF in the solar wind has southward orientation, opposite to the magnetospheric magnetic field at the magnetopause, the interacting field lines reconnect in a diffusion region. This means that field lines that were once 'closed' with footpoints at Earth's magnetic poles become 'open' to connect the IMF and geomagnetic field. The

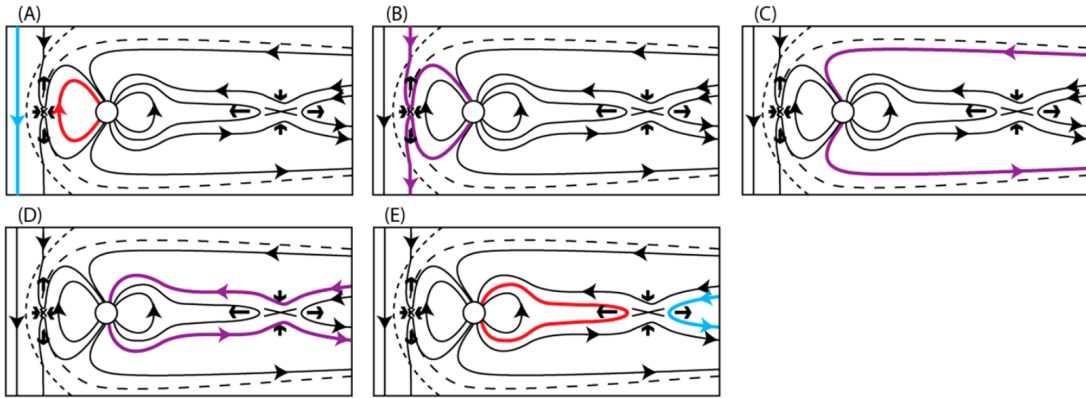


Figure 1.1: The Dungey Cycle, taken from Eastwood et al. [2014]. The approaching IMF has opposite orientation to Earth’s magnetic field (A), where they reconnect on the nose of the magnetopause (B). The newly formed open field lines are carried anti-sunward by the prevailing solar wind to the magnetotail (C), where reconnection occurs again (D). The newly formed closed field lines then convect back towards the dayside (E) where the cycle starts over.

prevailing solar wind carries these newly-formed open field lines anti-sunward around the magnetospheric flanks and into the *magnetotail* where they build up. When the dragged open field lines rooted in opposite hemispheres meet in the magnetotail reconnection occurs again. These newly closed field lines then convect back towards the dayside carrying accelerated particles and plasma instabilities. Once the convection ceases the entire process, known as the Dungey Cycle (Dungey [1961]), starts over. A schematic of the Dungey Cycle is shown in Figure 1.1. In addition, the explosive and unstable reconnection events in the tail that result in large transfers of energy from stored magnetic field energy to particle kinetic energy are known as *substorms*.

A schematic of the resulting magnetosphere is shown in Figure 1.2. Since plasma particles are coupled to magnetic field lines (see Section 1.2), the Dungey Cycle is a large source of particles in the magnetosphere. Other sources exist (visible in Figure 1.1) such as the *plasma sheet* which contains the plasma populations (of solar or terrestrial origin) trapped by the tailside reconnection, or the ionosphere as source of ions in the plasmasphere (e.g. Horwitz et al. [1982]). We discuss the plasmasphere alongside the radiation belts next.

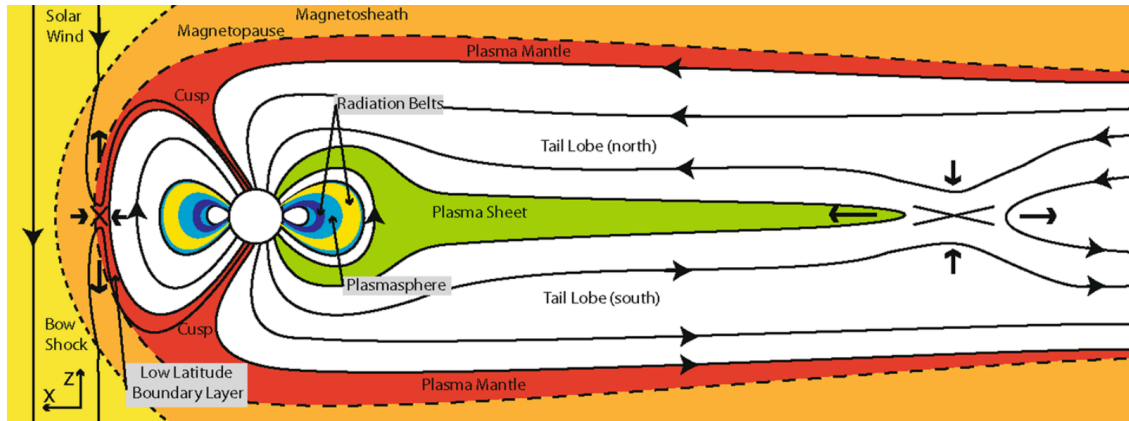


Figure 1.2: A diagram of the Earth’s magnetosphere undergoing the Dungey Cycle, taken from Eastwood et al. [2014].

### 1.1.3 Van Allen radiation belts

One of the first major discoveries of the Space Age was the discovery of the Earth’s Van Allen radiation belts, two concentric torus shaped regions charged particles seemingly trapped by the Earth’s magnetic field (Van Allen and Frank [1959]). Spatially the radiation belts have considerable overlap with the *plasmasphere* (see Figure 1.2), a region of cold, dense plasma situated above the ionosphere (with outer boundary the *plasmopause*) that co-rotates with the Earth. The *inner belt* extends approximately 2-3 Earth radii ( $R_E$ ) and is predominantly made up of energetic protons (exceeding 100MeV) and some lower-energy electrons (hundreds of keV). The *outer belt*, where this thesis is focused, consists mainly of energetic electrons (0.1-10MeV) and extends roughly 3-10 $R_E$ . Many modern technologies depend on satellites that operate within the outer radiation belt. Powerful mechanisms can drive high energy electrons deep within the Earth’s magnetosphere (Baker et al. [1998]), such as the acceleration of particles travelling Earthwards with convecting field lines following tailside reconnection, and satellites almost always degrade if they experience this penetrating radiation (Baker and Lanzerotti [2016]). Between both radiation belts is the *slot zone*, a region relatively free of charged particles (Lyons and Thorne [1973]).

While the location of the inner belt is relatively stable, the extent of the outer belt is highly variable. The particle flux contained in the belt is also highly variable, although the

greatest fluxes are typically around  $4-5R_E$ . The outer belt is largely produced by *inward radial diffusion* (see Section 1.3.1 and Elkington et al. [2001]; Shprits and Thorne [2004]) and *local particle acceleration* due to wave-particle energy transfer from whistler mode waves to radiation belt electrons (Horne et al. [2005]). Conversely, outer belt electrons are also lost from the belt due to atmospheric collisions (Horne et al. [2003]), magnetopause shadowing (Yu et al. [2013]) and *outward radial diffusion* (see Section 1.3.1 and Turner et al. [2012]). A number of other wave-particle interactions have been deemed important in the radiation belts. Very low frequency (VLF) whistler mode chorus waves mediate energy diffusion (Thorne et al. [2013]), whereas VLF whistler mode hiss (Lyons and Thorne [1973]; Meredith et al. [2007]) and ULF electromagnetic ion cyclotron (EMIC) waves (Kersten et al. [2014]) predominantly diffuse in pitch-angle and therefore contribute to loss. The energetic particle fluxes also vary significantly in response to changes in geomagnetic activity (Shprits et al. [2008b]), in particular geomagnetic storms, where we see both enhancements related directly to the source of the storm as well as plasma injections convecting from the tail (i.e. substorms), and dropouts mentioned previously. Due to its highly dynamic nature, understanding the formation, evolution and variability of the outer belt is an ongoing area of research.

A final note is that while the radiation belts are generally considered as two separate entities, there has been evidence of a third belt forming near the inner edge of and separate to the typical outer belt (Baker et al. [2013]), explainable by rapid outward radial diffusion coupling to the dynamic outer belt boundary (Mann et al. [2016]).

## 1.2 Plasma physics

Plasma is one of the four observable states of matter, along with solids, liquids and gases. A plasma is a *quasi-neutral* gas comprised of charged (positively and negatively) particles which exhibit collective behaviour. By quasi-neutrality, we mean that the overall charge of the plasma is neutral, but local scales may give rise to charged regions and electric fields. A plasma is defined by three criteria: the *Debye length*, conditions necessary for *Debye shielding* to be effective and a final condition to ensure collective behaviour of the

plasma. We outline each of these below.

The Debye length is a characteristic length scale of a plasma and is the distance over which charge separation can occur and is given by

$$\lambda_D = \sqrt{\frac{\epsilon_0 k_B T_e}{e^2 n_e}} \quad (1.1)$$

where  $\epsilon_0$  is the permittivity of free space,  $k_B$  the Boltzmann constant,  $T_e$  the electron temperature,  $e$  the electron charge and  $n_e$  the electron density. The Debye length is the distance for which the electrostatic effect of an electric field persists over other charged particles (ions) in the plasma. Processes on scales larger than this will only be minimally effected by local charges. On scales smaller than the Debye length, charged electrons will group around ions due to the electrostatic effects which acts as a shield to any other electric field in the plasma. These regions of grouped particles are known as Debye spheres. To ensure effective Debye shielding, we require a certain number of electrons in a Debye sphere to adhere to (Baumjohann and Treumann [2012])

$$N_D = \frac{4\pi}{3} n_e \lambda_D^3 \gg 1 \quad (1.2)$$

Now, we consider the displacement of electrons from a background state of ions. This results in electric fields which aim to pull the electrons back towards the ions to maintain neutrality. Since the electrons have finite mass they oscillate around the (fixed) ions with respect to the electron plasma frequency

$$\omega_{pe} = \sqrt{\frac{n_e e^2}{m_e \epsilon_0}} \quad (1.3)$$

where  $m_e$  is the electron mass. Collisions of oscillating electrons with any remaining neutrals affect the motion of the plasma. In order for the plasma to behave as expected, we finally require the time between collisions ( $\tau_n$ ) to satisfy

$$\omega_{pe} \tau_n \gg 1 \quad (1.4)$$

where  $1/\tau_n$  denotes the frequency of collisions.

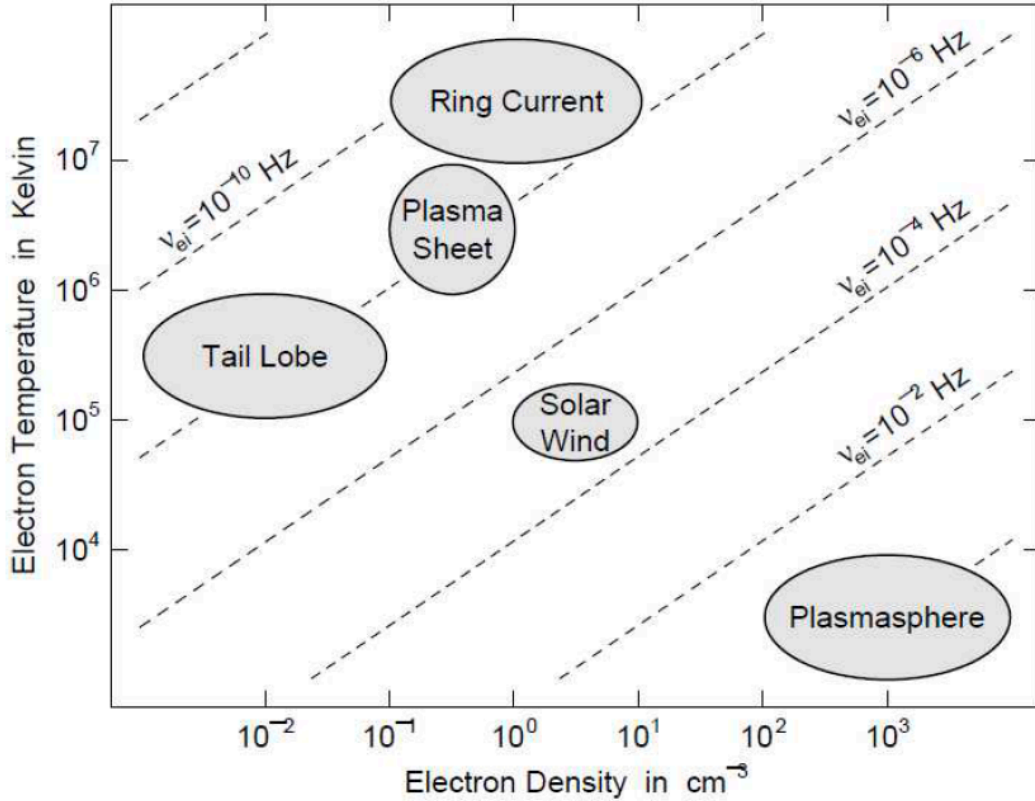


Figure 1.3: Coulomb collision frequencies between ions and electrons for a number of plasma population examples. Taken from Baumjohann and Treumann [2012].

Throughout the remainder of this thesis we consider an ideal plasma where there are no collisions. This is sensible for many of the plasma populations in the magnetosphere or interacting solar wind, where respective Coulomb (between two charged particles interacting through their own electric field) collision frequencies are negligible, as illustrated in Figure 1.3. Note that this assumption breaks down near planetary atmospheres, where radiation belt particles can be lost to atmospheric collisions (Jursa [1985])

In a plasma mostly formed from charged electrons and ions, the magnetic ( $\mathbf{B}$ ) and electric ( $\mathbf{E}$ ) fields are vital for the governing equations of motion, and we model their respective fields with *Maxwell's Equations* (in a collisionless plasma)

$$\nabla \cdot \mathbf{E} = \frac{\rho_q}{\epsilon_0} \quad (1.5)$$

$$\nabla \cdot \mathbf{B} = 0 \quad (1.6)$$

$$\nabla \times \mathbf{E} = -\frac{\partial \mathbf{B}}{\partial t} \quad (1.7)$$

$$\nabla \times \mathbf{B} = \mu_0(\hat{\mathbf{j}} + \epsilon_0 \frac{\partial \mathbf{E}}{\partial t}) \quad (1.8)$$

where  $\mu_0$  is the permeability of free space,  $\rho_q$  is the charge density and  $\hat{\mathbf{j}}$  is the current density. In order, the equations correspond to Gauss' laws for electric and magnetic fields, the Maxwell-Faraday equation (Faraday's law of induction) and Ampère's circuital law (with Maxwell's addition).

### 1.2.1 Single particle motion in a plasma and adiabatic invariants

We now take a step back from the collective view of plasmas and consider the motion of individual particles within the plasma themselves under the influence of the magnetic and electric fields. The three particle motions described in this section are illustrated in Figure 1.4, which we now describe in detail. Lorentz' equation considers the force exerted on a charged particle  $q$  with velocity  $\mathbf{v}$  moving through an electric and magnetic field and is given by (Baumjohann and Treumann [2012]; Roederer and Zhang [2014]; Schulz and Lanzerotti [1974])

$$\mathbf{F} = q(\mathbf{E} + \mathbf{v} \times \mathbf{B}) \quad (1.9)$$

It is often to useful to consider  $\mathbf{F} = \frac{d\mathbf{p}}{dt}$  where  $\mathbf{p} = m\mathbf{v}$  is the particle's momentum with respect to the mass  $m$ .

#### 1.2.1.1 Gyromotion and magnetic moment

First, we consider the case of a uniform magnetic field  $\mathbf{B}$  and the absence of any electric field  $\mathbf{E} = 0$ . If we separate the velocity ( $\mathbf{v}$ ) into its parallel and perpendicular components

we have

$$m \frac{d\mathbf{v}_{\parallel}}{dt} = 0 \quad (1.10)$$

$$m \frac{d\mathbf{v}_{\perp}}{dt} = q(\mathbf{v}_{\perp} \times \mathbf{B}) \quad (1.11)$$

$$(1.12)$$

Integrating Equation 1.10 with respect to time we find the solution  $\mathbf{v}_{\parallel} = \text{const}$  and the particle moves parallel to  $\mathbf{B}$  at a constant speed. On the other hand, according to Equation 1.11, the charged particle will move in a circular motion in the  $\mathbf{v}_{\perp} - \mathbf{B}$  plane ( $\mathbf{v}_{\perp}$  magnitude remains constant), dependent on the charge of the particle where opposite charges gyrate in opposite directions. This circular motion, known as *gyromotion*, has gyroradius and angular cyclotron frequency (or gyrofrequency)

$$r_g = \frac{mv_{\perp}}{B|q|}, \quad \omega_g = \frac{|q|B}{m} \quad (1.13)$$

With any parallel velocity present we will therefore have a helical trajectory with the centre of the gyromotion (guiding centre) drifting with velocity  $\mathbf{v}_{\parallel}$ .

We define the *pitch angle* ( $\alpha$ ) as the angle between the the magnetic field and particle velocity

$$\alpha = \arctan(v_{\perp}/v_{\parallel}) \quad (1.14)$$

When  $\alpha$  is near  $90^{\circ}$  we can expect a nearly circular trajectory with  $v_{\parallel} \ll 1$ , whereas for  $\alpha$  near  $0^{\circ}$  the helical trajectory will become severely constricted, since the gyroradius is directly proportional to  $v_{\perp}$  which will be  $\ll 1$ .

Referring back to Equation 1.9, in the case of a uniform magnetic field and no electric field we can rearrange and take the dot product of both sides to get, with  $\mathbf{v} \cdot (\mathbf{v} \times \mathbf{B}) = 0$ ,

$$\mathbf{v} \cdot m \frac{d\mathbf{v}}{dt} = \frac{d}{dt} \left( \frac{1}{2} m |\mathbf{v}|^2 \right) = 0 \quad (1.15)$$

We see that kinetic energy ( $K = K_{\perp} + K_{\parallel}$ ) is conserved. Using this result we define the first adiabatic invariant, the *magnetic moment*, by

$$\mu = \frac{mv_{\perp}^2}{2B} = \frac{p_{\perp}^2}{2mB} \quad (1.16)$$

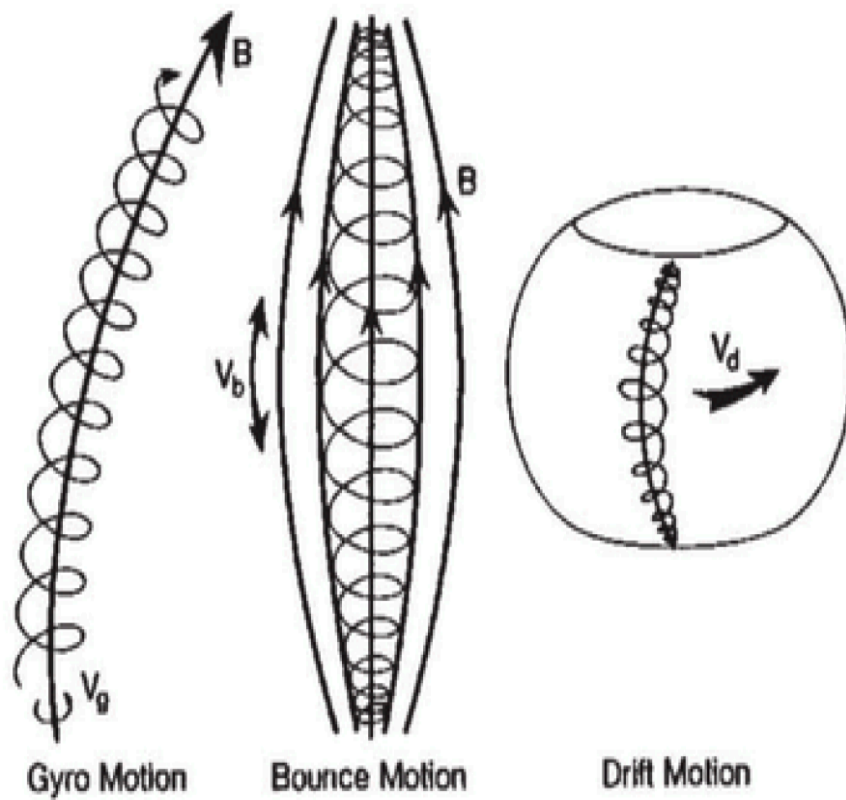


Figure 1.4: Illustration of the three types of particle motion in an electromagnetic field. Adapted from Kivelson and Russell [1995].

Comparing Equation 1.15 with the Lorentz equations for the decomposed velocity components in Equations 1.10 and 1.11, the magnetic moment simply states that the ratio between the perpendicular motion's kinetic energy and magnetic field strength is conserved. By adiabatically invariant, we mean that this is conserved when changes in the magnetic field  $B$  are small over one gyroperiod.  $\mu$  has the characteristic timescale  $\tau_{gyro}$  which in Earth's radiation belts, is on the order of milliseconds.

### 1.2.1.2 Bounce motion and the second adiabatic invariant

Suppose that the magnetic field is no longer uniform but in fact has a gradient, much like the Earth's magnetic field which increases in strength towards the poles. As the particle spirals along the field line from a region of low to high magnetic field strength,  $v_{\perp}$  must increase in order to conserve  $\mu$  (and so the gyroradius becomes ever tighter), whilst  $v_{\parallel}$  must decrease in order to conserve  $K$ . If  $B$  continually and gradually increases, such as in the case of a particle converging towards the Earth's poles,  $v_{\parallel}$  will converge to zero. This is analogous to  $\mathbf{v} = \mathbf{v}_{\perp}$  and  $\alpha = 90^{\circ}$ . In this instance the particle motion becomes unstable and is *reflected* (or *mirrored*) so its direction is reversed. When two mirror points exist along a field line, specifically in both hemispheres for the radiation belts, it creates a magnetic mirror in which a charged particle can become temporarily trapped. The particle will reflect back and forth between the mirror points in what is known as the *bounce motion*. The second adiabatic invariant associated with the bounce motion is

$$J = \oint_{m_1}^{m_2} p_{\parallel} ds \quad (1.17)$$

here  $m_1, m_2$  are the mirror points in each hemisphere,  $p_{\parallel} = mv_{\parallel}$  is the parallel momentum and  $ds$  a length element along the field line.  $J$  has characteristic timescale  $\tau_{bounce} \gg \tau_{gyro}$  which is on the order of seconds.

For particles initially at the magnetic equator with magnetic field  $B_{eq}$  and equatorial

pitch angle  $\alpha_{eq}$ , the magnetic field for which mirroring occurs satisfies

$$B_M = \frac{B_{eq}}{\sin^2 \alpha_{eq}} \quad (1.18)$$

dependent only on the equatorial magnetic field strength and pitch angle, not the charge or momentum of the particle. Increasingly smaller  $\alpha_{eq}$  require a stronger magnetic field to mirror. Defining  $B_{max}$  as the magnetic field strength at the location where collisions with atmospheric constituents remove particles from the system, we can specify the minimum equatorial pitch angle necessary for mirroring to occur

$$\alpha_{min} = \sin^{-1} \left( \sqrt{\frac{B_{eq}}{B_{max}}} \right) \quad (1.19)$$

For all  $\alpha_{eq} < \alpha_{min}$  in a planetary dipole particles will be lost to collisions in the Earth's atmosphere and lost to the system. These collisions are the cause of the *aurora borealis*. Particles satisfying this inequality are collectively known as being in the *loss cone*.

### 1.2.2 Drift motion and the third adiabatic invariant

For the final periodic motion we reintroduce electric fields which, combined with the non-uniformity of the magnetic field, result in a number of drifts which culminate in a periodic azimuthal particle drift around the Earth. Electrons drift westward whilst ions drift eastward. Significant drifts of note are the  $\mathbf{E} \times \mathbf{B}$ , gradient and curvature drifts and are given by

$$\mathbf{v}_{E \times B} = \frac{\mathbf{E} \times \mathbf{B}}{B^2} \quad (1.20)$$

$$\mathbf{v}_{grad} = \frac{mv_{\perp}^2}{2qB^3} (\mathbf{B} \times \nabla B) \quad (1.21)$$

$$\mathbf{v}_{curv} = \frac{mv_{\parallel}^2}{qR_C^2} \frac{\mathbf{R}_C \times \mathbf{B}}{B^2} \quad (1.22)$$

where  $\mathbf{R}_C$  is the local radius of curvature of the magnetic field line.  $\mathbf{v}_{E \times B}$  is a natural consequence of adding electric fields to Equation 1.9 and obtaining a drift motion perpendicular to both  $\mathbf{B}$  and  $\mathbf{E}_{\perp}$ , where  $\mathbf{E}_{\perp}$  is relative to the magnetic field ( $\mathbf{E}_{\parallel}$  is typically non-existent over a bounce period due to the acceleration of oppositely charged particles

in opposite directions relative to  $\mathbf{E}_{\parallel}$  cancelling each other out).  $\mathbf{v}_{grad}$  is a result of inhomogeneities in the non-uniform magnetic field that a particle experiences over a gyroperiod, where gradients in the magnetic field which control gyroradius variations creating a net drift. Finally,  $\mathbf{v}_{curv}$  is due to the centripetal force experienced by a particle due to field line curvature resulting in a drift motion perpendicular to the curvature.

The third adiabatic invariant requires that the flux enclosed by a particle's azimuthal drift contour (bounce and gyro-averaged) is conserved

$$\Phi = \int_S \mathbf{B} \cdot d\mathbf{S} \quad (1.23)$$

For the radiation belts it is often more useful to consider the Roederer [1970]  $L^*$  parameter

$$L^* = \frac{2\pi B_E R_E}{\Phi} \quad (1.24)$$

where  $B_E$  is the equatorial magnetic field strength at the Earth's surface.  $L^*$  can be understood as the equatorial radius of the drift contour (in Earth radii  $R_E$ ) subject to the 'switching off' of magnetospheric drivers and relaxation of magnetic field lines back to an axi-symmetric dipole (Roederer [1970]; Roederer and Zhang [2014]; Roederer and Lejosne [2018a]).  $\Phi$  has characteristic timescale  $\tau_{drift} \gg \tau_{bounce} \gg \tau_{gyro}$  on the order of tens of minutes for which it is conserved.

Conservation of the three adiabatic invariants (periodic motions) results in particles being trapped in the inner magnetosphere. The sum of the periodic motions defines the net motion of a particle, which is illustrated in Figure 1.5.

### 1.3 Radiation belt modelling

We have seen that the adiabatic invariants are conserved for processes that occur on longer timescales than those of their periodic motion. If a process occurs on comparable timescales to any of the invariants we consider them to be *violated*. Due to the hierarchical structure of the characteristic timescales,  $\tau_{drift} \gg \tau_{bounce} \gg \tau_{gyro}$ , violation of a lower rank invariant (with smaller characteristic timescale) also violates those at higher ranks. For example, violation of  $\mu$  also violates  $(J, \Phi)$ , but for violation of  $\Phi$  alone (ie for some process

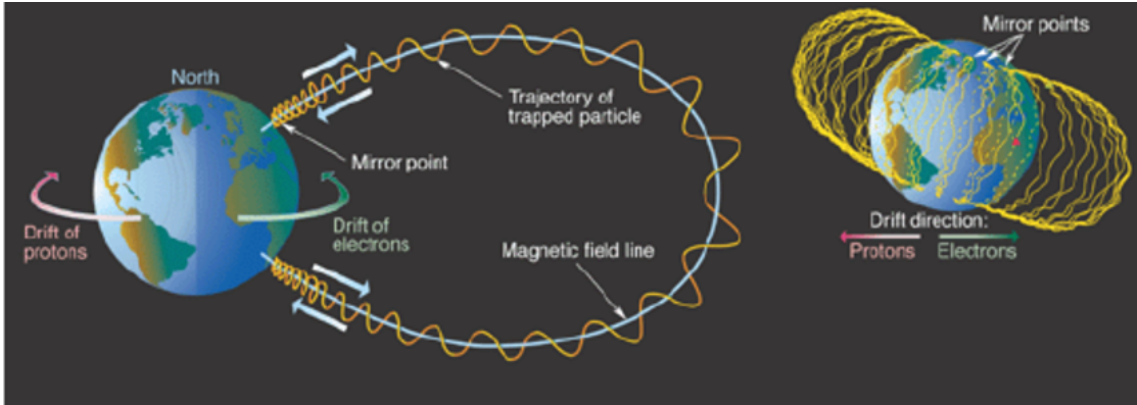


Figure 1.5: The net motion of a particle in the inner magnetosphere when all adiabatic invariants are conserved. Taken from Anagnostopoulos et al. [2010].

occurring on minute timescales),  $(\mu, J)$  remain conserved. Particles with varying kinetic energies also have varying periodic frequencies, which are shown for equatorially mirroring ( $\alpha_{eq} = 90^\circ$ ) charged particle populations in Figure 1.6 as an example.

Violation of any of the adiabatic invariants results in particle loss, transport or acceleration in the radiation belts. Since a variety of magnetospheric waves exists on timescales comparable to those of the adiabatic invariants, we study these *wave-particle* interactions to inform the physics of the radiation belts. In this thesis we concern ourselves with violation of the third adiabatic invariant  $\Phi$  and therefore processes which occur on the order of minutes. Violation of  $\Phi$  with  $(\mu, J)$  conserved causes particles to migrate to other drift shells radially, which also changes the particles' net perpendicular energy. Moving radially inwards causes particles to gain energy since the magnetic field is stronger, and *vice versa*. We model the evolution of particles experiencing violation of the adiabatic variations as *diffusive* processes, where the motion of particles under  $\Phi$  violation undergo *radial diffusion*. Here, we derive the *Fokker-Planck* equation which describes the evolution of radiation belt particles through these processes.

### 1.3.1 Fokker-Planck equation

The derivation outlined here can be found in detail in Roederer and Zhang [2014]. To reach the Fokker-Planck equation, we must first consider an ensemble of charged particles

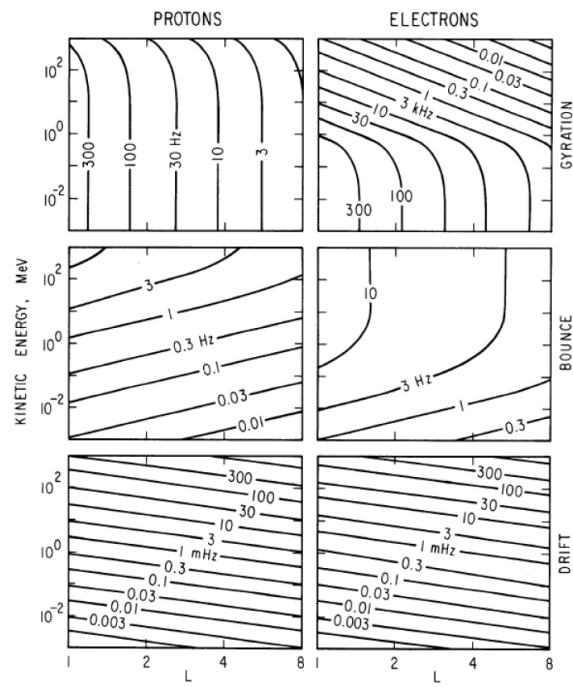


Figure 1.6: Drift, bounce and gyrofrequencies for equatorially mirroring ( $\alpha_{eq} = 90^\circ$ ) charged particle populations, across a range of kinetic energies and drift shells in a dipole magnetic field. Here,  $L^* = L = r_0/R_E$  where  $r_0$  is the particle position in Earth radii  $R_E$ . Taken from Schulz and Lanzerotti [1974].

within an electromagnetic field as a distribution function

$$f_p = f_p(\mathbf{x}, \mathbf{p}, t) \quad (1.25)$$

Here,  $f_p$  determines the probability distribution function of the particle ensemble in the six-dimensional *phase-space*: three directions for position and momentum which evolve in time. The phase-space density between momentum and velocity space is given by  $f_p = m^{-3}f_v(\mathbf{x}, \mathbf{v}, t)$ . To obtain the total number of particles present in a plasma we calculate

$$N = \int f_p d\mathbf{x}d\mathbf{p} \quad (1.26)$$

It is useful to relate the phase space density to something measurable. Satellites provide information about the particle flux  $\mathbf{j}$ .  $f_p$  is the distribution function of the particles' guiding centres, which is proportional to the particle density in phase space and therefore to the measurable quantity  $\mathbf{j}(\mathbf{x}, K, \alpha)/p^2$  (for kinetic energy  $K$  and pitch angle  $\alpha$ ).

Suppose we have a set of new variables ( $Y_1(p_1, p_2, p_3), Y_2(p_1, p_2, p_3), Y_3(p_1, p_2, p_3)$ ) that are functions of, say, the particle's momentum space ( $p_1, p_2, p_3$ ). The inverse transformations are  $p_k = p_k(Y_1, Y_2, Y_3)$ . Let  $\delta n$  be the number of particles in a spatial volume  $\delta x^3$  whose momentum fall into given ranges of magnitude and direction at time  $t$ . This is proportional to  $\delta x^3, \delta p^3$  and it follows we must have

$$\delta n/\delta x^3 = f_{new}(Y_1, Y_2, Y_3)dY_1dY_2dY_3 = f_{old}(p_1, p_2, p_3)dp_1dp_2dp_3 \quad (1.27)$$

Integrating over the new variables gives the number density of the particle ensemble at point  $\mathbf{x}$  and time  $t$

$$n(\mathbf{x}, t) = \int_{Y_i} f(\mathbf{x}, Y_1, Y_2, Y_3, t)dY_1dY_2dY_3 \quad (1.28)$$

The volume elements in Equation 1.27 are related by the rule of the Jacobian  $dY_1dY_2dY_3 = G_{YP}dp_1dp_2dp_3$ , where  $G_{YP}$  is the Jacobian

$$G_{YP} = \begin{vmatrix} \frac{\partial Y_1}{\partial p_1} & \frac{\partial Y_1}{\partial p_2} & \frac{\partial Y_1}{\partial p_3} \\ \frac{\partial Y_2}{\partial p_1} & \frac{\partial Y_2}{\partial p_2} & \frac{\partial Y_2}{\partial p_3} \\ \frac{\partial Y_3}{\partial p_1} & \frac{\partial Y_3}{\partial p_2} & \frac{\partial Y_3}{\partial p_3} \end{vmatrix} \quad (1.29)$$

We consider a transformation to adiabatic invariant coordinates

$$f(x_1, x_2, x_3, p_1, p_2, p_3, t) \rightarrow f(\mu, J, \Phi, \phi_\mu, \phi_J, \phi_\Phi, t) \quad (1.30)$$

where  $\phi_\mu, \phi_J, \phi_\Phi$  are the relevant phases for each of the adiabatic invariants. We consider the case where particles are distributed equally across each gyro, bounce and trajectories and are not *bunched* anywhere (see Figure 1.7). Now, we can average out the phase angles and reduce the dimensions from six to three

$$f = f_0(\mu, J, \Phi, t) \quad (1.31)$$

To derive an evolution equation for the phase space density  $f_0$ , the distribution function of the particles' guiding centers, we must relate the distribution function at time  $t + \Delta t$  with the distribution function of the same group of particles at time  $t$ . Let  $\mathbf{\Lambda} = (\mu, J, \Phi)$ . We assume that during the interval  $\Delta t$  there are significantly many stochastic interactions of all adiabatic invariants with a small net effect. We define the *probability function*

$$F(\mathbf{\Lambda} - \Delta\mathbf{\Lambda}, \Delta\mathbf{\Lambda}, t, \Delta t) \quad (1.32)$$

which describes the probability that a particle with adiabatic coordinate  $\mathbf{\Lambda} - \Delta\mathbf{\Lambda}$  at time  $t$  will end up with coordinate  $\mathbf{\Lambda}$  at time  $t + \Delta t$ . All perturbations imposed on the adiabatic invariants which affect their position in adiabatic space are contained in this probability function, including those caused by magnetic field inhomogeneities, induced electric field accelerations, collisions, natural random fluctuations, etc. As with any other probability function

$$\int_{\mathbf{\Lambda}} F d\mathbf{\Lambda} = 1 \quad \forall t \quad (1.33)$$

The time evolution of the phase space density from time  $t$  to  $t + \Delta t$  can then be expressed as

$$f_0(\mathbf{\Lambda}, t + \Delta t) = \int_{\mathbf{\Lambda}} f_0(\mathbf{\Lambda} - \Delta\mathbf{\Lambda}, t) F(\mathbf{\Lambda} - \Delta\mathbf{\Lambda}, \Delta\mathbf{\Lambda}, t, \Delta t) d\mathbf{\Lambda} + (Q(\mathbf{\Lambda}, t) - S(\mathbf{\Lambda}, t)) \Delta t \quad (1.34)$$

where  $Q, S$  represent any sources and sinks per unit time, respectively. If we Taylor expand both  $f_0$  and  $F$  up to second order in  $\mathbf{\Lambda}$  in the integral, and  $f_0$  up to first order in  $t$  on

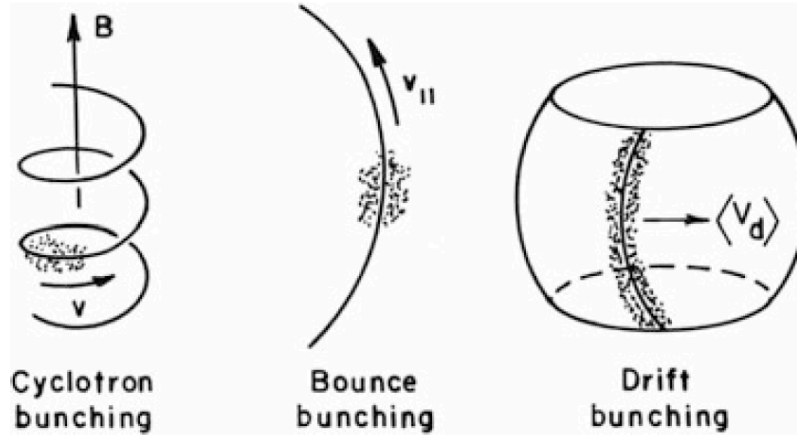


Figure 1.7: Three cases in which the particle phase angles are not distributed equally (bunching). Taken from Roederer and Zhang [2014].

the left hand side, after grouping and rearranging the terms we obtain the Fokker-Planck equation

$$\frac{\partial f_0}{\partial t} = - \sum_i \frac{\partial (D_{\Lambda_i} f_0)}{\partial \Lambda_i} + \sum_i \sum_j \frac{\partial^2 (D_{\Lambda_i \Lambda_j} f_0)}{\partial \Lambda_i \partial \Lambda_j} + Q - S \quad (1.35)$$

where  $\Lambda_i$  is each  $i$ th adiabatic invariant in  $\mathbf{\Lambda}$ . The average change per unit time for a single particle at  $\mathbf{\Lambda}$ ,  $D_{\Lambda_i}$ , is known as the first order Fokker-Planck *diffusion coefficient*

$$D_{\Lambda_i} = \frac{\langle \Delta \Lambda_i \rangle}{\Delta t} = \frac{1}{\Delta t} \int \Lambda_i F D \Lambda_i \quad (1.36)$$

$D_{\Lambda_i \Lambda_j}$ , the second order diffusion coefficients, are defined as

$$D_{\Lambda_i \Lambda_j} = \frac{\langle \Delta \Lambda_i \Delta \Lambda_j \rangle}{2 \Delta t} = \frac{1}{2 \Delta t} \int \int \Lambda_i \Lambda_j F D \Lambda_i \Lambda_j \quad (1.37)$$

We can interpret these as the *strength* of the diffusive processes. When they are zero, no diffusion occurs. On the other hand, the first order diffusion coefficients may be zero even if diffusion is present. Equation 1.35 is analogous to an adiabatic drift-diffusion equation to describe particle transportation. If we were to consider the distribution function over the full six-dimensional space by inclusion of adiabatic phase angles, we would end with 6 'drift' coefficients and 36 'diffusion' coefficients. However by reducing to three-dimensions and acknowledging that  $D_{\Lambda_i \Lambda_j} = D_{\Lambda_j \Lambda_i}$  are symmetric, we now have 3 and 6, respectively.

To satisfy classical diffusion, Fick's first law states that the particles will diffuse from regions of high density to regions of low density with a magnitude that is proportional to the spatial gradient (Fick [1855]). Therefore, whatever particles move out of their initial  $\mathbf{\Lambda}$  bin must be replaced by an equal number of particles coming into that bin during  $\Delta t$  in a state of equilibrium. Suppose we define the *net diffusion velocity*,  $\dot{\mathbf{\Lambda}}$ , as the average collective displacement per unit time in invariant space of an ensemble of trapped particles due to diffusion. The continuity equation to conserve the number of particles would then be

$$\frac{\partial f_0}{\partial t} = -\nabla_{\mathbf{\Lambda}} \cdot (\dot{\mathbf{\Lambda}} f_0) \quad (1.38)$$

If we consider a uniform distribution of particles, such that  $\partial_{\Lambda_i} = \dot{\mathbf{\Lambda}} = 0$  by Fick's law, substituting Equation 1.38 into Equation 1.35 and integrating with respect to  $\mathbf{\Lambda}$  allows us to write the simplifying relationship (in the absence of sources and sinks)

$$D_{\Lambda_i} = \frac{\partial(D_{\Lambda_i \Lambda_i})}{\partial \Lambda_i} \quad (1.39)$$

The final, simplified, Fokker Planck equation can now be written as

$$\frac{\partial f_0}{\partial t} = \sum_{i=1}^3 \sum_{j=1}^3 \frac{\partial}{\partial \Lambda_i} \left( D_{\Lambda_i \Lambda_j} \frac{\partial f_0}{\partial \Lambda_j} \right) + Q - S \quad (1.40)$$

As relevant for this thesis, we consider only radial diffusion due to violation of the third adiabatic invariant

$$\left. \frac{\partial f}{\partial t} \right|_{(\mu, J)} = \left. \frac{\partial f}{\partial \Phi} \left( D_{\Phi \Phi} \frac{\partial f}{\partial \Phi} \right) \right|_{(\mu, J)} \quad (1.41)$$

Earlier we mentioned that it is more practical to use the Roederer [1970]  $L^*$  parameter in place of  $\Phi$ . Suppose we want to transform distribution functions  $f(\mu, J, \Phi) \rightarrow g(\mu, J, L^*)$ . For an arbitrary coordinate system  $(I_1, I_2, I_3)$  the Fokker-Planck equations can then be transformed via the following

$$\frac{\partial}{\partial t} f(I_1, I_2, I_3, t) = \sum_{i,j=1}^3 \frac{1}{J_{\Lambda I}} \frac{\partial}{\partial I_i} \left( G_{\Lambda I} \hat{D}_{I_i I_j} \frac{\partial f}{\partial I_j} \right) \quad (1.42)$$

where  $G_{\Lambda I}$  is the Jacobian as in Equation 1.29.  $\hat{D}$  are the diffusion coefficients in the new coordinate system

$$\hat{D}_{I_i I_j} = \sum_{k,l=1}^3 \frac{\partial I_i}{\partial \Lambda_k} D_{\Lambda_{kl}} \frac{\partial I_j}{\partial \Lambda_l} \quad (1.43)$$

Using the definition for  $L^*$  in Equation 1.24 such that  $G_{\Phi L} = |\partial L / \partial \Phi| = L^2 / 2\pi B_E R_E^2$  we obtain the transformed radial diffusion equation

$$\left. \frac{\partial f}{\partial t} \right|_{(\mu, J)} = L^2 \left. \frac{\partial f}{\partial L} \left( \frac{D_{LL}}{L^2} \frac{\partial f}{\partial L} \right) \right|_{(\mu, J)} \quad (1.44)$$

where we have dropped the \*'s for simplicity and the radial diffusion coefficient is defined as

$$D_{LL} = \frac{\langle (\Delta L)^2 \rangle}{2\tau_{drift}} \quad (1.45)$$

Development of well-performing radial diffusion coefficients is an open problem in space physics. All are based on radial diffusion driven by ultralow frequency (ULF) waves (specifically, ULF wave power) which have periods of  $\sim$ minutes capable of violating the third adiabatic invariant. A number of parameterized models already exist, which are based on a number of theoretical descriptions of magnetic and electric field perturbations (Fälthammar [1965]; Fei et al. [2006]; Lejosne [2019]) and generally developed empirically (Ali et al. [2015, 2016]; Brautigam and Albert [2000]; Brautigam et al. [2005]; Huang et al. [2010b]; Liu et al. [2016]; Ozeke et al. [2012, 2014]). These deterministic empirical models, however, can differ by orders of magnitude (Huang et al. [2010b]).

Roederer and Zhang [2014] state that Fokker-Planck diffusion theory is *"the art of creating pleasing diffusion coefficients (where 'pleasing' means yielding solutions of the diffusion equation that are in agreement with the data)"*. In this thesis we aim to satisfy this quote by modelling  $D_{LL}$  probabilistically, that is, allowing for the natural variability of  $D_{LL}$  (and implicitly ULF wave power) in the radial diffusion coefficient and explore the impact in the radial diffusion equation. This means that  $D_{LL}$  will be described by probability distributions rather than deterministic values, known as *stochastic parameterization*. Such an approach in modelling has already shown significant accuracy gains in other scientific fields, such as meteorology (e.g. Berner et al. [2017]).

After reviewing the theory and current state of  $D_{LL}$  modelling, we illustrate the impact of accounting for diffusion coefficient variability in ULF wave driven radial diffusion models (Thompson et al. [2020b]). Following this, we explore the data which comprise  $D_{LL}$ , finding sound probabilistic descriptions for each relevant variable with uncertainties quantified. To finish, we revisit the radial diffusion equation with an authentic proba-

bilistic  $D_{LL}$  model to highlight the shortfall of current models and provide a novel way to model radial diffusion henceforth.

## CHAPTER 2

## RADIAL DIFFUSION

The concept of radial diffusion is one of the oldest areas of magnetospheric research, first postulated to describe the existence of the Van Allen radiation belts (Van Allen and Frank [1959]) a year after their discovery (Parker [1960]). Since then it is viewed as one of the dominant source and loss mechanisms of outer radiation belt particles. Determining uncertainties in state-of-the-science descriptions of radial diffusion is not straightforward, comprising many elements. As perfectly put by Lejosne and Kollmann [2020]

*“...radial diffusion remains an elusive process despite many years of research. Doubts upon the efficacy of the radial diffusion process remain. Various definitions exist. There is a variety of analytic expressions to quantify radial diffusion present in the literature. The role played by the different possible drivers of radial diffusion remains uncertain. For all these reasons, advancing radial diffusion research constitutes a major scientific challenge...”*

The point about the efficacy of radial diffusion is notable. Quantifying uncertainty in radial diffusion does not primarily concern obtaining accurate diffusion amplitudes as inferred from observations (Roederer and Zhang [2014]), but rather to gain a better understanding of the relative contributions of other processes which influence the outer belt particle distribution too. Specifically, phase space density peaks in the heart of the belts which are enhanced during magnetically active periods are more indicative of local

acceleration (energy diffusion, Horne and Thorne [1998]). Indeed, there is an ongoing debate between the relative importance of radial diffusion and local acceleration as the dominant acceleration process in the radiation belts (Jaynes et al. [2018b]), as shown in Figure 2.1.

As such, in the radial diffusion equation we saw that the rate of particle transport is controlled by the radial diffusion coefficient  $D_{LL}$ . It is useful to remember that  $D_{LL}$  is not an observable *physical quantity*, however - the radial diffusion equation describes the net outcome of changes in particle drifts due to electric and magnetic field perturbations, which individually act like random walks under the diffusive approximation. A range of electromagnetic phenomena and wave modes could therefore contribute to  $D_{LL}$  which together alter the spatial distribution and acceleration of outer radiation belt electrons (e.g. Shprits et al. [2008a]). It is generally accepted, however, that the driver of the electromagnetic perturbations which violate the third adiabatic invariant resulting in radial diffusion is ULF waves (e.g. Elkington et al. [1999]; Shprits et al. [2006]; Ukhorskiy et al. [2009]), which have long azimuthal wavelengths, in the Pc5 band ( $\sim 1.67$ - $6.67$  mHz, Jacobs et al. [1964]). In fact, theoretical derivations for  $D_{LL}$  found it to be proportional to a stationary power spectral density (Fälthammar [1965]; Fei et al. [2006]; Lejosne [2019]), which has been subsequently attributed to ULF wave power.

Unpacking the uncertainty in state-of-the-science  $D_{LL}$  models may be addressed by incorporating the full distribution (in a probabilistic sense) of ULF wave power. However, this is too simplistic. The approaches taken to derive each  $D_{LL}$  parameterization all take different approaches - they are based on a number of simplifying assumptions and theoretical frameworks, whilst using a multitude of different instrumentation to derive the function form of  $D_{LL}$  (which have associated calibration and observation errors). It is clear that uncertainties are compounded by the multiple approximations required in each of these different approaches. These functional forms of  $D_{LL}$  are not the only source of uncertainty for radial diffusion. Implementation of the radial diffusion equation in a given transport model is dependent on numerical schemes (William et al. [1989]), as well as boundary conditions inferred from electron flux data at the inner and outer radial boundaries (e.g. Glauert et al. [2014a, 2018]), each with associated uncertainties.

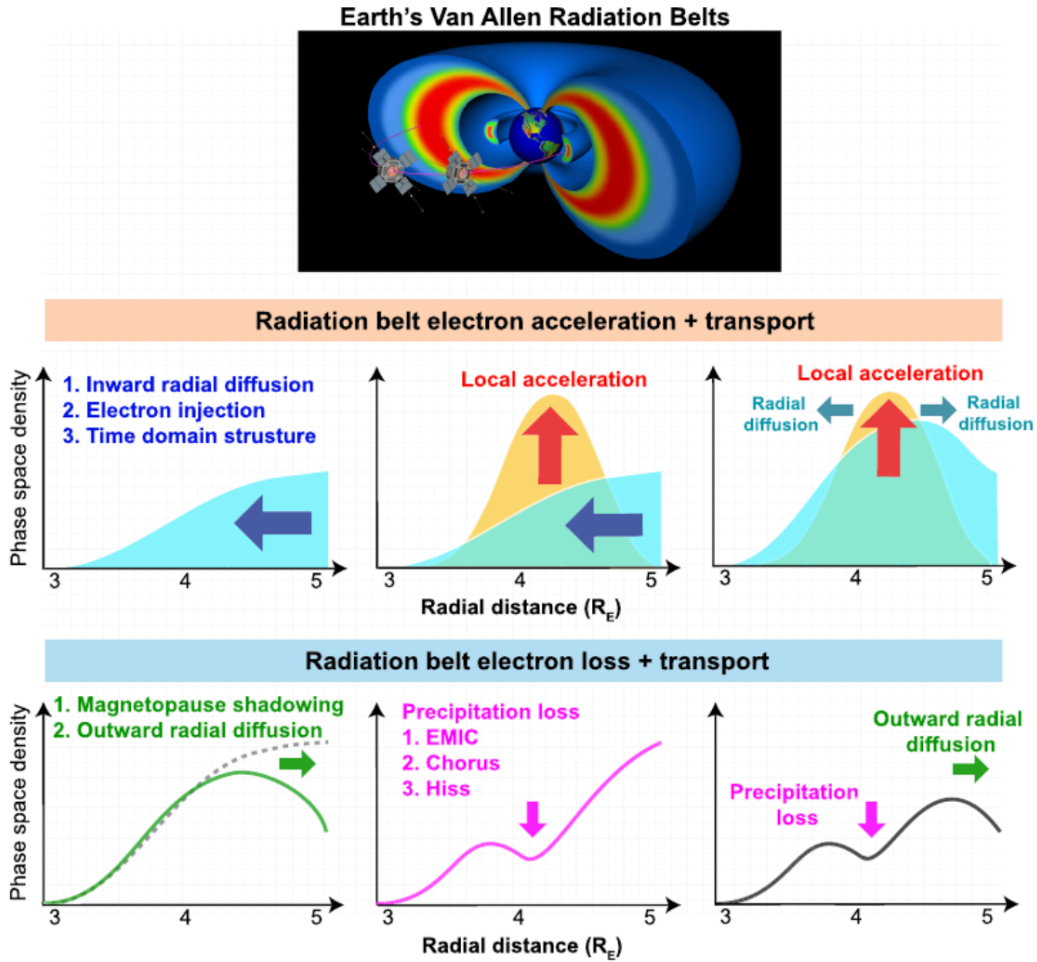


Figure 2.1: A schematic illustration summarizing the acceleration and loss processes of outer radiation belt electrons. (top) 3-D structure of the Van Allen radiation belts and the twin Van Allen Probes. (middle) Physical processes leading to radiation belt electron acceleration and transport. (bottom) Physical mechanisms driving radiation belt electron loss and transport. The Figure in the top panel was produced by Johns Hopkins University Applied Physics Laboratory/National Aeronautics and Space Administration. EMIC = Electromagnetic Ion Cyclotron. Taken from Li and Hudson [2019].

To illustrate the scope of this problem it is useful to create an *uncertainty tree diagram* stemming from the radial diffusion equation, which we have done in Figure 2.2. The goal of this thesis is to address and quantify some of the larger sources of uncertainty present in the tree. Specifically, we consider a number of these uncertainties which relate to ULF wave power spectral density (PSD in Figure 2.2), the drift-shell parameter  $L^*$  (in the assignment of observations of ULF wave power to drift-shells), and the applicability of ground-based instrumentation for remotes sensing  $D_{LL}$ .

This work does not provide a full solution the problem, but should open the door for researchers to be inquisitive about the impact of choices made when constructing  $D_{LL}$  and the imposed effect on the radial distribution of particles, relative to inclusion of the natural variability of  $D_{LL}$ , following application of the radial diffusion equation (see Chapter 3, Thompson et al. [2020b]). To gain a deeper understanding of the current state of  $D_{LL}$  modelling and the corresponding uncertainties within, in this Chapter we begin by deriving the theoretical 'pillars' upon which most radial diffusion coefficients are based, which introduce the connection to ULF wave power. Following this we detail existing formulations of  $D_{LL}$ , some of which are used operationally in radiation belt models (e.g. Glauert et al. [2018]). With a detailed understanding of how  $D_{LL}$  have been created, we can begin to explore how they might be modified to include any natural variability in a more informative, probabilistic representation of radial diffusion.

## 2.1 Theoretical frameworks for radial diffusion

Most modern radial diffusion coefficient parameterizations are based upon two central analytic formalisms - the works by Fälthammar [1965, 1968] and Fei et al. [2006]. While the approaches to their derivations are similar, both investigating the radial displacement of particles due to linear electric and magnetic field perturbations, there is one key difference: one method is fully inclusive of the underlying physics, the other is fully described by observations, respectively. This difference is that Fälthammar [1965, 1968] considered the phase relation between the magnetic field variations and the induced electric fields (as found in observations, see Perry et al. [2005] Figure 1), whereas Fei et al. [2006] consid-

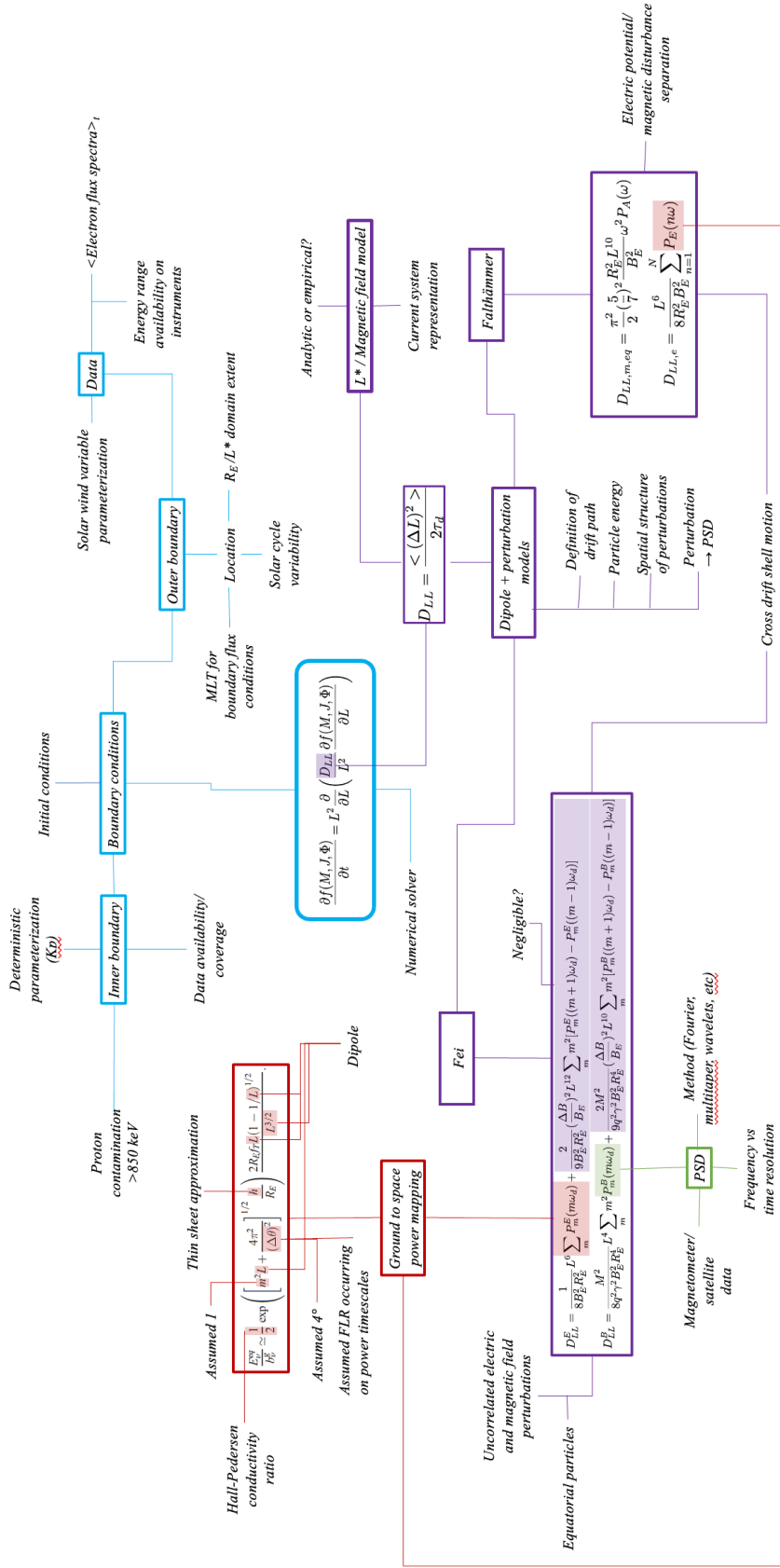


Figure 2.2: Uncertainty tree diagram for radial diffusion, which lists sources of uncertainty relevant to parameterization of the diffusion coefficient  $D_{LL}$ , as well as numerical implementation of the radial diffusion equation itself.

ered them independent. We note that Fei's assumption of independence was based on an erroneous misinterpretation of the work by Brizard and Chan [2001a] and is also inconsistent with Faraday's Law (Lejosne and Kollmann [2020]). This allowed Fei et al. [2006] to separate the radial diffusion coefficients into independent compressional magnetic and azimuthal electric components, whilst Fälthammar [1965, 1968] considers the electromagnetic and electrostatic. Since the separation of single-point measured electric fields into its convective and inductive components is very difficult (e.g. Brautigam et al. [2005]), the Fei et al. [2006] coefficients are clearly more suited to observations at the expense of omitting the relationship between the electric and magnetic field components.

The Fälthammar [1965] electromagnetic (which includes the induced electric field) and electrostatic radial diffusion coefficients are given by

$$D_{LL,m,eq} = \frac{\pi^2}{2} \left(\frac{5}{7}\right)^2 \frac{L^{10} R_E^2}{B_E^2} \omega^2 P_A(\omega) \quad (2.1)$$

$$D_{LL,e} = \frac{L^6}{8R_E^2 B_E^2} \sum_{n=1}^N P_E(n\omega) \quad (2.2)$$

where  $L$  is the L-Shell,  $R_E$  the Earth's radius,  $B_E$  the equatorial magnetic field strength at the Earth's surface,  $\omega$  is the electron drift frequency (resonant with the ULF wave via the drift-resonance condition  $\omega = m\omega_d$  for ULF wave frequency with  $\omega_d$  and azimuthal wavenumber  $m$ ) and  $P_A, P_E$  are the power spectra of the asymmetric electromagnetic field and electrostatic perturbations, respectively.

On the other hand, the Fei et al. [2006] compressional magnetic and azimuthal electric radial diffusion coefficients are given by

$$D_{LL}^{B,Sym} = \frac{\mu^2 L^4}{8q^2 \gamma^2 B_E^2 R_E^4} \sum_n n^2 P_n^B(n\omega) \quad (2.3)$$

$$D_{LL}^{E,Sym} = \frac{1}{8B_E^2 R_E^2} L^6 \sum_n P_n^E(n\omega) \quad (2.4)$$

where  $\mu$  is the magnetic moment and  $P^B, P^E$  are the power spectra of the magnetic and electric perturbations, respectively.

For a full derivation of these equations please refer to the Appendix at the end of this thesis. A schematic showing both the discrepancies and similarities between Fälthammar

Study	Diffusion Coefficient	Component	Perturbations
Fälthammar [1965]	$D_{LL,m,eq} = \frac{\pi^2}{2} \left(\frac{5}{7}\right)^2 \frac{L^{10} R_E^2}{B_E^2} \omega^2 P_A(\omega)$	Electromagnetic	Magnetic
	$D_{LL,e} = \frac{L^6}{8R_E^2 B_E^2} \sum_{n=1}^N P_E(n\omega)$	Electrostatic	Electric potential
Fei et al. [2006]	$D_{LL}^{B,Sym} = \frac{\mu^2 L^{*4}}{8q^2 \gamma^2 B_E^2 R_E^4} \sum_n n^2 P_n^B(n\omega)$	Magnetic	Magnetic
	$D_{LL}^{E,Sym} = \frac{1}{8B_E^2 R_E^2} L^{*6} \sum_n P_n^E(n\omega)$	Electric	Electric

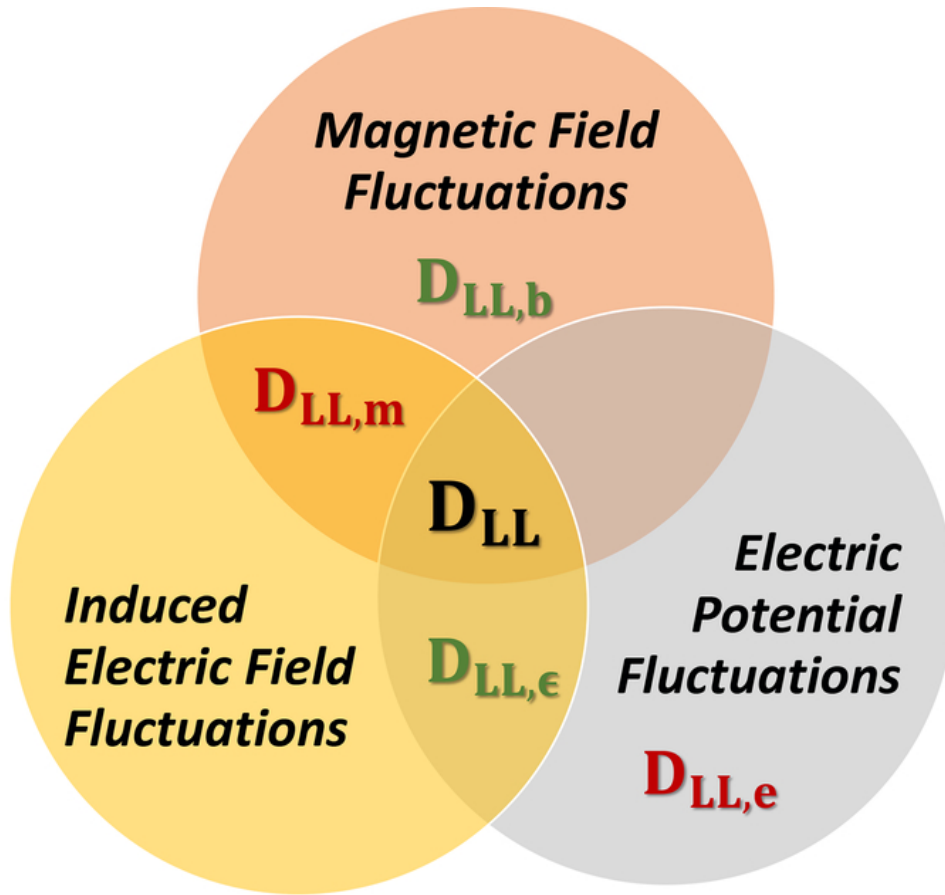
Table 2.1: Summary of the descriptions of radial diffusion by Fälthammar [1965] and Fei et al. [2006]. Diffusion coefficients are shown for each relevant component in the separation of  $D_{LL}$ , as well as the field perturbations from which they were derived. Note that only the symmetric components of Fei et al. [2006] are shown as the asymmetric components are often smaller by many orders of magnitude (see Fei et al. [2006]).

[1965, 1968] and Fei et al. [2006] is given in Figure 2.3. In the following Section we discuss flaws in these theoretical approaches along with recent advances which aim to address some of the flaws in both approaches (Lejosne [2019]).

### 2.1.1 Beyond Fälthammar and Fei

A summary of the Fälthammar [1965] and Fei et al. [2006] descriptions of radial diffusion is given in Table 2.1. While these are the prevailing formalisms from which modern parameterizations of  $D_{LL}$  were derived, they are limited in scope for use in radiation belt models. For example:

- Both assumed that the background magnetic field is mostly dipolar. In reality, the background field is more complex than this and is modelled as a gradient of a magnetic scalar potential, which varies over time to encapsulate the secular variation of the Earth’s magnetic field (Thébault et al. [2015]).
- Perturbations to the magnetic and electric fields are presumed to be linear although this may not be the case.
- The Fei et al. [2006] approach is only valid for equatorial particles. However, *in situ* it is often used for off-equatorial particles (e.g. Sandhu et al. [2021]).



**Fälthammar (1965):**  $D_{LL} = D_{LL,m} + D_{LL,e}$

**Fei et al. (2006):**  $D_{LL} = D_{LL,b} + D_{LL,\epsilon}$

Figure 2.3: Fälthammar [1965, 1968] and Fei et al. [2006] made different choices when separating the different radial diffusion drivers. Fälthammar [1965, 1968] studied radial diffusion due to magnetic field fluctuations, including the effect of the induced electric fields ( $D_{LL,m}$ ). He also studied radial diffusion due to electric potential fluctuations ( $D_{LL,e}$ ). On the other hand, Fei et al. [2006] studied radial diffusion driven by magnetic field fluctuations, in the absence of any kind of electric field fluctuation ( $D_{LL,b}$ ). They also studied independently radial diffusion driven by electric field fluctuations, regardless of their nature ( $D_{LL,\epsilon}$ ). In all cases, the total radial diffusion coefficient  $D_{LL}$  is usually introduced as an aggregate, equal to the sum of the different contributions. Taken from Lejosne [2019].

Recent work by Lejosne [2019] has directly challenged a number of these limitations taking steps toward more consistent  $D_{LL}$  parameterizations, providing a more general approach (although still simplified) which is independent of magnetic field topology (starting from the equations of third adiabatic invariant violations, Northrop [1963]) and does not decouple any of the magnetic and electric perturbations. Notably, they also quantified the error in the Fei et al. [2006] equations, by applying the Fei et al. [2006] approach to the Fälthammar [1965] perturbation description, finding a shortfall of Fei et al. [2006] by a factor of 2 (provided no electric potential disturbances).

In any case, while adopting a self-consistent theoretical description of  $D_{LL}$  at this stage would be the most timely and intuitive approach, it would require a complete upheaval of the modern, empirical  $D_{LL}$  parameterizations based on ULF wave power observations which simplify the work of Fälthammar [1965, 1968] and Fei et al. [2006] (e.g. Ali et al. [2015, 2016]; Brautigam and Albert [2000]; Brautigam et al. [2005]; Huang et al. [2010a]; Liu et al. [2016]; Ozeke et al. [2012, 2014]). An intermediate, manageable step would be to quantify uncertainties in these simplified, modern approaches relative to their umbrella Fälthammar [1965, 1968] and Fei et al. [2006] formalisms, and then determine these uncertainties relative to more advanced theoretical descriptions once they become available. We outline the current state of modern  $D_{LL}$  parameterizations in the following Section.

## 2.2 Modern parameterizations of the radial diffusion coefficient

Due to the practicality of separating magnetic and electric field perturbations it is unsurprising that many of the modern  $D_{LL}$  parameterizations are based upon the Fei et al. [2006] approach. On the other hand, it has been found that inclusion of the electrostatic component from Fälthammar [1965, 1968] often results in overestimation of electron density in the slot region (Kim et al. [2011]; Ozeke et al. [2012]) and is usually omitted, allowing use of the electromagnetic component alone (which can be constrained by observations) in operational models (e.g. Glauert et al. [2014b]). Here, we detail the state-of-the-art deterministic parameterizations of  $D_{LL}$  in chronological order.

### 2.2.1 Brautigam and Albert [2000]

One of the earliest works, Brautigam and Albert [2000] parameterized the electromagnetic radial diffusion coefficient from  $L = 3 - 6.6$  ( $L = r/R_E$ ) as a function of geomagnetic index  $K_p$ , based on discrete values of ULF wave power spectra measured at  $L = 4$  (Lanzerotti and Morgan [1973]) and  $L = 6.6$  (Lanzerotti et al. [1978]). In Lanzerotti and Morgan [1973], calculations for  $L^{-10}D_{LL}^{EM}$  (where superscript  $EM$  denotes electromagnetic) were made over 18 days from ULF wave spectra measured by ground magnetometers at  $L = 4$ . These were drift-averaged, since local night values were somewhat larger than local day, and showed a dependency on the daily averaged magnetic index from Fredericksburg ( $K_{FR}$ ). Similarly in Lanzerotti et al. [1978],  $L^{-10}D_{LL}^{EM}$  was calculated from a month of geosynchronous *in situ* measurements at  $L = 6.6$ , which were drift-averaged and parameterized by the 12 hour sum of geomagnetic index  $K_p$  ( $K_{p12}$ ).

In Figure 7 of Lanzerotti and Morgan [1973], at  $L = 4$ , daily drift-averaged values of  $L^{-10}D_{LL}^{EM}$  were plotted against the daily-averaged  $K_{FR}$  index. Each of the drift-averaged values corresponded to electrons with  $\mu = 750$  MeV/G. Brautigam and Albert [2000] calculated a best fit line to these discrete measurements to obtain the relationship  $\log_{10}(L^{-10}D_{LL}^{EM}(L = 4)) = 0.75K_{FR} - 10.2$ . In Figure 4 of Lanzerotti et al. [1978], at  $L = 6.6$  a similar plot is shown, although  $L^{-10}D_{LL}^{EM}$  were plotted separately for local day and local night as a function of  $K_{p12}$ . In this Figure values were shown for  $\mu = 115$  and 500 MeV/G. Averaging the day and night measurements (although unstated as to which  $\mu$ ) Brautigam and Albert [2000] found a best fit line of  $\log_{10}(L^{-10}D_{LL}^{EM}(L = 6.6)) = 0.07K_{p12} - 8.5$ .

Applying a linear fit to these curves over the domain  $L = 3.6 - 6$  for  $K_p = 1 - 6$  (see Brautigam and Albert [2000] Figure 5), it was found that each did not exhibit the theoretical  $L^{10}$  dependence assumed in their determination. Yet, Brautigam and Albert [2000] still sought an  $L^{10}$  dependence,  $10^{aK_p-b}L^{10}$ , that maximised agreement with the discrete values (ie Brautigam and Albert [2000] Figure 5) via a least-squares fit. The resulting electromagnetic radial diffusion coefficient parameterized by geomagnetic index

Kp was

$$D_{LL,B\&A}^{EM}(L, Kp) = 10^{0.506Kp-9.325} L^{10} \quad (\text{day}^{-1}) \quad (2.5)$$

where *B&A* denotes *Brautigam and Albert* and valid for  $Kp = 1 - 6$ .

At this time there was a lack of *in situ* measurements to estimate radial diffusion driven by electric potential disturbances. However, Brautigam and Albert [2000] employed the derivation proposed by Cornwall [1968], which assumed a substorm convection electric field fluctuation spectrum characterized by a rapid rise time and exponential decay. We omit the equation here since an updated electrostatic diffusion coefficient based on observations was formulated in Brautigam et al. [2005]. Implementing these radial diffusion coefficients over an isolated geomagnetic storm (with a time-dependent boundary condition and electron lifetime), Brautigam and Albert [2000] found excellent agreement with Combined Release and Radiation Effects Satellite (CRRES) data for electrons with energies  $\leq 314\text{MeV}/G$ , but discrepancies (up to a factor of 5) for high-energy electrons  $> 700\text{MeV}/G$ .

### 2.2.2 Brautigam et al. [2005]

Near-equatorial CRRES observations from the on-board Electric Field Instrument (EFI) and spanning January-October 1991 were used to develop the electrostatic diffusion coefficient in an assumed purely electrostatic field (Brautigam et al. [2005]). To simplify the calculation it was assumed that only the  $m = 1$  ULF azimuthal wavenumber (the global mode) was non-zero, that  $x, y$  (Cartesian) azimuthal electric field measurements are independent of azimuth, and that the FFT window over which power spectral density is calculated remains fixed at a particular L-Shell (this assumption is more appropriate for increasing radial distance). Following the framework of Fälthammar [1965] and the azimuthal electric field perturbation description from Holzworth and Mozer [1979], fits were made to the power spectral density averages at each frequency of the form

$$P(f_d, L, Kp) = aL^b \exp(cKp) \quad (2.6)$$

using singular value decomposition (William et al. [1989]). Here,  $f_d$  is the drift frequency and the units of  $P$  are  $(mV/m)^2 mHz^{-1}$ , valid for  $L = 3.5 - 6.5$  and  $Kp = 1 - 6$ . Values

for  $a, b, c$  for fixed drift frequency (independent of L-Shell) can be found in Table 3 of Brautigam et al. [2005]. The drift-frequency formula for an equatorially mirroring particle of specified energy in a dipole is (Schulz and Lanzerotti [1974])

$$f_d = \frac{0.1183\mu}{\sqrt{L^4 + 1.2133L + \mu}} \quad (2.7)$$

where magnetic moment  $\mu$  is in units of MeV/G. The resulting electrostatic (ES) radial diffusion coefficient is then

$$D_{LL,B\&A}^{ES}(f_d, L, Kp) = \frac{L^6}{8B_E^2 R_E^2} P(f_d, L, Kp) \quad (\text{day}^{-1}) \quad (2.8)$$

As mentioned previously, it has been found that inclusion of  $D_{LL,B\&A}^{ES}$  in radiation belt simulations leads to unrealistic outputs of electron density (c.g. Kim et al. [2011]) and is often omitted. Common practice therefore assumes that

$$D_{LL,B\&A} = D_{LL,B\&A}^{EM} \quad (2.9)$$

and energy dependence from  $D_{LL}$  is no longer present.

### 2.2.3 Ozeke et al. [2012, 2014]

One of the most widely used  $D_{LL}$  in modern radiation belt models is that of Ozeke et al. [2012, 2014], found using the Fei et al. [2006] formalism. As in Brautigam and Albert [2000]; Brautigam et al. [2005], both the magnetic and electric radial diffusion coefficients are parameterized by geomagnetic index Kp. For the magnetic component hourly compressional magnetic power spectral densities from 9 years of GOES spacecraft data at L=6.6 (Ozeke et al. [2012]) and 4 years of each Time History of Events and Macroscale Interactions during Substorms (THEMIS) spacecraft data, were considered for statistical analysis. Splitting the power into functions of L-Shell, Kp and frequency, power-law fits were made to the median power

$$P_{Total,Oz}^B = f^{-2} 10^{0.0327L^2 + 0.625L - 0.0108Kp^2 + 0.499Kp - 25.9} \quad (2.10)$$

which has units  $\text{nT}^2 \text{ mHz}^{-1}$ . To arrive at the magnetic and electric radial diffusion coefficients, several assumptions were made about the measured power spectral densities.

Firstly all wavenumbers  $m$  are assumed to be non-negative. Secondly the measured power is representative of the sum of power at all wavenumbers. Finally, power measured at a single wavenumber can be represented by some weighting ( $a_m$ ) of the total power (independent of wave frequency or L-shell), with weights across all wavenumbers summing to one.

The resulting compressional magnetic radial diffusion coefficient (Fei et al. [2006]) is then

$$D_{LL,Oz}^B(f, L, Kp) = \frac{\mu^2 L^4}{8q^2 \gamma^2 B_E^2 R_E^4} \sum_m m^2 a_m P_{Total,Oz}^B \quad (2.11)$$

$$= \frac{\mu^2 L^4}{8q^2 \gamma^2 B_E^2 R_E^4} \sum_m m^2 a_m \left( \frac{m\omega_d}{2\pi} \right)^{-2} 10^{0.0327L^2 + 0.625L - 0.0108Kp^2 + 0.499Kp - 25.9} \quad (2.12)$$

The angular drift frequency,  $\omega_d$ , for  $90^\circ$  pitch-angle radiation belt electrons in the equatorial plane of a dipole is given by

$$\omega_d = \frac{-3\mu}{q\gamma(LR_E)^2} \quad (2.13)$$

where  $\gamma$  is the relativistic correction factor and  $q$  the electron charge. Substituting this in the energy dependence is removed and we arrive at the desired diffusion coefficient

$$D_{LL,Oz}^B(L, Kp) = 6.62 \times 10^{-3} L^8 10^{0.0327L^2 + 0.625L - 0.0108Kp^2 + 0.499Kp} \quad (2.14)$$

The electric component, unlike any other diffusion coefficients in this Section, was found empirically using ground-data. Ozeke et al. [2014] used >15 years of power spectral densities calculated from ground magnetometer measurements at 7 different L-Shells. These measurements were mapped using an analytic relationship between the ground magnetic toroidal component ( $b_{\phi,ob}^g$ ) and the azimuthal equatorial electric field ( $E_\phi^{eq}$ ) assuming a *field line resonating* (see Chapter 6) ULF wave (Ozeke et al. [2009])

$$P_{eq}^E = \left[ \frac{E_\phi^{eq}}{b_{\phi,ob}^g} \right]^2 P_g^B \quad (2.15)$$

$$\frac{E_\phi^{eq}}{b_{\phi,ob}^g} = \frac{2f_{ob}}{3mHz} \frac{E_\phi^{eq}}{b_\nu^i} \exp \left( \left[ m^2 L + \frac{4\pi^2}{(\Delta\theta)^2} \right]^{1/2} \frac{h}{R_E} \right) \quad (2.16)$$

Here,  $b_\nu^i$  is the poloidal magnetic field component just above the ionosphere,  $f_{ob}$  is the observed wave frequency at the ground,  $\Delta\theta$  is the latitudinal width of the wave as seen

at the ground,  $h$  is the height of the ionosphere and  $m$  is the azimuthal wavenumber of the ULF wave. In current manifestations of this model,  $\Delta\theta$  is assumed to be  $4^\circ$ , and  $m$  is assumed to be 1.

For each magnetometer station (L-Shell) the power spectral densities were split into frequency and Kp with the medians determined. Each of these medians were then mapped to the equatorial electric field using Equation 2.16. To obtain the total electric power, the median power across frequency was determined at each  $(L, Kp)$ . The  $\log_{10}$  median power was then determined and, using the method of least squares, these  $\log_{10}$  median values were fit to linear functions of Kp and L-shell. By taking the mean across frequencies, Ozeke et al. [2014] effectively removed any energy dependence in the electric diffusion coefficient. In many instances, the median power varies very little with the logarithm of frequency, which justified the removal of energy dependence. However, there are circumstances where it varies strongly (see Ozeke et al. [2014], Figure 1), which introduces some uncertainty in this approach.

Nonetheless, following the assumptions for total power used for the compressional magnetic component, the resulting azimuthal electric radial diffusion coefficient was

$$D_{LL,Oz}^B(L, Kp) = \frac{1}{8B_E^2 R_E^2} L^6 P_{Total,Oz}^E \quad (2.17)$$

$$= \frac{1}{8B_E^2 R_E^2} L^6 10^{0.217L+0.461Kp-4.11} \quad (2.18)$$

$$= 2.16 \times 10^{-8} L^6 10^{0.217L+0.461Kp} \quad (\text{days}^{-1}) \quad (2.19)$$

We note that both coefficients are only valid for  $Kp \leq 6$ .

There are a number of uncertainties associated with the Ozeke et al. [2014] coefficients, outside of those associated with Fei et al. [2006]. Firstly, simplifying fits to the power were made to remove energy dependence. The resulting coefficients were successfully compared to mapped median ground power (see Ozeke et al. [2014]) demonstrating that the energy invariance assumption may be reasonable for the electric component. However, the energy dependence of the magnetic component has not been fully investigated. Another uncertainty is the use of median power to define  $D_{LL}$  - it is not certain how representative median power is of radial diffusion when compared to observations in general. Fortunately, Ozeke et al. [2014] reported that the interquartile-range lies 3 times above and below

(ie log-symmetric) their analytic expressions, which some provides some insight into the potential uncertainty of  $D_{LL}$ . However as we will demonstrate in Chapter 3, it would be useful to also know the shape of the distributions, as well as the coherence across drift-shells, to determine the impact of this uncertainty in the radial diffusion equation.

#### 2.2.4 Ali et al. [2015, 2016]; Ali [2016]

Ali et al. [2015] also adopted the Fei et al. [2006] formalism and used CRRES data to investigate the magnetic ULF wave power spectra in space and the subsequent magnetic diffusion coefficient. The goal was to compare to the works of Brautigam and Albert [2000]; Brautigam et al. [2005] to determine the relative importance of each of the components (electromagnetic and electrostatic) in radial diffusion. Since the electromagnetic Brautigam and Albert [2000] coefficient was based on severely temporally and spatially limited data, this study also provides further insight into the statistical nature of magnetic power. As in Brautigam et al. [2005] only the global azimuthal wavenumber ( $m = 1$ ) was considered, however, Ali et al. [2015] also considered the power distribution in azimuth, with 6h bins centered at midnight, dawn, noon, and dusk (hereby denoted *MLT sectors*).

Median magnetic wave power were separated into ( $L, Kp, MLT$ ) bins and a nonlinear least squares fit was performed across frequency of the form

$$P^B(f) = a_1 \exp\left(-\left(\frac{f - a_2}{a_3}\right)^2\right) + a_4 f + a_5 \quad (2.20)$$

The non-linear fit was used to circumvent misconceptions of the least-squares fits used in other studies (Brautigam and Albert [2000]; Ozeke et al. [2014]). For least-squares to work errors must have zero mean (exogeneity). Previous studies used least-squares on logarithmic representations of wave power. If errors for wave power measurements satisfy exogeneity, upon taking the logarithm this condition is violated. This can lead to biasing of least-squares estimates on the log-transformed data (see Ali et al. [2015] for full details).

When obtaining the drift-averaged wave power at each frequency Ali et al. [2015] acknowledged the bias of CRRES data to certain MLT sectors, taking a weighted arithmetic mean normalized by CRRES dwell time in each MLT sector. Therefore, weights were somewhat inversely proportional to the number of observations in each sector.

After computing  $D_{LL}^B$  for a number of  $(L, f, Kp)$  bins, a clear frequency dependence was found, scaling as a power law for lower frequencies while leveling off at higher frequencies. Fits were then made to these in a least-squares sense, with functional form of a Gaussian function plus a power law

$$D_{LL,A}^B[CRRES] = b_1 \exp\left(-\left(\frac{f - b_2}{b_3}\right)^2\right) + b_4 f^{b_5} \quad (2.21)$$

where the coefficients at each L-Shell can be found in a lookup table for different levels of geomagnetic activity. Using the same data set, in their thesis Ali [2016] extended this work to construct a diffusion coefficient with explicit energy dependence

$$D_{LL,A}^B[CRRES] = \exp(L + 0.00060104\mu + 0.10003KpL - 16.618) \quad (\text{days}^{-1}) \quad (2.22)$$

which is valid for  $L = 4 - 6.5$ ,  $Kp = 1 - 7$  and  $\mu = 500 - 5000 \text{ MeV}/G$ .

In Ali et al. [2016] the electric component was considered, but the paper also served as an update to the magnetic component. This time, data from the Electric Fields and Waves (EFW, Wygant et al. [2013]) and Electric and Magnetic Field Instrument Suite (EMFISIS, Kletzing et al. [2013]) instruments on board the Van Allen Probes were used. One key difference in this study is that a more complex description of the magnetic field topology was used (rather than a dipole), specifically, the empirical Tsyganenko and Sitnov [2005] storm-time magnetic field model. Therefore, diffusion will explicitly be in  $L^*$  as expected in Fokker-Planck diffusion theory (see Equation 1.45 in Chapter 2). Separating data in the same way and applying similar fits as in Ali [2016], the resulting magnetic and electric diffusion coefficients are

$$D_{LL,A}^B[RBSP] = \exp(-16.253 + 0.224KpL^* + L^*) \quad (2.23)$$

$$D_{LL,A}^E[RBSP] = \exp(-16.951 + 0.181KpL^* + 1.982L^*) \quad (2.24)$$

in units of  $\text{days}^{-1}$  and valid for  $Kp = 0 - 5$ . Note that the energy dependence was removed in the same way as in Ozeke et al. [2014] after finding that the median power spectra was seemingly invariant across frequency.

### 2.2.5 Liu et al. [2016]

This study followed Fei et al. [2006] but only the electric diffusion coefficient was considered due to the assumption that it is always orders of magnitude larger than the magnetic component. Seven years of near-equatorial electric field measurements from the Electric Field Instrument (EFI) on board THEMIS-D were used to calculate the azimuthal electric wave power. A dipole magnetic field was considered and power measurements were split into  $(L, f, Kp, MLT)$ , this time with hourly MLT discretization rather than MLT sector. Drift-averaged wave power was simply the median of all values on a given drift-shell at each frequency, which is likely biased to discrepancies in observation counts in each MLT bin. By using a multiparameter linear regression fitting technique, the resulting drift-averaged electric diffusion coefficient was given by

$$D_{LL,L}^E[THEMIS] = 1.115 \times 10^{-6} 10^{0.281Kp} L^{8.184} \mu^{-0.608} \quad (2.25)$$

A summary of the modern parameterizations of  $D_{LL}$  is provided in Table 2.2.

## 2.3 Assumptions and uncertainties

While modern parameterizations provide simple equations that are easy to implement in operational modelling, they collectively and individually have inherent uncertainty resulting from their construction. The most glaring, shared by almost all of the models, concerns the use of the median ULF power to describe radial diffusion at all times. The earliest works of Lanzerotti and Morgan [1973] and Lanzerotti et al. [1978] showed significant  $D_{LL}$  variability on relatively short timescales which is certainly important when trying to model radial diffusion through geomagnetic storms. They also considered  $D_{LL}$  averaged over different time scales, through parameterization of their respective indices ( $K_{FR}$  and  $Kp_{12}$ ), which may indicate that the temporal variability of  $D_{LL}$  is an important factor to consider. Biasing of observations to mostly quiescent times is likely to mask any variability when we consider median wave power. It will overestimate for very quiet periods and underestimate for very active periods, which could be a reason for the unreasonable

Diffusion Coefficient	Formalism	Component	Energy-dependence
$D_{LL,B\&A}^{EM}(L, Kp) = 10^{0.506Kp-9.325} L^{10}$	Fälthammar [1965]	Electromagnetic	No
$D_{LL,B\&A}^{ES}(f_d, L, Kp) = \frac{I^6}{8B_z^2 R_z^2} P(f_d, L, Kp)$	Fälthammar [1965]	Electrostatic	Yes
$D_{LL,Oz}^B(L, Kp) = 6.62 \times 10^{-3} L^8 10^{0.0327L^2+0.625L-0.0108Kp^2+0.499Kp}$	Fei et al. [2006]	Magnetic	No
$D_{LL,Oz}^B(L, Kp) = 2.16 \times 10^{-8} L^6 10^{0.217L+0.461Kp}$	Fei et al. [2006]	Electric	No
$D_{LL,A}^B[CRRES] = \exp(L + 0.00060104\mu + 0.10003KpL - 16.618)$	Fei et al. [2006]	Magnetic	Yes
$D_{LL,A}^B[RBSP] = \exp(-16.253 + 0.224KpL^* + L^*)$	Fei et al. [2006]	Magnetic	No
$D_{LL,A}^E[RBSP] = \exp(-16.951 + 0.181KpL^* + 1.982L^*)$	Fei et al. [2006]	Electric	No
$D_{LL,L}^E[THEMIS] = 1.115 \times 10^{-6} 10^{0.281KpL^{8.184}} \mu^{-0.608}$	Fei et al. [2006]	Electric	No

Table 2.2: Summary of modern parameterizations of  $D_{LL}$ . The formalism and respective component from which each was derived is provided, as well as whether they model energy dependence.

electron populations seen at lower drift shells when the electrostatic diffusion coefficient is included (e.g. Kim et al. [2011]). Inclusion of the natural variability of ULF wave power can have a significant impact on the phase space density undergoing radial diffusion, but we must also consider the multidimensional, multivariate distribution of ULF wave power which includes covariance across frequency, drift shell and azimuth (e.g. see Chapter 3, Thompson et al. [2020b]).

Encapsulating covariance means that **when** averages are taken becomes important. This is an issue for those  $D_{LL}$  models which consider drift-averaging (Ali et al. [2015, 2016]; Liu et al. [2016]) where the median power in each MLT sector was drift-averaged. The more accurate alternative is to obtain the median of a set of drift-averaged *in-situ* observations, but this requires a set of contemporaneous measurements in azimuth over a long period of time. When to apply averages is also an issue when wave power is remote sensed from the ground, as in Ozeke et al. [2014]. Coupling of ground observations to the equatorial electric field through an analytic mapping (Ozeke et al. [2009]) is an innovative approach to constructing  $D_{LL}$ , allowing for ways to capture both azimuthal and radial covariance of ULF wave power if the network of ground instruments is extensive enough. Problems arise when we consider that Ozeke et al. [2014] mapped the ground median power rather than calculating the median of the mapped power distribution. Of course, assumptions made on the parameters for the mapping (see below) render it constant for a given L-Shell and frequency, but if these assumptions are relaxed (see Chapter 6) the decision of when to perform averaging or median calculations becomes important. The average ground power mapped using the average mapping values (where no assumptions have been made on wavenumber, resonance width, etc) is unlikely to be equal to the average of individually mapped ground power observations. The concept of "diffusion coefficients resulting from the average of individual variables not being equal to the average of their collective distribution" has already been considered and shown to result in different levels of diffusion (Watt et al. [2021]).

Assumptions about the topology of the magnetic field is also a large source of uncertainty in the resulting  $D_{LL}$  formulations. Many of the parameterizations assume a dipolar background magnetic field. Although this can be attributed to the topologies considered

by Fälthammar [1965, 1968] and Fei et al. [2006], it is inconsistent with Fokker-Planck diffusion theory (Roederer and Zhang [2014]). By definition, the radial diffusion coefficient concerns the Roederer [1970]  $L^*$  parameter (or third adiabatic invariant  $\Phi$ ) which is generally not equal to the McIlwain [1961] L-Shell. This is mostly because  $L^*$  does not resemble a physical location (Roederer and Lejosne [2018b]). There is a misconception that the term radial diffusion implies the reference variable is equatorial radial distance (or L-Shell), however  $L^*$  accounts for changes in particle drift motions resulting from the difference between the real magnetic field and a magnetic dipole field under stationary conditions (Lejosne and Kollmann [2020]) - the two are clearly not interchangeable.

Finally, many of the parameterizations made assumptions concerning the structure of ULF waves. In many cases it was considered that only the  $m = 1$  azimuthal wavenumber contributed to the radial diffusion coefficients. This significantly simplified the algebra whilst also directly equating the ULF wave frequency to the drift frequency. However, both modelling (e.g. Tu et al. [2012]; Li et al. [2017]) and observational (e.g. Murphy et al. [2018]; Sarris et al. [2013]) studies have shown that instances of large power are ascribed to larger wavenumbers. This results in an overestimation of power in the  $m = 1$  mode (Drozdov et al. [2021]). Similarly, Ozeke et al. [2014] assumed that the latitudinal width of the resonant wave to enable mapping was  $\Delta\theta = 4^\circ$ . This assumption was seemingly subjective, as previous observational studies found larger widths (Rae et al. [2005]), and the variability of resonance width with azimuth has also been found and correlated with wave power variability (Glassmeier and Stellmacher [2000]).

While we have mentioned a number of uncertainties here, this list is not exhaustive. Observation errors from spacecraft are also present (Drozdov et al. [2020]), as well as calibrations between ground instruments. Since ULF wave power is approximated from discrete signals, whereas true power is defined over infinite time, there are also uncertainties in the spectral analysis techniques used to approximate power (see Chapter 6). Parameterization by Kp implicitly assumes three-hour temporal variability of ULF wave power and carries any inaccuracies of the index itself. In any case, listing the uncertainties provides a means to explore how to counter them. In the remainder of this thesis, we consider uncertainty resulting from descriptions of the magnetic field topology, non-

inclusion of the full distribution of statistical ULF wave power, and in the mapping of ground-observed field line resonances to infer equatorial azimuthal wave power. Following this we discuss how other uncertainties can be accounted for in future work. To motivate the importance of this work, in the next Chapter we illustrate the impact of accounting for variability in ULF wave radial diffusion models (Thompson et al. [2020b]).

## CHAPTER 3

# PILOT STUDY: ACCOUNTING FOR VARIABILITY IN ULF WAVE RADIAL DIFFUSION MODELS

The following manuscript has been published in the *Journal of Geophysical Research: Space Physics*. The full reference for this publication can be found in the bibliography under Thompson et al. [2020b].

## JGR Space Physics



## RESEARCH ARTICLE

10.1029/2019JA027254

## Special Section:

Particle Dynamics in the Earth's Radiation Belts

## Key Points:

- Ensemble numerical experiments of radial diffusion are performed using stochastic parameterization of diffusion coefficients
- When reasonable temporal and spatial variability of diffusion is included, the temporal evolution of phase space density changes
- Diffusion depends on temporal and spatial scales of variability, and the size and shape of the distribution of diffusion coefficients

## Supporting Information:

- Supporting Information S1
- Figure S1
- Figure S2
- Figure S3
- Figure S4
- Figure S5
- Figure S6

## Correspondence to:

R. L. Thompson,  
r.l.thompson@pgr.reading.ac.uk

## Citation:

Thompson, R. L., Watt, C. E. J., & Williams, P. D. (2020). Accounting for variability in ULF wave radial diffusion models. *Journal of Geophysical Research: Space Physics*, 125, e2019JA027254. <https://doi.org/10.1029/2019JA027254>Received 15 AUG 2019  
Accepted 9 JUN 2020  
Accepted article online 20 JUL 2020

©2020. The Authors.

This is an open access article under the terms of the Creative Commons Attribution License, which permits use, distribution and reproduction in any medium, provided the original work is properly cited.

## Accounting for Variability in ULF Wave Radial Diffusion Models

R. L. Thompson<sup>1</sup> , C. E. J. Watt<sup>2</sup> , and P. D. Williams<sup>2</sup> <sup>1</sup>Department of Mathematics and Statistics, University of Reading, Reading, UK, <sup>2</sup>Department of Meteorology, University of Reading, Reading, UK

**Abstract** Many modern outer radiation belt models simulate the long-time behavior of high-energy electrons by solving a three-dimensional Fokker-Planck equation for the drift- and bounce-averaged electron phase space density that includes radial, pitch-angle, and energy diffusion. Radial diffusion is an important process, often characterized by a deterministic diffusion coefficient. One widely used parameterization is based on the median of statistical ultralow frequency (ULF) wave power for a particular geomagnetic index Kp. We perform idealized numerical ensemble experiments on radial diffusion, introducing temporal and spatial variability to the diffusion coefficient through stochastic parameterization, constrained by statistical properties of its underlying observations. Our results demonstrate the sensitivity of radial diffusion over a long time period to the full distribution of the radial diffusion coefficient, highlighting that information is lost when only using median ULF wave power. When temporal variability is included, ensembles exhibit greater diffusion with more rapidly varying diffusion coefficients, larger variance of the diffusion coefficients and for distributions with heavier tails. When we introduce spatial variability, the variance in the set of all ensemble solutions increases with larger spatial scales of variability. Our results demonstrate that the variability of diffusion affects the temporal evolution of phase space density in the outer radiation belt. We discuss the need to identify important temporal and length scales to constrain variability in diffusion models. We suggest that the application of stochastic parameterization techniques in the diffusion equation may allow the inclusion of natural variability and uncertainty in modeling of wave-particle interactions in the inner magnetosphere.

**Plain Language Summary** The Van Allen outer radiation belt is a region in near-Earth space containing mostly high-energy electrons trapped by the Earth's geomagnetic field. It is a region populated by satellites that are vulnerable to damage from the high-energy environment. Many modern radiation belt models simulate the behavior of the high-energy electrons with a diffusion model, which describes how electrons spread out from areas of higher concentration to areas of lower concentration. An important process in these models is radial diffusion, driven by ultralow frequency (ULF) waves, where electrons are drawn from the outer boundary and accelerated toward Earth, or pushed away from the outer radiation belt and lost to interplanetary space. Radial diffusion is generally characterized by a parameter that provides a single output from the specified inputs and does not allow for any variability in the physical process. In this study we present a series of numerical experiments on radial diffusion, which allow for natural variability in both time and space and see how modeling of radial diffusion is impacted. Our results find that better understanding of temporal and spatial variations of ULF wave interactions with electrons, and being able to characterize these variations to a good level of accuracy, is vital to produce a robust description of radial diffusion over long timescales in the outer radiation belt.

## 1. Introduction

The Van Allen outer radiation belt is a typically quiescent torus-shaped region in near-Earth space between 13,000 and 40,000 km radial distance consisting mainly of electrons between 100s of keV and multiple MeV trapped by the Earth's geomagnetic field. Protons are also present and modeled in the radiation belts (Vacaresse et al., 1999), but here we focus on the high-energy electron population. The behavior of electrons in the outer radiation belt is affected by multiple processes, some of which are immediate responses to solar wind forcing, whereas some are more indirect energy pathways involving energy stored in the substorm cycle. Numerical modeling is a powerful tool to provide deep understanding of the behavior of the outer

radiation belt, allowing us to quantify the effects of different processes (e.g., Glauert et al., 2014; Reeves et al., 2012; Shprits et al., 2008).

From a more practical standpoint, the ability to model these physical processes is becoming increasingly important as Earth becomes more dependent on space-based technologies. As of 31 March 2020 there were 135 satellites operating in medium Earth orbit (MEO; 2,000–35,786 km) and 554 in geostationary orbit (GEO; 35,786 km), therefore operating in the heart of the belt (<https://www.ucsusa.org>). Outer radiation belt electrons can be hazardous to these spacecraft, but there are insufficient in situ measurements available to monitor the radiation environment directly. There remains a pressing need to develop accurate models of the outer radiation belt for operational purposes in addition to promoting further physical understanding.

One effective method to study the dynamics of the outer belt electrons is to model the evolution of electron phase space density (PSD)  $f(M, J, \Phi; t)$  by a Fokker-Planck equation as a function of the three adiabatic invariants and time (Schulz & Lanzerotti, 1974). Here  $M$ ,  $J$ , and  $\Phi$  are the first, second, and third adiabatic invariants, respectively. It is helpful to consider  $\Phi$  in terms of the adiabatic reference parameter  $L^*$ , defined by  $L^* = 2\pi B_E R_E^2 / \Phi$  (Roederer, 1970). Since a first-principles model of wave-particle interactions in the outer radiation belt is intractable across its large volume and long timescales, all the physics within the outer radiation belt can be effectively described by diffusive processes. Each type of diffusion—pitch angle, energy, and radial—by each wave mode is described in the Fokker-Planck equation by a diffusion coefficient  $D_{ij}$ . A myriad of different wave-particle interactions is important for the radiation belts. For example, very low frequency (VLF) whistler mode chorus mediate energy diffusion (Thorne et al., 2013), whereas VLF whistler mode hiss (Lyons & Thorne, 1973; Meredith et al., 2007) and ULF electromagnetic ion cyclotron (EMIC) waves (Kersten et al., 2014) predominantly diffuse in pitch-angle and therefore contribute to loss. ULF wave-driven radial diffusion at Pc-5 frequencies is considered to be an important and effective mechanism to transport and accelerate relativistic electrons in the outer radiation belt (Elkington et al., 2003; Mann et al., 2013; Ozeke et al., 2017, 2018; Shprits et al., 2008).

In this paper we focus on radial diffusion as a result of ULF waves, which in the diffusion framework can be modeled as a straightforward one-dimensional problem. All of the physics is contained in the radial diffusion coefficient  $D_{LL}$ , which is proportional to ULF wave power. A wealth of data exists both on the ground and in space to calculate ULF wave power and construct  $D_{LL}$  (Dimitrakoudis et al., 2015; Li et al., 2017; Liu et al., 2016; Ozeke et al., 2012, 2014; Ukhorskiy et al., 2009). Empirical models formulate analytic expressions for  $D_{LL}$  from ULF wave power data over long timescales, aiming to capture the spatiotemporal evolution of  $D_{LL}$  in such a way that although rapid changes cannot be accurately captured, the long timescale behavior of the outer radiation belt may be adequately described (e.g., Ozeke et al., 2018). In this paper, we wish to highlight the numerical consequences of using different methods for modeling the temporal and spatial variability of  $D_{LL}$  with more realistic values that represent the underlying probability distribution of ULF wave power.

Many theoretical approximations exist for the radial diffusion coefficient  $D_{LL}$  based on a variety of assumptions and approximations (Ali et al., 2016; Birmingham, 1969; Cornwall, 1968; Elkington et al., 2003; Fälthammar, 1966, 1968; Fei et al., 2006; Lejosne et al., 2013; Liu et al., 2016; Schulz & Lanzerotti, 1974). All of these approximations are constrained by some statistical parameterization of ULF wave power obtained from many years of space or ground-based observations. The most widely used  $D_{LL}$  parameterizations in radiation belt models parameterize by the geomagnetic index  $K_p$  (Brautigam & Albert, 2000; Ozeke et al., 2012, 2014). These parameterizations are deterministic with a single output for each value of  $K_p$ .

Typical approaches in radiation belt modeling follow a classical parameterization approach whereby average or median  $D_{LL}$  values are used. These values only change when the fit parameters change, and therefore, there is a chance that the full range of variability of  $D_{LL}$  is not captured in this classical approach. In numerical weather prediction and climate modeling, classical parameterizations have proven to be insufficient. Instead, stochastic parameterizations are used to capture the whole distribution of behavior in underlying physical processes to yield improved results. Note that previous attempts to capture more realistic variability in ULF-mediated radial diffusion have used observations to recreate event-specific models of diffusion (Perry et al., 2005; Riley & Wolf, 1992; Tu et al., 2012). These types of study, although potentially more accurate, are limited to test cases with available data in space and time. We propose that in cases where direct data is

lacking, it is still possible to capture the full range of behavior in the problem using stochastic parameterizations (e.g., Watt et al., 2017), and we demonstrate a simple implementation of this technique in this paper.

Here we present a series of idealized numerical experiments of radial diffusion over a hypothetical period of constant geomagnetic activity. These experiments offer a proof of concept intended to explore the spatiotemporal impacts of including stochastic variability in comparison with the (Ozeke et al., 2014) ULF radial diffusion coefficients in the radial diffusion equation and highlight current deterministic model limitations. Any significant discrepancies between the deterministic and stochastic models should motivate further research questions to better understand the physical processes underlying ULF wave-driven radial diffusion to include in our models for improved accuracy. The remainder of this paper is structured as follows. Sections 2–4 describe the radial diffusion problem, implementation of stochastic parameterization, and setup and description of the idealized experiments, respectively. Section 3 presents the results from the numerical experiments. Section 4 discusses the impact of the results in the wider context of the outer radiation belt. Section 5 describes conclusions and remarks from this paper.

## 2. Modeling the Radial Diffusion Equation

We focus on the radial diffusion equation as a simplified approximate model of electron behavior in the outer radiation belt. Although the one-dimensional description of radial diffusion has successfully reproduced electron behavior during some events (e.g., Ozeke et al., 2018; Shprits et al., 2005), the diffusion framework itself is not always accurate. Previous studies have calculated radial diffusion coefficients directly in “event-specific” analysis (e.g., Ukhorskiy et al., 2009) and demonstrate that diffusion-based models can have difficulty accurately rendering event-specific dynamics (Ukhorskiy et al., 2009). Here, we intend these numerical experiments as a straightforward demonstration of the concept of stochastic parameterization. Radial diffusion is also a valid and important part of more complicated outer radiation belt models, where it is joined by diffusion processes in velocity space due to other wave modes. Over the long timescales studied in diffusion models, we observe that empirical models for  $D_{LL}$ , in whichever theoretical framework they are constructed, naturally have some uncertainty. Investigating the consequences of that uncertainty is our aim in this work.

In this demonstration we simplify the behavior of high-energy electrons in the outer radiation belt and focus on radial diffusion across Roederer  $L^*$  (Roederer, 1970), hereon denoted  $L$ . Here, the first and second adiabatic invariants,  $M$  and  $J$ , are conserved. The evolution of the distribution function of trapped particles  $f(M, J, \Phi; t)$  can be related to the distribution function at time  $t + \Delta t$  (without sources or sinks)

$$f(M, J, \Phi; t + \Delta t) = \int_{\Phi} f(\Phi - \phi, t) \Pi(\Phi - \phi, \phi, t) d\phi, \quad (1)$$

where  $\Pi(\Phi - \phi, \phi, t)$  is the probability that a particle with an invariant shell coordinate  $\Phi - \phi$  at time  $t$  will end up with coordinate  $\Phi$  at time  $t + \Delta t$ . By Taylor expanding  $f, \Pi$  to first order in  $t$  on the left and second order in  $\Phi$  in the integral, we obtain the one-dimensional Fokker-Planck equation

$$\frac{\partial f(M, J, \Phi)}{\partial t} = -\frac{\partial}{\partial \Phi} (D_{\Phi} f) + \frac{1}{2} \frac{\partial^2}{\partial \Phi^2} (D_{\Phi \Phi} f). \quad (2)$$

Here  $D_{\Phi}$  and  $D_{\Phi \Phi}$  are the first- and second-order Fokker-Planck diffusion coefficients, respectively. If we assume the following relation for  $D_{\Phi}$ , the average change of  $\Phi$  per unit time for one particle on the shell  $\Phi$  during that time interval

$$D_{\Phi} = \frac{1}{2} \left( \frac{\partial D_{\Phi \Phi}}{\partial \Phi} \right) \quad (3)$$

and convert  $\Phi$  into  $L$ , the evolution of the PSD of electrons may be modeled by a simplified radial diffusion equation in terms of  $L$

$$\frac{\partial f(M, J, \Phi)}{\partial t} = L^2 \frac{\partial}{\partial L} \left( \frac{D_{LL}}{L^2} \frac{\partial f(M, J, \Phi)}{\partial L} \right). \quad (4)$$

For radial diffusion to be effective, a radial gradient in the PSD is required, which we assume here. A precipitation loss term is often also added to Equation 4, which is ignored here in the idealized case. Radial diffusion is considered across  $L = 2.5$ –6. Dirichlet and Neumann boundaries are imposed on the inner and outer boundaries, respectively:

$$f_{L=2.5}(t) = f_{L=2.5}(0) \quad \forall t, \quad (5)$$

$$\nabla f_{L=6}(t) = 0 \quad \forall t. \quad (6)$$

In reality the gradient across the outer boundary will not be 0, and many radiation belt models either determine the outer boundary from electron flux data observed by spacecraft (e.g., Drozdov et al., 2017; Glauert et al., 2018; Shin & Lee, 2013) or use plasmashet characteristics (Christon et al., 1988, 1991) and magnetic activity dependencies (Bourdardie & Maget, 2012) for analytic fits (Maget et al., 2015).

In Equation 4,  $D_{LL}$  represents the ULF wave radial diffusion coefficient. Constructed through a coordinate transform of the flux invariant diffusion coefficient,  $D_{\Phi\Phi}$ ,  $D_{LL}$  is formally defined by (Roederer & Zhang, 2014)

$$D_{LL} = \frac{\langle (\Delta L)^2 \rangle}{\tau_d} \propto R_s^{-8} L^{10} (\Delta R_s / R_s)^2, \quad (7)$$

where  $R_s$ ,  $\Delta R_s / R_s$ , and  $\tau_d$  are the dipole-distortion parameter, its relative fluctuation, and the drift period, respectively. Here,  $\langle \rangle$  denotes the drift-average operator. In a realistic setting,  $R_s$  would be represented by a parameter that globally describes magnetospheric activity, such as Kp or ULF wave power. Application of different frameworks to describe large-scale fluctuations of electric and magnetic fields (e.g., Brautigam & Albert, 2000; Brautigam et al., 2005; Lejosne et al., 2013; Ozeke et al., 2012, 2014) employ different assumptions, but many ultimately require some estimate of the power spectral density of ULF fluctuations in electric and/or magnetic fields. We note that from Equation 7 and from theoretical estimates of  $D_{LL}$ , there are inherent minimum temporal scales on which  $D_{LL}$  is constructed: by definition  $D_{LL}$  is constructed for timescales longer than the drift period of the electrons, longer than a few periods of the ULF wave fluctuations, and of the same order or longer than the solar wind driving processes that induce the ULF fluctuations. In many cases, ULF power spectral density is estimated from observations over a period of at least an hour (see Ozeke et al., 2014), and so we employ this as the smallest timescale of variability in our study.

We consider as a deterministic reference model the empirical  $L$  and  $K_p$  parameterized  $D_{LL}$  presented by Ozeke et al. (2012, 2014). This model is a simplification of the theoretical analysis presented by Fei et al. (2006) and assumes that median ULF wave power is representative of expected ULF wave power. The most notable feature of this model is that the uncertainty in the statistical representation of ULF power spectral density has been quantified, allowing us to perform this demonstration using observationally derived constraints. Other models exist, which are similarly parameterized by Kp activity, with some following the same theoretical framework as Fei et al. (2006) (e.g., Brautigam et al., 2005) and others pursuing other frameworks (e.g., Lejosne et al., 2013), but all do not explicitly state and characterize the uncertainty in their models as in Ozeke et al. (2012, 2014). We note that the accuracy of the theoretical framework used to estimate  $D_{LL}$  is beyond the scope of this paper and direct the interested reader toward Lejosne (2019) for a thorough review of such frameworks. We reiterate that since the (Ozeke et al., 2014) empirical  $D_{LL}$  model contains explicit estimates of uncertainty, that makes it appropriate for use in our demonstration.

Since the azimuthal electric field radial diffusion coefficient,  $D_{LL}^E$ , typically dominates, in these idealized experiments we omit the compressional magnetic component and base our stochastic parameterization around the model for  $D_{LL} = D_{LL}^E$ , expressed per day by

$$D_{LL}^E = 2.16 \times 10^{-8} L^6 10^{0.217L + 0.461K_p}. \quad (8)$$

We describe in the following section how we implement our estimates of  $D_{LL}^E(t)$ , by perturbing Equation 8 in such a way as to recover a better representation of the underlying distribution of  $D_{LL}^E$  across a period of time.

We solve the radial diffusion equation using a modified Crank-Nicolson second-order finite difference scheme presented by Welling et al. (2011), which is semi-implicit and unconditionally stable:

$$\frac{f_j^{n+1} - f_j^n}{\Delta t} = \frac{L_j^2}{2} \left[ \frac{D_{j+\frac{1}{2}}n + \frac{1}{2}(f_{j+1}^n - f_j^n) - D_{j-\frac{1}{2}}n + \frac{1}{2}(f_j^n - f_{j-1}^n)}{(\Delta L)^2} + \frac{D_{j+\frac{1}{2}}n + \frac{1}{2}(f_{j+1}^{n+1} - f_j^{n+1}) - D_{j-\frac{1}{2}}n + \frac{1}{2}(f_j^{n+1} - f_{j-1}^{n+1})}{(\Delta L)^2} \right], \quad (9)$$

where  $L_j = 2.5 + j\Delta L$ ,  $t_n = n\Delta t$ ,  $f_j^n = f(L_j, t_n)$ ,  $D_jn + \frac{1}{2} = D_{LL}(L_j, t_n + \frac{1}{2})$  and  $D_{LL} = \frac{D_{LL}}{L^2}$  for modeling simplicity. The chosen grid and time steps for our numerical experiments are  $0.1L$  and  $1$  s, respectively, following extensive model verification of the numerical scheme to determine a suitable trade off between numerical error and computational cost for the experiments (see the supporting information).

### 3. Stochastic Parameterization

We suggest that the most physically intuitive method to implement stochastic parameterization is to focus efforts on the representation of the diffusion coefficient, since it is the variable that contains all the information about the wave-particle interaction. The diffusion coefficient parameterization has been shown to result in a large amount of variability, especially during storm times (Murphy et al., 2016). In this work, we choose a straightforward method to model  $D_{LL}(L, t)$  that involves constructing a noisy temporal or spatial series that retains the key known properties of the distribution of  $D_{LL}$ . More sophisticated techniques, such as autoregressive moving average (ARMA) models, can be used to create spatiotemporal series of the diffusion coefficients with the appropriate autocorrelative properties. However, these rely on important characteristic scales of spatial and temporal variability that are not yet known.

We do, however, have access to some information constraining the expected distribution of  $D_{LL}$ . Bentley et al. (2018) found that the probability distribution of ground-based ULF wave power appears log-normal (LN). We infer from this that  $D_{LL}$  is also likely to be approximately LN; indeed, Ozeke et al. (2014) confirm that the distribution of  $D_{LL}$  in space is not Gaussian and is log-symmetric, since the interquartile range (IQR) is reported between one third and three times the median. Hence, it is appropriate to construct a noisy time series for  $D_{LL}$  by multiplying the median  $D_{LL}$  by a random LN noise factor  $\epsilon$ , resulting in a time series that, when aggregated over a long period of time, reproduces the required LN distribution. If we constructed a noisy temporal or spatial series by adding Gaussian noise to the median  $D_{LL}$ , the resulting distribution of  $D_{LL}$  cannot be LN since it has the potential to include negative values of diffusion, which would also be difficult to interpret in this context.

To investigate the consequences of variability, we consider ensembles of numerical experiments. In each case we compute the solutions of the radial diffusion equation using Equation 9, where  $D_{LL}(t)$  is separately constructed each time using the methods described below. Our recreations of  $D_{LL}(t)$  do not alter the underlying Fokker-Planck diffusion theory but produce realizations of  $D_{LL}$  that better recover the underlying distribution of ULF power spectral density. Future work will seek to identify the most appropriate methods to model both the diffusion coefficient and its variability, but the straightforward methods we adopt here serve to illustrate the behavior of the radial diffusion equation when stochastic parameterization is adopted using known constraints.

### 4. Numerical Experiments

We consider radial diffusion under a constant state of low geomagnetic activity, with  $K_p$  fixed for 2 days. Although  $K_p$  is not typically constant over 2 days, we keep it fixed in these experiments in order to isolate the effects of the natural temporal and spatial variability that is concealed within the  $K_p$  parameterization. Any temporal changes to  $D_{LL}$  occur on timescales of hours in our experiments.

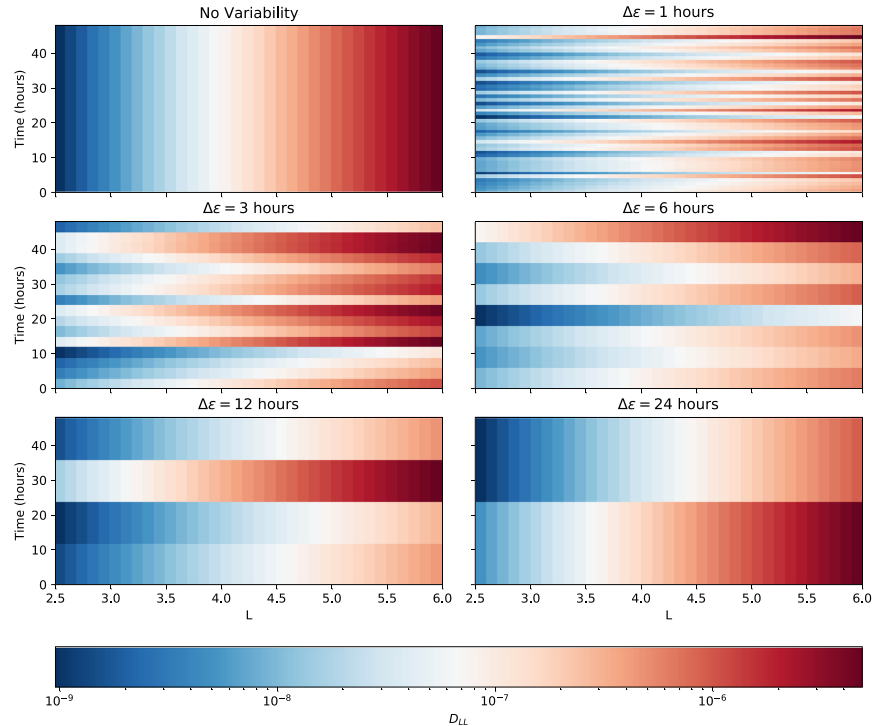


**Figure 1.** Example ensemble member  $D_{LL}$  time series shown for a range of temporal variability scales. In each case, the constant (Ozeke et al., 2014) deterministic  $D_{LL}$  is multiplied by a log-normal variability at the relevant hour of variability, constrained by the empirical model and ULF wave power observations, and persists until the next hour of variability where the process is repeated. Examples are shown for variability temporal scales of 1, 3, 6, 12, and 24 hr, along with the constant  $D_{LL}$  with no variability.  $D_{LL}$  shown here has units  $s^{-1}$  in line with the 1 s time step used in our numerical scheme.

In each numerical experiment we run an ensemble with 250 ensemble members, providing a span of possible realizations of 48 hr  $D_{LL}$  time series resulting from the inclusion of a stochastic variability. Convergence testing of our numerical experiments (see the supporting information) demonstrates that 250 ensemble members is sufficient to realize the behavior of the experiment.

In all experiments we choose  $K_p = 3$ , corresponding to “unsettled” geomagnetic activity. Unsettled geomagnetic activity allows us to explore stochastic variabilities during periods where the radial diffusion coefficients are large enough to see changes after 48 hr. We also wish to avoid the illogical situation of having a very high level of geomagnetic activity while enforcing a constant outer boundary. For the demonstrations approximated in this paper, a compromise of  $K_p = 3$  was felt to be appropriate. The initial PSD is chosen to provide a peak inside the computational domain as expected in the outer radiation belt, and a zero gradient at the outer boundary, for ease of computation in these illustrative experiments

$$f(M, J, \Phi; t = 0) = A \exp\left(-\frac{(L - \mu)^2}{2\sigma^2}\right) + \frac{1}{2}AB [\text{erf}(\gamma(L - \mu)) + 1], \quad (10)$$

where we have chosen  $A = 9 \times 10^4$ ,  $\mu = 4$ ,  $\sigma = 0.38$ ,  $B = 0.05$ , and  $\gamma = 5$  and  $\text{erf}$  is the error function. Such a profile is reasonable when compared to satellite observations (e.g., see Figures 1 and 2 in Boyd et al., 2018).

If one wanted to do the equivalent in  $L$  space (with a transformed diffusion equation), it suffices to use (Roederer & Zhang, 2014)

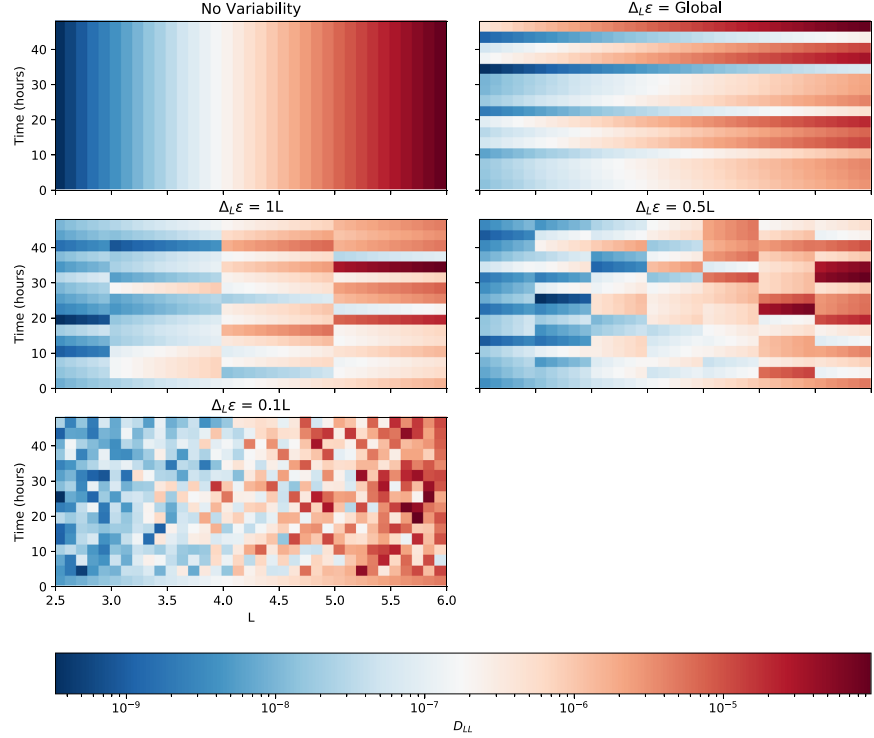


**Figure 2.** Example ensemble member  $D_{LL}$  time series shown for a range of spatial variability scales. In each case, every 3 hr the constant (Ozeke et al., 2014) deterministic  $D_{LL}$  is multiplied by log-normal variabilities on a variety of local spatial variability scales, constrained by the empirical model and ULF wave power observations, and persists for 3 hr where the process is then repeated. Examples are shown for variability spatial scales of  $1L$ ,  $0.5L$ , and  $0.1L$ , along with the global variability case and constant  $D_{LL}$  with no variability.  $D_{LL}$  shown here have units  $s^{-1}$  in line with the 1 s time step used in our numerical scheme.

$$f(M, J, L; t = 0) = f(M, J, \Phi; t = 0) \times 2\pi B_E R_E^3 L^{-2}. \quad (11)$$

The initial PSD profile and proposed boundary conditions result in the expected radial diffusion process drawing PSD from central  $L$  toward both boundaries.

#### 4.1. Experiment 1: Temporal Variability of $D_{LL}$

Our first experiment focuses on the temporal variation of  $D_{LL}$  across a range of timescales. We employ a simple method, where the  $D_{LL}$  in Equation 8 is multiplied by a random factor  $\epsilon$ , which changes every  $\Delta t$ . The same factor  $\epsilon$  is applied at each value of  $L$  in the model. The choice of distribution of  $\epsilon$  is guided by the statistical analysis presented by Ozeke et al. (2014), who found that the IQR of observed wave power implies that  $D_{LL}$  lies between a third of and three times the model value 50% of the time. We use this information to control the variance of the noise. Combined with recent studies that suggest that ULF wave power spectral densities appear LN (Bentley et al., 2018), we construct a log-normally distributed variability with the following parameters:

$$\epsilon \sim \text{LogNormal}(\mu_N, \sigma_N^2), \quad (12)$$

where  $(\mu_N, \sigma_N) = (0, \frac{2\log(3)}{1.34896})$  are the parameters of the normally distributed  $\log(\epsilon)$ . Note that for a normally distributed random variable, the IQR is approximately 1.34869 multiplied by the standard deviation. We consider variability  $\Delta t = 1, 3, 6, 12,$  and  $24$  hr, and example ensemble members for each of these cases are shown in Figure 1. They are effectively artificial representations of what might be observed in situ.

#### 4.2. Experiment 2: Spatial Variability of $D_{LL}$

In Experiment 1,  $D_{LL}$  was constructed with perfect correlation across all  $L$ , with the same  $\epsilon$  applied to all  $L$ -shells. This is one extreme of  $L$  spatial correlation, with the (Ozeke et al., 2014)  $D_{LL}$  scaling as a smooth, monotonically increasing profile. We hereon refer to this approach as *global* variability. However, we must consider that although the statistical profile of  $D_{LL}(L)$  is smooth, individual cases of  $D_{LL}(L,t)$  may be less smooth. In this experiment, we investigate how radial diffusion responds to a realized  $D_{LL}$ , which may vary on local spatial scales, and not necessarily be a smooth monotonically increasing function of  $L$ .

We now consider the log-normally distributed variability applied every 3 hr, comparing the global variability with local spatial correlation scales. We consider cases where  $D_{LL}$  varies independently on spatial scales of  $1L, 0.5L$ , and  $0.1L$ . Example ensemble members for each of these cases are shown in Figure 2. The final case denotes the other extreme where measures of  $D_{LL}(L,t)$  are independent at all grid points, that is, that independent  $\epsilon$  is applied at each grid point in  $L$  to create an ensemble of  $D_{LL}$  both spatially and temporally. We have retained temporal variability in this experiment to maintain our goal of creating  $D_{LL}$  time series that represent realistic values. Ground magnetometer ULF wave power measurements, and consequently  $D_{LL}$ , do not typically remain constant over 2 days (e.g., Olifer et al., 2019). Results from differing spatial variability scales can therefore be interpreted in conjunction with the 3-hourly temporal variability.

In a more physical realization, we would expect spatial correlations across  $L$  to be less crude and abrupt, and are likely to exhibit smoother variations with appropriate length scales. However, for the purpose of this demonstration, we have chosen the simplest way to apply spatial variability in the model to motivate the importance of understanding the spatial structure of radial diffusion across  $L$ .

#### 4.3. Experiment 3: Width of the $D_{LL}$ Probability Distribution

The empirical (Ozeke et al., 2014)  $D_{LL}$  parameterization is based on the median of statistical ULF wave power, and uncertainty in the parameterization has the multiplicative IQR  $\left[\frac{1}{3}D_{LL}, 3D_{LL}\right]$  mentioned previously. We compare the IQR suggested by Ozeke et al. (2014) with larger and smaller IQRs, namely,  $\left[\frac{1}{2}D_{LL}, 2D_{LL}\right]$ ,  $\left[\frac{1}{6}D_{LL}, 6D_{LL}\right]$ , and  $\left[\frac{1}{10}D_{LL}, 10D_{LL}\right]$ . Larger variances may be necessary if the variability of  $D_{LL}$  is not simply due to the variability in observed ground-based ULF power spectral density. Smaller variances have been considered to see the effect of an “improved” parameterization (i.e., one where the parameters are chosen in a way that minimizes the variance). In each of these cases, ensemble  $D_{LL}$  time series are formulated by applying variability globally across  $L$  every 3 hr, with the distribution of the variability LN.

#### 4.4. Experiment 4: Shape of the $D_{LL}$ Probability Distribution

Each experiment (1–3) utilized a log-normally distributed variability, chosen based on statistical studies of ULF wave power spectral densities parameterized by solar wind variables (Bentley et al., 2018). The IQR presented by Ozeke et al. (2014) describes the uncertainty in the deterministic parameterization, but we do not know how the  $D_{LL}$ s are distributed in a  $K_p$ -based model. Adopting the values and log-symmetric nature of the (Ozeke et al., 2014) IQR in order to preserve statistical averages (a zero mean and median in the logarithm), a range of log-symmetric distributions for the variability are tested. We consider log-uniform (LU), LN, log-Laplace (LL) and log-Cauchy (LC) distributions, which provides a set of distributions ranging from bounded to heavy tailed (for further information about each of these distributions, please see the supporting information). Since the heavy tailed distributions can easily produce variabilities resulting in a  $D_{LL}$  which is unrealistically many orders of magnitude larger than the deterministic solution, for this experiment we bound the variability by 3 orders of magnitude (i.e., the variability can increase/decrease  $D_{LL}$  up to a maximum/minimum of 3 orders of magnitude compared to the reference value). The respective probability density functions (PDFs) of the variability distributions are as follows:

$$f_{LU}(x) = \frac{I_{[a^{\epsilon}, b^{\epsilon}]}(x)}{x(b-a)}, \quad (13)$$

$$f_{LN}(x) = \frac{1}{x\sigma_N\sqrt{2\pi}} \exp\left(-\frac{(\ln x)^2}{2\sigma_N^2}\right), \quad (14)$$

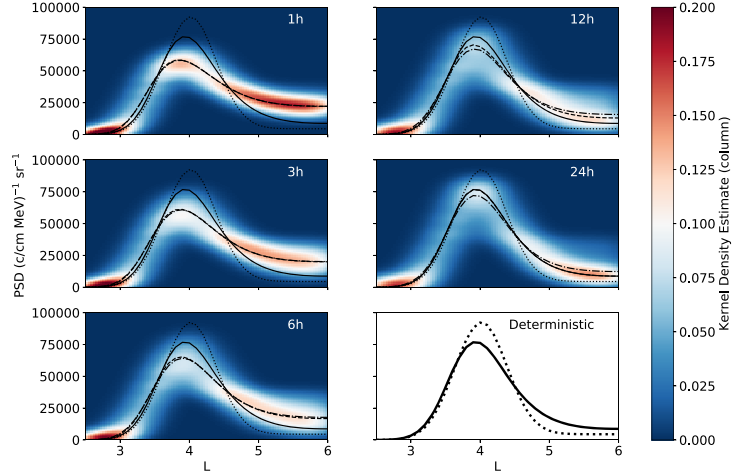


**Figure 3.** Ensemble results for the final PSD at the end of Experiment 1 for a range of temporal variability scales (1, 3, 6, 12, and 24 hr, respectively). The median (dashed), mean (dash-dot) ensemble profiles are shown, as well as the initial PSD profile (dotted) and the deterministic solution with constant deterministic  $D_{LL}$  (solid). Ensemble kernel density estimates of the resulting electron PSD are also shown.

$$f_{LL}(x) = \frac{1}{2\sigma_L x} \exp\left(-\frac{|\ln x|}{\sigma_L}\right), \quad (15)$$

$$f_{LC}(x) = \frac{1}{x\pi} \left[ \frac{\sigma_C}{(\ln x)^2 + \sigma_C^2} \right] \quad (16)$$

for  $x > 0$ , where  $I_{[j]}$  is the characteristic function. Here the quantities  $a$ ,  $b$ ,  $\sigma_N$ ,  $\sigma_L$ , and  $\sigma_C$  are the parameters of the underlying uniform, normal, Laplace, and Cauchy distributions, respectively. The parameters were calculated from their corresponding cumulative density functions in order to preserve the IQR specified by Ozeke et al. (2014) (see the supporting information).

## 5. Results

The figures showcasing results for each experiment generally follow the same format. The initial PSD and resulting PSD from the constant deterministic  $D_{LL}$  are shown. By the log-symmetric nature of the  $D_{LL}$  probability distributions in each experiment, the constant deterministic  $D_{LL}$  is precisely the median diffusion coefficient from the ensemble and a natural reference for comparison. The mean diffusion coefficient is deliberated in section 6. There is no convention regarding which statistical measure is most appropriate in ensemble modeling (Knutti et al., 2010), and we have therefore shown two natural measures, the ensemble mean and median. By ensemble mean (median) PSDs, we imply the PSD profile resulting from taking the mean (median) across all ensemble members at each  $L$ , and not representing a specific member of the ensemble. The kernel density estimates (KDEs) of the ensembles are also shown. Kernel density estimation is a mathematical process of finding an estimate PDF of a random variable, inferring attributes of a population based on a finite data set. In the case of our ensembles, the contribution of each ensemble member value in  $L$ -PSD space is smoothed out into a region of space surrounding it. Aggregating each of these smoothed points provides an image of the overall ensemble structure and density function. Ensemble modes, another useful measure of the ensemble result, can be estimated from this density function (Kourentzes et al., 2014). In our figures KDEs shown are relative to each column, meaning that if a single  $L$  column were extracted, the result would be a PDF estimate of the PSD at that particular  $L$ . KDEs are therefore useful in an ensemble setting since they allow us to see where ensemble member solutions cluster in the phase space. In our estimates the KDEs are calculated over 100 bins.

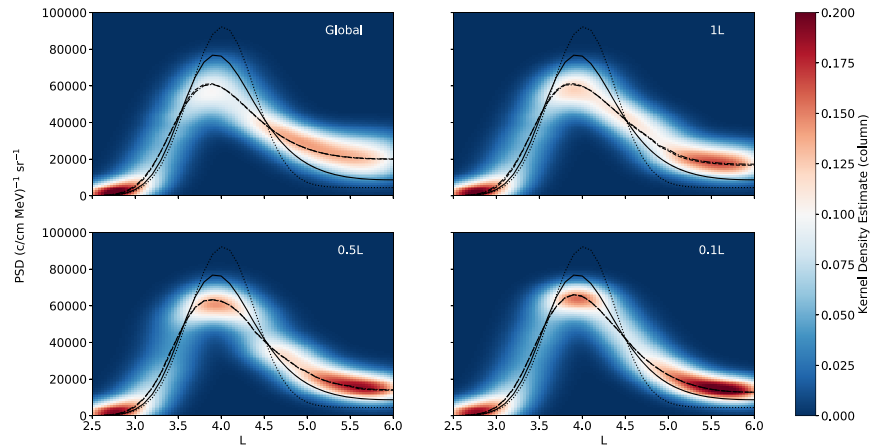


**Figure 4.** Ensemble results for the final PSD at the end of Experiment 2 for a range of spatial variability scales (global, 1L, 0.5L, and 0.1L, respectively). The description of lines and KDEs are as in Figure 3.

### 5.1. Experiment 1—Temporal Scales

Results of the ensembles for the variety of temporal variability scales are shown in Figure 3. For ensemble medians, inclusion of a LN variability results in more diffusion than the constant deterministic  $D_{LL}$  at all variability temporal scales less than 24 hr, with the magnitude of diffusion increasing as the temporal scale decreases. The ensemble median for a temporal variability of 24 hr is identical to the deterministic solution, suggesting that on long timescales, a deterministic parameterization of  $D_{LL}$  is sensible for a  $D_{LL}$  with daily variation. Results for the ensemble mean are similar, except we observe more diffusion than the constant  $D_{LL}$  at all temporal scales. This is unsurprising since the (Ozeke et al., 2014)  $D_{LL}$  is based on the median of log-symmetric distributions, where means are larger than medians. Therefore, the ensemble  $D_{LL}$  time series at all temporal scales will have a mean larger than both the deterministic approximation and ensemble median, resulting in more diffusion. An interesting result lies in the comparison of ensemble medians and means. On the most rapid temporal  $D_{LL}$  variability of 1 hr, results from the ensemble mean and median are identical. As the temporal variability becomes less rapid, both exhibit less diffusion, but the profiles separate with the ensemble median displaying increasingly less diffusion than the mean as it approaches the deterministic solution at daily variability.

Over all temporal variability scales, the occurrence of possible states in the set of all ensemble solutions spans similar regions. For the rapid 1 hr variability, the set of all solutions is more diffusive than the deterministic case. The deterministic solution becomes increasingly closer to the denser region of ensemble solutions with larger temporal scales, falling exactly in the region of highest probability for daily variation. We see that increasing the frequency of  $D_{LL}$  variability tends to a single mode solution in density, which is more diffusive than that produced by the deterministic model. Inclusion of the variability expressed by Ozeke et al. (2014) in their 3-hourly deterministic model produces a span of solutions, which vary greatly from the deterministic case at all  $L$ , most of which are more diffusive. The use of the median-based deterministic parameterization may therefore not be robust. When we allow the stochastic  $D_{LL}$  to vary daily, however, the deterministic solution fell exactly in the regions of highest probability, emphasizing again that the deterministic approximation is more suitable for a daily varying  $D_{LL}$ . When including variability, the deterministic parameterization frequently produces lower estimates of radial diffusion, so understanding the temporal variability of ULF wave power spectral density is important to know the extent of potential underestimation.

### 5.2. Experiment 2—Spatial Scales

Ensemble results for Experiment 2 are shown in Figure 4. We find that on average all spatial scales of variability result in similar levels of diffusion, but all exhibit more diffusion than the deterministic solution. In each case the ensemble means and medians are almost identical. Most importantly, we observe variance

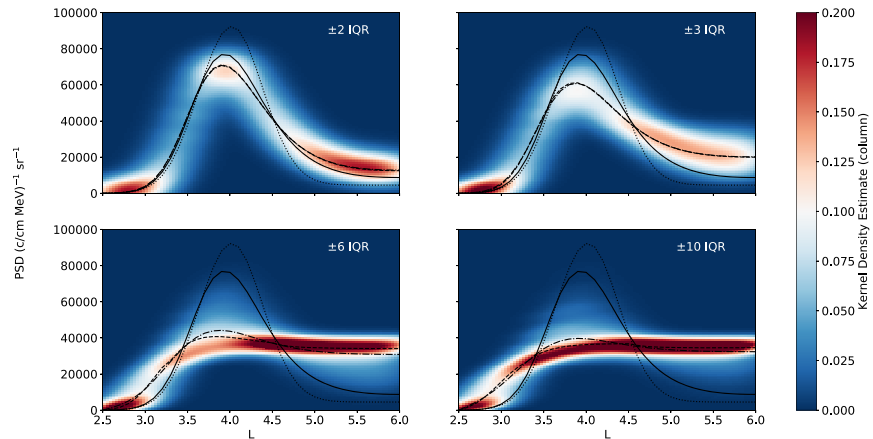


**Figure 5.** Ensemble results for the final PSD at the end of Experiment 3 for a range of log-normal variability IQRs ( $\pm 2$ ,  $\pm 3$ ,  $\pm 6$ , and  $\pm 10$  of the deterministic  $D_{LL}$ , respectively). The description of lines and KDEs are as in Figure 3.

reduction in the set of ensemble solutions as independence of  $D_{LL}$  measurements occurs on increasingly smaller spatial scales, with the distributions tending toward a single mode solution of diffusion similar to those exhibited by the ensemble median and mean. A smaller variance implies possibility of a stronger parameterization with reduced uncertainty. It is important to investigate instantaneous observations of ULF wave power across multiple latitudes to better understand spatial correlations and coherence across  $L^*$ , since regions of independent power measurements could allow for better parameterizations of  $D_{LL}$ .

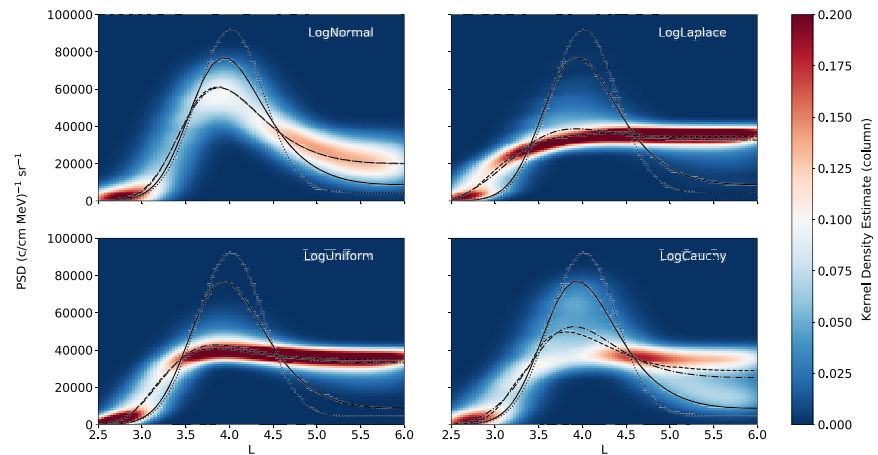
### 5.3. Experiment 3—Variance

Figure 5 shows the ensemble results for Experiment 3, with each variance expressed in terms of the variability IQR. It is evident that radial diffusion is very sensitive to the width of the variability distribution. Just doubling the multiplicative scaling of the IQR suggested by Ozeke et al. (2014) results in significantly more diffusion in both ensemble averages, reducing the peak in PSD by around 20,000. The shape of the distribution for the set of all ensemble solutions also drastically changes, with a large density of solutions tending to the asymptotic result controlled by the boundary conditions. Although a wider variability distribution equally allows for both significantly larger and smaller values of  $D_{LL}$ , the radial diffusion equation is clearly heavily sensitive to the larger values that drive radial diffusion to significant levels beyond the deterministic approximation.

As seen in the other experiments, introduction of any variability regardless of its width results in more diffusion than the deterministic solution, when considering ensemble averages. However, if the uncertainty in the deterministic model were to have a slightly smaller multiplicative IQR of  $\pm 2$  (Ozeke et al., 2014)  $D_{LL}$ , the variance of all ensemble solutions decreases significantly. With this smaller variance, the ensemble mean and median PSDs are closer to the deterministic model, which also falls within the set of ensemble solutions. This suggests that parameterization of ULF radial diffusion coefficients should prioritize variance reduction in order to be better representative of the underlying physical process, which draws upon the efficiency of binning by geomagnetic index  $K_p$ , from which most of the uncertainty arises (Ozeke et al., 2014).

### 5.4. Experiment 4—Underlying Distribution

Ensemble results for Experiment 4 are shown in Figure 6. Differences between the heavy and nonheavy tailed distributions are apparent in the ensemble medians. Although studies suggest that ground-based ULF power spectral density is LN when parameterized by solar wind variables (Bentley et al., 2018), the distribution of uncertainty in the  $K_p$ -based (Ozeke et al., 2014) model is not disclosed. If the distribution were to be heavy tailed or LU (which may be considered to have the heaviest tail as all values in the uniformly distributed component have equal chance of being sampled), we see more than double the median diffusion than for a log-normally distributed variability. For scenarios where the expected ULF wave power is not a



**Figure 6.** Ensemble results for the final PSD at the end of Experiment 4 for a range of variability probability distributions (Log-Normal, Log-Laplace, Log-Uniform, and Log-cauchy, respectively). The description of lines and KDEs are as in Figure 3.

statistical average, the assumed LN variability can exhibit as much diffusion as some of the heavy tailed variabilities, but this is more unlikely as shown in the KDEs. In any case, with the inclusion of variability in  $D_{LL}$  for all probability distributions, we see significantly more diffusion than the deterministic solution, with notable variance in ensemble solutions for all variability distributions. The heavier tailed variabilities have denser regions approaching that of the asymptotic solution, and the shape of the KDEs across L-shells is quite distorted contrary to the smoothness seen for a LN  $D_{LL}$ . Since there are multiple components of interest in the ensemble results, studies investigating the true underlying probability distribution of ULF wave power are vital to quantifying the shortfall and uncertainty introduced by a deterministic empirical  $D_{LL}$  based upon statistical averages.

## 6. Discussion

In the outer radiation belt, radial diffusion has the ability to both accelerate electrons to relativistic energies and produce fast losses, where the efficiency of the acceleration increases with increasing ULF wave activity (Elkington et al., 2003; Shprits et al., 2008). Many models use an empirical deterministic radial diffusion coefficient dependent on  $L$  and  $K_p$ , which may sacrifice accuracy (Brautigam & Albert, 2000; Brautigam et al., 2005; Ozeke et al., 2012, 2014). In this paper we present idealized numerical experiments, which investigate the impact of including variability in the radial diffusion equation. Our experiments reintroduce the variability into a parameterized model, where  $D_{LL}$  has been binned by  $K_p$ . We use the observationally constrained variability in the model to model a variable  $D_{LL}$  that reproduces a realistic distribution of values and compare against the constant parameterized value. We employ constant boundary conditions and only study one value of the controlling parameter  $K_p$ . In this way, we isolate only the variability of  $D_{LL}$  due to its parameterization by  $K_p$ .

In all experiments we found that the mean and median of the ensembles exhibit increased diffusion above that for the deterministic approximation. One way to interpret these results is that when the likelihood of strong radial diffusion is large over a particular period (either because the variance in the parameterization is large or because the underlying distribution has a heavy tail), then the diffusion exceeds what one would expect from using a constant diffusion coefficient. It is important to bear in mind that the times where diffusion is weak will not counteract the times when diffusion is strong because there is no means of reversing the diffusion; hence, the periods when diffusion is much stronger than the median will dominate the temporal evolution of the experiment. When the diffusion varies more rapidly, then each member of the ensemble is more likely to contain a period of strong diffusion over the fixed 48-hr experiment length, thus contributing to a stronger diffusion in the mean/median of the ensemble. The ensembles are also sensitive to the size of

the variance (see Experiment 3), again suggesting that it is the likelihood of ensemble members containing periods of very strong diffusion that dominates the ensemble results.

The collected range of numerical experiments suggests that over extended time periods, infrequent instances of very efficient ULF wave-particle interactions make important contributions to radial diffusion and should be included in models in some way. We also note that by using an ensemble framework, the uncertainty in the PSD is explicitly quantified, providing the means to provide a range of confidence in the model for more accurate radiation belt modeling. The quantification of uncertainty in  $D_{LL}$  is also important for future data assimilation methods.

Experiment 1 indicates that the amount of diffusion depends upon how rapidly the diffusion coefficient varies. Hence, it is important to understand the timescales of variability. ULF wave power can vary on a range of timescales, which would ideally be accounted for in the radial diffusion coefficient. For example, ULF wave power can increase and persist on the order of tens of minutes during an auroral activation due to substorms (Rae et al., 2011), while decaying on hourly timescales during strong poloidal wave events (Liu et al., 2011). Parameterization of  $D_{LL}$  with  $K_p$  may therefore not be optimal, since it may not vary quickly enough.

We found that variation of  $D_{LL}$  with the added inclusion of local spatial variabilities on a range of length scales resulted in more diffusion than the deterministic solution (see Experiment 2). However, when considering the ensemble averages, all levels of spatial coherence across  $L^*$  performed similarly. Since applying variability to subglobal spatial scales still allows for an enhanced  $D_{LL}$  at several  $L$ , this result is somewhat counterintuitive to those found in the other experiments. While it was found that instances of weaker diffusion cannot counteract the temporal evolution imposed by instances of stronger diffusion, counteractions can occur across spatial scales, creating a net diffusion that seems to follow that observed by a globally applied variability. More interestingly, we found that the variance of the possible states in the set of all ensemble solutions decreases significantly with variability applied to increasingly smaller subglobal spatial scales. It is important to understand and quantify these spatial scales. Rae et al. (2019) showed the evolution of ground-based ULF wave power during geomagnetic storms. ULF wave power can exhibit spatial coherence across ranges of  $L$  but does not rise and fall everywhere simultaneously due to the complicated evolution of cold plasma density and magnetic field strength in the inner magnetosphere. They also present evidence that the temporal variability of ULF wave power may vary with  $L$ . It may also be that spatial coherence varies with time and geomagnetic activity. The spatial variability (in the radial direction) of drift-averaged diffusion due to ULF waves throughout the outer radiation belt promises a rich vein of future work.

Sensitivity of radial diffusion to the variance of the full probabilistic distribution of  $D_{LL}$  was explored in Experiment 3. For small variances, the diffusion results approach those of the deterministic model, as expected. But as the variance is increased, the diffusion results rapidly diverge. These results suggest that it is worth seeking alternative parameterizations that focus on variance reduction in the construction of the diffusion model. Another way to reduce the variance in the parameterization may be to focus on the calculation of  $D_{LL}$  itself. For example,  $D_{LL}^E$  in the Ozeke et al. (2014) model was constructed via a mapping technique that utilized several assumptions: constant (low) wave number  $m = 1$ , constant width of the wave activity in latitude, and constant ionospheric conductance parameters (Ozeke et al., 2009). These quantities are typically not constant and contribute to the uncertainty in the deterministic model and should be included in the stochastic parameterization. The theoretical background from which  $D_{LL}$  is based may also produce uncertainties. Several analytical diffusion rates based on magnetic and electric field assumptions exist, with  $L$  dependence ranging from  $L^6-L^{11}$  and frequency dependence on a range of wave modes (e.g., Birmingham, 1969; Cornwall, 1968; Elkington et al., 2003; Fälthammar, 1966, 1968; Fei et al., 2006; Schulz & Lanzerotti, 1974). If enough of the underlying variability in the deterministic model is known, the better the variability in the stochastic models can be characterized or accounted for. It should be mentioned however that natural variability might exist, which cannot be parameterized by any means. Deducing levels of natural variability in ULF wave-driven radial diffusion is necessary in understanding information always lost by a deterministic model. If these levels are substantial, our results suggest that a stochastic approach to modeling radial diffusion may be more robust.

The response of radial diffusion to higher likelihoods of an enhanced  $D_{LL}$ , which dominates temporal evolutions, was explored in Experiment 4. It is evident that significantly more radial diffusion occurs for heavier

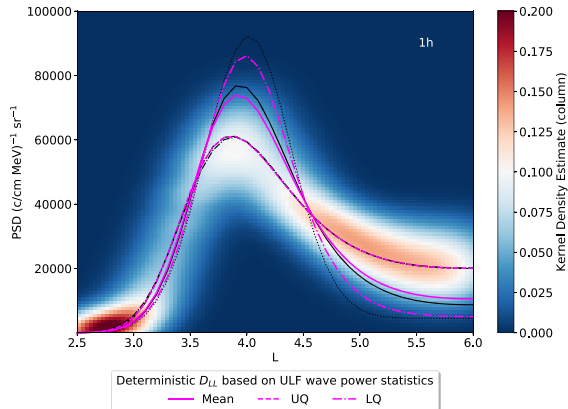


**Figure 7.** PSD resulting from the radial diffusion equation after 2 days with constant  $K_p = 3$ , shown for a constant deterministic  $D_{LL}$  based on the mean (solid pink), LQ (dash-dot pink) and UQ (dashed pink) of ULF wave power. These plots are laid over the first subplot in Figure 3.

tailed variabilities, indicating that the amount of diffusion is controlled by the relative importance of the large values of  $D_{LL}$  in the distribution. A global upper bound for possible ULF wave power is justified since it is counterintuitive for ULF waves to have infinitely large power in a finite-sized magnetosphere. The shape of the distribution is therefore important. It may also be that the shape of the distribution of  $D_{LL}$  is not constant. During quiet times when the outer radiation belt is relatively quiescent, the variability might be better represented heavily skewed to the left with a single small upper bound on ULF wave power. In a storm-time model where ULF wave activity is enhanced during the main and recovery phase (Murphy et al., 2011; Murphy et al., 2015; Rae et al., 2011), a right skewed ULF wave power distribution that favors larger ULF wave powers might be more suitable. Further research into tail values of the distribution of ULF wave power is important to constrain the physical upper bound of power variability to include in stochastic models.

In each of our experiments, ensemble averages and KDEs were compared to a (Ozeke et al., 2014) constant deterministic solution, which is based on the median of statistical ULF wave power. However, it may be more fair to compare the evolution of our numerical ensembles with an experiment

where  $D_{LL}$  is kept constant, but at the mean value of the distribution, especially since the ethos of constructing a diffusion coefficient is to consider the average behavior of the waves. Figure 7 indicates the results of a number of numerical experiments with constant  $D_{LL}$  (mean, solid pink; upper quartile, dashed pink; and lower quartile, dash-dot pink) compared with the ensemble result using a LN distribution with  $\Delta t = 1$  hr. We observe that the mean-based  $D_{LL}$  only causes slightly more diffusion than the median based and is also significantly less diffusive than the ensemble averages. While inclusion of the LQ- and UQ-based  $D_{LL}$  does result in a broad span of possible PSD solutions, the UQ produces diffusion only as strong as the ensemble averages, falling short of the regions of highest density seen in the ensemble solutions. It is apparent that having a deterministic representation of  $D_{LL}$  fails to represent the underlying distribution of radial diffusion solutions found from the stochastic  $D_{LL}$  time series, which better represent the true underlying distribution of ULF wave power. Our ensemble modeling highlights where efforts should be placed to get a better description of  $D_{LL}$ , so that we can aim for a parameterization with a quantified uncertainty that truly represents the underlying distribution of possible solutions of the radial diffusion equation.

Diffusion due to other types of wave-particle interactions is important in the outer radiation belt, and similar modeling strategies may be required. Diffusion in pitch angle and energy due to higher-frequency waves is also highly variable (Watt et al., 2019), potentially with different time and length scales depending on location in the magnetosphere. It will be necessary to repeat similar numerical experiments to determine the stochastic parameters necessary to use in stochastic parameterizations of pitch angle and energy diffusion and then design observational analyses that can best constrain those parameters.

## 7. Conclusions

Our idealized experiments highlight the spatiotemporal impacts of including stochastic parameterizations in the ULF wave-driven radial diffusion. We have shown that diffusion is increased above the deterministic model when the diffusion coefficients vary more rapidly, when the spatial correlation of the diffusion across L-shells ranges from fully coherent to completely independent, and when the variance of the distribution is increased, or a more heavy-tailed distribution is used. We have demonstrated that future research should focus on the temporal evolution of ULF wave power, the spatial correlations of diffusion across L-shells, and the underlying distribution and variance of the radial diffusion coefficients. The successful implementation of a stochastic radial diffusion model requires variability parameters that are derived appropriately; that is, spatial and temporal scales of the variability may themselves vary in time and space. Our research motivates further investigation of stochastic methods for use in radiation belt diffusion models as a method to include the variability of wave-particle interactions in the inner magnetosphere.

# CHAPTER 3. ACCOUNTING FOR VARIABILITY IN ULF WAVE RADIAL DIFFUSION MODELS



## Data Availability Statement

Experiment results presented are freely available online (at <https://doi.org/10.17864/1947.248>).

## Acknowledgments

R. L. T. was supported by the Engineering and Physical Sciences Research Council (EPSRC) Grant EP/L016613/1. C. E. J. W. is supported by Natural Environment Research Council (NERC) Grant NE/P017274/1 and Science and Technology Facilities Council (STFC) Grant ST/R000921/1.

## References

- Ali, A. F., Malaspina, D. M., Elkington, S. R., Jaynes, A. N., Chan, A. A., Wygant, J., & Kletzing, C. A. (2016). Electric and magnetic radial diffusion coefficients using the Van Allen probes data. *Journal of Geophysical Research: Space Physics*, *121*, 9586–9607. <https://doi.org/10.1002/2016JA023002>
- Bentley, S. N., Watt, C. E. J., Owens, M. J., & Rae, I. J. (2018). ULF wave activity in the magnetosphere: Resolving solar wind interdependencies to identify driving mechanisms. *Journal of Geophysical Research: Space Physics*, *123*, 2745–2771. <https://doi.org/10.1002/2017JA024740>
- Birmingham, T. J. (1969). Convection electric fields and the diffusion of trapped magnetospheric radiation. *Journal of Geophysical Research*, *74*(9), 2169–2181. <https://doi.org/10.1029/JA074i009p02169>
- Bourdarie, S. A., & Maget, V. F. (2012). Electron radiation belt data assimilation with an ensemble Kalman filter relying on the Salammbó code. *Annales Geophysicae*, *30*(6), 929–943. <https://doi.org/10.5194/angeo-30-929-2012>
- Boyd, A. J., Turner, D. L., Reeves, G. D., Spence, H. E., Baker, D. N., & Blake, J. B. (2018). What causes radiation belt enhancements: A survey of the Van Allen Probes era. *Geophysical Research Letters*, *45*, 5253–5259. <https://doi.org/10.1029/2018GL077699>
- Brautigam, D. H., & Albert, J. M. (2000). Radial diffusion analysis of outer radiation belt electrons during the October 9, 1990, magnetic storm. *Journal of Geophysical Research*, *105*(A1), 291–309. <https://doi.org/10.1029/1999JA900344>
- Brautigam, D. H., Ginet, G. P., Albert, J. M., Wygant, J. R., Rowland, D. E., Ling, A., & Bass, J. (2005). CRRES electric field power spectra and radial diffusion coefficients. *Journal of Geophysical Research*, *110*, A02214. <https://doi.org/10.1029/2004JA010612>
- Christon, S. P., Mitchell, D. G., Williams, D. J., Frank, L. A., Huang, C. Y., & Eastman, T. E. (1988). Energy spectra of plasma sheet ions and electrons from ~50 eV/e to ~1 MeV during plasma temperature transitions. *Journal of Geophysical Research: Space Physics*, *93*(A4), 2562–2572. <https://doi.org/10.1029/JA093iA04p02562>
- Christon, S. P., Williams, D. J., Mitchell, D. G., Huang, C. Y., & Frank, L. A. (1991). Spectral characteristics of plasma sheet ion and electron populations during disturbed geomagnetic conditions. *Journal of Geophysical Research*, *96*(A1), 1–22. <https://doi.org/10.1029/90JA01633>
- Cornwall, J. M. (1968). Diffusion processes influenced by conjugate-point wave phenomena. *Radio Science*, *3*(7), 740–744. <https://doi.org/10.1002/rds196837740>
- Dimitrakoudis, S., Mann, I. R., Balasis, G., Papadimitriou, C., Anastasiadis, A., & Daglis, I. A. (2015). Accurately specifying storm-time ULF wave radial diffusion in the radiation belts. *Geophysical Research Letters*, *42*, 5711–5718. <https://doi.org/10.1002/2015GL064707>
- Drozdzov, A. Y., Shprits, Y. Y., Aseev, N. A., Kellerman, A. C., & Reeves, G. D. (2017). Dependence of radiation belt simulations to assumed radial diffusion rates tested for two empirical models of radial transport. *Space Weather*, *15*(1), 150–162. <https://doi.org/10.1002/2016SW001426>
- Elkington, S. R., Hudson, M. K., & Chan, A. A. (2003). Resonant acceleration and diffusion of outer zone electrons in an asymmetric geomagnetic field. *Journal of Geophysical Research*, *108*(A3), 1116. <https://doi.org/10.1029/2001JA009202>
- Fälthammar, C.-G. (1966). On the transport of trapped particles in the outer magnetosphere. *Journal of Geophysical Research*, *71*(5), 1487–1491. <https://doi.org/10.1029/JZ071i005p01487>
- Fälthammar, C.-G. (1968). Radial diffusion by violation of the third adiabatic invariant. In B. M. McCormac (Ed.), *Earth's particles and fields: proceedings of the NATO Advanced Study Institute held at Freising, Germany, July 31-August 11, 1967* (p. 157). New York: Reinhold Book Corporation.
- Fei, Y., Chan, A. A., Elkington, S. R., & Wiltberger, M. J. (2006). Radial diffusion and MHD particle simulations of relativistic electron transport by ULF waves in the September 1998 storm. *Journal of Geophysical Research*, *111*, A12209. <https://doi.org/10.1029/2005JA011211>
- Glauert, S. A., Horne, R. B., & Meredith, N. P. (2014). Simulating the Earth's radiation belts: Internal acceleration and continuous losses to the magnetopause. *Journal of Geophysical Research: Space Physics*, *119*, 7444–7463. <https://doi.org/10.1002/2014JA020092>
- Glauert, S. A., Horne, R. B., & Meredith, N. P. (2018). A 30-year simulation of the outer electron radiation belt. *Space Weather*, *16*, 1498–1522. <https://doi.org/10.1029/2018SW001981>
- Kersten, T., Horne, R. B., Glauert, S. A., Meredith, N. P., Fraser, B. J., & Grew, R. S. (2014). Electron losses from the radiation belts caused by EMIC waves. *Journal of Geophysical Research: Space Physics*, *119*, 8820–8837. <https://doi.org/10.1002/2014JA020366>
- Knutti, R., Furrer, R., Tebaldi, C., & Meehl, G. A. (2010). Challenges in combining projections from multiple climate models. Retrieved from <http://www.pcmdi.llnl.gov/ipcc/>. <https://doi.org/10.1175/2009JCLI3361.1>
- Kourentzes, N., Barrow, D., & Crone, S. (2014). Neural network ensemble operators for time series forecasting. *Expert Systems with Applications*, *41*, 4235–4244. <https://doi.org/10.1016/j.eswa.2013.12.011>
- Lejosne, S. (2019). Analytic expressions for radial diffusion. *Journal of Geophysical Research: Space Physics*, *124*, 4278–4294. <https://doi.org/10.1029/2019JA026786>
- Lejosne, S., Boscher, D., Maget, V., & Rolland, G. (2013). Deriving electromagnetic radial diffusion coefficients of radiation belt equatorial particles for different levels of magnetic activity based on magnetic field measurements at geostationary orbit. *Journal of Geophysical Research: Space Physics*, *118*, 3147–3156. <https://doi.org/10.1002/jgra.50361>
- Li, Z., Hudson, M., Patel, M., Wiltberger, M., Boyd, A., & Turner, D. (2017). ULF wave analysis and radial diffusion calculation using a global MHD model for the 17 March 2013 and 2015 storms. *Journal of Geophysical Research: Space Physics*, *122*, 7353–7363. <https://doi.org/10.1002/2016JA023846>
- Liu, W., Sarris, T. E., Li, X., Zong, Q.-G., Ergun, R., Angelopoulos, V., & Glassmeier, K. H. (2011). Spatial structure and temporal evolution of a dayside poloidal ULF wave event. *Geophysical Research Letters*, *38*, L19104. <https://doi.org/10.1029/2011GL049476>
- Liu, W., Tu, W., Li, X., Sarris, T., Khotyaintsev, Y., Fu, H., et al. (2016). On the calculation of electric diffusion coefficient of radiation belt electrons with in situ electric field measurements by THEMIS. *Geophysical Research Letters*, *43*, 1023–1030. <https://doi.org/10.1002/2015GL067398>
- Lyons, L. R., & Thorne, R. M. (1973). Equilibrium structure of radiation belt electrons. *Journal of Geophysical Research*, *78*(13), 2142–2149. <https://doi.org/10.1029/JA078i013p02142>

## CHAPTER 3. ACCOUNTING FOR VARIABILITY IN ULF WAVE RADIAL DIFFUSION MODELS



- Maget, V., Sicard-Piet, A., Bourdarie, S., Lazaro, D., Turner, D. L., Daglis, I. A., & Sandberg, I. (2015). Improved outer boundary conditions for outer radiation belt data assimilation using THEMIS-SST data and the Salammbó-EnKF code. *Journal of Geophysical Research: Space Physics*, *120*, 5608–5622. <https://doi.org/10.1002/2015JA021001>
- Mann, I. R., Lee, E. A., Claudepierre, S. G., Fennell, J. F., Degeling, A., Rae, I. J., et al. (2013). Discovery of the action of a geophysical synchrotron in the Earth's Van Allen radiation belts. *Nature Communications*, *4*, 2795. <https://doi.org/10.1038/ncomms3795>
- Meredith, N. P., Horne, R. B., Glauert, S. A., & Anderson, R. R. (2007). Slot region electron loss timescales due to plasmaspheric hiss and lightning-generated whistlers. *Journal of Geophysical Research*, *112*, A08214. <https://doi.org/10.1029/2007JA012413>
- Murphy, K. R., Mann, I. R., Rae, I. J., Sibeck, D. G., & Watt, C. E. J. (2016). Accurately characterizing the importance of wave-particle interactions in radiation belt dynamics: The pitfalls of statistical wave representations. *Journal of Geophysical Research: Space Physics*, *121*, 7895–7899. <https://doi.org/10.1002/2016JA022618>
- Murphy, K. R., Mann, I. R., & Sibeck, D. G. (2015). On the dependence of storm time ULF wave power on magnetopause location: Impacts for ULF wave radial diffusion. *Geophysical Research Letters*, *42*, 9676–9684. <https://doi.org/10.1002/2015GL066592>
- Murphy, K. R., Rae, I. J., Mann, I. R., & Milling, D. K. (2011). On the nature of ULF wave power during nightside auroral activations and substorms: 1. Spatial distribution. *Journal of Geophysical Research*, *116*, A00121. <https://doi.org/10.1029/2010JA015757>
- Olifer, L., Mann, I. R., Ozeke, L. G., Rae, I. J., & Morley, S. K. (2019). On the relative strength of electric and magnetic ULF wave radial diffusion during the March 2015 geomagnetic storm. *Journal of Geophysical Research: Space Physics*, *124*, 2569–2587. <https://doi.org/10.1029/2018JA026348>
- Ozeke, L. G., Mann, I. R., Murphy, K. R., Degeling, A. W., Claudepierre, S. G., & Spence, H. E. (2018). Explaining the apparent impenetrable barrier to ultra-relativistic electrons in the outer Van Allen belt. *Nature Communications*, *9*(1), 1844. <https://doi.org/10.1038/s41467-018-04162-3>
- Ozeke, L. G., Mann, I. R., Murphy, K. R., Jonathan Rae, I., & Milling, D. K. (2014). Analytic expressions for ULF wave radiation belt radial diffusion coefficients. *Journal of Geophysical Research: Space Physics*, *119*, 1587–1605. <https://doi.org/10.1002/2013JA019204>
- Ozeke, L. G., Mann, I. R., Murphy, K. R., Rae, I. J., Milling, D. K., Elkington, S. R., et al. (2012). ULF wave derived radiation belt radial diffusion coefficients. *Journal of Geophysical Research*, *117*, A04222. <https://doi.org/10.1029/2011JA017463>
- Ozeke, L. G., Mann, I. R., Murphy, K. R., Sibeck, D. G., & Baker, D. N. (2017). Ultra-relativistic radiation belt extinction and ULF wave radial diffusion: Modeling the September 2014 extended dropout event. *Geophysical Research Letters*, *44*, 2624–2633. <https://doi.org/10.1002/2017GL072811>
- Ozeke, L. G., Mann, I. R., & Rae, I. J. (2009). Mapping guided Alfvén wave magnetic field amplitudes observed on the ground to equatorial electric field amplitudes in space. *Journal of Geophysical Research*, *114*, A01214. <https://doi.org/10.1029/2008JA013041>
- Perry, K. L., Hudson, M. K., & Elkington, S. R. (2005). Incorporating spectral characteristics of Pc5 waves into three-dimensional radiation belt modeling and the diffusion of relativistic electrons. *Journal of Geophysical Research*, *110*, A03215. <https://doi.org/10.1029/2004JA010760>
- Rae, I. J., Murphy, K. R., Watt, C. E. J., & Mann, I. R. (2011). On the nature of ULF wave power during nightside auroral activations and substorms: 2. Temporal evolution. *Journal of Geophysical Research*, *116*, A00122. <https://doi.org/10.1029/2010JA015762>
- Rae, I. J., Murphy, K. R., Watt, C. E. J., Sandhu, J. K., Georgiou, M., Degeling, A. W., et al. (2019). How do ultra-low frequency waves access the inner magnetosphere during geomagnetic storms? *Geophysical Research Letters*, *46*, 10,699–10,709. <https://doi.org/10.1029/2019GL02395>
- Reeves, G. D., Chen, Y., Cunningham, G. S., Friedel, R. W. H., Henderson, M. G., Jordanova, V. K., et al. (2012). Dynamic radiation environment assimilation model: DREAM. *Space Weather*, *10*, S03006. <https://doi.org/10.1029/2011SW000729>
- Riley, P., & Wolf, R. A. (1992). Comparison of diffusion and particle drift descriptions of radial transport in the Earth's inner magnetosphere. *Journal of Geophysical Research*, *97*(A11), 16,865–16,876. <https://doi.org/10.1029/92JA01538>
- Roederer, J. G. (1970). *Dynamics of geomagnetically trapped radiation* / J.G. Roederer. Berlin: Springer-Verlag.
- Roederer, J. G., & Zhang, H. (2014). *Dynamics of magnetically trapped particles* (Vol. 403). Berlin, Heidelberg: Springer. <https://doi.org/10.1007/978-3-642-41530-2>
- Schulz, M., & Lanzerotti, L. (1974). Particle diffusion in the radiation belts / [by] M. Schulz [and] L. J. Lanzerotti. Springer-Verlag Berlin.
- Shin, D.-K., & Lee, D.-Y. (2013). Determining radial boundary conditions of outer radiation belt electrons using THEMIS observations. *Journal of Geophysical Research: Space Physics*, *118*, 2888–2896. <https://doi.org/10.1002/jgra.50334>
- Shprits, Y. Y., Elkington, S. R., Meredith, N. P., & Subbotin, D. A. (2008). Review of modeling of losses and sources of relativistic electrons in the outer radiation belt I: Radial transport. *Journal of Atmospheric and Solar-Terrestrial Physics*, *70*(14), 1679–1693. <https://doi.org/10.1016/j.jastp.2008.06.008>
- Shprits, Y. Y., Thorne, R. M., Reeves, G. D., & Friedel, R. (2005). *Annales Geophysicae* Radial diffusion modeling with empirical lifetimes: comparison with CRRES observations. (Vol. 23; Tech. Rep.)
- Thorne, R. M., Li, W., Ni, B., Ma, Q., Bortnik, J., Chen, L., et al. (2013). Rapid local acceleration of relativistic radiation-belt electrons by magnetospheric chorus. *Nature*, *504*, 411. <https://doi.org/10.1038/nature12889>
- Tu, W., Elkington, S. R., Li, X., Liu, W., & Bonnell, J. (2012). Quantifying radial diffusion coefficients of radiation belt electrons based on global MHD simulation and spacecraft measurements. *Journal of Geophysical Research*, *117*, A10210. <https://doi.org/10.1029/2012JA017901>
- Ukhorskiy, A. Y., Sitnov, M. I., Takahashi, K., & Anderson, B. J. (2009). Radial transport of radiation belt electrons due to stormtime Pc5 waves. *Annales Geophysicae*, *27*(5), 2173–2181. <https://doi.org/10.5194/angeo-27-2173-2009>
- Vacaresse, A., Boscher, D., Bourdarie, S., Blanc, M., & Sauvaud, J. A. (1999). Modeling the high-energy proton belt. *Journal of Geophysical Research*, *104*(A12), 28,601–28,613. <https://doi.org/10.1029/1999JA900411>
- Watt, C. E. J., Allison, H. J., Meredith, N. P., Thompson, R. L., Bentley, S. N., Rae, I. J., et al. (2019). Variability of quasilinear diffusion coefficients for plasmaspheric hiss. *Journal of Geophysical Research: Space Physics*, *124*, 8488–8506. <https://doi.org/10.1029/2018JA026401>
- Watt, C. E. J., Rae, I. J., Murphy, K. R., Anekallu, C., Bentley, S. N., & Forsyth, C. (2017). The parameterization of wave-particle interactions in the Outer Radiation Belt. *Journal of Geophysical Research: Space Physics*, *122*, 9545–9551. <https://doi.org/10.1002/2017JA024339>
- Welling, D., Koller, J., & Camporeale, E. (2011). Verification of SpacePy's radial diffusion radiation belt model. *Geoscientific Model Development*, *5*, 277–287. <https://doi.org/10.5194/gmdd-4-2165-2011>

## CHAPTER 4

### VARIABILITY OF $L^*$ WITH OBSERVATION LOCATION

In this Chapter we are going to investigate the variability of  $L^*$ , a parameter which is key for assessing the transport of particles as a function of drift-shell in non-dipolar magnetic fields and subsequently for constructing  $D_{LL}$ . In the pilot study (Chapter 3, Thompson et al. [2020b]) which investigated the impact of including the natural variability of  $D_{LL}$  in the radial diffusion equation, we discovered that the rate of radial diffusion was significantly enhanced by including variability in wave power with a significant spectral tail and perfectly correlated, monotonic  $\mathcal{P}$  across  $L^*$ . Since  $L^*$  is not a fixed coordinate in real space, it is imperative to ascribe  $\mathcal{P}$  observations to the correct  $L^*$  or risk driving the sensitive radial diffusion equation with unrealistic  $\mathcal{P}$  descriptions.

Deriving empirical models of  $D_{LL}$  typically adheres to the following:

1. Assume a magnetic field geometry to group power spectral density observations into  $L^*$
2. Bin power spectral density at each  $L^*$  by some variable(s) describing geomagnetic activity, with frequency/energy dependence if necessary
3. Fit a power law to  $\langle \mathcal{P}(L^*, \cdot) \rangle$  and infer  $D_{LL}$ , where  $\cdot$  are the controlling dependent variables concerning geomagnetic activity and/or energy dependence

The pioneering analytic expressions for  $D_{LL}$  from Fälthammar [1965]; Fei et al. [2006] were based on a magnetic field that was exactly or very near to dipolar. Likewise, many of their descendants (e.g. Liu et al. [2016]; Ozeke et al. [2012, 2014]) which are implemented in operational radiation belt models (e.g. Glauert et al. [2018]) assumed a pure-dipole to bin  $\mathcal{P}$  observations and infer an empirical  $D_{LL}$ .  $\mathcal{P}$  distributions ascribed to drift shells fixed in real space by a simple analytic magnetic field geometry actually sample many  $L^*$ , aliasing an observation's location in adiabatic invariant space and introducing uncertainty in any derived descriptions of  $D_{LL}$ .

We should therefore look to collecting  $\mathcal{P}$  observations in  $L^*$  approximated by more complex magnetic field geometries, namely, empirical models which evolve with changes in solar wind driving and geomagnetic activity. Some empirical  $D_{LL}$  models have attempted this (Brautigam and Albert [2000]; Brautigam et al. [2005]; Ali et al. [2015, 2016]) but yield vastly different results upon comparison (Drozdov et al. [2020]). Of course, we must remember that applying  $L^*$ -assigned power into the Fälthammar [1965]; Fei et al. [2006]  $D_{LL}$  derived using McIlwain [1961] L-Shell is ambiguous. True  $D_{LL}$  must be derived using  $L^*$  from first principles (e.g. Lejosne and Kollmann [2020]), however, this is beyond the scope of this thesis.

While differences may result due to the formalism from which the  $D_{LL}$  were derived (Fälthammar [1965] vs Fei et al. [2006]), a likely contributor is discrepancy between the empirical magnetic field models used to bin  $\mathcal{P}$  observations at each  $L^*$ . A number of empirical magnetic field models exist but lead to substantial differences when approximating  $L^*$  (e.g. Albert et al. [2018]) due to the complexities of magnetospheric current systems included, or not, in each model. Model validation is also difficult; satellite observations are too sparse with limited, spatially imbalanced observations of the global magnetosphere (see Brito and Morley [2017], Figure 2) with which to fully determine a model's performance. In any case model accuracy for approximating  $L^*$  might be spatially dependent, ie one model may have a better description of the dayside magnetosphere, and one may provide a better description of the nightside. Since the magnetic field geometry provides the foundation for determining  $L^*$  and subsequently  $D_{LL}$ , minimising uncertainties in the adiabatic mapping to mitigate future error propagation becomes vital.

In this Chapter we describe how we created a probabilistic  $L^*$  model with predictive capabilities that can be integrated with operational radiation belt models (Thompson et al. [2020a]). Pro- $L^*$  is a probabilistic  $L^*$  mapping tool for ground observations in the Northern Hemisphere to the magnetic equator for a multitude of renowned empirical magnetic field models. Using Pro- $L^*$  we are able to quantify  $L^*$  variability between and within empirical magnetic field models at fixed observation locations on the ground and in space (where space locations are precisely the radial positions on the magnetic equator mapped from the ground). We further explore how the empirical  $L^*$  distributions respond to increasing levels of geomagnetic activity, specifically throughout geomagnetic storm phases. The motivation for Pro- $L^*$  was to create a computationally inexpensive model at point of use that can reduce uncertainty for calculated  $D_{LL}$  for both ground and space observations, as well as providing tools for more accurate statistical studies. Further models are discussed for space-based observations in three-dimensions (radius, latitude, longitude), including the variation of  $L^*$  with pitch angle.

## 4.1 Pro- $L^*$ - A Probabilistic $L^*$ Mapping Tool for Ground Observations

The following manuscript has been published in the journal *Space Weather*. The full reference for this publication can be found in the bibliography under Thompson et al. [2020a].

# Space Weather



## RESEARCH ARTICLE

10.1029/2020SW002602

### Key points:

- Pro- $L^*$  uses multiple magnetic field models to estimate  $L^*$  corresponding to ground footprints across the Northern Hemisphere
- The use of multiple models reduces systematic bias from single models, and introduces variability which informs us of model weaknesses
- Pro- $L^*$  is a rapid alternative to computationally expensive standard techniques and quantifies inherent uncertainty from model biases

### Supporting Information:

- Supporting Information S1
- Data Set S1
- Data Set S2
- Data Set S3
- Data Set S4
- Data Set S5
- Data Set S6
- Data Set S7
- Data Set S8
- Data Set S9
- Data Set S10
- Data Set S11
- Data Set S12
- Data Set S13
- Data Set S14
- Figure S1
- Figure S2
- Figure S3
- Figure S4
- Figure S5

### Correspondence to:

R. L. Thompson,  
[r.l.thompson@pgr.reading.ac.uk](mailto:r.l.thompson@pgr.reading.ac.uk)

### Citation:

Thompson, R. L., Morley, S. K., Watt, C. E. J., Bentley, S. N., & Williams, P. D. (2021). Pro- $L^*$  - A probabilistic  $L^*$  mapping tool for ground observations. *Space Weather*, 18, e2020SW002602. <https://doi.org/10.1029/2020SW002602>

Received 4 AUG 2020  
 Accepted 11 DEC 2020

© 2020. The Authors.  
 This is an open access article under the terms of the [Creative Commons Attribution License](#), which permits use, distribution and reproduction in any medium, provided the original work is properly cited.

## Pro- $L^*$ - A Probabilistic $L^*$ Mapping Tool for Ground Observations

Rhys L. Thompson<sup>1</sup> , Steven K. Morley<sup>2</sup> , Clare E. J. Watt<sup>3</sup> , Sarah N. Bentley<sup>3</sup> , and Paul D. Williams<sup>3</sup> 

<sup>1</sup>Department of Mathematics and Statistics, University of Reading, Reading, UK, <sup>2</sup>Space Science and Applications, Los Alamos National Laboratory, Los Alamos, NM, USA, <sup>3</sup>Department of Meteorology, University of Reading, Reading, UK

**Abstract** Both ground and space observations are used extensively in the modeling of space weather processes within the Earth's magnetosphere. In radiation belt physics modeling, one of the key phase-space coordinates is  $L^*$ , which indicates the location of the drift paths of energetic electrons. Global magnetic field models allow a subset of locations on the ground (mainly subauroral) to be mapped along field lines to a location in space and transformed into  $L^*$ , provided that the initial ground location maps to a closed drift path. This allows observations from ground, or low-altitude space-based platforms to be mapped into space in order to inform radiation belt modeling. Many data-based magnetic field models exist; however, these models can significantly disagree on mapped  $L^*$  values for a single point on the ground, during both quiet times and storms. We present a state of the art probabilistic  $L^*$  mapping tool, Pro- $L^*$ , which produces probability distributions for  $L^*$  corresponding to a given ground location. Pro- $L^*$  has been calculated for a high resolution magnetic latitude by magnetic local time grid in the Earth's Northern Hemisphere. We have developed the probabilistic model using 11 years of  $L^*$  calculations for seven widely used magnetic field models. Usage of the tool is highlighted for both event studies and statistical models, and we demonstrate a number of potential applications.

**Plain Language Summary** Observations made by ground and space based instruments are used extensively in modeling of space weather processes within the Earth's radiation belts, regions of charged and energetic particles trapped by Earth's magnetic field. The shape of the magnetic field is not fixed, however, and there is not a consistent relationship between the footprint location of a ground measurement and its respective position in space. With no way to validate the global true magnetic field, numerous models exist to approximate it. We often envision the radiation belts in a fixed coordinate system representative of the motions of the trapped particles. Often considered a proxy for distance is  $L^*$ , a quantity related to the radial motion of electrons. Once an observation's respective location in the magnetic field is approximated it can be transformed into  $L^*$ , provided the electrons at the measurement's physical location remain trapped. Dependency of  $L^*$  on magnetic field model accuracy is paramount, yet models can significantly disagree on the  $L^*$  of colocated observations. We present a state-of-the-art tool, Pro- $L^*$ , which for any ground observation provides the probabilities of corresponding  $L^*$  values. Usage is highlighted for both event studies and statistical models, and we demonstrate a number of potential applications.

## 1. Introduction

The operational and research-focused modeling of high-energy electron fluxes in Earth's radiation belts is based upon the physics of electron motion in the Earth's magnetic field. High-energy electrons are trapped in the approximately dipolar magnetic field and execute three motions: very fast gyromotion (with periods of less than 1 ms), fast bounce motion between hemispheres (with periods of  $\sim 1$  s) and drift motion around the planet (with periods of minutes). Models of radiation belt dynamics use a coordinate system based upon these motions, which can be described using a system of adiabatic invariants  $\mu$ ,  $J$ , and  $L^*$ . This means that slow, reversible changes to the energy and path of electrons due to slow changes in the magnetic field are automatically taken into account in the model, since the computational grids themselves are based upon the invariant. It therefore becomes very important to be able to map between real space, and energy space, to the values of these adiabatic invariants at every stage in model development. The creation of initial conditions, boundary conditions (e.g., Glauert et al., 2018), diffusion matrices (e.g., Horne et al., 2018),

and indeed the calculations within the models themselves (e.g., Loridan et al., 2019) all require mapping between observation space and adiabatic invariant space. The mapping depends acutely on the details of the global magnetic field, and so can be model-dependent. In this paper, we focus on the third adiabatic invariant,  $L^*$ , the invariant associated with the drift of the high-energy electron around the Earth. We highlight differences and similarities between  $L^*$  calculated using a number of different global magnetic field models. We highlight how a probabilistic model can be used to map observations to computational grid locations in an operational or research-focused radiation belt model in a way that helps to quantify the uncertainty in the relationship.

The Earth's magnetic field is a vast and complex environment, dynamically driven by both internal fields and interactions with solar wind plasma external fields. Although typically in a quiescent state, morphological changes of the magnetic field can be rapid during geomagnetic storms and substorms (Ganushkina et al., 2010; Kubyshkina et al., 2011). Modeling the Earth's magnetic field is therefore a challenging task, and numerous magnetic field models have been introduced, combining mathematical frameworks with both ground and space observations to better describe the magnetic field morphology on timescales of variability (of which the external field can vary from seconds, to hours, days, and beyond the 11-year solar cycle period; e.g., Fairfield & Mead, 1975; Tsyganenko, 1989, 1995, 1996, 2002a, 2002b).

Our ability to perform research within the magnetosphere, to create models and to interpret our findings, hinges crucially on our ability to relate our location in real space to a meaningful position in the Earth's magnetic field. When constructing statistical analyses of datasets, one can use extensive satellite data archives and/or ground-based observing platforms such as magnetometers. Ground observations typically have continuous data-sets with better global coverage, naturally lending themselves to replace satellites in studies when the latter has insufficient data coverage. For example, ground magnetometers in the Canadian Array for Realtime Investigations of Magnetic Activity (CARISMA) contributed to NASA's Time History of Events and Macroscale Interactions during Substorms (THEMIS) mission by investigating macroscale substorm instabilities, storm-time high energy electron production, and solar wind-magnetosphere coupling control mechanisms (Angelopoulos, 2008; Mann et al., 2008; Sibeck & Angelopoulos, 2008).

In this paper, we focus specifically on the relationship between ground-based magnetometer stations and a coordinate set that is appropriate for the study of trapped electrons in Earth's radiation belts. In radiation belt physics the parameter  $L^*$  (Roederer, 1970) is a function of the third adiabatic invariant  $\Phi$  and describes the location of a closed drift path of a charged particle in near-Earth space. This parameter is not a location per se, but it is a useful measure of the behavior of charged particles in Earth's magnetic field and is often used in modeling. Although  $L^*$  is not defined on the Earth's surface, ground instruments are used for radiation belt physics through mapping along respective field lines and calculating  $L^*$  for equatorially mirroring particles. For example, ULF waves are mapped from ground to space via their footprint locations to infer radial diffusion coefficients dependent on  $L^*$  (e.g., Fei et al., 2006; Ozeke et al., 2014, 2012), which inform Fokker-Planck radiation belt models (Roederer & Zhang, 2014). The precise value, or indeed existence, of  $L^*$  requires knowledge of the instantaneous global magnetic field configuration across the entire magnetosphere. There are a range of available models, configured for different magnetospheric states and geometries. These can disagree on  $L^*$  approximations over a multitude of magnetic latitudes and longitudes (e.g., model comparisons for the last closed drift shell (LCDS) during four events in Albert et al. (2018) (Figures 6–9)). As each model is usually constructed either with a specific set of data or to represent specific magnetospheric conditions, utilizing only one will introduce an inherent bias in the mapped location of the ground observation, which may propagate through the remainder of the study.

In this manuscript, we present Pro- $L^*$ , a freely available probabilistic  $L^*$  mapping tool for ground observations to  $L^*$  at the magnetic equator. Pro- $L^*$  covers a high resolution grid of ground locations in magnetic latitude, longitude, and magnetic local time (MLT) in the Northern Hemisphere, where the majority of ground instruments are located. Pro- $L^*$  combines multiple magnetic field models probabilistically producing multiple realistic outputs instead of a single value. We specifically embrace the uncertainty inherent in using different magnetic field models to calculate  $L^*$ , making an attempt to highlight and quantify it. As  $L^*$  is an abstract quantity, it cannot be directly measured and so there is no observed "global truth" with which to compare. Therefore, model produced estimates of  $L^*$  would benefit from uncertainty quantification which Pro- $L^*$  provides by design.

The remainder of the manuscript is structured as follows. In Section 2 we explain the method for calculating  $L^*$  from a ground location. Section 3 discusses the data which comprises Pro- $L^*$ . Section 4 presents statistical results for each independent magnetic field model from the 11-year data set, and also their combination into a simple probabilistic model for  $L^*$ . Section 5 displays usage of Pro- $L^*$  for the Quantitative Assessment of Radiation Belt Modeling (QARBM) 2013 GEM challenge events, with interpolation capability across grid-cells to user-specified locations explored in Section 6. The method for calculating  $L^*$ , how to effectively combine magnetic field models into a probabilistic representation, and later developments of Pro- $L^*$  into a functioning model are discussed in Section 7.

## 2. Computation of $L^*$

The third adiabatic invariant  $\Phi$  measures the magnetic flux through drift contours of azimuthally drifting energetic particles trapped in the Earth's magnetic field.  $\Phi$  is typically conserved for processes occurring on timescales less than the drift period, and is formally expressed as the total magnetic flux enclosed by the drift trajectory

$$\Phi = \int \mathbf{B} \cdot d\mathbf{S} \quad (1)$$

where  $\mathbf{B}$  is the total magnetic field strength and  $\mathbf{S}$  is the surface contained within the drift trajectory. The Roederer (1970)  $L^*$  is often used as a proxy for distance in adiabatic invariant space, but can be thought of physically as the value which would be equal to the McIlwain  $L_m$  (McIlwain, 1961) after a "freezing" of the magnetic field and adiabatically turning off all external currents, relaxing to a geomagnetic dipole field (Roederer & Lejosne, 2018).  $L^*$  is given by the transformation

$$L^* = 2\pi B_E R_E^2 / \Phi \quad (2)$$

where  $B_E$  is the equatorial magnetic field strength at one Earth radii ( $R_E$ ).

The Earth's magnetic field  $\mathbf{B}$  can be expressed in terms of its internal (I) and external (E) components

$$\mathbf{B} = \mathbf{B}_I + \mathbf{B}_E \quad (3)$$

For all magnetic field models considered in this manuscript we adopt the International Geomagnetic Reference Field (IGRF) internal field model (Finlay et al., 2010; Thébaud et al., 2015). The external field is more complicated, and contains contributions from the ring current,  $\mathbf{B}_{RC}$ , tail current sheet,  $\mathbf{B}_{TC}$ , large-scale field-aligned current systems,  $\mathbf{B}_{FAC}$  (including both Region 1 and 2, see Carter et al., 2016, Figure 1), and the magnetopause currents,  $\mathbf{B}_{MP}$  (Tsyganenko, 2013). The total field may therefore be expressed as

$$\mathbf{B} = \mathbf{B}_I + \mathbf{B}_{RC} + \mathbf{B}_{TC} + \mathbf{B}_{FAC} + \mathbf{B}_{MP} \quad (4)$$

The external magnetic field requires models which aim to include some or all of the underlying components, with more advanced empirical models describing the complex geometries with space and ground-based measurements. Since  $L^*$  is dependent on the assumed magnetic field model, it is useful to have software containing a range of magnetic field models easily accessible, from which  $L^*$  can be determined.

### 2.1. SpacePy and IRBEM-Lib

SpacePy (Morley et al., 2010) is an open source package in Python, which aims to make data science, modeling and visualizations easier for space sciences (see also Burrell et al., 2018). The package provides a convenient interface to the IRBEM (formally the ONERA) library, a collection of FORTRAN 77 routines for radiation belt modeling, including calculation of magnetic coordinates and drift shells using a range of user-specified magnetic field models (Boscher, 2013).

The IRBEM-Lib calculates  $L^*$  via the procedure given in Sections 3.2 and 3.5 of Roederer and Zhang (2014). The second adiabatic invariant  $J$  is associated with the bounce motion of trapped particles between magnetic mirror points. Defined as the integral taken along the guiding field line for a complete bounce cycle, in the case of a static magnetic field without field-aligned currents  $J$  may be mathematically given as

$$J = 2pI, \quad I = \int_{s_m}^{s'_m} \sqrt{1 - B(s) / B_m} ds \quad (5)$$

where  $p$  is the particle's momentum,  $I$  is a line integral function between magnetic mirror points  $s_m, s'_m$  on a given field line, a function of the magnetic field  $B$  along the field line and the mirror point field intensity  $B_m$ . The conservation of  $J$  implies that of  $I$ . For a specified location and pitch angle,  $B_m$  is determined and  $I$  is calculated by tracing the field line between the two initial conjugate mirror points. To determine the drift shell, points are found at other longitudes where  $B = B_m$ . Using these points an iterative search is executed to find the field lines with  $I_{\text{point}} = I \pm$  some prefixed error. These field lines have an associated footprint on the Northern Hemisphere. If the algorithm fails at a particular longitude, the particle has left its trapping region.

With the located field lines defining the drift shell and their corresponding latitudinal footprints, it suffices to calculate  $\Phi$  numerically as the magnetic flux through the region on the polar cap  $\Pi$  enclosed by the Northern Hemispheric footprints

$$\Phi = \int_{\pi} \mathbf{B} \cdot d\mathbf{S} \quad (6)$$

using the Earth's known surface field  $B_s$  in the polar cap (for most models it is sufficient to use a dipole approximation here). With the third invariant calculated, we can therefore obtain  $L^*$  using the Roederer (1970) expression. This approach, along with its implementation in SpacePy and IRBEM-Lib, employs several assumptions and limitations which will be explored later in the discussion.

For ground observations, calculation of  $L^*$  involves two steps—mapping from the ground station to the magnetic equator, followed by estimating  $L^*$  for equatorially mirroring particles at the mapped location. The latter step is therefore a reduced version of the above, since  $I = 0$ . The same magnetic field model is used in both steps.

### 3. Data Processing

We seek an  $L^*$  database which covers a high enough resolution to sufficiently represent a high proportion of ground observation locations. A significant majority of ground observations are located in the Northern Hemisphere, suggesting that this should be our primary focus. Since there are interhemispheric differences in the ground magnetic field, a separate database should be produced for the Southern Hemisphere. This is a goal of future work. Since a dipole approximation is sufficient for low latitudes, and moderately high latitudes experience mostly open field lines, we focus on magnetic latitudes in Altitude-Adjusted Corrected Geomagnetic (AACGM) coordinates that map to the dipole  $L$  range  $L = 2.5$ – $10$ , with  $0.5 L$  spacing. The choice of uniformity in dipole  $L$  rather than magnetic latitude was made to promote a higher density of points at mid-high latitudes, where ground observations are frequently sought. For magnetic longitudes we use a  $15^\circ$  resolution around the Earth from  $0^\circ$ – $360^\circ$ , in order to provide good MLT resolution and capture diurnal variations. The grid is illustrated in Figure 1.

At each gridpoint over the years 2006–2016, hourly equivalent  $L^*$  is estimated using seven magnetic field models, outlined in Table 1, chosen for their credibility and relevance to current modeling standards (Olson & Pfizter, 1974; Ostapenko & Maltsev, 1997; Tsyganenko, 1989, 1995, 1996, 2002a, 2002b; Tsyganenko et al., 2003; Tsyganenko & Sitnov, 2005). For the remainder of this study we will refer to magnetic field models via the model code in Table 1. The earliest of the models is OPQUIET, which unlike the others is analytic. Constructed to take into account the depressed nature of the magnetic field in the inner magnetosphere caused by the presence of the distributed ring current, it well represented currents that flow in a distributed way through a large volume. Initially describing only the symmetric component of the magnetosphere, the model was later developed to include dipole-tilt effects. These significant limitations are balanced by the

property that the OPQUIET model can always provide a value for the magnetic field and does not require input data that may be lacking from the monitoring record or in real-time.

As time progressed, magnetic field models evolved from analytic approaches to incorporate satellite data and more sophisticated parameterization. T89 was among the first, constructing a simple empirical approximation for the global magnetosphere, binned into several intervals of the geomagnetic disturbance index  $K_p$ . The model incorporated a thin current sheet with two-dimensional warping near the inner edge of the plasma sheet in the nightside which plays a key role in the dynamics of disturbances, since it is at the boundary between the internal field sources and the magnetotail currents. Since a simple parameterization by  $K_p$  combined a collection of physical processes together, it was recognized that the current solar wind state might add more information to the parameterization. T96 adopted this approach and developed on the T89 model, explicitly defining a realistic magnetopause, large-scale Regions 1 and 2 Birkeland current systems, and interplanetary magnetic field (IMF) penetration across the boundary. The nature of subsequent Tsyganenko models prior to 2016 was to update and expand on previous models. T01QUIET updated the approaches given in T96, introduced a partial ring current, and included integrals of geoeffective IMF-related parameters with hourly time history into the model parameterization. T01STORM configured T01QUIET for a set of rare geomagnetic storms, taking into account the nonlinear response of the magnetosphere to abnormally strong disturbances in solar wind, which previous models ignored. T05 recognized that different sources of the geomagnetic field have different response and decay times, which was overlooked in T01STORM, and introduced terms in the model parameterization to account for these response and decay times. The most recent Tsyganenko models fit the magnetic fields using basis functions and no longer use parameterized representations of current systems (see Tsyganenko & Andreeva, 2016, 2017). These models are currently not available in SpacePy and therefore not included in Pro- $L^*$ .

The final model we use to construct Pro- $L^*$  is OSTA, which is parameterized by solar wind properties yet independent of the Tsyganenko models. Using a database of more than 14,000 magnetic measurements by Fairfield et al. (1994), the statistical connection between the external field, satellite data and geomagnetic indices was explored, resulting in a magnetic field with dipolar azimuthal symmetry, with additive day-night asymmetry and dipole-tilt effects. Further models relevant to this study exist, but are not available in our chosen software. Incorporation of more recent models (Tsyganenko or otherwise) is a goal of future development. Some models are more suitable for quiet or storm times, and many of the Tsyganenko family of models are developments of previous versions. In this work, we assume that all magnetic field models are independent and therefore contribute equally to our  $L^*$  estimate. We discuss comparisons between the models, validity and weightings later.

In addition to  $L^*$ , for each magnetic field model we also store the McIlwain (1961)  $L_m$ , equatorial magnetic field amplitude  $B$ , and geographic Cartesian location  $\mathbf{x}$  at the point on the magnetic equator mapped from each ground location. These variables are also stored for the case of no external magnetic field, that is, purely the IGRF. The MLT of each gridpoint is also stored. Collecting these variables hourly for each gridpoint over 11-year results in Pro- $L^*$  containing approximately  $\sim 1.9$  billion entries.  $L^*$  calculations alone account for  $\sim 260$  million. Creating the database is a very computationally expensive task. Calculating  $L^*$  for a single hour, across all seven models and the full grid, takes approximately 13 h on a single core. The total number of CPU hours used in calculating the data set is in the vicinity of 127,000. Although parallelization of  $L^*$  calculations across multiple cores has drastically reduced the database formulation time to the order of weeks, it is clear that the mapping of ground-based data and calculation of adiabatic coordinates is unreasonably expensive. A key benefit of Pro- $L^*$  as a statistical model for radiation belt applications is that calculations need only to be executed once; any subsequent statistical results can be derived from Pro- $L^*$  on timescales much shorter than manual computation.

#### 4. Statistical Results

In this section, we present individual model statistics deduced from Pro- $L^*$ , and demonstrate a simple approach to combining all models into probabilistic models. These models allow for an extensive statistical study in multidimensional space, and we present key results in this manuscript. Further relevant results are provided in the Supporting Information.

#### 4.1. Individual Model Statistics

Global  $L^*$  median and interquartile range (IQR) maps for each magnetic field model are shown in Figures 2 and 3. Each plot depicts a polar projection of our grid looking down on the magnetic North Pole. Magnetic latitude decreases radially from the center and MLT extends anticlockwise from midnight at the rightmost point (an imaginary Sun is to the left of each diagram). However, since we are mapping these ground locations to the magnetic minimum in space along the same field line, we choose to indicate the equivalent dipole  $L$  value on each plot, rather than magnetic latitude (remember that our grid is uniformly spaced in equivalent dipole  $L$ , not magnetic latitude). Note that the equivalent dipole  $L$  decreases from the pole outwards in the plot.

White regions in each radial plot indicate the absence of any mapped  $L^*$  estimates at that grid location. To accompany Figures 2 and 3, occurrence maps with the same plot format for each magnetic field model are shown in Figure 4, to demonstrate the occurrence of successful  $L^*$  estimates in all regions. Note that we assume that where the  $L^*$  calculation fails, it does so because that ground location does not map to a closed drift path. This could be because (a) there is no equivalent closed drift path at the mapped location for a  $90^\circ$  pitch-angle electron; or (b) the  $L^*$  determination was not completed due to constraints in the IRBEMlib calculation ( $L_m > 10$  for all models, or if the  $x < -15R_E$  in geocentric solar magnetospheric coordinates for T05). All input variable data for the empirical magnetic field models contain no gaps (with interpolation performed as in Qin et al., 2007) and is not a cause for model default.

As expected, almost all models fail to provide  $L^*$  values on the nightside at high latitudes.  $L^*$  values begin to fail on the dawn and dusk flanks at the highest latitudes, and only succeed at lower latitudes closer to midnight. Coverage for all Tsyganenko models remains fairly consistent, but T01STORM has the best coverage suggesting that T01STORM provides storm-time configurations that support closed drift paths at higher latitudes. Conversely, OSTA has full global coverage and is defined for both quiet and disturbed times. This model should be used with caution, however, since median  $L^*$  values at high latitudes on the nightside do not monotonically increase with latitude and are therefore unphysical.

We should note that a failure to calculate  $L^*$  is not a failure of the magnetic field model and instead reflects the fact that  $L^*$  is only defined on a closed drift path. We do not expect our chosen ground-based grid to map to valid  $L^*$  on the entirety of the nightside, because high latitude stations map to open-field lines, or to regions of the magnetosphere just inside the open-closed field line boundary, that may not support closed drift paths. Where multiple magnetic field models produce an  $L^*$  value at the same location is a good indication of where  $L^*$  truly exists. When only one model produces an estimate of  $L^*$ , it suggests that we should be less confident in the estimate. We discuss in Section 4.2 methods for combining results from multiple magnetic field models.

All magnetic field models exhibit similar median  $L^*$  spatial profiles. The dayside has full coverage of  $L^*$ , increasing steadily in magnetic latitude with the compressed field lines at noon, attaining its maximum at the highest latitude. As we extend round the dawn-dusk flanks, the location of maximum  $L^*$  values fall to lower latitudes. This day-night asymmetry is not surprising due to the nature of field line compressions, stretching and reconnections throughout the Dungey cycle. More recent models tend to estimate larger values of  $L^*$  values from dusk through midnight to dawn. There is a small patch of low  $L^*$  estimates at high latitude on the nightside in the T05 model, which are also likely to be unphysical.

Differences appear between models once we consider the IQR of the estimated  $L^*$ . Generally speaking,  $L^*$  estimates are highly reproducible in all magnetic field models for all latitudes below  $60^\circ$  ( $L_{\text{dip}} = 4$ ). Here, IQR values are less than 0.1. This is unsurprising as we expect the internal magnetic field to dominate at lower latitudes. As expected, the early OPQUIET model has the least variability over all latitudes. It should be stressed however that a model with low variability does not suggest an accurate model. The magnetosphere is a very dynamic environment, and variability in  $L^*$  should be anticipated. All other models exhibit bell-shaped regions of heightened uncertainty, somewhat symmetric through the noon-midnight plane. These regions extend from around  $66^\circ$  ( $L_{\text{dip}} = 6$ ) to the highest latitude on the dayside, and from  $60^\circ$  ( $L_{\text{dip}} = 4$ ) to the  $L^*$ -definition boundary on the nightside. Although successive Tsyganenko models partially reduce the extent of the uncertainty region on the dayside, the nightside region remains considerably variable, with IQR  $\sim 1$ . This is likely the result of changing conditions in the magnetic field due to the solar wind

and geomagnetic activity being more prevalent at high latitudes on the nightside. The T01STORM and T05 models, which were configured to geomagnetic storms, also show enhanced variability during predawn at higher latitudes. In all models the quantified uncertainties in the bell-shaped regions are large enough from a modeling perspective to justify that a probabilistic  $L^*$  is necessary.

The shape of model distributions in each MLT sector (dawn [3–9], noon [9–15], dusk [15–21], and midnight [21–23]) for a selection of magnetic latitudes is shown in Figure 5. The remainder of magnetic latitudes studied are provided in the Supporting Information. In all MLT sectors  $L^*$  displays little variability at the lowest latitude, with variability small enough to appear almost as a delta function when viewed on the same scale as the other latitudes. As magnetic latitude increases, the analytic OPQUIET model quickly breaks from the empirical models across all MLT sectors and does not resemble the shape of any well-known distribution. Concurrently at dawn and dusk, the remaining distributions of  $L^*$  display increasing variability as latitude increases. The distributions are quite positively skewed at  $66.91^\circ$  and  $67.79^\circ$ , before becoming increasingly Gaussian at  $71.57^\circ$ . Comparing between the Tsyganenko family of models, the Gaussian profile becomes smoother progressively with each successive model release. At noon, the distribution of  $L^*$  also displays increasing variability with increasing latitude, but the distributions are negatively skewed for  $66.91^\circ$  and  $67.79^\circ$ , before becoming more Gaussian at  $71.57^\circ$ . Comparisons between model distributions of  $L^*$  are unfair for high latitudes in the midnight sector because not all models return  $L^*$  values in this region. However, it is surprising that the shapes of the midnight distributions at  $66.91^\circ$  are similar to those at the highest latitude in all other sectors.

The distributions demonstrate that constructing models of variability in  $L^*$  is a complex problem since we have multiple sources of uncertainty. In our probabilistic model, it is imperative to distinguish when variability in our  $L^*$  estimate represents variability in the true  $L^*$  value. In some regions the variability in our  $L^*$  estimates is magnetic field model dependent. At other locations where  $L^*$  distributions are roughly the same for all magnetic field models, any variability in our  $L^*$  estimate is mainly due to changing conditions in the magnetosphere which are correctly captured using our magnetic field models. We must both identify and treat these as distinct sources of uncertainty.

#### 4.2. Simple Global Probabilistic $L^*$ Models

The most simple approach for combining colocated  $L^*$  values calculated by individual magnetic field models is to equally weight the  $L^*$  estimate from each magnetic field model and provide the median. This is the most straightforward approach, but each model used in our study is not fully independent. For example, on a technical level each Tsyganenko model is a development on the one preceding it, and we expect each successive model to provide a better description of the magnetic field geometry and thus hold more weight in a probabilistic model. It must also be stressed that determining when  $L^*$  is not physically defined is as important as accurately calculating its value when it is. Combining models in a simple equally weighted averaging approach would combine NaN values (i.e., no  $L^*$  defined at this time for this ground-based location) with finite values in a way that could prove to be misleading.

Instead, we define confidence in  $L^*$  (both the existence of  $L^*$  and the estimated value) as the number of models that return a value. Then, we can naively combine the finite values of  $L^*$  in a simple way to investigate how model uncertainty might affect the distribution of  $L^*$ . Contour maps for the median, IQR, and occurrence regions of the global probabilistic models are illustrated in Figure 6. Each probabilistic model is described by the threshold confidence value  $m$ —the number of magnetic field models required to return an  $L^*$  value at any given time. From Figure 6, we immediately observe that a confidence level of at least  $m = 3$  is necessary to obtain physical (monotonically increasing with latitude)  $L^*$  distributions on the nightside. Assuming that  $m = 3$  is satisfactory for estimating  $L^*$  from combined model outputs, it may be sensible to assume that  $L^*$  is always undefined for ground locations beyond the vicinity of  $68^\circ$  ( $L_{\text{dip}} = 7$ ) on the nightside. As we trace through predawn and postdusk, the definition boundary, the latitudinal boundary between defined and undefined  $L^*$ , increases smoothly until  $L^*$  is fully defined at dawn and dusk. As we increase the number of models required the  $L^*$  definition boundary erodes to lower latitudes. Note that we can only infer this boundary from our calculations at discrete locations in magnetic latitude. We do not expect the true latitudinal boundary for  $L^*$  existence, analogous to the LCDS, to exist precisely at one of our grid locations.

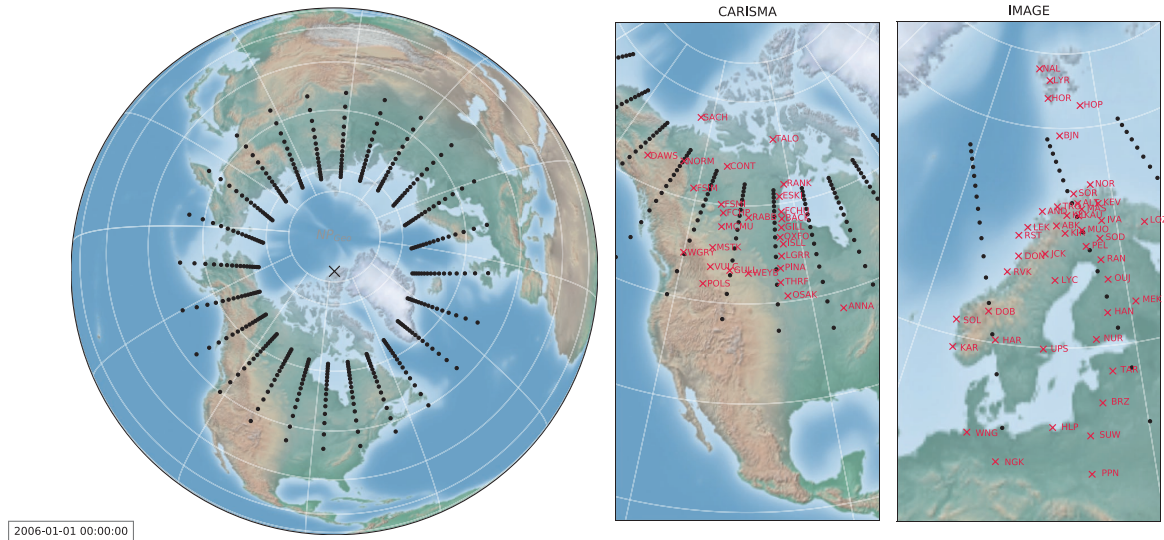


**Figure 1.** A snapshot of January 1, 2006 showing (left) the Pro- $L^*$  spatial domain in AACGM coordinates projected down onto the magnetic North Pole (x), as well as onto two popular magnetometer arrays: CARISMA (center) and International Monitor for Auroral Geomagnetic Effects (IMAGE, right). The associated geographic locations of the magnetic coordinates will vary with time. AACGM, Altitude-Adjusted Corrected Geomagnetic; CARISMA, Canadian Array for Realtime Investigations of Magnetic Activity.

The largest values of  $L^*$  exist in small bands close to the definition boundary. For  $m = 3$ , the largest values fall between  $10 < L^* < 11$ , from dusk to dawn. As  $m$  increases, the median value of  $L^*$  close to the  $L^*$  definition boundary reduces, largely because the location of the boundary is eroded to lower latitude. The spatial distribution of  $L^*$  on the dayside appears stable regardless of  $m$ , with  $L^*$  defined at all latitudes and very little reduction in IQR as  $m$  increases. Increasing  $m$  reduces the extent of the region of large IQR on the flanks and at midnight, but again this is largely because the  $L^*$  definition boundary is eroded to lower latitude. Across the nightside magnetosphere from dusk until dawn, the IQRs in the region of highest  $L^*$  values remain in the vicinity of 1, even with the model number threshold at its highest. It is interesting to note that the median  $L^*$  values observed at the highest latitude at noon are around  $2L^*$  smaller than those seen at the definition boundary at midnight, with similar variability. This suggests the ability to explore dynamics on the nightside over a considerably larger range of  $L^*$  than the dayside, but for ground stations only spanning mid-low latitudes.

Figure 7 shows probability density function (PDF) estimates for  $L^*$  at  $67.79^\circ$  ( $L_{\text{dip}} = 7$ ) as a function of  $m$  and MLT sector, notable as the typical latitude of the  $L^*$  definition boundary for the majority of magnetic field models on the nightside. Each PDF estimate was found using kernel density estimation (KDE) with a Gaussian kernel and Scott's rule (Scott, 1979) to determine the bandwidth (see Haiducek et al., 2020; Morley et al., 2018; Watt et al., 2019 for other examples of KDE usage in space physics). Similar figures containing all magnetic latitudes can be found in the Supporting Information.

The effects of increasing  $m$  shown in Figure 7 are representative of all latitudes above  $64.76^\circ$  ( $L_{\text{dip}} = 5.5$ ), with the exception of the midnight sector where distributions break down beyond  $67.79^\circ$  and should be used cautiously. At latitudes below this, the addition of further models appears to have minimal influence on the shape or variability of the resulting distributions, most likely due to the dominance of the internal IGRF field. Nevertheless, the noon sector appears resilient to increasing  $m$  even at higher latitudes, with only a slight decrease in variability at the inner edge of the distribution when we require an  $L^*$  output from all magnetic field models. Dawn and dusk exhibit multimodal distributions. Increasing  $m$  significantly reduces variability in the tail of the distribution (and slightly at the inner edge). Reductions in variability (about  $1L^*$  from the lowest to highest  $m$  value) make peaks in the heart of the distributions more prominent, although they are well defined by  $m = 3$ . The multimodal nature of the distributions are unsurprising when

**Table 1**  
*Magnetic Field Models Used for  $L^*$  Calculations*

Code	Citation	Quiet/storm	Model parameters
OPQUIET	Olson and Pfitzer (1974)	Quiet	Analytic
T89	Tsyganenko (1989)	Both	Kp
T96	Tsyganenko (1995, 1996)	Both	Pdyn <sup>a</sup> , Dst, $B_y$ -IMF, $B_z$ -IMF
OSTA	Ostapenko and Maltsev (1997)	Both	Pdyn, Dst, $B_z$ -IMF, Kp
T01QUIET	Tsyganenko (2002a, 2002b)	Quiet	Pdyn, Dst, $B_y$ -IMF, $B_z$ -IMF, G1 <sup>b</sup> , G2 <sup>b</sup>
T01STORM	Tsyganenko et al. (2003)	Storm	Pdyn, Dst, $B_y$ -IMF, $B_z$ -IMF, G2 <sup>b</sup> , G3 <sup>b</sup>
T05	Tsyganenko and Sitnov (2005)	Storm	Pdyn, Dst, $B_y$ -IMF, $B_z$ -IMF, W1-W6 <sup>c</sup>

<sup>a</sup>Pdyn—Solar wind dynamic pressure. <sup>b</sup>G#—Integrals of geoeffective interplanetary magnetic field (IMF)-related parameters over the preceding 1-h interval. <sup>c</sup>W#—G# plus further terms to include response and decay times exceeding 1-h.

we view the changes in dawn and dusk median  $L^*$  values at high latitudes in Figure 2, suggesting higher MLT resolution of  $L^*$  is required in these regions for more accurate modeling. In the midnight sector increasing  $m$  drastically reduces both variability and the distribution center. This is a direct result of model variability becoming more dominant over physical variability with increasing latitude, which does not seem to occur in other MLT sectors. In all MLT sectors, it is important to remember that a reduction in variability is not indicative of more accurate modeling. On the surface, requiring that more models return a  $L^*$  is likely to remove any real physical variability gained from the inclusion of current systems not shared between all models (although this is more complex due to the different ways in which magnetic field models are built—see Section 7). Choosing  $m$  is a trade-off between avoiding model bias and preserving the underlying physical variability of the system.

Creating the probabilistic models illustrated here was a simple attempt to reduce some of the uncertainty between magnetic field model configurations. We did not address any of the variability due to changing physical conditions, however, other than those physical processes which might be gained by the addition of particular current systems in more sophisticated magnetic field models. Most observed times are quiescent which dominate the  $L^*$  distributions, and results shown might not be indicative during times with enhanced activity. A natural next step would be to separate  $L^*$  distributions further, in the more simple case between quiet and storm phases, to investigate whether variability due to changing conditions is significant.

Since Pro- $L^*$  contains a wealth of calculated  $L^*$  values it is also a useful tool to look at individual test cases which might have unique or well-defined properties. In these scenarios we are able to compare performance of individual magnetic field models against probabilistic techniques, illuminating benefits that a probabilistic model can yield over an arbitrary choice of a singular magnetic field model.

### 5. Case Study: 2013 GEM Challenge Events

A great deal of magnetospheric research uses select ground instruments to track and measure physical quantities over continuous periods of time. These may provide insight into global responses to geomagnetic storms (e.g., Xu et al., 2017) and substorms (e.g., Forsyth et al., 2015; Orr et al., 2019), as well as supplying evidence of expected phenomena such as magnetic pulsations (e.g., C. P. Wang et al., 2018). It is therefore important to see how  $L^*$  varies with ground location over time, in addition to statistical MLT variation, to relate these ground observations to adiabatic locations in space for radiation belt studies. However, classical approaches require a decision for which magnetic field model to use, or an assumption for  $L^*$  must be made (ie. a dipole), which we have shown brings inherent uncertainty. Here, we demonstrate usage of Pro- $L^*$  as a probabilistic alternative to reduce model selection systematic biases, for four events in 2013 which comprise the radiation belt challenge set by the QARBM focus group within the GEM program (Tu et al., 2019). For each of the events we consider four grid locations in the vicinity of four popular ground magnetometer sta-

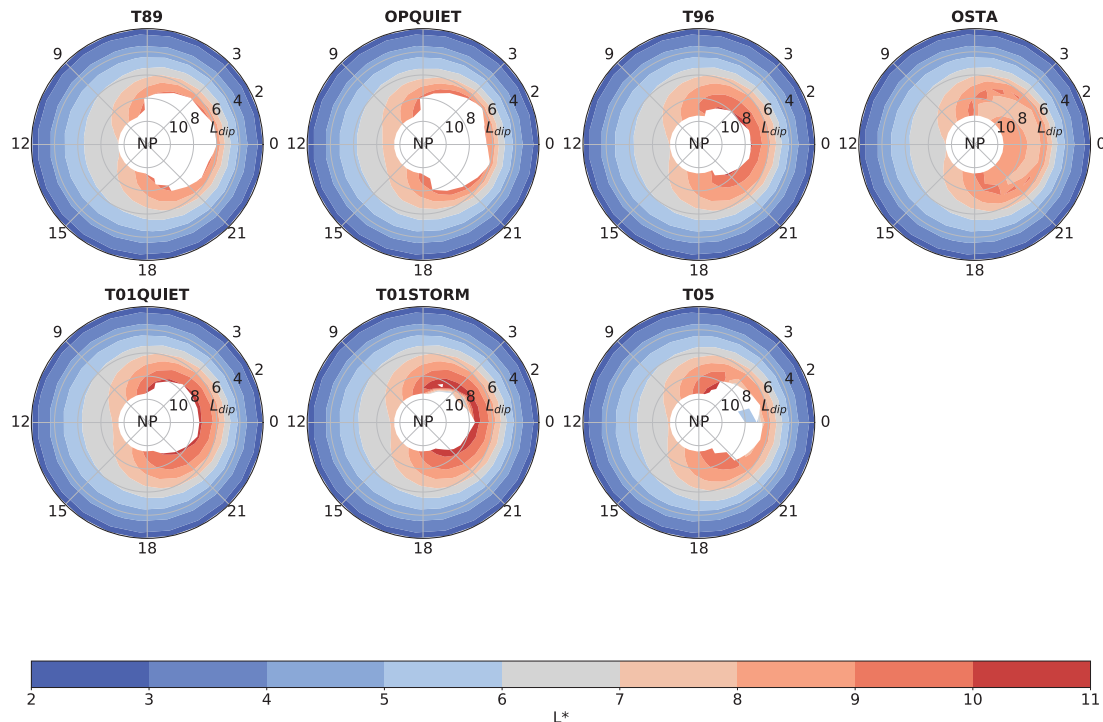
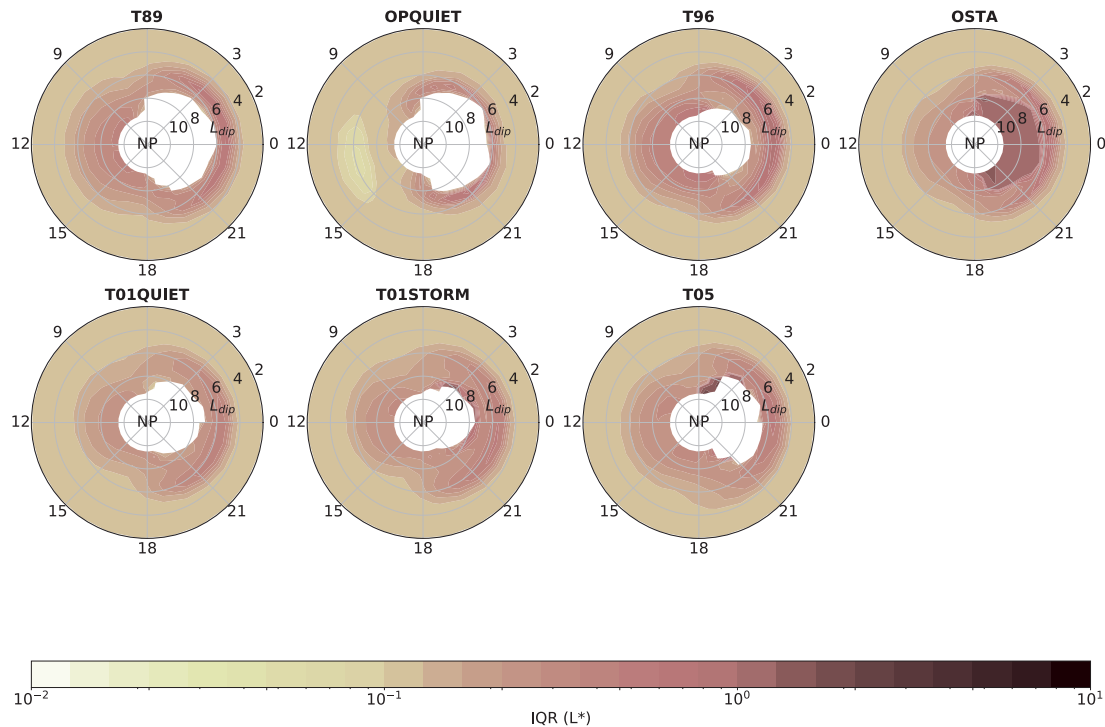


**Figure 2.** Global median  $L^*$  maps shown for each magnetic field model. The maps are displayed in MLT and dipole  $L$ , projected onto the magnetic North Pole with the Sun to the left. Magnetic latitudes have been converted to dipole  $L$  for display purposes. Codes for each model are as in Table 1. MLT, magnetic local time.

tions in the CARISMA array at around  $330^\circ$  magnetic longitude: Pinawa (PINA), Island Lake (ISLL), Gillam (GILL), and Fort Churchill (FCHU). A summary of the four events is as follows:

- **March 17, 2013 through March 19, 2013 Storm Enhancement:** A strong acceleration event on March 17 and 18 following a coronal mass ejection impact on March 17. Beginning around 8:00 UT on 17 March, there was a period of 18 h of continuous southward IMF  $B_z$ . During this time there was considerable substorm activity, indicated by the elevated Auroral Electrojet Index. This was a moderately strong storm with a minimum Dst index of 130 nT (e.g., Boyd et al., 2014; Hudson et al., 2015; Z. Li et al., 2015; W. Li et al., 2014; Ma et al., 2018; Olifer et al., 2018; Shprits et al., 2015; Ukhorskiy et al., 2015; C. Wang et al., 2017; Xiao et al., 2014).
- **May 31, 2013 through June 3, 2013 Storm Dropout:** Characterized by a minimum Dst of  $-119$  nT on June 1, 2013, strong MeV electrons before and after the storm were recorded with a clear, nonadiabatic main phase dropout (e.g., Clilverd et al., 2015; Kang et al., 2018).
- **September 19, 2013 through September 21, 2013 Nonstorm Enhancement:** Identified on September 19–20, 2013, with a minimum Dst of  $-19$  nT. No storm like profile, but some substorm activity (e.g., Ma et al., 2018; Pakhotin et al., 2014).
- **September 23, 2013 through September 26, 2013 Nonstorm Dropout:** Recorded on September 24, 2013 with a minimum Dst of  $-22$  nT. Yet, there was not a classic storm profile in Dst accompanying the rapid depletion in MeV electron responses (e.g., Capannolo et al., 2018; Pakhotin et al., 2014; Su et al., 2016).

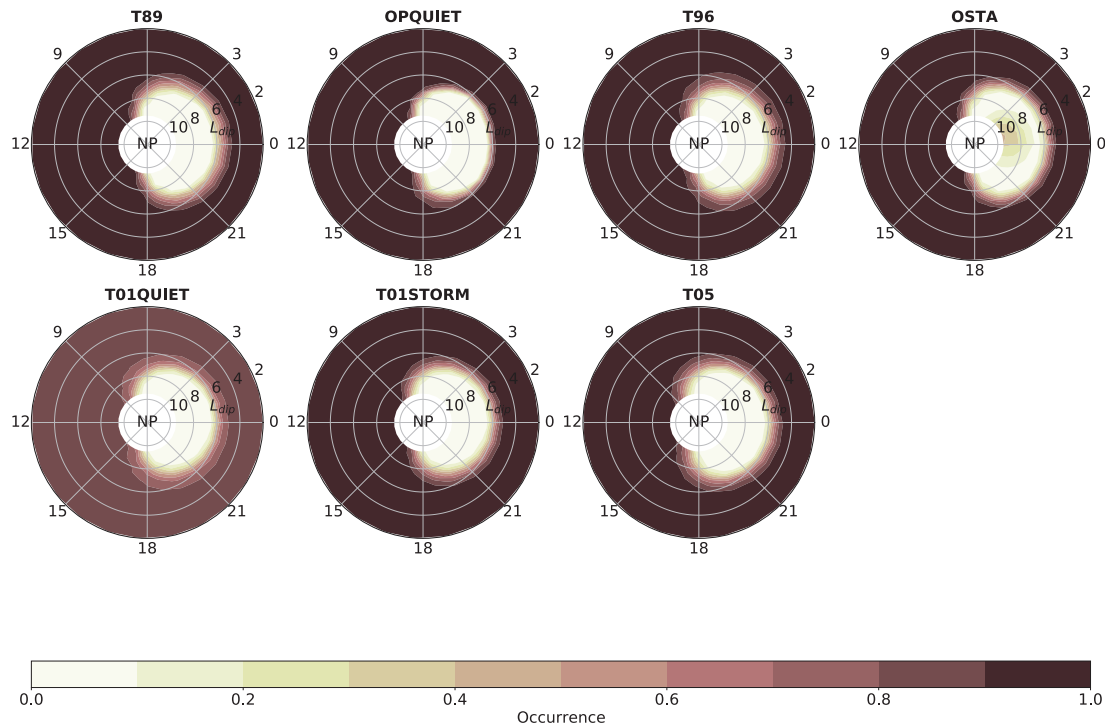
We present here the results for the storm time dropout and enhancement, respectively, in Figures 8 and 9, with the remaining two events provided in the Supporting Information. The results for the nonstorm events are similar to their storm counterparts, but of a smaller magnitude and with little variation at lower



**Figure 3.** Global  $L^*$  IQR maps shown for each magnetic field model. Each figure follows the same format at Figure 2. Codes for each model are as in Table 1. IQR, interquartile range.

latitudes. In the figures, the bottom four panels display  $L^*$  outputs for all magnetic field models at each considered latitude, increasing in latitude as we travel down the panels. Each  $L^*$  output is normalized by its respective constant dipole approximation at that particular magnetic latitude, so that variation at different latitudes can be considered on a similar scale. We have also included a median  $L^*$  subject to the requirement that at least three magnetic field models return an  $L^*$  value (a subset of values from our threshold = 3 probabilistic model). Each panel time series covers a period which spans the particular event plus/minus a day and a half. The Dst and Kp indices are also shown for the entire period in the top panel.

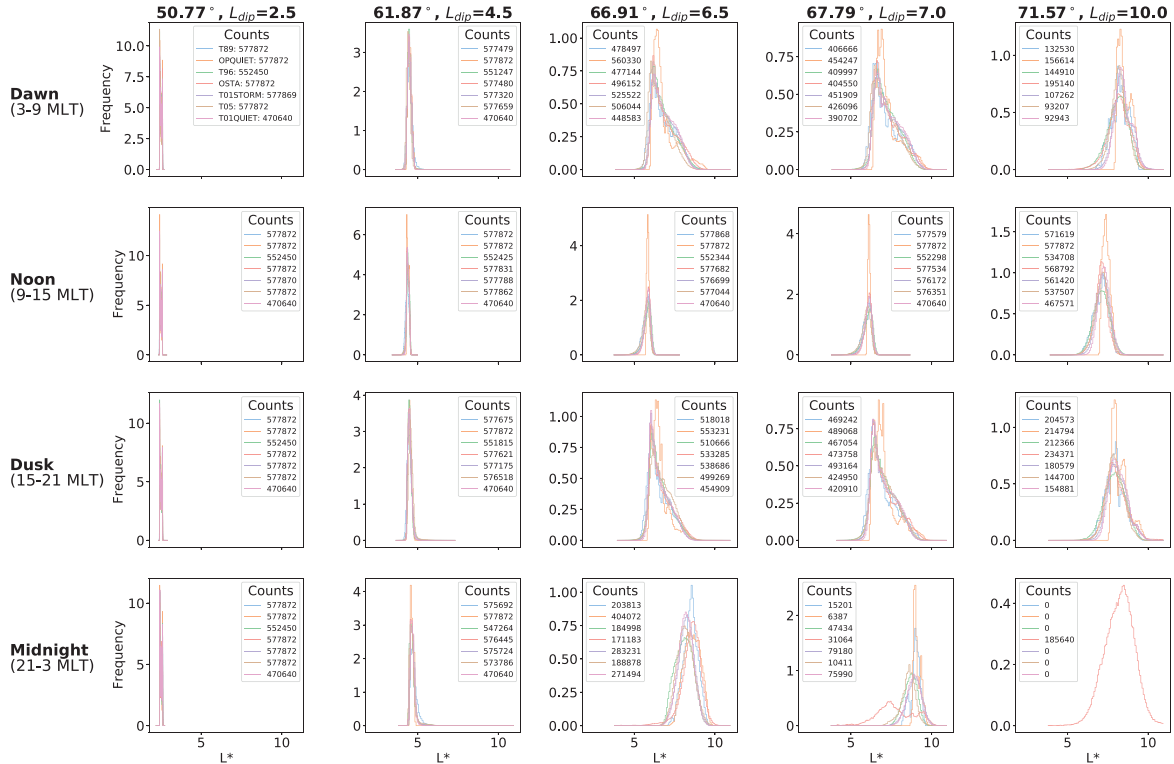
In Figure 8, we observe that there is an immediate response to the enhancement at all latitudes, characterized by a sharp drop in Dst and heightened Kp, for all magnetic field models. The event begins while our ground locations of interest are on the nightside, and most of the magnetic field models immediately appear to indicate open drift paths at much lower latitudes than expected at quiet times. While a significant proportion of models produce an  $L^*$  output at the lowest latitude, the variability between models is significant compared to the rest of the time series and persists throughout the main phase of the storm. During the enhancement, all empirical models predict an  $L^*$  which is significantly larger (where  $L^*$  is not undefined) than that given by a simple dipole approximation or the OPQUIET model on the nightside, and significantly less on the dayside. This clustering of the empirical models appears to be stronger on the dayside. Model variability extends throughout the recovery phase, still visibly apparent 1.5 days after event onset, with lower latitudes stabilizing faster. However, the absence of a storm does not guarantee a constant magnetospheric state, as there are diurnal variations between day and night. The empirical magnetic field models disagree on the nightside preceding enhancement, although this is definitely exacerbated during the storm commencement. This re-emphasises that a simple storm/quiet  $L^*$  probabilistic model may not be sufficient since variability can occur at all times, even in the absence of heightened geomagnetic activity.



**Figure 4.** Global occurrence maps for a defined  $L^*$  shown for each magnetic field model. Each figure follows the same format at Figure 2. The occurrence values were calculated as the ratio between the number of  $L^*$  values returned to the total number of observations ( $L^*$  defined and undefined) in each bin. Codes for each model are as in Table 1.

The behaviors of the magnetic field models preceding the storm, during enhancement onset, and extending into the recovery phase are generally the same as for the dropout event. However, the immediate default of magnetic field models to open-drift paths at dropout onset appears to penetrate deeper to lower latitudes, with most models defaulting at all latitudes except the lowest. By the recovery phase, the boundary for closed drift paths on the nightside has retreated slightly but still penetrates deep into the mid-latitudes. The only models with reasonable coverage at onset for all magnetic latitudes are the analytic OPQUIET quiet-time model, which is not valid for storms or the nightside, and the empirical OSTA model. Remarkably, the latter reverses the standard diurnal variation in  $L^*$  approximations at dropout onset, re-emphasizing that this model should be used with vigilance when it is the only empirical model returning an output. The pre-dropout variability is also different to the pre-enhancement variability on the nightside. Prior to the dropout, the empirical models post-T89 are well clustered, with nightside variability predominantly due to the analytic and aforementioned T89 models. Since these models are the eldest we anticipate they are likely to be most inaccurate. Therefore, the clustering of the other empirical models in the nightside suggests that the possibility of a more stable  $L^*$  structure in this region, spanning multiple latitudes, generally exists.

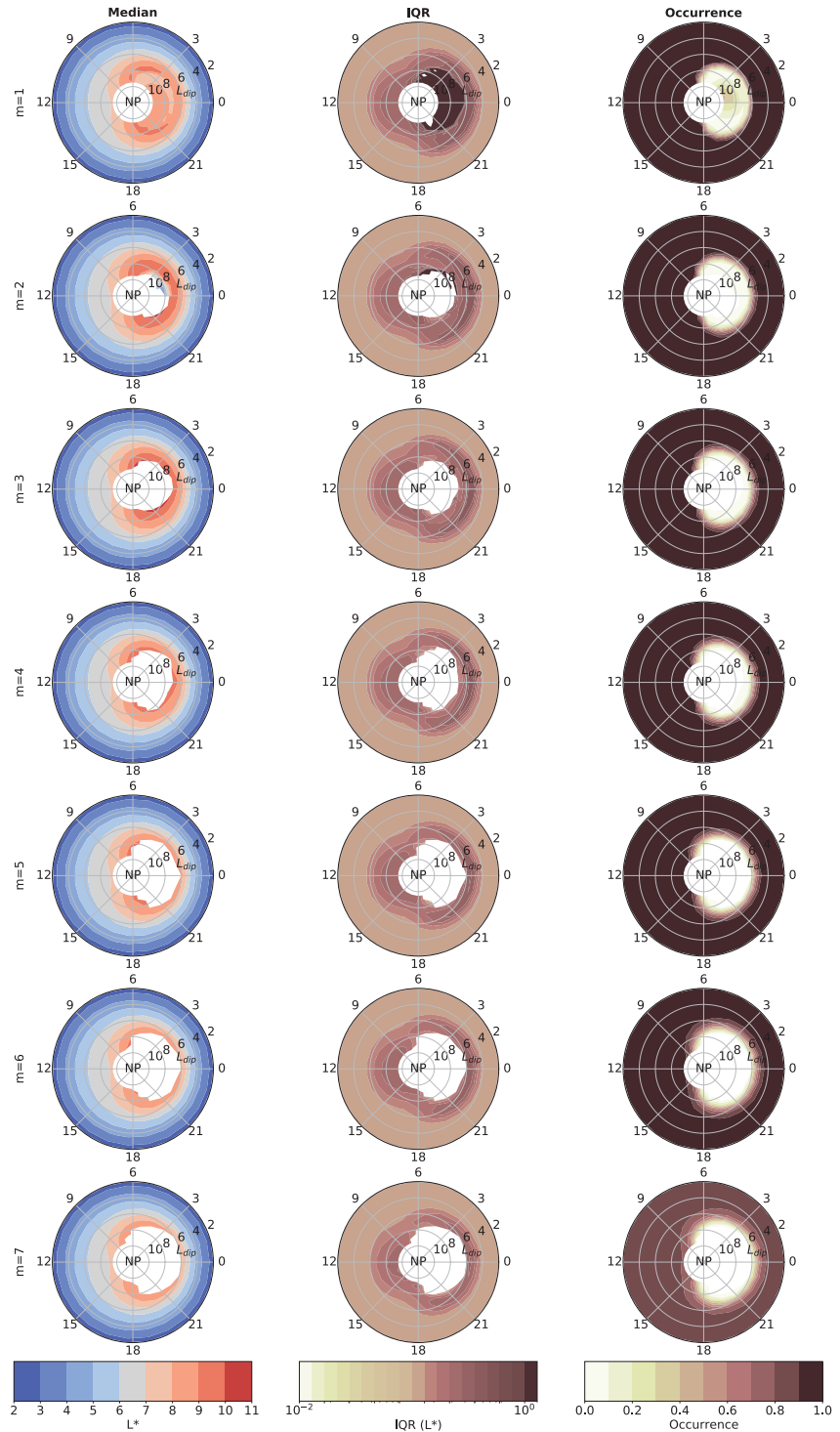
In both test cases the median  $L^*$  based on the model threshold follows the clustering of magnetic field models, and is therefore likely to be more representative of the *best estimate* of  $L^*$ . The model also defaults in regions where we would expect and highlights structure within the variable regions that can be easily compared to the quiescent diurnal variations. Model uncertainty during both storm and nonstorm events is profound, and decisions to simply use a singular magnetic field model can immediately introduce large uncertainty in the associated adiabatic location, which progresses through all remaining analysis (e.g., Loridan et al., 2019). Since a probabilistic model offsets some of the outlier model bias the benefits are immediate.



**Figure 5.** Step-histograms for each magnetic field model, shown for a selection of magnetic latitudes and separated into MLT sectors. The number of bins is 100 for all histograms, with bin locations identical over all MLT sectors for each magnetic latitude. Occurrences of defaulting  $L^*$  calculations are not taken into consideration. MLT, magnetic local time.

### 6. Grid Interpolation

The  $L^*$  time series produced from a probabilistic model are useful for researchers using magnetometers off-grid to Pro- $L^*$ . Our static geomagnetic grid used for Pro- $L^*$  was chosen to give uniform global coverage, focusing on areas in the Northern Hemisphere where ground instruments are generally located, but with not such a high resolution as to demand unfeasible computing costs. These choices mean that the gridpoints in Pro- $L^*$  will not line up exactly with the coordinates of several ground instruments. Making the best use of magnetic field measurement output combinations, we can formulate a realistic global  $L^*$  manifold on which interpolation between locations may be possible. In this case, calculating  $L^*$  for any ground magnetometer would be simple with quantified uncertainty (i.e., IQR) and avoids the computationally demanding process of calculating  $L^*$  directly. For successful usage of Pro- $L^*$  in real world applications, it is important to know when and how  $L^*$  values can be interpolated across gridpoints to ground instruments of interest. In Figures 10 and 11, we show the latitudinal and longitudinal changes in median  $L^*$  from the Pro- $L^*$  model across the four different events displayed in Section 5. These figures help to demonstrate visually when and where interpolation between gridpoints would be appropriate. There are two points to consider when making interpolations. First, the physical definition of  $L^*$  does not hold if it is not monotonically increasing with magnetic latitude. Second, there appears to be a diurnal variation through day and night, with pivots for increases and decreases in  $L^*$  occurring at midnight and midday, respectively. This can act as an indicator for reliable interpolation across magnetic longitude. During dropouts and enhancements the second criteria may break down, but this does not necessarily mean that interpolation should be avoided.



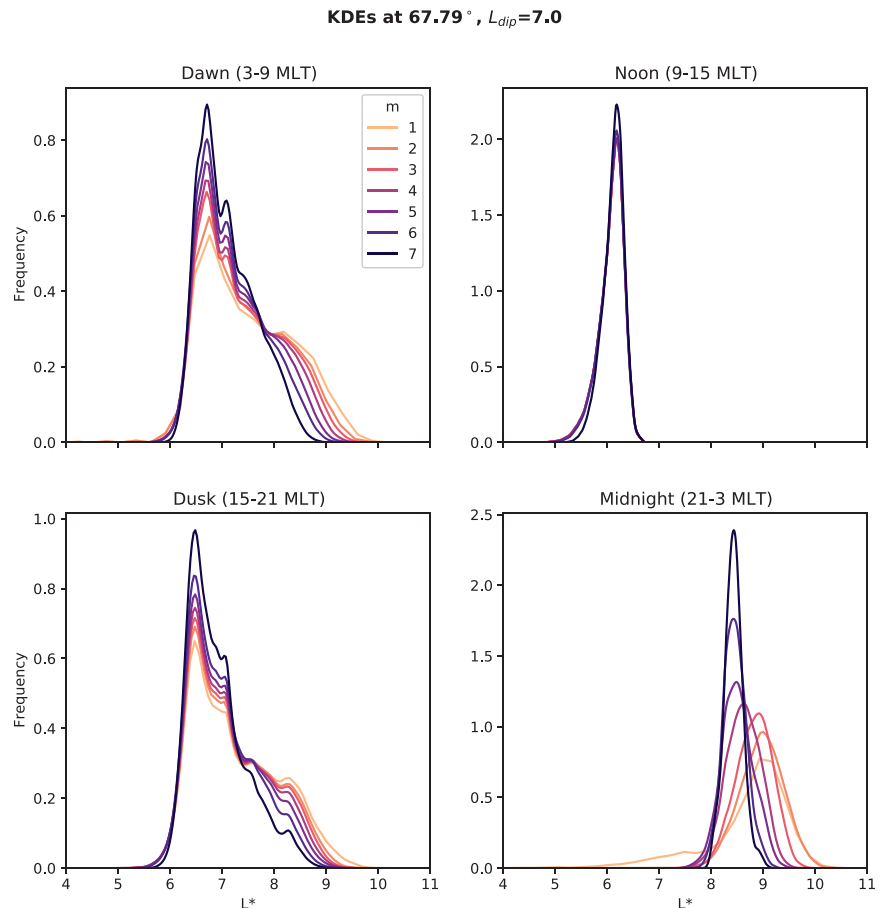


**Figure 7.** KDEs of global probabilistic  $L^*$  models at 67.79° magnetic latitude ( $L_{dip} = 7$ ) separated into MLT sector. The KDEs are shown as a function of the model threshold number  $m$ . MLT, magnetic local time; KDE, kernel density estimation.

Figure 10 shows the northward latitudinal changes in  $L^*$ , with respect to magnetic latitudes in the Pro- $L^*$  domain, for the four 2013 GEM challenge events at 330° magnetic longitude. Here,  $L^*$  is the median of all magnetic field outputs provided that at least three magnetic field models to provide an  $L^*$  output (else  $L^*$  is assumed to be undefined). For each event we have also shown the boundary for monotonic increases, indicating where  $L^*$  no longer has physical meaning. In quiescent times there is a clear boundary which follows a periodic diurnal variation with MLT. At midnight the boundary typically sits around 66.9° but is very sensitive to enhancements in geomagnetic activity which pushes the  $L^*$  definition boundary to lower latitudes. At noon we appear to always have full interpolation capability in quiescent times. During geomagnetically active events we see that this periodic structure immediately breaks down. Interpolation throughout dawn, noon, and dusk appears mostly resilient to event dynamics, except for the storm enhancement. At midnight we see an immediate response to the event onset with significant latitudinal decreases of the interpolation boundary, which is pushed lower for storm events than nonstorm. In fact, distortion of the boundary for nonstorm events is not too dramatic, and interpolation is possible with larger confidence.

**Figure 6.** Global  $L^*$  median (left) and IQR (center) maps as a function of  $m$  models determining the existence of  $L^*$  at any given time. Occurrence maps (right) for each value of  $m$  are also shown. Each figure follows the same format at Figure 2. IQR, interquartile range.

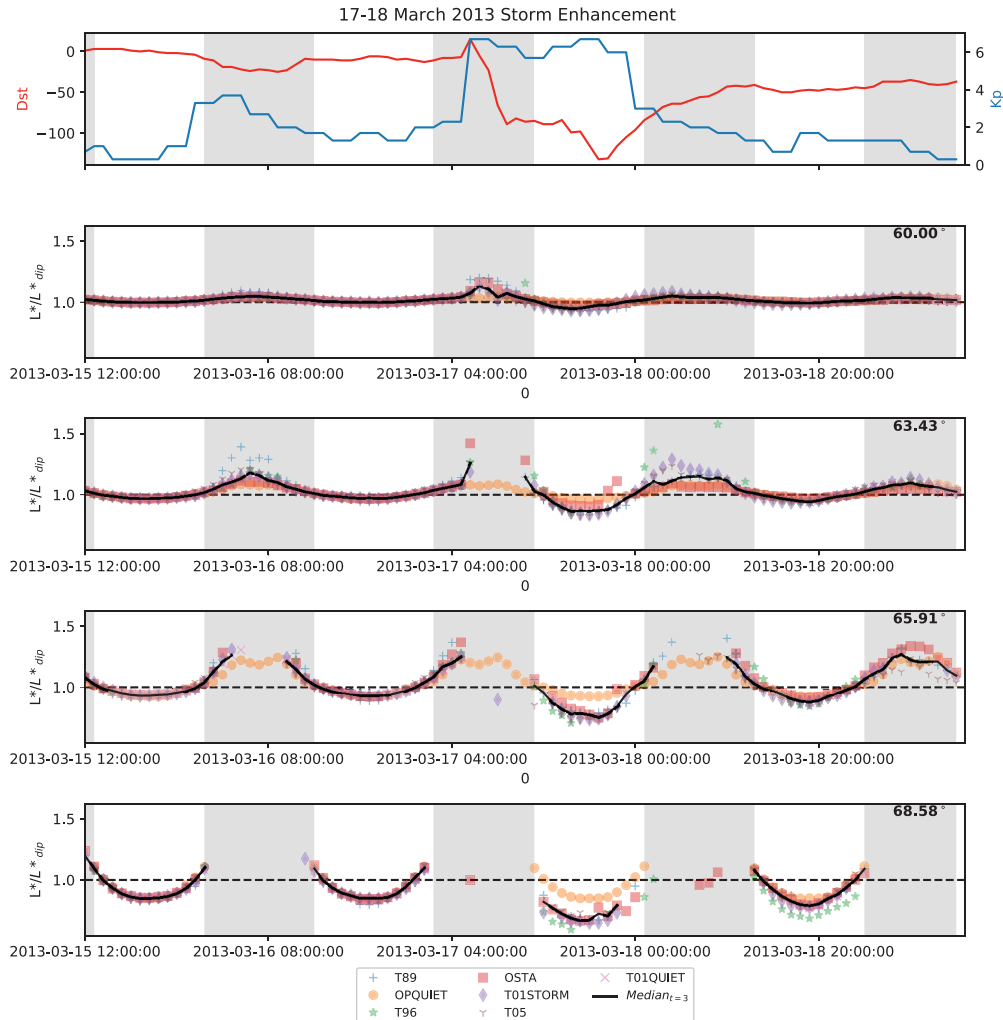


**Figure 8.** The response of  $L^*$  magnetic field models to the March 17–18, 2013 storm enhancement, for a selection of magnetic latitudes at  $330^\circ$  magnetic longitude, where ground observations are frequently of interest. The median  $L^*$  is also given provided that at least three magnetic field models return a  $L^*$  value. All returned  $L^*$  are normalized by their respective constant dipole approximation for comparison of latitudes on the same scale. The Dst and Kp indices are also provided over the given time period. Shaded bars indicate times where observed values are on the nightside.

Figure 11 shows the eastwards longitudinal change in  $L^*$ , for the four 2013 GEM challenge events at the magnetic latitudes used for the test cases in Section 5.  $L^*$  is again defined as in Figure 10 and approximate locations of midday and midnight have been indicated by black-dot and pink-dot markers, respectively. The expected diurnal variation can be seen both for individual longitudes as they progress through time as well as across longitudes in a single time instance. Surprisingly, this structure weakens with decreasing magnetic latitude, with longitudinal changes in  $L^*$  more oscillatory at the lowest latitude. However, the oscillating changes are small in magnitude. The smoothness in interpolation is highly sensitive to both enhanced geomagnetic activity and magnetic latitude, with disruptions seen clearly at relatively low latitudes in both storm and non-storm events. Shortly after event onset the general structure of diurnal variation is largely unaffected at the lowest latitude, yet disrupted at all other latitudes (excluding the nonstorm enhancement at  $63.43^\circ$ ) with either more intense changes in  $L^*$  between successive longitudes or  $L^*$  no longer being defined over varying regions across the nightside. During these instances, we should approach interpolation

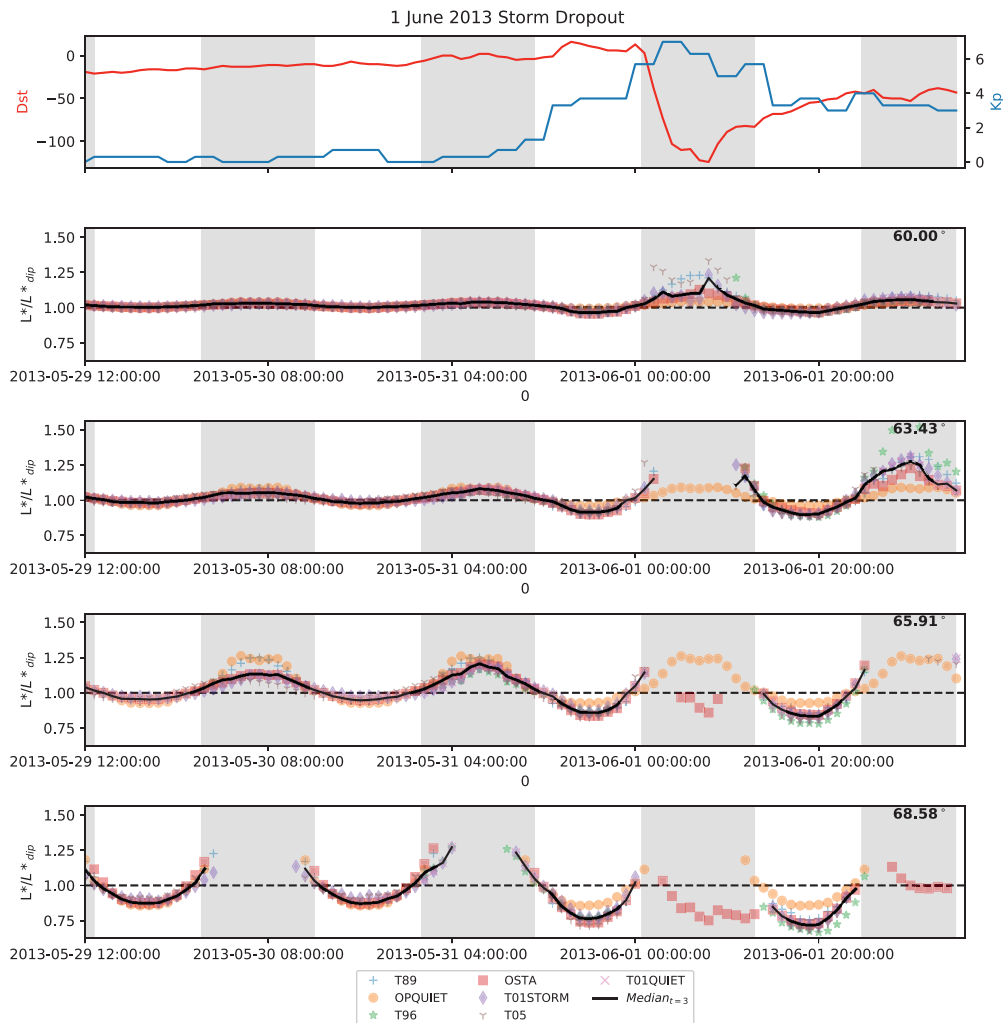


**Figure 9.** The response of  $L^*$  magnetic field models to the June 1, 2013 storm dropout, for the same magnetic latitudes as in Figure 8. This Figure follows the same format as Figure 8.

across these longitudes with caution. We note that for the highest latitude, however, caution should always be taken when making interpolations, and that problems are exacerbated during storm onset. Generally speaking, in any instance where the diurnal variation holds interpolation of  $L^*$  across magnetic longitudes should be acceptable.

### 7. Discussion

In order to use ground observations in radiation belt models, whether for operational applications or for research purposes, usually a single choice must be made of which magnetic field model to use to map the ground location to  $L^*$  in the magnetosphere. There are numerous magnetic field models in existence, ranging from analytic to empirical, which generally do not give identical results. Currently, studies make use of a single magnetic field model meaning that subsequent  $L^*$  values adhere to ingrained model biases. In operational space weather models of Earth’s radiation belts, the use of different magnetic field models

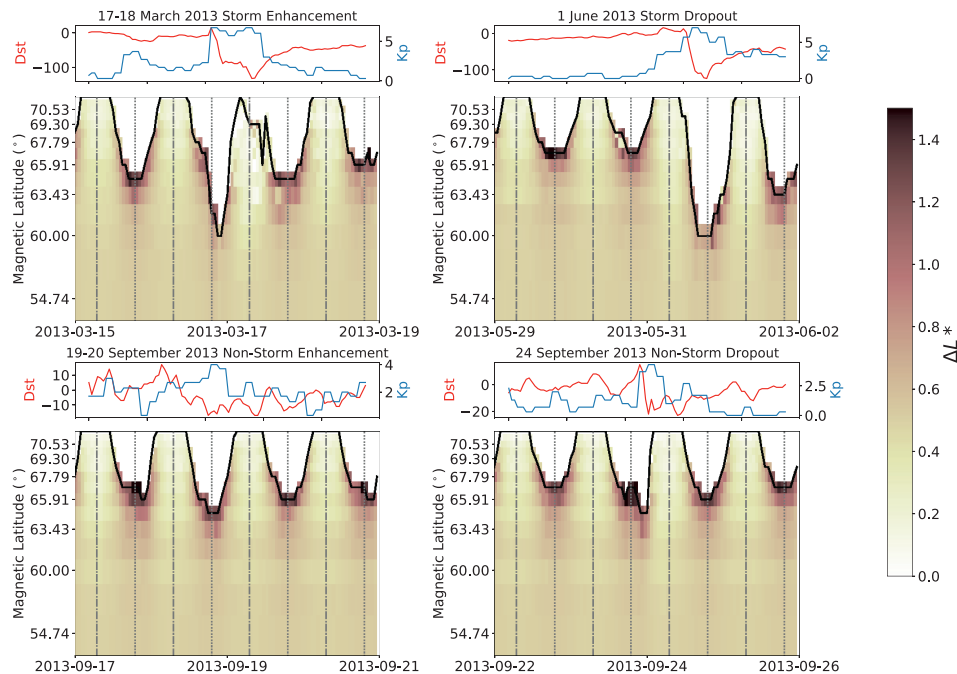


**Figure 10.** The latitudinal change in  $L^*$  (northwards), where  $L^*$  is the median of all magnetic field outputs provided that at least three magnetic field models to provide an  $L^*$  output (else  $L^*$  is assumed to be undefined), shown for the four 2013 GEM challenge events at  $330^\circ$  magnetic longitude. The color in each cell corresponds to the difference in  $L^*$  at the particular timestamp between the cell's respective magnetic latitude (y-axis) and the magnetic latitude immediately below in the Pro- $L^*$  domain. The boundary for monotonic increases is illustrated with a black line. Vertical lines for midday (dash-dot) and midnight (dotted) are also shown. The Dst and Kp indices are provided above each event.

for  $L^*$  is just one of many sources of uncertainty in the model. However, it is an important source of uncertainty, since  $L^*$  is used throughout the construction of radiation belt models, from the wave databases that provide diffusion (e.g., Horne et al., 2018) to the construction of spatial boundary conditions (e.g., Glauert et al., 2018), to the computations within the model itself (e.g., Loridan et al., 2019). Here, we have attempted to quantify the uncertainty, and demonstrate where there may be systematic bias between one magnetic field model and another. In results presented in this manuscript, we found that within regions where ground-to-space mapped  $L^*$  is defined for all magnetic field models, the global structure and values for “typical” (median) values were very similar. Notwithstanding any variability, decisions to use a singular model are therefore not too damaging provided modeling is of a climatological nature (modeling how average conditions change over longer time periods). Variability is also small enough (with an IQR ceiling of  $0.1 L^*$ ) for ground magnetometers below  $60^\circ$  ( $66^\circ$ ) on the nightside (dayside) that singular model use may still be warranted. However, while shapes of the  $L^*$  distributions for each magnetic field model share some similarities at a number of latitudes (see Figure 5), the variabilities in  $L^*$  are notable and arbitrary decisions to use a single model will introduce systematic biases which propagate through all further analysis. These biases are evident in Figures 8 and 9 (and Figures S4 and S5 in Supporting Information) with clear systematic differences in  $L^*$  between models in the quiet period prior to event onset, which are naturally amplified on the nightside.

We revisit the proposition by Roederer and Lejosne (2018) that  $L^*$  for equatorial pitch angles should be given as default in data packages and computed with a “reliable magnetic field model.” Based on the model uncertainty found in our results (an extension of the underlying physical variability in  $L^*$ ), determination of a reliable magnetic field model is not straightforward. Not only are they configured on a number of (not necessarily the same) complex interacting current systems and driving parameters, they are also approximations to the magnetic field geometry only with no way to benchmark against a true state. The distinction

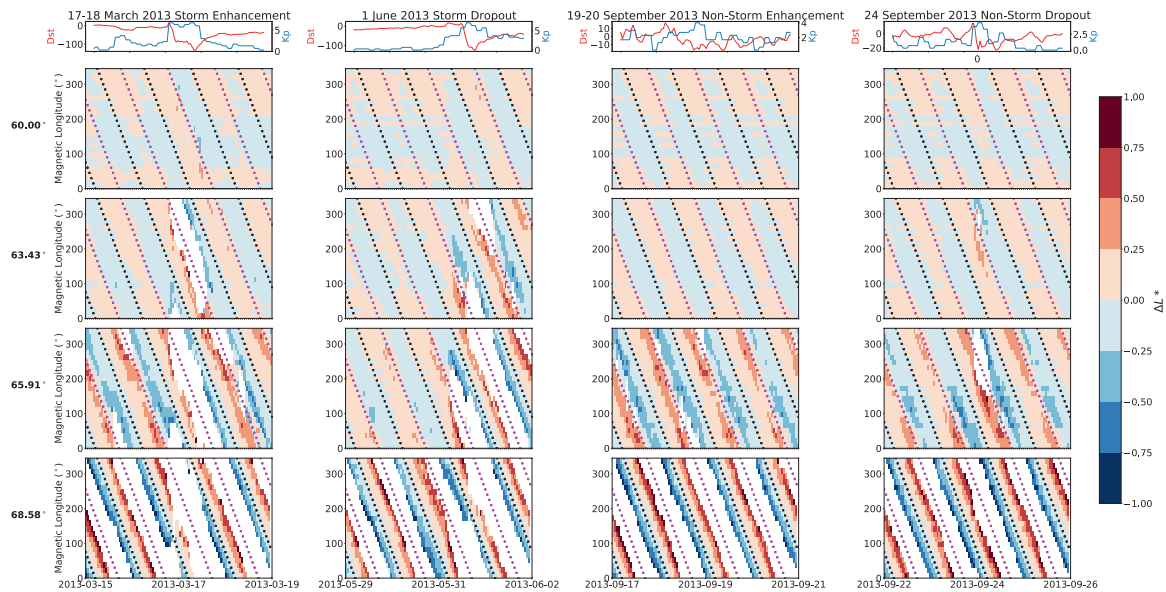


**Figure 11.** The longitudinal change in  $L^*$  (eastwards), where  $L^*$  is the median of all magnetic field outputs provided that at least three magnetic field models to provide an  $L^*$  output (else  $L^*$  is assumed to be undefined), shown for the four 2013 GEM challenge events (columns) and a selection of magnetic latitudes (rows). The color in each cell corresponds to the difference in  $L^*$  at the particular timestamp between the cell's respective magnetic longitude (y-axis) and the magnetic longitude immediately west in the Pro- $L^*$  domain. Markers for midday (black-dot) and midnight (pink-dot) are also shown. The Dst and Kp indices are provided over each event in the top row.

between reliability as accuracy instead of reliability as availability is also vital. Since  $L^*$  is a property of stably trapped particles and not a physical location, knowledge of its existence is as important as its estimated value. In numerical modeling of processes across a fixed mesh, time-varying latitudinal extents of  $L^*$  existence can prove problematic. This could be overcome by opting for the analytic OPQUIET model to reliably guarantee  $L^*$  values in the domain, but at the cost of some inaccuracies. Modeling should be informed by accurate  $L^*$  values, which should fail gracefully when unavailable, rather than reporting best guesses under all conditions which may result in poor approximations. Reliability of a magnetic field model should therefore accurately decide when  $L^*$  is unphysical and provide plausible values for when it is. Unfortunately, quantifying these criteria for comparison across individual magnetic field models is complex.

We have presented a possible solution to these complications in the form of Pro- $L^*$ , an extensive database of  $L^*$  approximations (and other magnetospheric parameters) made by several popular magnetic field models, covering a high-resolution domain. Pro- $L^*$  provides the potential to combine  $L^*$  values and distributions from magnetic field models probabilistically, reducing and quantifying the uncertainty associated with a single model choice. It also allows us to highlight when the description of  $L^*$  as a physical entity is not appropriate. As an illustration, we constructed simple probabilistic  $L^*$  models based solely on the number of magnetic field models providing an  $L^*$  output (Figures 6 and 7), a proxy for uncertainty in  $L^*$  existence. For accepted times of existence the median of returned  $L^*$  values is taken in an attempt to further remove model uncertainty. This approach highlighted significant risks when opting for particular magnetic field models, notably OSTA, which exhibited unphysical  $L^*$  distributions on the nightside. Physical distributions are observed once we require at least three magnetic field model outputs, with the increase of the model number threshold eroding the boundary of  $L^*$  existence to lower latitudes on the nightside. This calls attention to the simplicity of the probabilistic models. The existence of  $L^*$  is more advanced than the frequency of returned values. We have mentioned that magnetic field models are configured on a number of current systems with complex interactions, and there appears to be significant disagreements between models at higher latitudes on the nightside. However, the complexity of some models may yield physical results in these regions, and should not be discarded based on simultaneous model outputs alone. A simple median which applies equal

weighting to all magnetic field models is therefore unfeasible in some regions. Developing on the previous argument for  $L^*$  existence,  $L^*$  values for certain models in regions of high disagreement should be given more weight. We have also observed clustering of models during varying levels of geomagnetic activity (Figures 8 and 9) which can act as an indicator for the best estimate of  $L^*$ .

At this stage any choice of weighting is completely arbitrary. Our next step in the development of Pro- $L^*$  is to find a quantitative way to benchmark the considered magnetic field models to deduce effective model weight values and  $L^*$  existence, as a function of space and time (with potential separation into quiet and storm time models). One possibility to achieve this is to compare magnetic field model performance against a range of error metrics. This has already been done independently for some of the magnetic field models considered in this study (see Brito & Morley, 2017; Huang et al., 2008; McCollough et al., 2008), but has also been part of model configurations initially. For example, after its configuration Ostapenko and Maltsev (1997) compared their models performance against T89 by the residual sum of squares. To remove systematic model bias entirely we could also benchmark estimated parameters against colocated satellite measurements. Following successful benchmarking we can construct more sophisticated probabilistic models to reduce model uncertainty.

In its current form Pro- $L^*$  may be used directly for both deterministic and probabilistic modeling. For each individual magnetic field model included in Pro- $L^*$  we have tabulated global  $L^*$  statistics (in magnetic latitude and MLT) which can be rapidly imported and attached to ground observations for implementation in radiation belt studies. The statistics include both the arithmetic median and mean as averages, with value uncertainty quantified by the IQR and existence uncertainty quantified by normalized occurrence statistics (see Supporting Information). In addition to these, we have also tabulated the same statistics for the simple global probabilistic  $L^*$  models presented in Section 4.2. All data sets have been provided alongside this manuscript.

We have not investigated uncertainties which can be introduced into the calculation of  $L^*$  using other numerical tracing methods. Other methods exist, including LANLGeoMag (Henderson et al., 2018), AFRL-Shell (see Albert et al., 2018), and LANLstar (Yu et al. [2012], also within SpacePy [Morley et al., 2010]) which each have different benefits and problems. Some methods are better for drift orbit bifurcations, for example (see Albert et al. (2018), for a discussion). Our presentation of Pro- $L^*$  in this work demonstrates how further uncertainties, such as those resulting from different numerical methods, could be incorporated into the probabilistic model.

In its current incarnation, model uncertainties culminated over the 11-year period in Pro- $L^*$  are significant, with physical uncertainties contained within. It may be that parameterization of Pro- $L^*$  probabilistic models could further reduce these uncertainties and produce better utility of the models. However, the choice of parameters to use requires thought, given the different inputs required for different magnetic field models and the fact that not all magnetic field models are independent.

For the ground-based Pro- $L^*$ , it may be important to determine sources of uncertainty in mapping the ground-location to the magnetic field minimum, and sources of uncertainty in tracing out the field globally in order to estimate  $L^*$ . Future improvements to Pro- $L^*$  will involve finding the sources of uncertainty. Assessing ionospheric-magnetospheric mapping is complex, however, as there is no conventional method for model validation. Attempts have been made to deduce mapping accuracy from the angular error in the direction of the magnetic field vector relative to magnetic field observations (Brilo & Morley, 2017; Pulkkinen & Tsyganenko, 1996), but this does not guarantee the accurate location of the ionospheric footprint. More complex approaches compare magnetically conjugate phenomena at the ionosphere and along the field line in the magnetosphere. For example, Weiss et al. (1997) compared electron spectra measurements between Defense Meteorological Satellite Program at low altitudes with geosynchronous Los Alamos National Laboratory (LANL) spacecraft, while Shevchenko et al. (2010) explored the isotropy boundary of precipitation of energetic particles deduced by low-altitude spacecraft, wherein particles are observed at ionospheric latitudes but their precipitation is governed by the magnetic field near the equator.

Pro- $L^*$  is freely available in its current incarnation both as a data set (available at <http://dx.doi.org/10.17864/1947.222>) where we supply  $L^*$  values (and related variables) calculated using the seven outlined magnetic field models over our specified high resolution spatial grid throughout 2006–2016, and a

freely available Python package (available at <https://github.com/Rhyst223/pro-lstar.git>). In the initial Python package release, users are able to quickly generate data for specific dates and ground locations relative to the Pro- $L^*$  data set (with built-in interpolation for off-grid locations), and automatically generate plots similar to the ones shown in this manuscript for the 2013 GEM challenge events. Global  $L^*$  statistics (mean, median, IQR, and occurrence rate) for all gridpoints in the Pro- $L^*$  (decomposed into magnetic latitude  $\times$  MLT) are also provided in the Supporting Information as readable data sets, including statistics for each individual external magnetic field model and the simple probabilistic models in Section 4.2. Statistics for the former are also given as tables in the Supporting Information. All subsequent improvements will be incorporated into the Python package and some the future planned developments are as follows:

- Statistical quantities for both user specified and predefined model weightings.
- Generation of user-specified latitude and MLT based probabilistic  $L^*$  distributions, parameterized by appropriate physical quantities or tuned to predetermined model accuracies, with interpolation managed under the hood when the specified location does not fall precisely on our grid in Figure 1.
- $L^*$  forecasting capabilities.

## 8. Conclusion

In this paper, we have presented for the first time a probabilistic aid for mapping ground observations to  $L^*$ , Pro- $L^*$ , which combines results from several magnetic field models in an extensive data set. Pro- $L^*$  covers a high resolution grid of ground locations in magnetic latitude, longitude, and MLT in the Northern Hemisphere, where the majority of ground instruments are located. Although the climatological structure of  $L^*$  is consistent between most magnetic field models, significant  $L^*$  variability exists across large regions of magnetic latitude and MLT on typical timescales of interest due to both systematic model biases and physical variability from magnetospheric processes. We have illustrated approaches to determine  $L^*$  probabilistically which removes some of the observed systematic biases, and also quantified this uncertainty. These illustrations were considered both in a distribution sense and real-life test cases. The possibility of  $L^*$  interpolation across gridpoints in probabilistic models was explored, and criteria for successful interpolation determined. The extension of Pro- $L^*$  from its current form as a data set into a fully functional Python package has been outlined, with the initial release locatable at <https://github.com/Rhyst223/pro-lstar.git>. The full Pro- $L^*$  data set is available at <http://dx.doi.org/10.17864/1947.222>.

### Acknowledgments

RLT is supported by the Engineering and Physical Sciences Research Council (EPSRC) (Grant no. EP/L016613/1). Contributions to this work by SKM were performed under the auspices of the U.S. Department of Energy and were supported by the U.S. Department of Energy Laboratory Directed Research and Development program award 20190262ER. This research used resources provided by the Los Alamos National Laboratory Institutional Computing Program, which is supported by the U.S. Department of Energy National Nuclear Security Administration under Contract No. 89233218CNA000001. This research has been approved for unlimited release and has been assigned the number LA-UR-20-25,802. CEJW is supported by Natural Environment Research Council (NERC) (Grant no. NE/P017274/1) and Science and Technology Facilities Council (STFC) (Grant no. ST/R000921/1). SNB is supported by Science and Technology Facilities Council (STFC) (Grant no. ST/R000921/1). PDW is supported by the Royal Society (Grant no. UF130571).

### Data Availability Statement

Pro- $L^*$  data set is freely available at <http://dx.doi.org/10.17864/1947.222>. The most up-to-date release of the Pro- $L^*$  Python package is available at <https://github.com/Rhyst223/pro-lstar.git>. Information on the GEM challenge events is available at <http://bit.ly/28UnLpw>.

### References

- Albert, J. M., Selesnick, R. S., Morley, S. K., Henderson, M. G., & Kellerman, A. C. (2018). Calculation of last closed drift shells for the 2013 GEM radiation belt challenge events. *Journal of Geophysical Research: Space Physics*, 123(11), 9597–9611. <https://doi.org/10.1029/2018JA025991>
- Angelopoulos, V. (2008). The THEMIS mission. *Space Science Reviews*, 141(1–4), 5–34. <https://doi.org/10.1007/s11214-008-9336-1>
- Boscher, B. S. O. T. P. (2013). *The International Radiation Belt Environment Modeling (IRBEM) library*. Retrieved from <https://sourceforge.net/projects/irbem/>
- Boyd, A. J., Spence, H. E., Claudepierre, S. G., Fennell, J. F., Blake, J. B., Baker, D. N., et al. (2014). Quantifying the radiation belt seed population in the 17 March 2013 electron acceleration event. *Geophysical Research Letters*, 41(7), 2275–2281. <https://doi.org/10.1002/2014GL059626>
- Brito, T. V., & Morley, S. K. (2017). Improving empirical magnetic field models by fitting to in situ data using an optimized parameter approach. *Space Weather*, 15(12), 1628–1648. <https://doi.org/10.1002/2017SW001702>
- Burrell, A. G., Halford, A., Klenzing, J., Stoneback, R. A., Morley, S. K., Annex, A. M., et al. (2018). Snakes on a spaceship—An overview of Python in heliophysics. *Journal of Geophysical Research: Space Physics*, 123(12), 10384–10402. <https://doi.org/10.1029/2018JA025877>
- Capannolo, L., Li, W., Ma, Q., Zhang, X., Redmon, R. J., Rodriguez, J. V., et al. (2018). Understanding the driver of energetic electron precipitation using coordinated multisatellite measurements. *Geophysical Research Letters*, 45(14), 6755–6765. <https://doi.org/10.1029/2018GL078604>
- Carter, J. A., Milan, S. E., Coxon, J. C., Walach, M., & Anderson, B. J. (2016). Average field-aligned current configuration parameterized by solar wind conditions. *Journal of Geophysical Research: Space Physics*, 121(2), 1294–1307. <https://doi.org/10.1002/2015JA021567>

- Cliiverd, M. A., Duthie, R., Hardman, R., Hendry, A. T., Rodger, C. J., Raita, T., et al. (2015). Electron precipitation from EMIC waves: A case study from 31 May 2013. *Journal of Geophysical Research: Space Physics*, *120*(5), 3618–3631. <https://doi.org/10.1002/2015JA021090>
- Fairfield, D. H., & Mead, G. D. (1975). Magnetospheric mapping with a quantitative geomagnetic field model. *Journal of Geophysical Research*, *80*(4), 535–542. <https://doi.org/10.1029/JA080i004p00535>
- Fairfield, D. H., Tsyganenko, N. A., Usmanov, A. V., & Malkov, M. V. (1994). A large magnetosphere magnetic field database. *Journal of Geophysical Research*, *99*(A6), 11319. <https://doi.org/10.1029/94JA00255>
- Fei, Y., Chan, A. A., Elkington, S. R., & Wiltberger, M. J. (2006). Radial diffusion and MHD particle simulations of relativistic electron transport by ULF waves in the September 1998 storm. *Journal of Geophysical Research: Space Physics*, *111*(A12). <https://doi.org/10.1029/2005JA011211>
- Finlay, C. C., Maus, S., Beggan, C. D., Bondar, T. N., Chambodut, A., Chernova, T. A., et al. (2010). International Geomagnetic Reference Field: The eleventh generation. *Geophysical Journal International*, *183*(3), 1216–1230. <https://doi.org/10.1111/j.1365-246X.2010.04804.x>
- Forsyth, C., Rae, I. J., Coxon, J. C., Freeman, M. P., Jackman, C. M., Gjerloev, J., & Fazakerley, A. N. (2015). A new technique for determining Substorm Onsets and Phases from Indices of the Electrojet (SOPHIE). *Journal of Geophysical Research: Space Physics*, *120*(12), 592–610. <https://doi.org/10.1002/2015JA021343>
- Ganushkina, N. Y., Liemohn, M. W., Kubyshkina, M. V., Ilie, R., & Singer, H. J. (2010). Distortions of the magnetic field by storm-time current systems in Earth's magnetosphere. *Annales Geophysicae*, *28*(1), 123–140. <https://doi.org/10.5194/angeo-28-123-2010>
- Glauert, S. A., Horne, R. B., & Meredith, N. P. (2018). A 30-year simulation of the outer electron radiation belt. *Space Weather*, *16*(10), 1498–1522. <https://doi.org/10.1029/2018SW001981>
- Haiducek, J. D., Welling, D. T., Morley, S. K., Ganushkina, N. Y., & Chu, X. (2020). Using multiple signatures to improve accuracy of substorm identification. *Journal of Geophysical Research: Space Physics*, *125*(4). <https://doi.org/10.1029/2019JA027559>
- Henderson, M., Morley, S., Niehof, J., & Larsen, B. (2018). *drsteve/LANLGeoMag: v1.5.16*. Retrieved from <https://zenodo.org/record/1195041#.XTiCoJNKgWo>; <https://doi.org/10.5281/ZENODO.1195041>
- Horne, R. B., Phillips, M. W., Glauert, S. A., Meredith, N. P., Hands, A. D. P., Ryden, K. A., & Li, W. (2018). Realistic worst case for a severe space weather event driven by a fast solar wind stream. *Space Weather*, *16*(9), 1202–1215. <https://doi.org/10.1029/2018SW001948>
- Huang, C.-L. L., Spence, H. E., Singer, H. J., Tsyganenko, N. A., Huang, C.-L., Spence, H. E., et al. (2008). A quantitative assessment of empirical magnetic field models at geosynchronous orbit during magnetic storms Recommended Citation A quantitative assessment of empirical magnetic field models at geosynchronous orbit during magnetic storms. *Journal of Geophysical Research*, *113*, 4208. <https://doi.org/10.1029/2007JA012623>
- Hudson, M. K., Paral, J., Kress, B. T., Wiltberger, M., Baker, D. N., Foster, J. C., et al. (2015). Modeling CME-shock-driven storms in 2012–2013: MHD test particle simulations. *Journal of Geophysical Research: Space Physics*, *120*(2), 1168–1181. <https://doi.org/10.1002/2014JA020833>
- Kang, S.-B., Fok, M.-C., Komar, C., Gloer, A., Li, W., & Buzulukova, N. (2018, 2). An energetic electron flux dropout due to magnetopause shadowing on 1 June 2013. *Journal of Geophysical Research: Space Physics*, *123*(2), 1178–1190. <https://doi.org/10.1002/2017JA024879>
- Kubyshkina, M., Sergeev, V., Tsyganenko, N., Angelopoulos, V., Runov, A., Donovan, E., et al. (2011). Time-dependent magnetospheric configuration and breakup mapping during a substorm. *Journal of Geophysical Research: Space Physics*, *116*, A00127. <https://doi.org/10.1029/2010JA015882>
- Li, Z., Hudson, M., Kress, B., & Paral, J. (2015). Three-dimensional test particle simulation of the 17–18 March 2013 CME shock-driven storm. *Geophysical Research Letters*, *42*(14), 5679–5685. <https://doi.org/10.1002/2015GL064627>
- Li, W., Thorne, R. M., Ma, Q., Ni, B., Bortnik, J., Baker, D. N., et al. (2014). Radiation belt electron acceleration by chorus waves during the 17 March 2013 storm. *Journal of Geophysical Research: Space Physics*, *119*(6), 4681–4693. <https://doi.org/10.1002/2014JA019945>
- Loridan, V., Ripoll, J., Tu, W., & Scott Cunningham, G. (2019). On the use of different magnetic field models for simulating the dynamics of the outer radiation belt electrons during the October 1990 storm. *Journal of Geophysical Research: Space Physics*, *124*(8), 6453–6486. <https://doi.org/10.1029/2018JA026392>
- Ma, Q., Li, W., Bortnik, J., Thorne, R. M., Chu, X., Ozeke, L. G., et al. (2018). Quantitative evaluation of radial diffusion and local acceleration processes during GEM challenge events. *Journal of Geophysical Research: Space Physics*, *123*(3), 1938–1952. <https://doi.org/10.1002/2017JA025114>
- Mann, I. R., Milling, D. K., Rae, I. J., Ozeke, L. G., Kale, A., Kale, Z. C., et al. (2008). The upgraded CARISMA magnetometer array in the THEMIS era. *Space Science Reviews*, *141*(1–4), 413–451. <https://doi.org/10.1007/s11214-008-9457-6>
- McCollough, J. P., Gannon, J. L., Baker, D. N., & Gehmeyr, M. (2008). A statistical comparison of commonly used external magnetic field models. *Space Weather*, *6*, S10001. <https://doi.org/10.1029/2008SW000391>
- McIlwain, C. E. (1961). Coordinates for mapping the distribution of magnetically trapped particles. *Journal of Geophysical Research*, *66*(11), 3681–3691. <https://doi.org/10.1029/JZ066i011p03681>
- Morley, S. K., Welling, D. T., Koller, J., Larsen, B. A., Henderson, M. G., & Niehof, J. (2010). *SpacePy-A Python-based Library of Tools for the Space Sciences (Tech. Rep.)*. Retrieved from <http://spacepy.lanl.gov>
- Morley, S. K., Welling, D. T., & Woodroffe, J. R. (2018). Perturbed input ensemble modeling with the space weather modeling framework. *Space Weather*, *16*(9), 1330–1347. <https://doi.org/10.1029/2018SW002000>
- Olifer, L., Mann, I. R., Morley, S. K., Ozeke, L. G., & Choi, D. (2018). On the role of last closed drift shell dynamics in driving fast losses and Van Allen radiation belt extinction. *Journal of Geophysical Research: Space Physics*, *123*(5), 3692–3703. <https://doi.org/10.1029/2018JA025190>
- Olson, W. P., & Pfizter, K. A. (1974). A quantitative model of the magnetospheric magnetic field. *Journal of Geophysical Research*, *79*(25), 3739–3748. <https://doi.org/10.1029/JA079i025p03739>
- Orr, L., Chapman, S. C., & Gjerloev, J. W. (2019). Directed network of substorms using SuperMAG ground-based magnetometer data. *Geophysical Research Letters*, *46*(12), 6268–6278. <https://doi.org/10.1029/2019GL082824>
- Ostapenko, A. A., & Maltsev, Y. P. (1997). Relation of the magnetic field in the magnetosphere to the geomagnetic and solar wind activity. *Journal of Geophysical Research: Space Physics*, *102*(A8), 17467–17473. <https://doi.org/10.1029/97JA00937>
- Ozeke, L. G., Mann, I. R., Murphy, K. R., Jonathan Rae, I., & Milling, D. K. (2014). Analytic expressions for ULF wave radiation belt radial diffusion coefficients. *Journal of Geophysical Research: Space Physics*, *119*(3), 1587–1605. <https://doi.org/10.1002/2013JA019204>
- Ozeke, L. G., Mann, I. R., Murphy, K. R., Rae, I. J., Milling, D. K., Elkington, S. R., et al. (2012). ULF wave derived radiation belt radial diffusion coefficients. *Journal of Geophysical Research*, *117*(A4). <https://doi.org/10.1029/2011JA017463>
- Pakhotin, I. P., Drozdov, A. Y., Shprits, Y. Y., Boynton, R. J., Subbotin, D. A., & Balikhin, M. A. (2014). Simulation of high-energy radiation belt electron fluxes using NARMAX-VERB coupled codes. *Journal of Geophysical Research: Space Physics*, *119*(10), 8073–8086. <https://doi.org/10.1002/2014JA020238>

- Pulkkinen, T. I., & Tsyganenko, N. A. (1996). Testing the accuracy of magnetospheric model field line mapping. *Journal of Geophysical Research: Space Physics*, 101(A12), 27431–27442. <https://doi.org/10.1029/96ja02489>
- Qin, Z., Denton, R. E., Tsyganenko, N. A., & Wolf, S. (2007). Solar wind parameters for magnetospheric magnetic field modeling. *Space Weather*, 5(11), S11003. <https://doi.org/10.1029/2006SW000296>
- Roederer, J. G. (1970). *Dynamics of geomagnetically trapped radiation*. Berlin: Springer-Verlag.
- Roederer, J. G., & Lejosne, S. (2018). Coordinates for representing radiation belt particle flux. *Journal of Geophysical Research: Space Physics*, 123(2), 1381–1387. <https://doi.org/10.1002/2017JA025053>
- Roederer, J. G., & Zhang, H. (2014). *Dynamics of magnetically trapped particles* (Vol. 403). Berlin, Heidelberg: Springer Berlin Heidelberg. <https://doi.org/10.1007/978-3-642-41530-2>
- Scott, D. W. (1979). On optimal and data-based histograms. *Biometrika*, 66(3), 605–610. Retrieved from <https://academic.oup.com/biomet/article-abstract/66/3/605/232642>
- Shevchenko, I. G., Sergeev, V., Kubysheva, M., Angelopoulos, V., Glassmeier, K. H., & Singer, H. J. (2010). Estimation of magnetosphere-ionosphere mapping accuracy using isotropy boundary and THEMIS observations. *Journal of Geophysical Research: Space Physics*, 115, A11206. <https://doi.org/10.1029/2010JA015354>
- Shprits, Y. Y., Kellerman, A. C., Drozdov, A. Y., Spence, H. E., Reeves, G. D., & Baker, D. N. (2015). Combined convective and diffusive simulations: VERB-4D comparison with 17 March 2013 Van Allen probes observations. *Geophysical Research Letters*, 42(22), 9600–9608. <https://doi.org/10.1002/2015GL065230>
- Sibeck, D. G., & Angelopoulos, V. (2008). THEMIS science objectives and mission phases. *Space Science Reviews*, 141(1–4), 35–59. <https://doi.org/10.1007/s11214-008-9393-5>
- Su, Z., Gao, Z., Zhu, H., Li, W., Zheng, H., Wang, Y., et al. (2016). Nonstorm time dropout of radiation belt electron fluxes on 24 September 2013. *Journal of Geophysical Research: Space Physics*, 121(7), 6400–6416. <https://doi.org/10.1002/2016JA022546>
- Thébault, E., Finlay, C. C., Beggan, C. D., Alken, P., Aubert, J., Barrois, O., et al. (2015). International Geomagnetic Reference Field: The 12th generation. *Earth, Planets and Space*, 67(1), 79. <https://doi.org/10.1186/s40623-015-0228-9>
- Tsyganenko, N. A. (1989). A magnetospheric magnetic field model with a warped tail current sheet. *Planetary and Space Science*, 37(1), 5–20. [https://doi.org/10.1016/0032-0633\(89\)90066-4](https://doi.org/10.1016/0032-0633(89)90066-4)
- Tsyganenko, N. A. (1995). Modeling the Earth's magnetospheric magnetic field confined within a realistic magnetopause. *Journal of Geophysical Research*, 100(A4), 5599. <https://doi.org/10.1029/94JA03193>
- Tsyganenko, N. A. (1996). Effects of the solar wind conditions on the global magnetospheric configuration as deduced from data-based field models. Retrieved from <https://ntrs.nasa.gov/search.jsp?R=19970016534>
- Tsyganenko, N. A. (2002a). A model of the near magnetosphere with a dawn-dusk asymmetry 1. Mathematical structure. *Journal of Geophysical Research*, 107(A8), 12–21. <https://doi.org/10.1029/2001JA000219>
- Tsyganenko, N. A. (2002b). A model of the near magnetosphere with a dawn-dusk asymmetry 2. Parameterization and fitting to observations. *Journal of Geophysical Research*, 107(A8), 10–11. <https://doi.org/10.1029/2001JA000220>
- Tsyganenko, N. A. (2013). Data-based modeling of the Earth's dynamic magnetosphere: A review. *Annales Geophysicae*, 31(10), 1745–1772. <https://doi.org/10.5194/angeo-31-1745-2013>
- Tsyganenko, N. A., & Andreeva, V. A. (2016). An empirical RBF model of the magnetosphere parameterized by interplanetary and ground-based drivers. *Journal of Geophysical Research: Space Physics*, 121(11), 786–810. <https://doi.org/10.1002/2016JA023217>
- Tsyganenko, N. A., & Andreeva, V. A. (2017). A hybrid approach to empirical magnetosphere modeling. *Journal of Geophysical Research: Space Physics*, 122(8), 8198–8213. <https://doi.org/10.1002/2017JA024359>
- Tsyganenko, N. A., Singer, H. J., & Kasper, J. C. (2003). Storm-time distortion of the inner magnetosphere: How severe can it get?. *Journal of Geophysical Research: Space Physics*, 108, A51209. <https://doi.org/10.1029/2002JA009808>
- Tsyganenko, N. A., & Sitnov, M. I. (2005). Modeling the dynamics of the inner magnetosphere during strong geomagnetic storms. *Journal of Geophysical Research*, 110(A3), A03208. <https://doi.org/10.1029/2004JA010798>
- Tu, W., Li, W., Albert, J. M., & Morley, S. K. (2019, 2). Quantitative assessment of radiation belt modeling. *Journal of Geophysical Research: Space Physics*, 124(2), 898–904. <https://doi.org/10.1029/2018JA026414>
- Ukhorskiy, A. Y., Sitnov, M. I., Millan, R. M., Kress, B. T., Fennell, J. F., Claudepierre, S. G., & Barnes, R. J. (2015). Global storm time depletion of the outer electron belt. *Journal of Geophysical Research: Space Physics*, 120(4), 2543–2556. <https://doi.org/10.1002/2014JA020645>
- Wang, C., Ma, Q., Tao, X., Zhang, Y., Teng, S., Albert, J. M., et al. (2017). Modeling radiation belt dynamics using a 3-D layer method code. *Journal of Geophysical Research: Space Physics*, 122(8), 8642–8658. <https://doi.org/10.1002/2017JA024143>
- Wang, C. P., Xing, X., Liu, Y. H., & Runov, A. (2018). A case study of connection between ground magnetic field perturbations and tail current sheet bursty flows at X=60RE. *Journal of Geophysical Research: Space Physics*, 123(3), 1822–1833. <https://doi.org/10.1002/2017JA024972>
- Watt, C. E. J., Allison, H. J., Meredith, N. P., Thompson, R. L., Bentley, S. N., Rae, I. J., et al. (2019). Variability of quasilinear diffusion coefficients for plasmaspheric hiss. *Journal of Geophysical Research: Space Physics*, 124(11), 8488–8506. <https://doi.org/10.1029/2018JA026401>
- Weiss, L. A., Thomsen, M. F., Reeves, G. D., & McComas, D. J. (1997). An examination of the Tsyganenko (T89a) field model using a database of two-satellite magnetic conjunctions. *Journal of Geophysical Research: Space Physics*, 102(A3), 4911–4918. <https://doi.org/10.1029/96JA02876>
- Xiao, F., Yang, C., He, Z., Su, Z., Zhou, Q., He, Y., et al. (2014). Chorus acceleration of radiation belt relativistic electrons during March 2013 geomagnetic storm. *Journal of Geophysical Research: Space Physics*, 119(5), 3325–3332. <https://doi.org/10.1002/2014JA019822>
- Xu, Z., Hartinger, M. D., Clauer, C. R., Peek, T., & Behlke, R. (2017). A comparison of the ground magnetic responses during the 2013 and 2015 St. Patrick's Day geomagnetic storms. *Journal of Geophysical Research: Space Physics*, 122(4), 4023–4036. <https://doi.org/10.1002/2016JA023338>
- Yu, Y., Koller, J., Zaharia, S., & Jordanova, V. (2012).  $L^*$  neural networks from different magnetic field models and their applicability. *Space Weather*, 10(2). <https://doi.org/10.1029/2011SW000743>

## 4.2 Physical variability of $L^*$ during geomagnetic storms

The probabilistic  $L^*$  models discussed in Thompson et al. [2020a] aimed to quantify and alleviate uncertainties in the mapping of ground observations due to magnetic field model configurations. While this is important for using ground observations to remote sense the magnetosphere, it does not provide any information about the physical variability of  $L^*$  and what impact that might have when constructing empirical  $D_{LL}$  models from observations, or modelling the radial diffusion equation. An important result in Thompson et al. [2020a] highlighted the systematic variation of  $L^*$  with ground magnetic latitude as we move through MLT, with average  $L^*$  contours moving inwards (with respect to magnetic latitude) approaching midnight. Since co-located latitudes fall on increasingly stretched field lines in this region, it is clear that  $L^*$  is sensitive to variations of the magnetic field in real-space. It is important to further explore this physical variability and investigate whether geomagnetic activity might drive additional systematic changes of  $L^*$  in physical space. For this analysis we largely consider  $L^*$  variability at fixed locations on the magnetic equator in  $R_E$  and MLT, as opposed to (ground) magnetic latitude and MLT, which is more illustrative of responses of the magnetic field to changes in solar wind driving.

Determining  $L^*$  relative to radial distance is critical for the creation of diffusion coefficients over numerous wave modes. Firstly, many empirical (Ali et al. [2015, 2016]; Brautigam and Albert [2000]; Fei et al. [2006]; Ozeke et al. [2012, 2014]) and event specific (Jaynes et al. [2018a]; Su et al. [2016]) radial diffusion coefficients are derived using electric and magnetic field ULF wave power spectra, from both ground-instruments and satellites. The ability to inform radial diffusion coefficients from observations requires a decision for the respective  $L^*$  of an observation in physical space. While using  $L^*$  from better performing (Brito and Morley [2017]) magnetic field models is more pragmatic to characterise the underlying distribution of  $\mathcal{P}$ , the drift-averaged power from these distributions are used to construct the empirical  $D_{LL}$  (Ali et al. [2015, 2016]). Studies have shown that these averaged models can differ by orders of magnitude when compared to *in situ* calculated  $D_{LL}$  using the same magnetic field models (Jaynes et al. [2018a]). Uncertainties arising from invoking a poor  $L^*$  descriptor, or omitting the variability of  $L^*$  at observation locations, can therefore propagate throughout all future diffusion analysis and can lead to

misleading results.

A robust description of  $L^*$  also underpins the efficacy of outer boundary conditions which drive radiation belt dynamics through interactions with the solar wind. Data-based approaches aim to map satellite flux measurements covering numerous energy channels to an electron distribution at a fixed  $L^*$  boundary before converting to phase space density (Glauert et al. [2018]; Maget et al. [2015]). Implementation of a global magnetic field model is necessary to partition flux data into  $L^*$  and infer a boundary condition. This problem is two-fold:

- Analytic magnetic field models project observations to a fixed (or little varying) outer boundary which is useful for numerical modelling of radial diffusion, at the expense of inaccurate projections to  $L^*$  (e.g. Glauert et al. [2018])
- Empirical magnetic field models provide a better means to project observations to  $L^*$ , but  $L^*$  variability in a single satellite orbit means that simplified boundary conditions (e.g. Fok et al. [2008]), extrapolation of observations to a fixed boundary in  $L^*$ -space (e.g. Glauert et al. [2018]) or updating the simulation domain to account for flux observations varying in  $L^*$  (e.g. Drozdov et al. [2020]) are needed to enable seamless numerical modelling

When considering the above, it is also important to consider whether  $L^*$  variability in real space is exacerbated by certain physical processes. Large distortions to the magnetic field occur during geomagnetic storms (e.g. Tsyganenko et al. [2003]). We proceed here to investigate the changes in  $L^*$  during geomagnetic storm phases (initial, main and recovery) relative to quiescent times to identify whether the  $L^*$  variability studied in Thompson et al. [2020a] displays repeatable patterns during storm times. We employ the storm list provided by Walach and Grocott [2019], which identified 52 storms (with times provided for each storm phase) in the period 2012-16 using SuperDARN ionospheric backscatter observations. We restrict the Pro- $L^*$  data-set (Thompson et al. [2020a]) to 2012-2016, and declare any times not in the Walach and Grocott [2019] storm list as quiescent. We are able to investigate the physical variability of  $L^*$  for both ground and space observations. Since Pro- $L^*$  contains information for discrete points at the Earth's surface and their varying

conjugate Cartesian locations at the magnetic equator, we are able to look at variability in both magnetic latitude and radial distance ( $R_E$ ).

Figure 4.1 shows the median  $L^*$  for a selection of magnetic field models during each geomagnetic storm phase as a function of magnetic latitude and MLT. The magnetic field models considered are Olson and Pfitzer [1974]; Tsyganenko [1989, 1996]; Tsyganenko and Sitnov [2005] (OPQUIET, T89, T96, T05, see Thompson et al. [2020a] for a full description of the models and the current systems they contain). Geomagnetic storm phase is ordered across each column, and magnetic field models are ordered and labelled by row. Occurrence plots for the existence of  $L^*$  are also shown for each ground location in Pro- $L^*$  to highlight where ground observations are invalid for  $\mathcal{P}$  parameterization due to non-existing  $L^*$ .

In Figure 4.2 we show the equivalent information, but now displayed on a  $R_E$  and MLT grid. In a dipole a 1-1 relationship exists between ground magnetic latitude and  $R_E$ , with all field lines closed in the Pro- $L^*$  domain (see grid in Thompson et al. [2020a]). We would therefore expect to see, in each storm phase, a similar number of observations in each  $R_E$ -MLT bin (subject to some differences as the Pro- $L^*$  grid rotates through MLT). To highlight any aliasing effects induced from assuming a dipolar magnetic field, or the misallocation of  $\mathcal{P}$  to  $L^*$  which doesn't exist,  $L^*$  occurrences in Figure 4.2 are normalized by the cumulative number of hours (the resolution of the Pro- $L^*$  dataset) in each storm phase. Occurrences which deviate from a value of 1 will therefore showcase where aliasing or misallocation of  $\mathcal{P}$  exists.

Figure 4.3 shows the distributions of  $L^*$  for each MLT sector during each geomagnetic storm phase characterized by the median and IQR. Distributions are given for the same magnetic field models as in Figures 4.1 and 4.2.

Figure 4.4 illustrates full non-parametric estimates to  $L^*$  probability density functions at geosynchronous orbit ( $\sim 6.6R_E$ ) at noon MLT (hereby called geosynchronous noon), using kernel density estimates (KDEs). Distributions again are given for the same magnetic field models as in Figures 4.1 and 4.2. Geosynchronous orbit was considered as it is a stable orbit which typically operates in the outer edge of the outer radiation belt. In fact,  $>2$ -MeV electron flux measurements from Geostationary Operational Environmen-

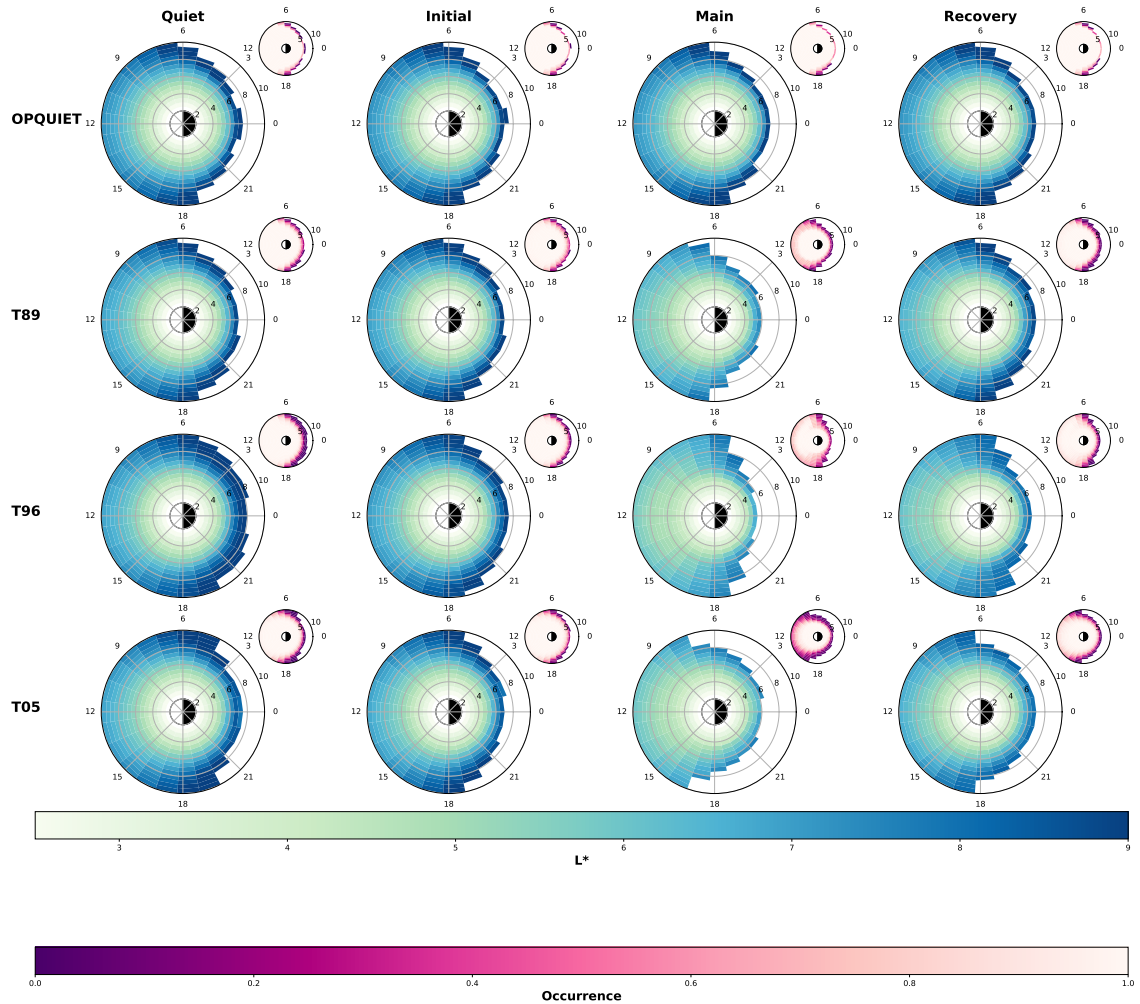


Figure 4.1: Median  $L^*$  distributions during each geomagnetic storm phase as a function of magnetic latitude and MLT, shown for a selection of magnetic field models (OPQUIET, T89, T96, T05). Since the magnetic latitude discretization in Pro- $L^*$  is non-linearly spaced, magnetic latitudes  $\lambda$  are converted to their dipole L-Shell equivalent  $L = 1/\cos^2(\lambda)$ , with  $\lambda$  increasing radially outwards. The occurrence of  $L^*$  existence during each storm phase is also shown above each sub-figure for the same spatial coordinates.

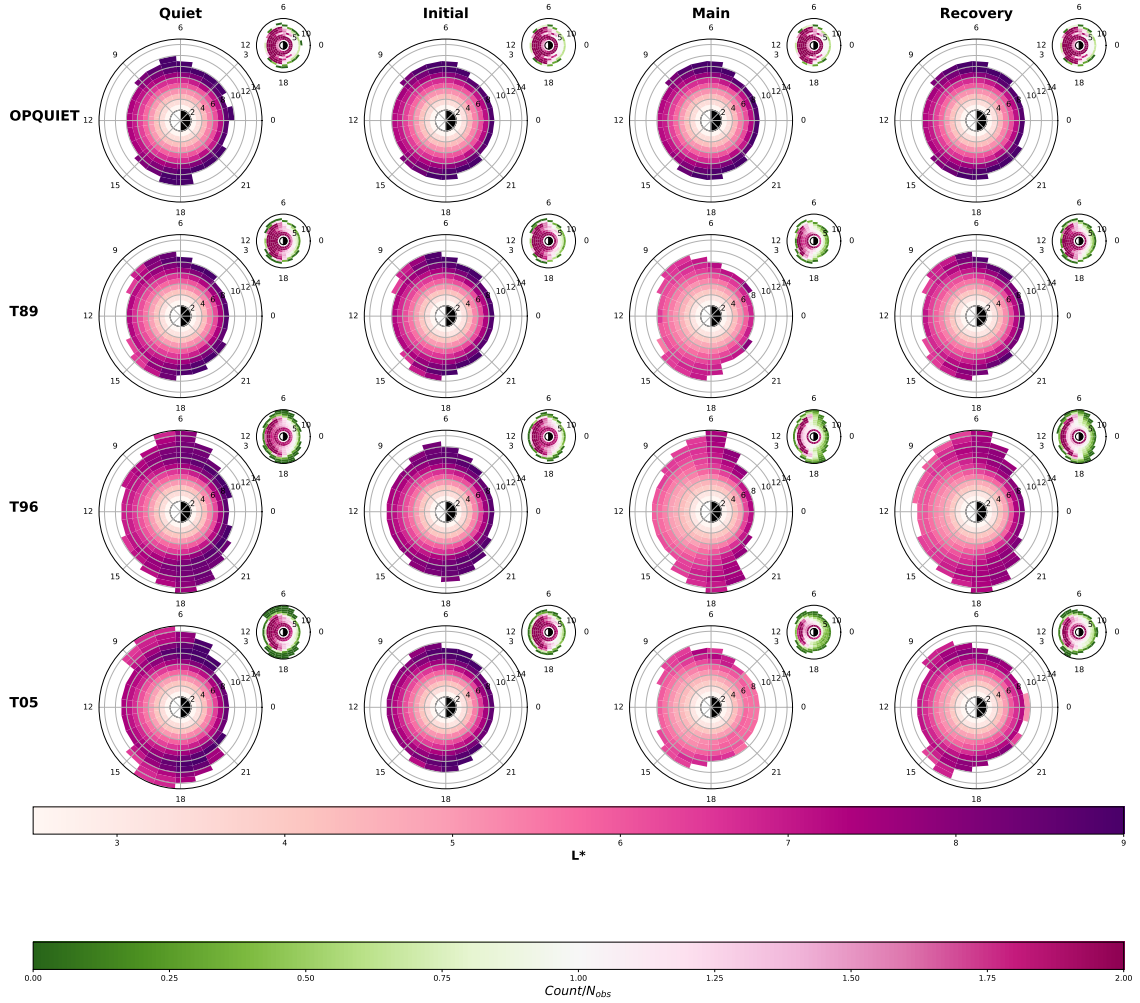


Figure 4.2: Median  $L^*$  distributions during each geomagnetic storm phase as a function of magnetic latitude and  $R_E$ , shown for the same magnetic field models as in Figure 4.1. The occurrence of  $L^*$  observations in each bin, normalized by the cumulative number of hours in each storm phase, is also shown above each sub-figure for the same spatial coordinates. This highlights the regions where aliasing, or misallocation of power to non-existing  $L^*$ , may occur when we parameterize  $D_{LL}$  assuming simple dipole-like magnetic field geometries.

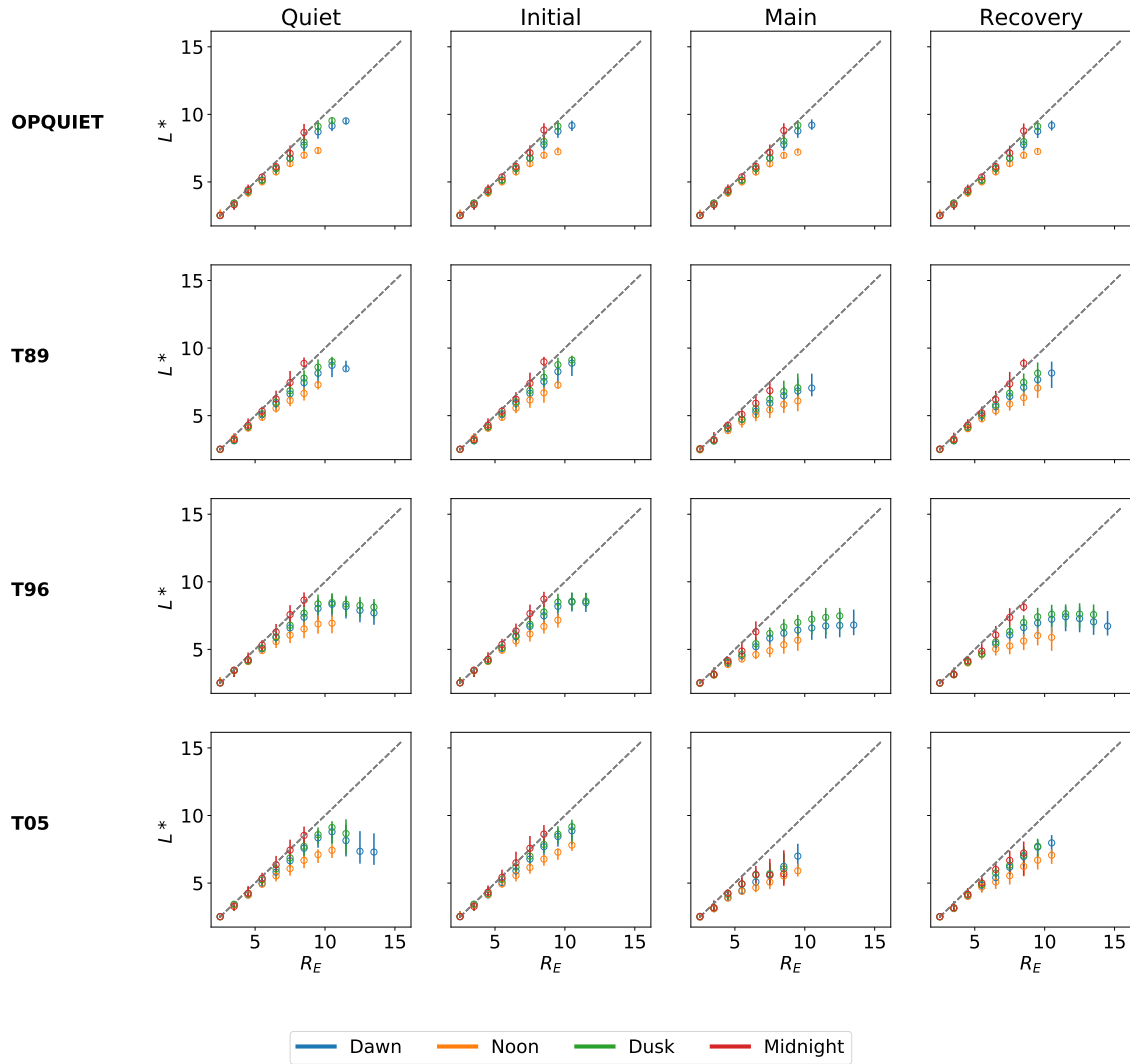


Figure 4.3:  $L^*$  distributions in each MLT sector, characterized by their median (circles) and IQRs (bars) during each geomagnetic storm phase (columns) and as a function of  $R_E$ . Distributions are shown for the same magnetic field models as in Figures 4.1 and 4.2. In each subplot the line representing  $L^* = r/R_E$  (dipole-L) has also been provided to illustrate the dipole approximation.

**$L^*$  KDEs at geosynchronous noon for quiet times vs. geomagnetic storm phase**

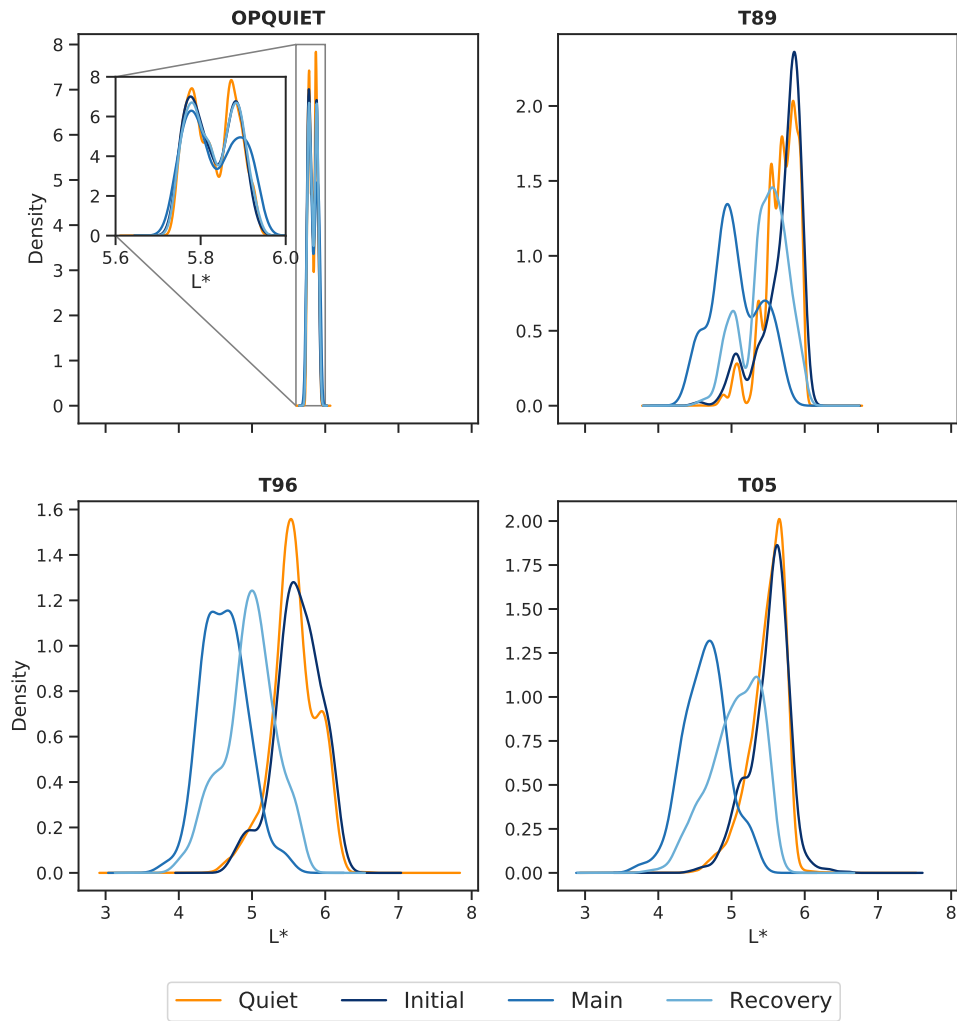


Figure 4.4: KDEs as estimates of  $L^*$  probability distribution functions at 12 MLT (noon) and geosynchronous radial distance ( $\sim 5.6R_E$ ), provided for each geomagnetic storm phase and the same magnetic field models as in Figures 4.1 and 4.2.

tal Satellites (GOES) which follow a geosynchronous orbit are used operationally in the British Antarctic Survey Radiation Belt Model (BAS-RBM) to determine the outer radial boundary condition (Glauert et al. [2018]).

KDEs are non-parametric, determining the probability density functions (PDFs) from the data itself when the structure is not defined *a priori*, and are useful when a PDF is not well explained by a theoretical distribution (such as multimodal, etc). Across the observed data samples we apply a *kernel* which controls the contributions of samples in a specified window toward estimating the probability of a new point. The window (or number) of samples used to approximate the probability for a new point is determined by the kernel *bandwidth* (or, *smoothing parameter*). Formally, if  $(x_1, \dots, x_n)$  are independent and identically distributed (iid) samples from some univariate distribution with an unknown density  $f$  at any given point  $x$ , then the kernel density estimator is

$$\hat{f}_h(x) = \frac{1}{n} \sum_{i=1}^n K_h(x - x_i) = \frac{1}{nh} \sum_{i=1}^n K\left(\frac{x - x_i}{h}\right) \quad (4.1)$$

for bandwidth  $h$  and scaled-kernel  $K_h(x) = 1/hK(x/h)$ . There are many possible choices for the kernel and we employ a Gaussian kernel  $K(x; h) \propto \exp(-x^2/2h)$ . The choice of  $h$  is more important for accuracy and acts as a bias-variance tradeoff for the estimator. If  $h$  is too small the kernel will have too narrow a window, exhibiting too much detail and not be smooth or general enough to correctly cover new or unseen examples. On the other hand if  $h$  is too large the wide kernel window may result in a coarse density with little details. Here we decide  $h$  using *Scott's Factor*  $n^{-1/5}$  (Scott [1992]), where  $n$  is the number of data samples, which is the coefficient that multiplies the data covariance matrix to obtain the kernel covariance matrix. A limitation of this approach is that Scott's Factor assumes that the underlying data is Gaussian to perform well, but Figure 4.4 demonstrates that this is a reasonable assumption.

As anticipated the analytic OPQUIET is inflexible to changes in geomagnetic activity, and while there exists an alternative dynamic model (Olson and Pfitzer [1982]),  $L^*$  variability throughout each storm phase would be impossible to capture. For the remainder of the analysis we consider the empirical field models (Tsyganenko [1989, 1996]; Tsyganenko and Sitnov [2005]) only.

### 4.2.1 Quiet→Initial phase

The only noticeable systematic changes between quiet and initial phases are the narrowing of  $L^*$  radial extent around dawn and dusk for the more complex models (see T96 and T05 in Figure 4.2). Minimal change in this transition is to be expected, as the initial phase by definition constitutes a relatively quiet period lasting a few hours before main phase onset. During this time the interplanetary shock wave advances ahead of the intense plasma flow by several hours, driving compressions which are in line with the observed dawn-dusk radial  $L^*$  narrowing (Ness et al. [1964]; Syun-Ichi [2018]).

Although average values of  $L^*$  appear not to vary between these phases, the altered shapes of the  $L^*$  distributions in Figure 4.4 are notable. Interestingly, alterations in shape between quiet and initial phases are not the same for each magnetic field model. The Kp-based T89 model approximates a multimodal distribution during quiet times which smooths to bimodal and less variable during the initial phase. While differences in modality are substantial, these are likely to be due to the significantly larger sample size for quiet times, and the inability of single parameterization by discrete Kp to fully characterize multiple magnetic field configurations. For the more advanced models, transitioning from quiet to the initial phase results in a widening of the distributions (increased variance) retaining a dominant peak in the same location as at quiet times, but also the formation of a second peak much lower in density near the inner edge of the distribution. This implies the existence of two initial phase types, one much more extreme than the other, in which typical  $L^*$  values vary by about 1. However, while the distribution shapes are similar for the more advanced models, their underlying values appear to be shifted by about  $0.5L^*$ .

In any case, although the quiet and initial phases correspond to typically quiescent conditions,  $L^*$  variability is considerable at physical locations beyond  $4R_E$  (see Figure 4.3), worsening as one moves further from the Earth.  $L^*$  variation with  $R_E$  is nonlinear at dawn, noon and dusk, with a dipole approximation increasingly overestimating  $L^*$  with increasing radial distance. Empirical  $D_{LL}$  based on a dipole-like magnetic field therefore sample  $\mathcal{P}$  at  $L^*$  much closer than we'd expect during both the initial phase and quiet times. At a single location we have variability from two sources: natural variability in

the complex magnetic field and the systematic shifts with geomagnetic activity. The natural variability is two-fold during quiet times, however, as it additionally alters the gradient of  $L^*$  with  $R_E$ . For the empirical models in Figure 4.3 we expect median  $L^*$  to monotonically increase with  $R_E$ , but for dawn and dusk we see a decrease after  $10R_E$ . This is possibly due to quiet times not actually being a period of *steady-state*, as they encompass isolated events such as substorms which can significantly drive magnetospheric dynamics. It appears that some processes during quiet times broaden  $L^*$  to larger radial distances, decreasing the gradient between physical and adiabatic space.

### 4.2.2 Initial→Main phase

In all Figures we observe a global broadening of  $L^*$  to higher radial distance (a decrease in  $L^*$  at a single point in real-space) and increased variability during the main phase. We attribute this to the enhanced storm time ring current which decreases the magnetic field in the inner magnetosphere (since the ring current operates in the opposite direction to the internal magnetic field). Due to right hand rule for current/magnetic field relationship, at radial distances further away than the ring current location, the magnetic field due to the ring current *adds* to the background field. Conservation of  $\Phi$  (and therefore  $L^*$ ) implies that the amount of magnetic flux contained by the drift path must remain constant. If the drift path remained where it was, and the perturbations in  $B$  due to the ring current act to diminish the magnetic field at/inside the drift path, then the amount of flux contained by the drift path would be smaller. In order to *contain* the same amount of magnetic flux, the drift path has to expand. ULF wave power increases in real space during the main phase (eg Sandhu et al. [2021]), so tail-values in L-shell based  $D_{LL}$   $\mathcal{P}$  distributions actually belong to much lower values of  $L^*$ . Since empirical fits are made to these distributions binned by geomagnetic activity (e.g. Kp), they are likely to underestimate  $D_{LL}$  during the main phase of a storm.

The radial broadening of  $L^*$  implies that more distant observations become useful during storms to approximate  $D_{LL}$  at larger  $L^*$ . However, we are still limited by the level of magnetospheric compression which controls  $L^*$  existence. For example, in Figure 4.1 we observe reductions in  $L^*$  existence globally at high-latitude ground locations, even

though they generally correspond to a reduction in  $L^*$  relative to the initial phase. This is consistent with dropouts during geomagnetic storms caused by magnetopause shadowing, where trapped particles are lost in their drift due to the combined effects of a significantly compressed magnetopause location on the dayside and enhanced convection (e.g. Li et al. [1997]; Yu et al. [2013]). The ability to predict  $L^*$  existence during the main phase therefore increases in importance, since a non-existing  $L^*$  needs to be incorporated as a dropout of electrons in the numerical radiation belt models.

### 4.2.3 Main→Recovery phase

During the recovery phase the median value of  $L^*$  begins to relax back towards pre-storm levels but the variability is still comparable to that in the main phase (see Figures 4.1, 4.2 and 4.3). At geosynchronous orbit (Figure 4.4) variability spans  $\sim 2L^*$  and aliasing effects for a fixed outer boundary remain significant. Similar variabilities persist at radial distances beyond  $6R_E$ . Since recovery phase  $L^*$  distributions significantly overlap both the quiet/initial and main phase distributions, associated recovery  $\mathcal{P}$  observations cannot be separated out as a separate population. For  $D_{LL}$ , ULF wave power remains closer than we'd expect compared to a simple magnetic field geometry (see Figure 4.3 comparing against the dipole-L profile with  $R_E$ ), sometimes as far as in the main phase. As  $\mathcal{P}$  intensity decays during the recovery phase, there is a danger of pronounced  $L^*$  aliasing for *typical* values in  $\mathcal{P}$  distributions.

## 4.3 Chapter summary

The construction of modern  $D_{LL}$  models did not account for the relationship between an observation's location and  $L^*$  variability at that location. It is either completely unaccounted for in assumed dipole-like fields (Brautigam and Albert [2000]; Brautigam et al. [2005]; Ozeke et al. [2012, 2014]), or masked in the averaged  $\mathcal{P}$  distributions binned by  $L^*$  (Ali et al. [2015, 2016]). In this Chapter we considered the uncertainty in  $D_{LL}$  which arises from mapping ULF wave power spectral density approximations to  $L^*$  at fixed observation locations, which is determined by the underlying magnetic field model. First we created

Pro- $L^*$  (Thompson et al. [2020a]), a probabilistic  $L^*$  mapping tool for ground-observations to the magnetic equator. Using Pro- $L^*$ , we found that although a number of magnetic field models had similar climatological (average) structures of approximated  $L^*$  mapped from the ground, on typical timescales of interest for radial diffusion there was profound variability across magnetic latitude and MLT, exacerbated by systematic magnetic field model biases and response to geomagnetic activity. In response, we demonstrated some approaches to construct a probabilistic  $L^*$  model which combines approximations from multiple magnetic field models to remove systematic biases.

Following this, we investigated the response of  $L^*$ -mapping radially along the magnetic equator to distortions of the magnetic field geometry throughout geomagnetic storms. In almost all instances (except very low latitudes/ $R_E$ ) dipole-like fields tend to overestimate the  $L^*$  they aim to represent, meaning that ULF wave power observations are at lower  $L^*$  values than we'd expect. How much closer is naturally variable, but there are systematic shifts in location associated with geomagnetic storm phases. This aliasing of  $L^*$  means that many  $D_{LL}$  models have been fit to  $\mathcal{P}$  distributions that actually represent multiple  $L^*$ . Further, since ULF wave power increases during geomagnetic storms, much of the values in the tails on the  $\mathcal{P}$  distributions belong to closer  $L^*$  and these  $D_{LL}$  models are likely to underestimate during storms. This issue extends to  $D_{LL}$  formed from  $L^*$  rather than L-Shell, fit to averaged  $\mathcal{P}$  values which are naturally biased to more frequently observed quiescent times, where  $\mathcal{P}$  is less intense as during storms.

It is critical to characterize  $D_{LL}$  by its full distribution across  $L^*$  when trying to model radial diffusion, since the variability of  $L^*$  governs both the intensity of  $D_{LL}$  and the outer boundary condition necessary for accurate modelling (Drozdo et al. [2021]; Fok et al. [2008]; Glauert et al. [2018]). It remains to be seen how  $\mathcal{P}$  distributions (and subsequently  $D_{LL}$ ) change when associated with more accurate magnetic field representations, compared to pre-existing  $D_{LL}$  models. Unfortunately, we remain faced with the uncertainty imposed from magnetic field model selection, which can only be mitigated from thorough magnetic field model validation.

Although uncertainty will always be present due to imperfection of magnetic field models (e.g. Brito and Morley [2017]), being able to quantify any uncertainty is still very

useful and important for radiation belt research. We are constantly learning more about the radiation belts, be that through case studies or large statistical studies of ground and satellite observations, not always in agreement with our current theoretical understanding or previous studies on the same phenomena. Quantifying magnetic field model uncertainty allows us to discern whether differences between certain studies are *physical* or a consequence of conflicting magnetic field geometries. Further, we can be conscious about *where* spatially certain models might produce erroneous results for more informed analysis. Interpreting our results through the lens of uncertainty starting at the foundation with magnetic field model selection, we are able to be more insightful about our findings and advance our knowledge of the radiation belts with confidence.

#### 4.4 Future work

While we have attempted to thoroughly address  $L^*$  variability in magnetic field model selection and in physical space, future work should widen the scope further to characterize  $L^*$  variability on a global scale:

- **Off-equatorial regions:** Throughout this section we have only considered  $L^*$  at the magnetic equator. While this is necessary to enable use of ground instruments for calculating the azimuthal equatorial electric field  $\mathcal{P}$ , satellites frequently operate in off-equatorial regions. Due to the complex nature of the magnetic field, it is not intuitive to assume that  $L^*$  variability at the equator extends to other latitudes and is something that needs to be explored for more accurate representation of satellite observations in magnetospheric processes.
- **Pitch angle distributions:** In our analysis we have only considered energetic particles with a trapped  $90^\circ$  equatorial pitch angle ( $\alpha_{eq}$ ). For pure radial diffusion we expect an anisotropic  $\alpha_{eq}$  distribution which is peaked near  $90^\circ$  (Horne et al. [2003]) and focusing only on these particles is a natural choice (other  $\alpha_{eq}$  distribution shapes are possible due to other magnetospheric processes, see Chen et al. [2014] Figure 1).  $\mathcal{P}$  exists along the field line with different magnitude and is sampled during a bounce for non-equatorially mirroring particles. Variability in *in situ*  $D_{LL}$  as a function of

$\alpha_{eq}$  is substantial (O'Brien [2014], Figure 4), yet the distribution of  $\mathcal{P}$  with  $(L^*, \alpha_{eq})$  along the bounce trajectory remains largely unknown.

- **Predictability for modelling:** Pro- $L^*$  is useful for developing novel ways to rapidly predict  $L^*$  for use in numerical radiation belt models. We have considered simple probabilistic models in this section, but future work should develop more sophisticated ones. It should also be noted that a model to predict  $L^*$  existence is as important as predicting the value of  $L^*$  when it does exist. Classical approaches for building statistical models from the Pro- $L^*$  data might be useful, but since we need to build both classification ( $L^*$  existence) and regression ( $L^*$  value) prediction models, a more intuitive approach could be to utilize machine learning capabilities which are beginning to make headway in space physics (e.g. Bentley et al. [2020]; Bloch et al. [2021]; Camporeale et al. [2021]; Smirnov et al. [2020]).

## CHAPTER 5

# VARIABILITY OF SPACE-BASED ULF WAVE POWER SPECTRAL DENSITY

The ensemble experiments in Chapter 3 (Thompson et al. [2020b]) concluded that a full characterization (shape and width) of  $D_{LL}$  variability in both space and time is necessary to quantify the impact when included in the radial diffusion equation. Both Fälthammar [1965] and Fei et al. [2006] demonstrated that the radial diffusion coefficient is proportional to the power spectra of magnetic and electric field perturbations, which are realizations of some stationary stochastic process (invariant mean and variance over time). Since we require physical processes varying on timescales relative to the particle drift period to violate the third adiabatic invariant and induce radial diffusion, these power spectra have become synonymous with that of ultralow frequency (ULF) waves in the 1-20mHz range. The spatial, temporal and spectral variability of  $D_{LL}$  is therefore governed by that of the ULF wave power spectral density ( $\mathcal{P}$ ).

$D_{LL}$  models which follow the Fei et al. [2006] approach are separated into two components, assumed to have little or no correlation, that are typically modelled using two sets of independent observations - the radial magnetic field for the compressional magnetic  $D_{LL}^B$  and the azimuthal electric field for  $D_{LL}^E$  (see Chapter 2 for a detailed derivation). These models feature some parameterization of  $\mathcal{P}_B$  and  $\mathcal{P}_E$  which feature some form of drift-

shell average, that can be scaled to infer  $D_{LL}$ . Classically this has been achieved via some deterministic fit to median  $\mathcal{P}$ , as a function of variables indicative of geomagnetic activity, in some magnetic field geometry with varying degrees of complexity. Consequently, in this Chapter we address a number of questions to discern, where possible, the variability of  $\mathcal{P}$  (and therefore  $D_{LL}$ ):

- In Chapter 4 we found the variability of observation location with  $L^*$  depends on the magnetic field model used. What does the distribution of  $\mathcal{P}$  look like when power measurements are binned by more realistic representations of the magnetic field and MLT?
- How much variability is lost by only considering median  $\mathcal{P}$ ?
- Are  $\mathcal{P}$  distributions well-described by theoretical distributions that can be fully characterized and implemented in probabilistic models?
- What are the temporal, spatial ( $L^*$ ) and spectral (frequency) auto-correlations of  $\mathcal{P}$ ?

In this Chapter we systematically investigate the compressional  $\mathcal{P}_B$  and azimuthal  $\mathcal{P}_E$  as inferred from a large collection of satellite observations, following an overview of magnetospheric ULF waves. Distribution shapes and variance are explored across various spatial domains and activity levels, and where relevant, compared to a number of well-known empirical  $D_{LL}$  models based on similar data splits. Based on similarities between  $\mathcal{P}$  distributions and a number of theoretical distributions, we apply a large number of parametric fits to fully describe the variability of  $\mathcal{P}$  for use in probabilistic models. We explore the correlations of  $\mathcal{P}$  across ULF frequencies, and discuss the difficulties in determining temporal and spatial correlations alongside other limitations of using satellite observations alone to construct robust  $D_{LL}$  models.

## 5.1 Magnetospheric ULF waves

Ultralow frequency (ULF) waves are known as the frequency oscillations of the magnetosphere with typical amplitudes much smaller than the background magnetic field strength. With observations dating back to the Carrington event in 1859 (Stewart [1861]), ULF waves observed at the ground were previously described in the literature as *micropulsations* and classified by Jacobs et al. [1964] as either continuous (Pc) or irregular (Pi). For radial diffusion, we are most interested in the subclass of Pc4-5 ULF waves at the lowest of frequencies ( $\sim 1 - 20\text{mHz}$ ), which have periods comparable to the electron drift period to violate the third adiabatic invariant. Magnetospheric ULF waves have a number external and internal generation mechanisms, many of which are not observable at the ground but are equally able to contribute to radial diffusion. Each of these mechanisms are represented in  $D_{LL}$  calculated from satellite observations of ULF wave power. Here, we outline some drivers of magnetospheric ULF which are relevant for radial diffusion for the reader's interest. For more detailed descriptions of ULF wave drivers see McPherron [2005] and Keiling et al. [2016]. It is useful to treat the drivers separately to enable comparison to ULF wave propagation in a 3D magnetosphere (e.g. Elsdén and Wright [2017, 2018, 2019]; Degeling et al. [2010, 2018]; Lysak et al. [2020]).

When external drivers compress the magnetosphere with perturbations on timescales comparable to ULF frequencies, waves are generated which propagate through the magnetosphere. At the lowest frequencies relative to radial diffusion, the main driver for these compressions is solar wind dynamic pressure driving (McPherron [2005]). Indeed, this is often considered the main source of ULF waves in the magnetosphere (Takahashi and Ukhorskiy [2007, 2008]). A way in which this occurs is due to density oscillations present in the ambient solar wind, already carrying ULF waves, striking the magnetosphere and activating discrete perturbations at those respective frequencies (Kepko et al. [2002]; Kepko and Spence [2003]). Another way is through broadband fluctuations in the solar wind stimulating the natural 'ringing' eigenmodes in the magnetospheric cavity (the space between the reflective plasmasphere and magnetopause), with cavity properties continually changing in response to the solar wind (Allan et al. [1986b]; Kivelson and Southwood [1985]; McPherron [2005]).

Other external drivers relate to macro-scale fluid instabilities, with the Kelvin-Helmholtz instability (KHI) receiving a lot of attention. First demonstrated by Southwood [1968] and similar to ocean surface waves driven by the wind, the KHI can drive ULF waves on the flanks of the magnetosphere via the shear between the fast magnetosheath flow and slow magnetospheric interior flow. Rayleigh-Taylor instabilities have also received notable attention (Keiling et al. [2016]), where for two fluids of different densities, the lighter one is accelerated into the heavier. In the magnetosphere, these can be seen when growth rates of instabilities are increased when the magnetopause undergoes accelerated motion (Mishin [1993]), or when less-dense plasma presses against denser plasma in the magnetosheath during magnetospheric expansion (Bentley et al. [2018]). The relative contributions of these instabilities to ULF wave power enhancements are spatially dependent and evident in a variety of statistical studies (e.g. Bentley et al. [2018, 2020]).

Much of the internally generated ULF waves are attributed to substorms or geomagnetic storms. During the substorm expansion phase, protons energized and injected near midnight create Pc 4–5 waves with small azimuthal wavelengths near the dusk meridian through the drift-mirror instability (McPherron [2005]). Instabilities in the cloud of drifting protons within geomagnetic storm-time ring current can excite poloidal standing Alfvén ULF waves via drift-bounce resonances (Keiling et al. [2016]), although this can also occur outside of storms. Since geomagnetic storms contain a number of substorms, this is a likely cause of ULF waves generated during geomagnetic storms (McPherron [2005]; Murphy et al. [2011]; Rae et al. [2011]).

## 5.2 Data, instrumentation and power spectral density approximation

We explore  $\mathcal{P}$  approximated using magnetic and electric field perturbations provided by the Van Allen Probes (Mauk et al. [2013]). The Van Allen Probe mission lasted from late 2012 to mid 2019 and had scientific objectives which focused on radiation belt processes which drive particle acceleration, transport and electron loss, as well as the radiation belt response to geomagnetic storms. Consisting of two spacecraft with identical instrumen-

tation (Probe A and B), both followed an orbit of 9 hours, inclination of  $10.2^\circ$ , apogee of 30,414 km and orbital perigee of 618km during the prime phase of the mission. In early 2019, perigee lowering maneuvers began, with Probes A and B ceasing to operate in October 2019 and July 2019, respectively. Due to the repeated sampling of the inner magnetosphere at multiple  $L^*$  and MLT, the Van Allen Probes provide a rich data set for statistical analysis of  $\mathcal{P}$ .

We employ electric field measurements from the Electric Field and Waves (EFW) instrument (Mauk et al. [2013]; Wygant et al. [2013]) and magnetic field measurements from the Electric and Magnetic Field Instrument Suite and Integrated Science (EMFISIS) instrument (Kletzing et al. [2013]). Magnetic field measurements were sampled every 4s. Electric field measurements, sampled every 10s are provided in a modified Geocentric Solar Ecliptic (mGSE) coordinate system, which are in the spin plane of the spacecraft. EFW provides measurements in both Y mGSE and Z mGSE, where Y mGSE points in the ecliptic plane and duskward and Z mGSE points along the positive normal to the ecliptic. X mGSE points along the spin axis and the electric field is estimated under the assumption  $E \cdot B = 0$ , suitable for ULF waves

$$E_x = -\left(\frac{B_y}{B_x}\right)E_y - \left(\frac{B_z}{B_x}\right)E_z \quad (5.1)$$

subject to the general constraints  $|B_y/B_x|, |B_z/B_x| < 4$  (Wygant et al. [2013]).

To extract perturbations (Sandhu et al. [2021]), the background magnetic and electric fields were identified by a running average over a 20 minute sliding window and subtracted for residual field observations. These are then projected onto a field aligned coordinate system, with parallel component aligned with the background magnetic field unit vector, azimuthal direction oriented eastwards and perpendicular to the geocentric position vector, and the radial (poloidal) direction which closes the system. Following the coordinate transformations, the parallel magnetic ( $B_{\parallel}$ ) and azimuthal electric ( $E_{\phi}$ ) perturbations were selected for P approximation.

The *in situ*  $\mathcal{P}$  dataset was provided by Dr Jasmine Sandhu and is the same as that used in Sandhu et al. [2021].  $\mathcal{P}$  were estimated across 20 minute windows sampled at 10s,

using a continuous wavelet transform (CWT) with Morlet mother wavelet and 4 number of voices per octave (Sandhu et al. [2021], for a full mathematical description of the CWT and associated parameters see Section 6.7.1). Frequencies are limited to the range of 1-15 mHz suitable for ULF waves, resulting in 16 discrete frequencies ranging from 1.1-14.87 mHz with a  $\log_2$  spacing of 0.25. We restrict the approximations to an  $L^*$  range of 3-6 due to the small number of observations at higher  $L^*$  and the inability to separate field perturbations from the rapidly varying background field at lower  $L^*$  (Sandhu et al. [2021]) (leading to pollution of the background magnetic field in the ULF wave power spectral density). For all statistical analysis we consider the  $\log_{10} \mathcal{P}$  and bin values by their  $L^*$  as determined by the T05 (Tsyganenko and Sitnov [2005]) magnetic field model.

### 5.2.1 Global distribution of ULF wave power

The most naive representation of ULF wave  $\log_{10} \mathcal{P}$  is one which is invariant with MLT, herein named the *global distribution*, which holds in the case of an axisymmetric dipole and formed the basis for a number of the deterministic radial diffusion coefficients (Brautigam and Albert [2000]; Brautigam et al. [2005]; Liu et al. [2016]; Ozeke et al. [2012, 2014]). Here, we group electric and magnetic  $\log_{10} \mathcal{P}$  approximations into  $L^*$  bins of width 0.5, with  $L^*$  determined by the Tsyganenko and Sitnov [2005] magnetic field model, and the global distributions are illustrated in Figure 5.1. Distributions are characterised by the median, and the interquartile/decile ranges (IQR/IDR) for measurements of variability. Empirical fits are often made to the median  $\mathcal{P}$  which then infer  $D_{LL}$  (e.g. Ali et al. [2015, 2016]; Brautigam and Albert [2000]; Brautigam et al. [2005]; Liu et al. [2016]; Ozeke et al. [2012, 2014]), and tend to show the typical behaviour of monotonic increase with  $L^*$  for  $\log_{10} \mathcal{P}_E$ , and monotonic decrease for  $\log_{10} \mathcal{P}_B$ , at all frequencies as observed in Figure 5.1. However, the IQRs follow no clear structure across frequency and  $L^*$  and frequently exceed an order of magnitude, especially in the heart of the radiation belts, near the outer boundary and for  $\log_{10} \mathcal{P}_B$  at the inner boundary where the magnetic field is stronger. For the IDR the bulk of measurements at all  $L^*$  and frequency span between 2-3 orders of magnitude for  $\log_{10} \mathcal{P}_E$  and 2-4 for  $\log_{10} \mathcal{P}_B$ . It is clear that substantial variability is lost when limiting models of  $\mathcal{P}$  to the median alone. Since the radial diffusion equation

is significantly driven by larger values of  $D_{LL}$  (Thompson et al. [2020b] and Chapter 3), median parameterization fails to capture those instances of intense diffusion. We will also suffer from over-diffusion during periods of very low activity, which is irreversible once passed through the diffusion equation.

The level of variability in the  $\mathcal{P}$  distributions motivates the use of probabilistic modelling. Since radial diffusion is also sensitive to  $D_{LL}$  sampled from heavy tailed distributions (Thompson et al. [2020b]), characterizing the shape of  $\mathcal{P}$  distributions is significant. Estimates of the  $\log_{10} \mathcal{P}(f, L^*)$  probability density functions (PDFs) found using kernel density estimation (KDE, see Chapter 4) are shown in Figure 5.2.

We acknowledge that at the lowest  $L^*$ ,  $\log_{10} \mathcal{P}_B$  for the lowest frequencies appear to be many orders of magnitude above the rest (top-right panel of Figure 5.2). We do not anticipate this to be physical, but rather a consequence of the difficulty to separate the background magnetic field from the perturbations at low  $L^*$  where the field is much stronger, introducing residual background field into the signal which leaks into the lower frequencies. Improving the wavelet frequency resolution may mitigate this issue. Disregarding this case, a persistent property at all  $L^*$  for both power components is a well-ordered rightward shift of power peaks from higher to lower frequencies. While many of the low-frequency electric wave power distributions are closely aligned before diverging at the higher frequencies, the separation for magnetic power distributions is consistent between all frequencies, i.e. the power at lower frequencies tends to be higher than the power at higher frequencies, as expected from the average power law behaviour of ULF waves as seen on the ground (e.g. Pahud et al. [2009]; Rae et al. [2012]). Distribution shapes are most similar across frequency at lower  $L^*$ . For  $\log_{10} \mathcal{P}_E$ , as  $L^*$  increases all distribution widths increase, at a larger rate for higher frequencies. Also, right-skewness appears to decrease in favour of left-skewness, with many of the distributions above 2mHz approaching bimodality with a smaller second peak near the inner edge. The response is somewhat reversed for  $\log_{10} \mathcal{P}_B$ , where we also see increase in distribution widths but an increase in right-skewness and bimodality at all frequencies at the highest  $L^*$  bin, this time with a smaller second peak near the outer edge. In terms of power values themselves, all electric field power distributions shift to higher values with  $L^*$ . On the other hand, for

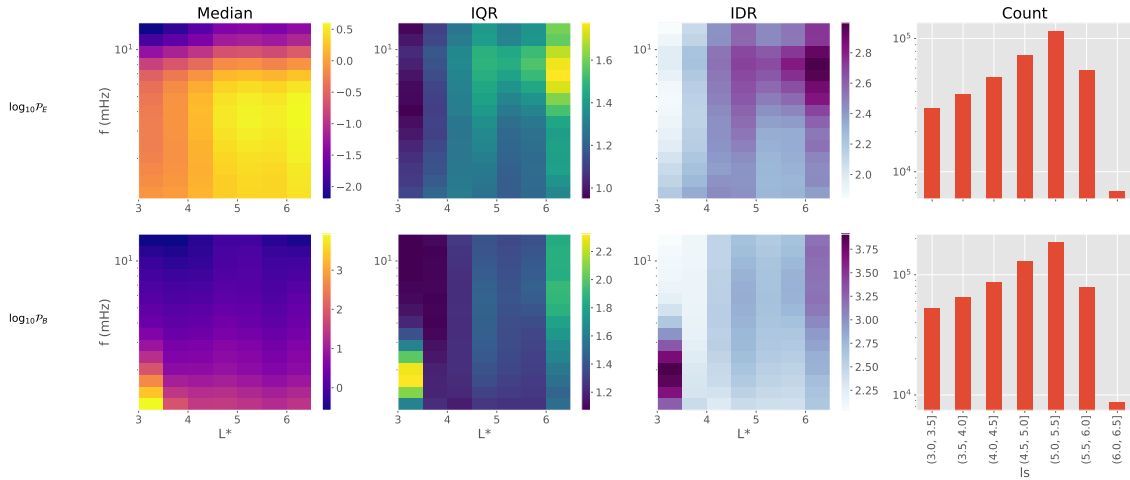


Figure 5.1: The global distribution of  $\log_{10} \mathcal{P}_E$  (top) and  $\log_{10} \mathcal{P}_B$  (bottom) binned by  $L^*$  (width 0.5), as described by the (left) median, (centre-left) IQR and (centre-right) IDR. Counts for each  $L^*$  bin are also provided (right), which is representative of all frequencies.

the magnetic distributions the lower frequencies shift to smaller values whilst the higher frequencies shift to higher values up until  $L^* = 5$  before decreasing again.

A large proportion of the distributions appear similar to a theoretical log-normal distribution. This is consistent with previous work by Bentley et al. [2018] who found the same for magnetic  $\mathcal{P}$  measured by ground magnetometers, and is especially satisfying for  $\log_{10} \mathcal{P}_E$  since we generally assume there to be a proportionality between the ground magnetic field and space electric field (Ozeke et al. [2009]). For the bimodal distributions, we postulate that distinct physical processes might be driving separable populations of ULF waves but an investigation of these physical processes is beyond the scope of this work.

Since a number of the  $\log_{10} \mathcal{P}$  KDEs are akin to theoretical distributions, we can attempt parametric fits to each of them to get closed form representations of their probability density function that can be easily implemented in probabilistic models. This would be more desirable than KDEs since we will no longer require the data itself to estimate the PDF. We fit 100 theoretical continuous distributions (<https://docs.scipy.org/doc/scipy/reference/stats.html>) to each of those in Figure 5.2, accepting the distribution

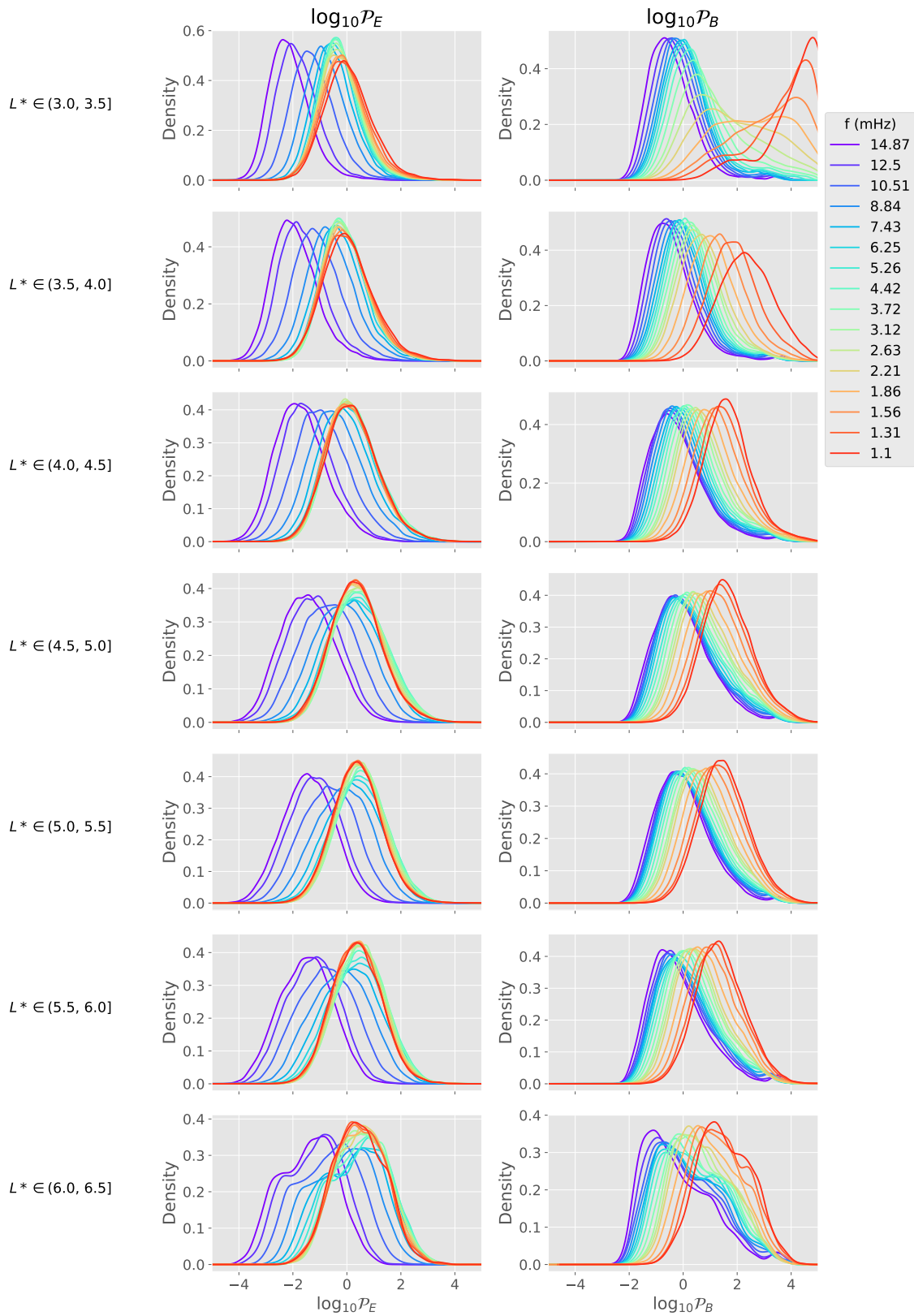


Figure 5.2: KDEs for  $\log_{10} \mathcal{P}_E$  (left) and  $\log_{10} \mathcal{P}_B$  (right) as non-parametric estimates of the probability density function, split by  $L^*$  and frequency.

with the smallest residual sum of squares

$$RSS = \sum_i (y_i - f(x_i))^2 \quad (5.2)$$

where  $x_i$  are the central values of the  $i$ th  $\mathcal{P}(f, L^*)$  histogram bin, with optimal bin-width determined by the *Freedman-Diaconis Rule*

$$\text{Bin-width} = 2 \frac{\text{IQR}(\mathbf{x})}{\sqrt[3]{n}} \quad (5.3)$$

and  $y_i$  are the values of the histogram at each  $i$ th bin and  $f(x_i)$  the values of the target theoretical distribution fit to each  $x_i$ .

Examples of parametric fits to empirical  $\log_{10} \mathcal{P}_E$  distributions in  $L^* \in (6, 6.5]$  at the highest (14.87 mHz) and lowest (1.1 mHz) ULF frequencies are demonstrated in Figure 5.3. For the lowest frequency, where the empirical distribution appears similar to an established distribution (in this case a Gaussian), we see that the best fit distribution is well-representative of the observed power. However, in the instance of a bimodal empirical distribution for the higher frequency, all theoretical distributions are a poor representation of the data and should be used with caution. We can get more robust fits to multimodality with distributions such as Gaussian Mixture models (the superposition of multiple Gaussian distributions, see Figure 5.3 for a simple demonstration), which should be explored in future work since the separable distributions might also be correlated. An example table depicting the best theoretical fits to each of the empirical  $\log_{10} \mathcal{P}_E(f, L^*)$  distributions is shown in Figure 5.4. We find that a significant proportion of  $\mathcal{P}_E$  distributions are variations of the log-normal distribution, whilst the rest exhibit assorted levels of (right or left) log-skewness. Since right-skewed heavy-tailed distributions for  $\log D_{LL}$  result in notably more radial diffusion (Thompson et al. [2020b]), it is likely in these instances that median-based power models are failing to capture times of intense diffusion. It remains to be seen how combined effects of the shape and width of the fitted distributions impact radial diffusion in a probabilistic model.

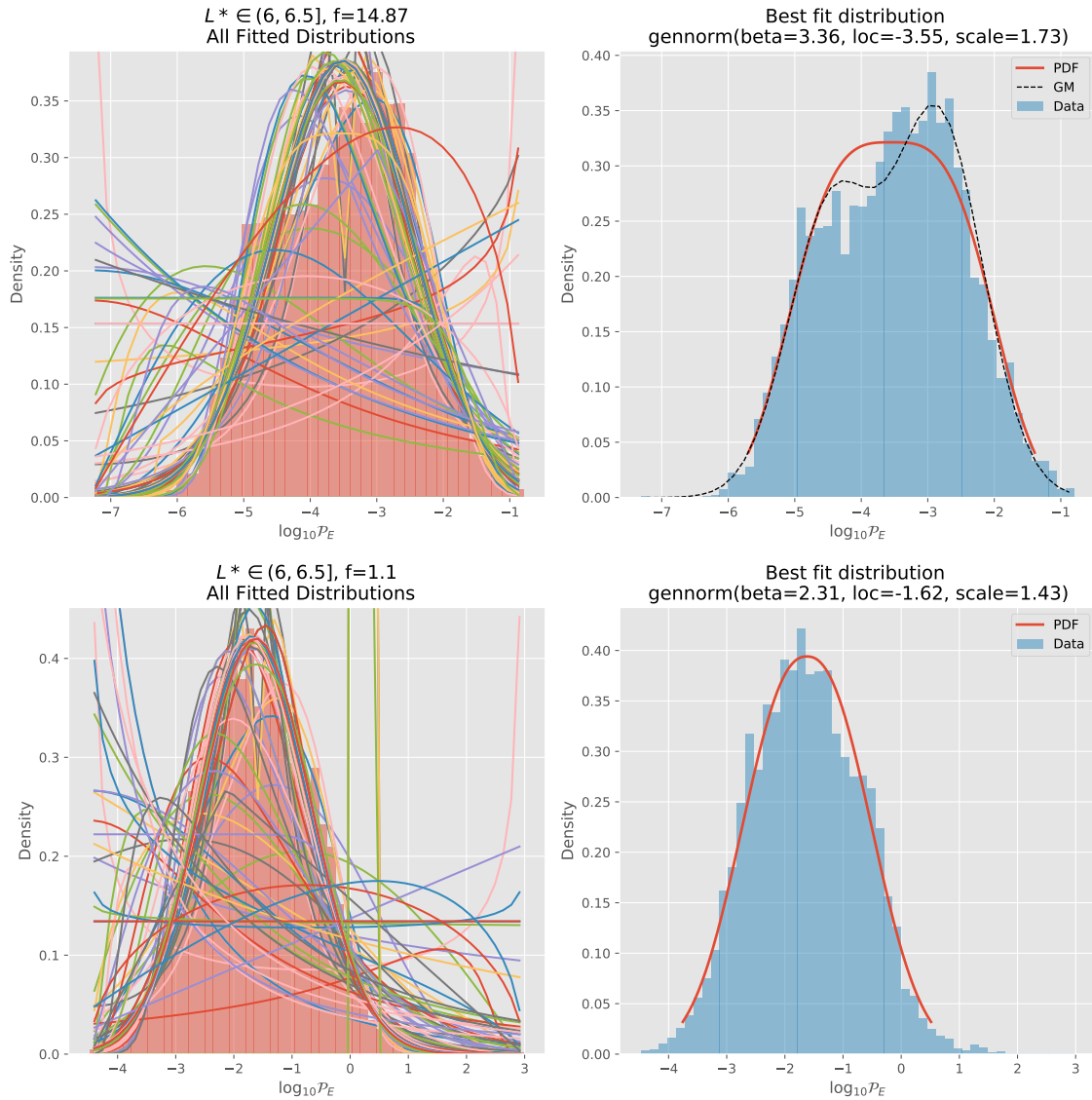


Figure 5.3: Demonstration of parametric fitting to 2 empirical  $\log_{10} \mathcal{P}_E(f, L^* \in (6, 6.5])$  distributions at (TOP)  $f = 14.87$  MHz and (BOTTOM)  $f = 1.1$  MHz. (LEFT) Fitting of 100 theoretical distributions to the empirical power histogram are illustrated, as is the (RIGHT) best fit distribution with associated parameters. For  $f = 14.87$  MHz, a two-component Gaussian Mixture (GM) fit is also shown.

CHAPTER 5. VARIABILITY OF SPACE-BASED ULF WAVE POWER SPECTRAL DENSITY

---

	(3.0, 3.5]	(3.5, 4.0]	(4.0, 4.5]	(4.5, 5.0]	(5.0, 5.5]	(5.5, 6.0]	(6.0, 6.5]
1.1	exponnorm	exponnorm	exponnorm	exponnorm	exponnorm	gengamma	gennorm
1.31	johnsonsu	johnsonsu	johnsonsu	exponnorm	exponnorm	powernorm	gennorm
1.56	johnsonsu	johnsonsu	erlang	alpha	exponnorm	gausshyper	exponweib
1.86	burr12	johnsonsu	invgauss	lognorm	nakagami	burr12	gennorm
2.21	exponnorm	johnsonsu	skewnorm	invgauss	powernorm	gengamma	gennorm
2.63	johnsonsu	johnsonsu	skewnorm	invgauss	johnsonsb	gengamma	gennorm
3.12	exponnorm	johnsonsu	skewnorm	powernorm	skewnorm	gengamma	gennorm
3.72	genlogistic	johnsonsu	skewnorm	nakagami	f	gennorm	gennorm
4.42	burr	johnsonsu	skewnorm	powernorm	powernorm	gennorm	exponpow
5.26	exponnorm	johnsonsu	skewnorm	beta	gennorm	gennorm	burr
6.25	exponnorm	johnsonsu	skewnorm	exponweib	gennorm	gennorm	mielke
7.43	exponnorm	exponnorm	skewnorm	gennorm	gennorm	gennorm	mielke
8.84	exponnorm	exponnorm	skewnorm	gennorm	gennorm	gennorm	mielke
10.51	skewnorm	johnsonsu	skewnorm	gennorm	gennorm	gennorm	burr
12.5	johnsonsu	johnsonsu	skewnorm	powernorm	gennorm	gennorm	burr
14.87	exponnorm	johnsonsu	invgamma	powernorm	gennorm	gennorm	exponpow

Figure 5.4: Best fit theoretical distributions to the empirical  $\log_{10} \mathcal{P}_E$  as a function of frequency (rows) and  $L^*$  bin (columns). Each distribution family is uniquely colour-coded for comparison, with label as in <https://docs.scipy.org/doc/scipy/reference/stats.html>.

### 5.2.2 Correlations of $\mathcal{P}$ in time, space and frequency

Naive application of the fitted distributions in a probabilistic model for  $D_{LL}$ , e.g. sampling  $\log \mathcal{P}$  randomly in an ensemble at the relevant frequencies over each  $L^*$  and converting to  $D_{LL}$ , fails to take into consideration any correlations in time, space, or frequency, however. For example, does  $\mathcal{P}$  increase with  $L^*$  at all times, or, are the median power structures with frequency at each  $L^*$  indicative of all times? We are only able to explore the frequency correlation of  $\mathcal{P}$ , since  $L^*$  correlations require simultaneous  $\mathcal{P}$  at multiple  $L^*$  which is impossible for a single spacecraft. Temporal correlation analysis is also difficult since it requires continuous measurements of ULF waver power at some fixed  $L^*$  and MLT, which is not the case for an orbiting spacecraft. Our data-set includes  $\mathcal{P}$  approximated by both Van Allen probes separately. They chase each other along the same orbit, and so it is possible to perform a limited temporal/spatial analysis using both spacecraft in tandem. This is beyond the scope of the current work but a possible approach to mitigating spacecraft limitations (see also Chapter 7 for other approaches to study temporal correlations of ULF wave power).

Pearson correlation coefficients across frequency and as a function of  $L^*$  are given in Figure 5.5. To calculate the correlation coefficients the  $\mathcal{P}$  data-set (including both spacecraft) was first sub-divided into the relevant  $L^*$  bins. Since each  $\mathcal{P}$  measurement is a spectrum across the same ULF wave frequencies, we can then calculate pair-wise correlations for all frequencies over the entire  $L^*$ -split data-sets. For panels in Figure 5.5, each cell shows the Pearson correlation between its relative row and column frequency. A coefficient value of 0 signifies no correlation whereas a value of 1 indicates perfect positive correlation. No frequencies exhibited negative correlation. Broadly speaking, the ULF wave power at different frequencies is more positively correlated for magnetic ULF wave power. We observe decaying correlation from low to high ULF frequencies for both components, but with magnitudes increasing with  $L^*$ . The gradients are smooth for  $\log_{10}\mathcal{P}_B$ , but for  $\log_{10}\mathcal{P}_E$  the highest 2 frequencies have correlations with the others which are notably stronger. It is clear that at low  $L^*$ , the power at different frequencies is only correlated with power at nearby frequencies. At high  $L^*$ , the power at different frequencies appears more coherent, as the correlations are much higher for frequencies that are far

apart in the spectra. This means that at low  $L^*$ , the power at each frequency is much more independent of power at other frequencies, and so we might expect spectra to show sharp peaks in power. At higher  $L^*$ , since the correlations between different frequencies are much higher, then we might expect smoother frequency spectra. If the power at one frequency increases, then it is quite likely that the power across a wide range of frequencies will increase, and vice versa. The absolute value of the power is different at different  $L^*$  however, typically with a peak near the auroral oval (e.g. Rae et al. [2012]), and the magnitudes of power at lower  $L^*$  for each frequency are likely to be similar even though correlations are smaller.

### 5.2.3 Variability of $\mathcal{P}$ with geomagnetic activity

Another important variability yet to consider is that due to geomagnetic activity. The correlation of ULF wave power with solar wind speed is well-known (Mathie and Mann [2001]), but ULF power is also controlled by other solar wind parameters (Bentley et al. [2018]), changes in the magnetospheric geometry (eg the magnetopause location Murphy et al. [2015]) and even long-term solar cycle variations (Hynönen et al. [2020]). Indeed, recent studies have shown systematic changes in ULF waver power distributions throughout each geomagnetic storm phase (Sandhu et al. [2021]). Since the Earth’s radiation belts are typically in a quiescent state of activity, much of this variability is masked in the tails of previous distributions discussed.

Classically, the geomagnetic index Kp has been used to separate power observations by activity and construct median-fitted power models which infer  $D_{LL}$  (Ali et al. [2015, 2016]; Brautigam and Albert [2000]; Brautigam et al. [2005]; Liu et al. [2016]; Ozeke et al. [2012, 2014]). Introduced by Bartels et al. [1939], discrete-valued Kp is measured every three hours as the weighted average of disturbances in the horizontal component of Earth’s magnetic field across a network of 13 ground magnetometer stations at mid-latitudes. Kp is practically useful for its rich data set dating back to 1932 and the possibility of nowcasting up to an hour ahead. Using the techniques previously discussed, we separate  $\mathcal{P}$  observations in Kp bins of width 1 and explore the  $\mathcal{P}$  distributions through theoretical fits under the assumption that  $\mathcal{P}$  remains MLT invariant.

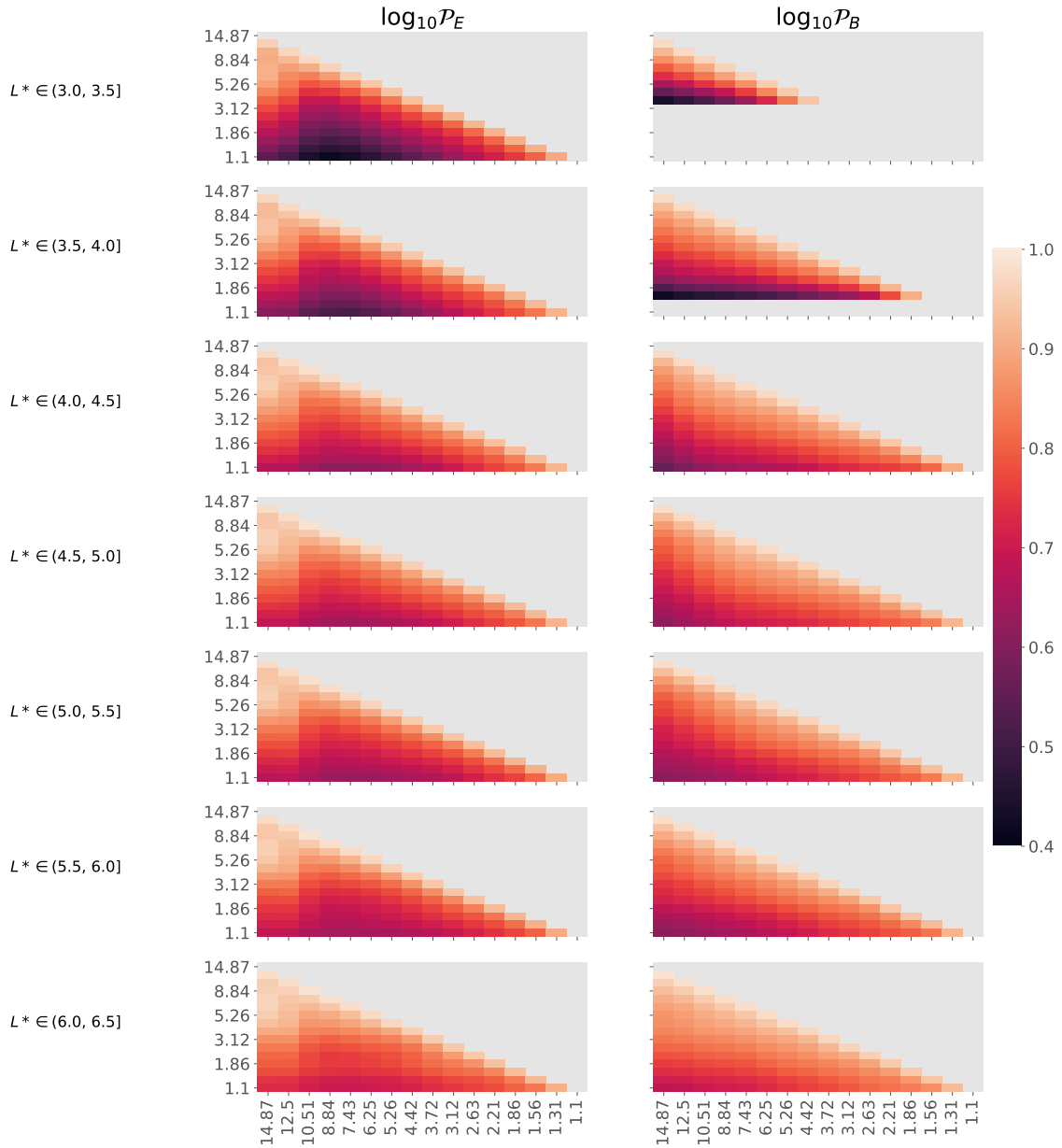


Figure 5.5: Pearson correlations of  $\log_{10} \mathcal{P}_E$  (left) and  $\log_{10} \mathcal{P}_B$  (right) across ULF wave frequencies, binned by  $L^*$  (rows). All colors for each field component are displayed on the same scale. Due to the expected spectral leakage for  $\log_{10} \mathcal{P}_B$  at the lower  $L^*$  bins, erroneous small correlations between low and high ULF frequencies have been omitted.

For a first glance, median  $\log_{10} \mathcal{P}(f, L^*, Kp)$  and corresponding IQRs are shown in Figures 5.6 and 5.7, respectively. The characteristic behaviour of median  $\mathcal{P}_E$  is present, exhibiting increases with both drift-shell and Kp at all frequencies. For  $\mathcal{P}_B$ , sensitivity to Kp decreases with frequency and power barely changes at all frequencies until  $Kp > 3$ . We find that the negative shift of high frequency distributions beyond  $L^* = 5$  seen in Figure 5.2 is attributed to more active periods. A result of note concerns the varying of median  $\mathcal{P}_E$  across frequency for any  $(L^*, Kp)$ . Ali et al. [2016]; Ozeke et al. [2012, 2014] found that median  $\mathcal{P}_E(L^*, Kp)$  was frequency invariant (when viewed in log-scaled space), which significantly simplifies the azimuthal electric field  $D_{LL}^E$  by removal of any energy dependence. In Figure 5.6 this is clearly the case only up to a certain frequency, before the medians begin a steady decline through multiple orders of magnitude. The shapes of median power-frequency curves, such as the location of peaks, also vary with Kp and are informative of the underlying physical processes driving activity. Constant fits on the assumption of invariance will therefore mask natural variability of the electric field wave power distribution. Conversely, the general shape of median magnetic power with frequency is more consistent. Flaws in median fitting become apparent when considering the IQRs in Figure 5.7, which frequently exceed an order of magnitude. Since frequency correlation is not perfect (see Figure 5.5), power invariance across frequency is unlikely to hold at all times. Whilst the IQR appears to increase smoothly with  $L^*$  at all ULF frequencies, the same cannot be said for Kp. Kp comprises of complex interactions between numerous physical processes, which are not necessarily the same at each Kp level. Comparison of variability across Kp may therefore be impractical. Since these processes are indicative of the natural state of the magnetosphere for different levels of magnetospheric driving, their respective variabilities should inform the expected degree of radial diffusion in our modelling.

Following previous analysis, we can fit the theoretical distributions to the Kp dependent distributions. As found previously, power distributions are a combination of log-normal and log-skewed with a variety of tail profiles.

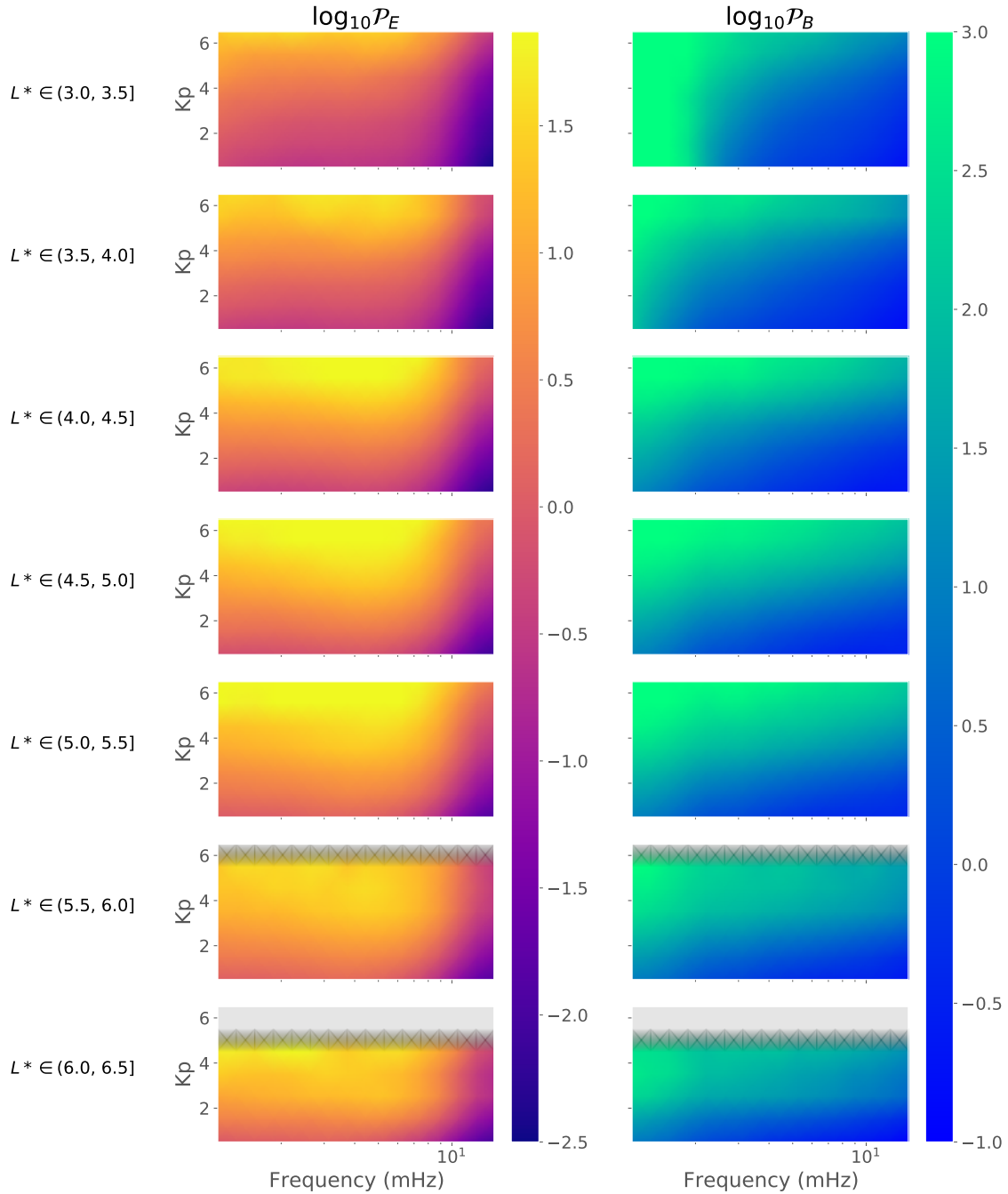


Figure 5.6: Median  $\log_{10} \mathcal{P}_E$  (left) and  $\log_{10} \mathcal{P}_B$  (right) as a function of  $L^*$ , frequency and geomagnetic index  $K_p$ . Values are nullified for bins containing less than 50 observations to avoid spurious statistics from a small sample size.

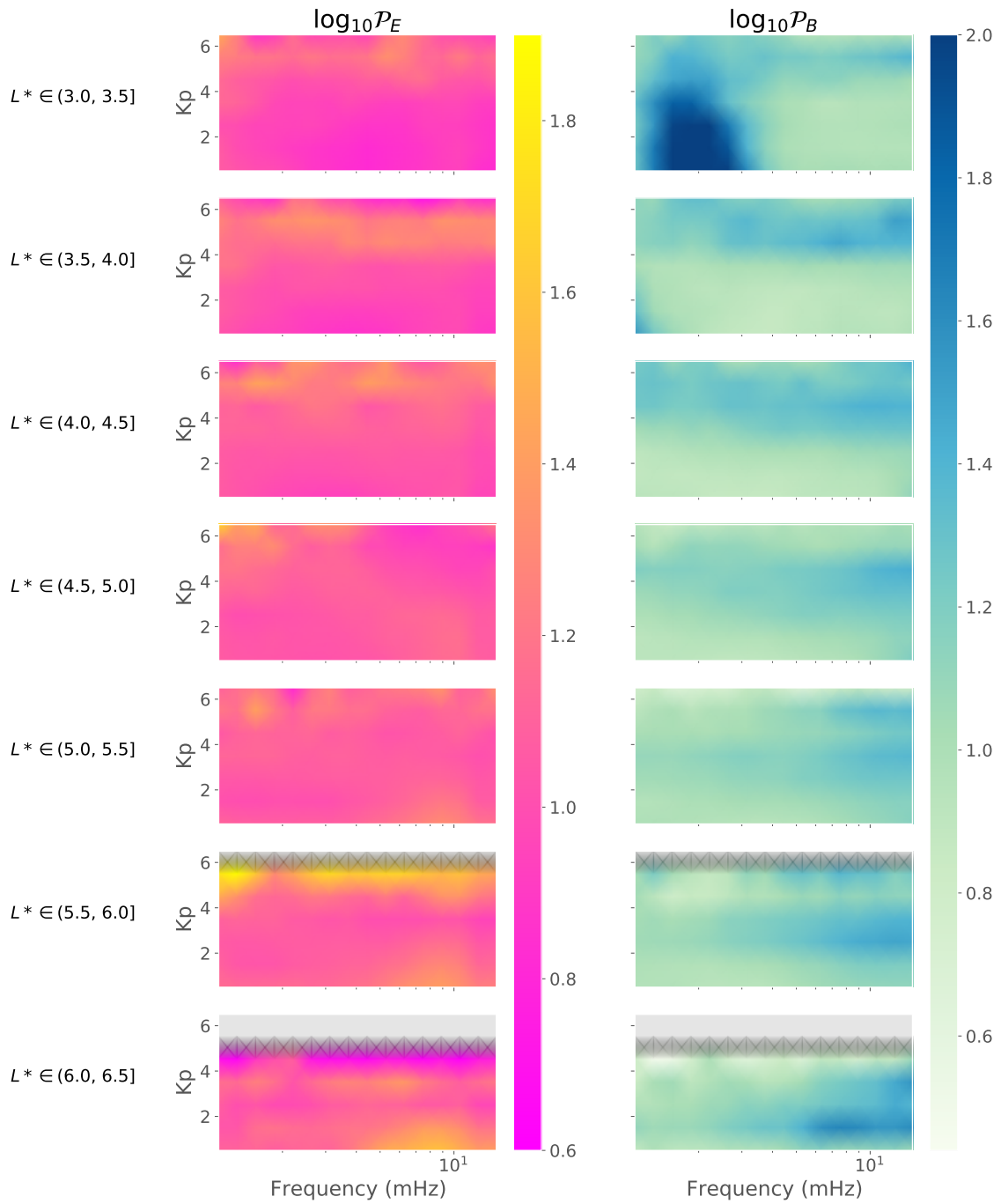


Figure 5.7:  $\log_{10} \mathcal{P}_E$  (left) and  $\log_{10} \mathcal{P}_B$  (right) IQRs as a function of  $L^*$ , frequency and geomagnetic index  $K_p$ . Values are nullified as in Figure 5.6. Recall that enhanced magnitudes in  $\log_{10} \mathcal{P}_B$  below  $L^* = 4$  are due to pollution of the background field in the power spectrum.

### 5.2.4 Drift-averaged ULF wave power

In reality, ULF wave power is not MLT invariant and  $D_{LL}$  must be constructed from the average wave power along a drift-shell. Since a global set of satellite observations are required across  $(L^*, MLT)$  at any given time to approximate  $D_{LL}$  *in situ*, drift-averaged radial diffusion coefficients must be inferred from the wave power probability distributions in regions sampled by spacecraft over an extended period. Classically, median ULF wave power at each frequency has been integrated (via a weighted sum) across MLT to inform drift-averaged power descriptions (Ali et al. [2015, 2016]). Mathematically speaking,

$$\mathcal{P}_{B,E}(L^*, f) = \sum_i w_i \langle \mathcal{P}_{B,E}(L^*, f, MLT_i) \rangle \quad (5.4)$$

where  $\langle \cdot \rangle$  denotes the median, MLT is discretized into  $i$  bins each with corresponding weight  $w_i$  and  $\sum_i w_i = 1$ . In the case of Ali et al. [2015, 2016], the weights were inversely proportional to the number of samples in each MLT bin to avoid undue influence by MLT with higher occurrences. This approach implicitly assumes that the median is well-aligned with a region of high probability density, and that the behaviour of ULF wave power can be characterized independently in a given bin regardless of any correlations across  $L^*$ , frequency or azimuth. We explore below the consequences of constructing medians and averages in different ways, focusing on the order in which averages or medians are obtained from the observations. Recent studies of the construction of diffusion coefficients (Watt et al. [2019]) and the outcome of numerical diffusion models (Thompson et al. [2020b]; Watt et al. [2021]) indicate that the use of averages, or the construction of averages, can significantly affect the response of numerical solutions to the diffusion equation.

We explore the suitability of the median to determine drift-averaged power descriptions in Figure 5.8. This Figure shows the  $\log_{10} \mathcal{P}_E(L^*, f, MLT)$  KDEs for  $f = 1.86$  mHz waves. We demonstrate results for a single frequency since all frequencies exhibited similar distribution variability across MLT sector. For illustration, we have chosen 4 MLT bins which are defined as follows: Dawn (3-9), Noon (9-15), Dusk (15-21) and Midnight (21-3). We have also separated geomagnetic activity into 3 categories: Quiet (Kp=0-3), Disturbed (Kp=3-5) and Storm (Kp=5-7). For all MLT there is substantial power variability spanning multiple orders of magnitude which increases with both  $L^*$  and activity level. Already

it is clear that extreme values are omitted by implementation of the median. For quiet and moderate times ( $Kp < 3$ ), at most  $L^*$  and MLT,  $\mathcal{P}_E$  exhibits log-symmetric-like distributions. The medians of each MLT distribution will therefore be offset to the right of the region with highest probability density, and often overestimate the wave power. During storms, when variability is at its maximum, all frequency distributions appear negatively skewed, meaning that often the median will underestimate storm time ULF wave power. In the highest  $L^*$  bin we also see pronounced differences in variability between each MLT sector, which may provide insight into the natural azimuthal variability of ULF waves. For example, ULF wave activity due to solar wind pressure variations tend to have higher power on the dayside (Claudepierre et al. [2009]; Huang et al. [2008]; Ukhorskiy et al. [2006]), whilst those driven by Kelvin-Helmholtz instabilities have higher power in dawn and dusk (Claudepierre et al. [2008]). These variabilities should therefore be included in any power representation (e.g. Bentley et al. [2020]).

As mentioned previously, we are restricted by the absence of cotemporal power approximations in azimuth to capture the variability in the drift-average for a given  $(L^*, f, Kp)$ . Assuming that power in each MLT sector is iid, however, allows us to recapture some of the variability through generation of synthetic data. Randomly sampling from the azimuthal distributions for a given  $(L^*, f, Kp)$  and integrating across each instance, we can create a probabilistic distribution of drift-averaged power for analysis. This will provide key insight on the differences between applying the median prior to drift-averaging using Equation 5.4 vs after from a set of drift-averaged power samples

$$\mathcal{P}_{B,E}(L^*, f) = \langle \sum_i w_i \mathcal{P}_{B,E}(L^*, f, MLT_i) \rangle \quad (5.5)$$

To generate synthetic data we fit *multivariate* KDEs across the frequency domain in each  $(L^*, MLT, Kp)$  bin. Let  $\mathbf{x}_1, \mathbf{x}_2, \dots, \mathbf{x}_n$  be a sample of d-variate random vectors drawn from a common distribution described by the density function  $f$ . Then, the multivariate KDE is defined as

$$\hat{f}_{\mathbf{H}}(\mathbf{x}) = \frac{1}{n} \sum_{i=1}^n K_{\mathbf{H}}(\mathbf{x} - \mathbf{x}_i) \quad (5.6)$$

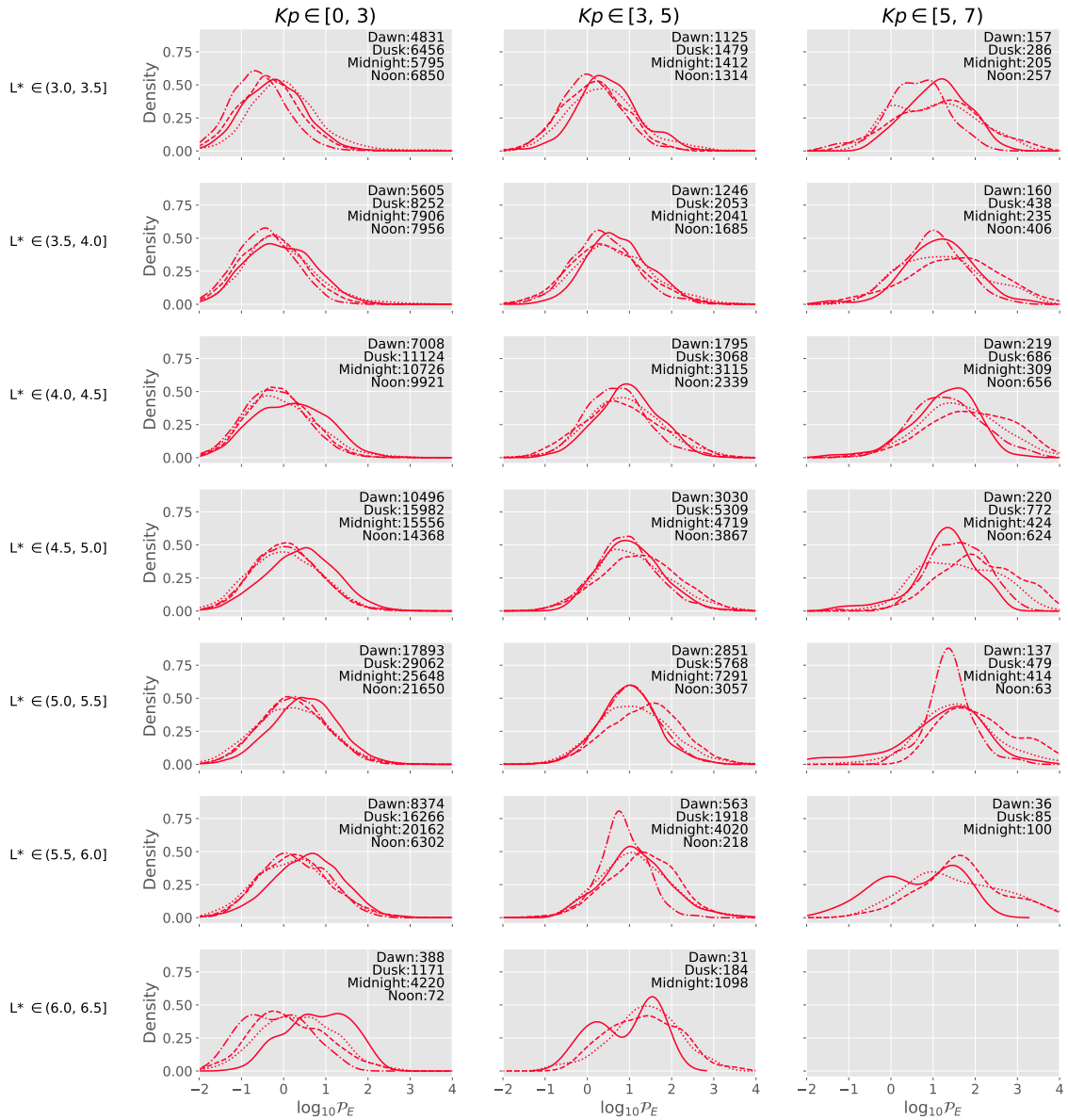


Figure 5.8: KDEs of the  $\log_{10} \mathcal{P}_E(L^*, f, MLT)$  probability density functions for 1.86 mHz ULF waves, as a function of MLT sector (Dawn (3-9, solid), Noon (9-15, dash-dot), Dusk (15-21, dashed) and Midnight (21-3, dotted)) and geomagnetic activity level (Quiet ( $K_p=0-3$ ), Disturbed ( $K_p=3-5$ ) and Storm ( $K_p=5-7$ )). Counts for each MLT sector are also given in the top right of each plot.

Here,  $\mathbf{x} = (\mathbf{x}_1, \mathbf{x}_2, \dots, \mathbf{x}_d)^T$ ,  $\mathbf{x}_i = (\mathbf{x}_{i1}, \mathbf{x}_{i2}, \dots, \mathbf{x}_{id})^T$ ,  $i = 1, 2, \dots, n$  are  $d$ -vectors,  $\mathbf{H}$  is the symmetric, positive-definite bandwidth matrix, and  $K_{\mathbf{H}}(\mathbf{x}) = |\mathbf{H}|^{-1/2}K(\mathbf{H}^{-1/2}\mathbf{x})$  is the kernel function. As for the univariate case we employ the Gaussian kernel  $K_{\mathbf{H}}(\mathbf{x}) = (2\pi)^{-d/2}|\mathbf{H}|^{-1/2}e^{-\frac{1}{2}\mathbf{x}^T\mathbf{H}^{-1}\mathbf{x}}$ . Here we have *bandwidth matrix*  $\mathbf{H}$  rather than a single value, which plays the role of a kernel *covariance matrix* across data dimensions. Frequency correlations are therefore encoded with an intuitive choice of  $\mathbf{H}$ . The choice of  $\mathbf{H}$  is the single most important choice for affecting the accuracy of the multivariate KDE, since it determines the amount of smoothing and orientation of the kernel across multiple dimensions (Wand and Jones [1994]). There are three main classes of parameterization for  $\mathbf{H}$  which we list in increasing order of complexity:

- *S-class*: The class of positive scalars multiplied by the identity matrix
- *D-class*: Diagonal matrices with positive values on the diagonal
- *F-class*: Symmetric positive-definite matrices (or covariance matrix), which allows for correlations between variables

An illustration of each class for the case of a bivariate distribution is shown in Figure 5.9. We employ an F-class parameterization on our  $(L^*, MLL, Kp)$  segmented data, where diagonal elements of  $\mathbf{H}$  are determined by Scott’s Factor (Scott [1992]) in 16 dimensions ( $n^{-1/d+4}$ ,  $d = 16$ , since we have power approximated for 16 discrete frequencies) with  $\sqrt{\mathbf{H}_{ii}} = n^{-1/20}\sigma_i$ , where  $\sigma_i$  is the standard deviation of the  $i$ -th variable. This is a reasonable assumption since many of our  $\log_{10} \mathcal{P}$  distributions appear similar to a Gaussian. Off-diagonal elements are as in the frequency covariance matrix. We acknowledge that there are other methods to construct  $\mathbf{H}$ , such as other *rule of thumb* alternatives to Scott’s Rule (e.g. Silverman [2018]), optimizing over multiple bandwidth values which minimise some metric, or through advanced empirical methods which circumvent any subjective bandwidth choices imposed by the user (Bernacchia and Pigolotti [2011]; O’Brien et al. [2016]). Due to the large number of dimensions and samples in each of our data bins, however, the second case becomes computationally expensive in the fitting of multiple KDEs for multiple bandwidth choices, whilst the third is subject to the *curse of dimensionality* (see Section 5 of O’Brien et al. [2016]).

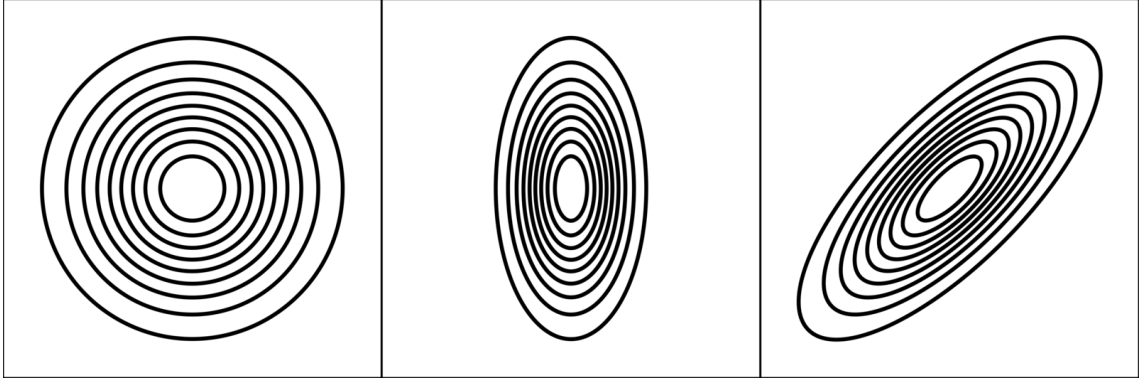


Figure 5.9: Comparison of kernels for the three main bandwidth parameterization classes. (LEFT) Positive scalar multiple times identity matrix, or S-class. (CENTRE) Diagonal matrix, or D-class. (RIGHT) Symmetric positive definite matrix, or F-class. Taken from [https://en.wikipedia.org/wiki/Multivariate\\_kernel\\_density\\_estimation](https://en.wikipedia.org/wiki/Multivariate_kernel_density_estimation).

Following the multivariate fits to our segmented data, we resample 1000 random *power curves* with encoded frequency correlations across all MLT sectors and drift shells. Provided power distributions on a particular drift shell are independent in each MLT sector as previously assumed, our synthetic samples represent a set of possible global, cotemporal ULF wave power observations. For each 'time instance' we calculate the drift-averaged power for each  $(L^*, f)$  as an *inverted weighted sum* as in Ali et al. [2015, 2016] so as to give each MLT sector equal weighting

$$\mathcal{P}_{\text{drift-averaged}}(L^*, f) = \sum_{i=1}^4 w_i \mathcal{P}(L^*, f, MLT_i) \quad (5.7)$$

$$w_i = \frac{1/[N_{MLT_i}/N_{\forall MLT}]}{\sum_i 1/[N_{MLT_i}/N_{\forall MLT}]} \quad (5.8)$$

where  $N$  is the number of multivariate samples considered for each  $i$ 'th MLT sector ( $N_{MLT_i}$ ) and across all MLT ( $N_{\forall MLT}$ ) on a given drift shell.

We can now discern the differences in distribution between *in situ* (synthetically speaking) drift-averaged wave power versus drift-averaged median wave power. We compare distributions to the following:

- *W-DAM* - Weighted drift-average of the median ULF wave power, as in Ali et al. [2015, 2016]

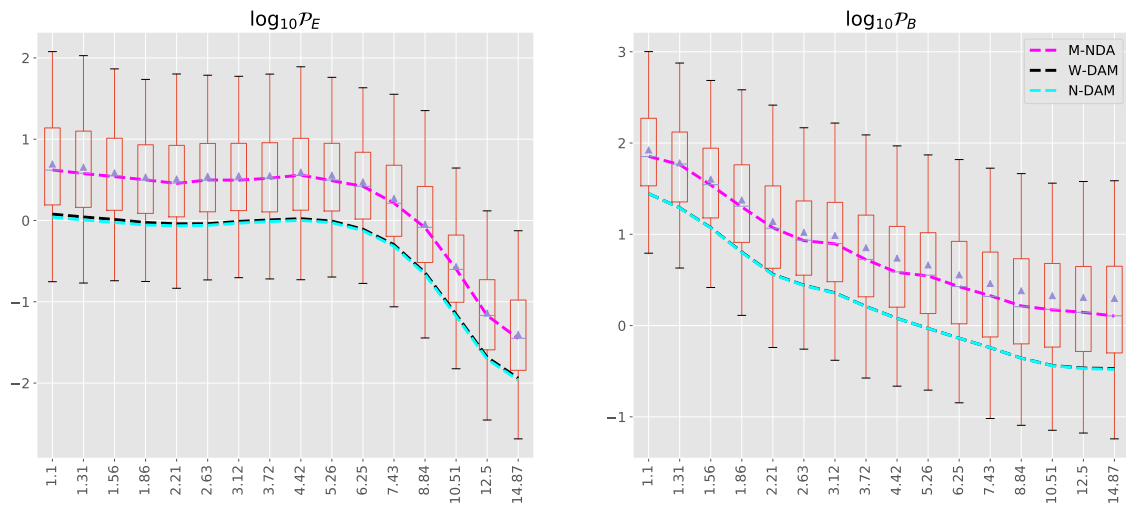


Figure 5.10: Boxplots for the cotemporally drift-averaged  $\log_{10} \mathcal{P}_E(f)$  (left) and  $\log_{10} \mathcal{P}_B(f)$  (right) provided by the synthetic data at  $L^* \in (4, 4.5]$  and  $Kp \in [0, 3)$ . Boxes enclose the IQR and the distribution means and medians are given by purple triangles and bars, respectively. Whiskers extend from the edges of the box by  $1.5IQR$  ( $IQR = Q3 - Q1$ ) to indicate the range of the data, with any remaining points outside the whiskers considered outliers and omitted. Overplotted are the weighted drift averages of the median ULF wave power (W-DAM, black), mean drift-average of the median ULF wave power (N-DAM, cyan), and the median of the mean drift-averaged synthetic data (M-NDA, magenta). Note the the y-scales are unique to each plot for readability.

- *N-DAM* - Naive drift-average (arithmetic mean) of the median ULF wave power
- *M-NDA* - Median of the naive drift-averaged (arithmetic mean) synthetic data

Differences between the drift-averaged power distributions and the M-NDA, W-DAM and N-DAM methods are very similar for all  $L^*$  and activity levels. In Figure 5.10 we therefore focus show only the solutions for  $L^* \in (4, 4.5]$  and  $Kp \in [0, 3)$ . We observe a significant loss of information by omitting the cotemporal azimuthal variability of wave power. Employing *W-DAM* as in previous constructions of  $D_{LL}$  underestimates the power in approximately 75% of our synthetic distributions, since *W-DAM* magnitudes are aligned near the lower quartile. There is a clear separation of average wave power depending on when drift-averages are taken, in many cases by almost an order of magnitude. Both approaches show similar variation across frequency, however. All approaches to estimate typical values of drift-averaged power fit in the range of the synthetic distributions, but these have considerable variability exceeding two orders of magnitude in all cases.

### 5.3 Chapter Summary

We demonstrate methods to construct probabilistic models of ULF wave power for aid in drift-averaging the power required to construct  $D_{LL}$  from multiple *in-situ* observations at different MLT. These methods are compared with the current, more naive method, of performing an average, or weighted average of the median power in each MLT sector in order to construct a drift-averaged power spectra. We show that current methods of combining medians significantly underestimate the power compared to constructing a probabilistic model. Our result rests on the assumption that the ULF power in one MLT sector (noon, dusk, midnight or dawn) is independent of the power in another sector. This assumption needs to be thoroughly tested, but can only be done so via contemporaneous observations from multiple satellites.

However, by nature using spacecraft data alone is restricted when constructing coherent radial diffusion coefficients. It is clear from our results that a global (in azimuth) set of cotemporal observations is necessary to construct drift-averaged power distributions which

infer  $D_{LL}$ . While we can employ synthetic data to mitigate limitations of point-based spacecraft observations, resulting insights are not definitive as we must assume some form of power structure in azimuth, in our case that power in each MLT sector is independent of others. This may not be the case and can also only be discovered through investigation of cotemporal measurements in azimuth. We also need similar measurements radially to determine the correlated (if at all) structure of radial diffusion across  $L^*$ .

Therefore, we must move beyond spacecraft measured ULF wave power distributions to quantify uncertainties in  $D_{LL}$ . Whilst we have touched briefly upon why throughout this Chapter, we summarise below:

- **Point-based power approximations:** Due to the limited number of spacecraft available in the vast magnetosphere at any one time, *in situ* wave power approximations have narrow spatial scope. Since true  $D_{LL}$  require the drift-averaged power for a set of cotemporal measurements globally across all  $L^*$  and MLT, we can only infer  $D_{LL}$  from binned power distributions (as considered in this Chapter). It is therefore impossible to get any information about coherence of power across both  $L^*$  and MLT, and any probabilistic drift-averaged power approximations must be independently, randomly sampled across these domains. Resulting power descriptions therefore fail to capture much of the natural structure and variability across the magnetosphere.
- **$\mathcal{P}$  observation window:** Due to the great speed of spacecraft travelling through the magnetosphere, especially during perigee passes, wave power approximations are limited to a short window of samples, else they risk conflating power from multiple regions of interest to a single measurement. Due to the *Heisenberg uncertainty principle* which presents a tradeoff between time and frequency in spectral analysis, the frequency resolution with which to explore ULF wave power on board spacecraft is restricted.
- **Mission lifetime:** All spacecraft missions are finite in time and while they provide us a large number of observations these are spread, in many cases unequally, across drift-shells and MLT. In fact, a number of  $(L^*, MLT)$  regions contain a negligible

number of observations for statistical analysis. Extrapolating any power model beyond the mission lifetime will therefore be difficult in such a limited, imbalanced distribution of the data.

A partial solution to the limitations of spacecraft observations is the use of ground-based instruments to remote sense the magnetosphere. Relativistic electrons have shown to be energized by a drift-resonance interaction with standing fundamental mode field-aligned guided Alfvén waves (Degeling et al. [2007]; Elkington et al. [1999, 2003]), and ground observations have unveiled a correlation between ULF wave power at frequencies suitable for radial diffusion (Jacobs et al. [1964]) and relativistic electrons (Mathie and Mann [2001]; O’Brien et al. [2001]; Rostoker et al. [1998]). This subclass of resonant ULF waves led to an analytic mapping from the ground magnetic field to the equatorial electric field (Ozeke et al. [2009]), for which the equatorial electric field amplitude controls the maximum amount of energy that the electrons can gain. Using this mapping, a proportionality between ground magnetic ULF wave power and azimuthal electric field wave power has been suggested (Ozeke et al. [2012]). Since ground-based magnetometers are readily available with a global extent across multiple  $L^*$  and MLT, using this mapping we can possibly overcome the limitations described above and gain better probabilistic descriptions for  $D_{LL}^E$ . The mapping, however, is subject to its own uncertainties which we explore fully in the next Chapter.

## CHAPTER 6

# MAPPING ULF WAVE POWER FROM THE GROUND INTO SPACE

When reviewing our current theoretical understanding of  $D_{LL}$  in Chapter 2 we saw that a majority of modern  $D_{LL}$  parameterizations adopt the Fei et al. [2006] formalism, which is to separate  $D_{LL}$  into magnetic and electric components,  $D_{LL}^B$  and  $D_{LL}^E$ , assumed to be uncorrelated. These are then typically modelled by two independent sets of ULF wave power spectral density ( $\mathcal{P}$ ) observations, those from space-based compressional magnetic field perturbations for  $D_{LL}^B$  and either space-based azimuthal electric field or mapped ground-based poloidal  $B$  perturbations for  $D_{LL}^E$ . In Chapter 4, we explored the importance of sound descriptions of the magnetic field to assign  $\mathcal{P}$  observations to appropriate  $L^*$  and infer  $D_{LL}$ . Re-binning space-based  $\mathcal{P}$  by  $L^*$  approximated by more sophisticated magnetic field models is relatively straightforward. Including realistic  $L^*$  from the ground and doing the right mapping of ground-based magnetic power to equatorial azimuthal electric field power, however, is much harder. We explore the mapping in this Chapter.

Ground observations are a desirable alternative to satellite observations when constructing  $D_{LL}^E$  due to being readily available and having a global extent covering multiple  $L^*$  and MLT (e.g. Gjerloev [2012]; Mann et al. [2008]). With them, we can explore global images of ULF wave power to discern the temporal and spatial variability of  $D_{LL}^E$ , as

well as *in situ* drift averaged wave power, which is not possible with point-based satellite measurements. The ability to use ground observations for remote sensing  $D_{LL}^E$  requires a mapping of ground magnetic  $\mathcal{P}$  to azimuthal electric  $\mathcal{P}$ , assuming such a mapping is physically viable. Note that for completeness, there is an argument that magnetic and electric correlations should be retained (Lejosne [2019]), but this is beyond the scope of this thesis.

To have such a mapping between ground magnetic  $\mathcal{P}$  and space electric  $\mathcal{P}$  rests on understanding the mechanisms which allow ULF waves energy to propagate along the magnetic field and be observed at the ground. For the only mapping that exists (Ozeke et al. [2012]) ULF wave energy is assumed to enter the system via field line resonance (FLR). In other words, the ULF wave propagating through the magnetosphere has a frequency which matches that of the local magnetic field line eigenfrequency to allow irreversible energy exchange. The transmission of the transferred ULF energy can then be analytically derived as it travels from the equatorial electric field ( $E^{eq}$ ) through to the ground magnetic field ( $b^g$ ) via the ionosphere (Ozeke et al. [2009]). This relationship between  $b^g$  and  $E^{eq}$  can subsequently be used to scale ground magnetic  $\mathcal{P}$  to equatorial electric field  $\mathcal{P}$  for use in  $D_{LL}^E$  (Ozeke et al. [2012]). The analytic mapping is useful in its simplicity and applicability but is only possible through a variety of simplifying assumptions, one of the main ones being a dipole magnetic field. Since assumptions imply uncertainty, it is also important to investigate performance of the mapping when these assumptions are relaxed.

In this Chapter, we explore the relationship between  $b^g$  and  $E^{eq}$  to enable mapping of ground magnetic  $\mathcal{P}$  for use in  $D_{LL}^E$ . We begin by reviewing existing magnetohydrodynamic (MHD) wave and FLR theory, and describe how FLRs are observed in latitudinal arrays of ground magnetometers. Following this we examine the analytic Ozeke et al. [2009] mapping and identify its uncertainties. We investigate the global characteristics of FLRs by designing a novel automatic FLR detection algorithm using sophisticated signal and image processing. Finally, we account for some of the variability in a probabilistic mapping and investigate how the resulting electric  $\mathcal{P}$  compares to probability distributions of space-based electric  $\mathcal{P}$ . Since the mapping is used to scale ground  $\mathcal{P}$  values, we hope

to gain further statistical insight into the distribution of azimuthal electric field  $\mathcal{P}$  and subsequently  $D_{LL}$ , which is vital for characterizing uncertainty in probabilistic modelling of radial diffusion (see Thompson et al. [2020b]).

## 6.1 MHD Waves

In the absence of all dissipative processes (finite viscosity, electrical resistivity and thermal conductivity), the *ideal* MHD equations are given by

$$\text{Mass continuity} \quad \frac{\partial \rho}{\partial t} + \nabla \cdot (\rho \mathbf{v}) = 0 \quad (6.1)$$

$$\text{Energy} \quad \frac{D}{Dt} \left( \frac{P}{\rho^\gamma} \right) = 0 \quad (6.2)$$

$$\text{Euler's equation} \quad \rho \frac{D\mathbf{v}}{Dt} = -\nabla P + \frac{1}{\mu_0} \mathbf{B} \times (\nabla \times \mathbf{B}) \quad (6.3)$$

$$\text{Induction} \quad \frac{\partial \mathbf{B}}{\partial t} = \nabla \times (\mathbf{v} \times \mathbf{B}) \quad (6.4)$$

$$\nabla \cdot \mathbf{B} = 0 \quad (6.5)$$

where  $\rho, \mathbf{v}, P$  are the plasma mass density, centre-of-mass velocity and centre-of-mass pressure, respectively,  $\mathbf{B}$  is the magnetic field vector,  $\mu_0$  is the permeability of free space and  $\gamma$  is the ratio of specific heats  $C_P/C_v$  (normally taken as 5/3). In the above,  $D/Dt = \partial_t + \mathbf{v} \cdot \nabla$  denotes the material derivative.

To examine the numerous types of pure MHD waves we apply linear perturbation theory. First, we linearise all fluid quantities by separation into 2 components - some equilibrium, steady-state component (herein called the basic state variable) plus a perturbation. Basic assumptions are that the basic state variables satisfy the governing equations in the absence of the perturbations, and  $|\text{perturbations}| \ll |\text{basic state}|$  so that nonlinear products of perturbation variables can be neglected. Here we assume a stationary plasma,

i.e. basic state velocity is 0. The full set of linearised variables are

$$\rho = \rho_0 + \delta\rho \quad (6.6)$$

$$P = P_0 + \delta P \quad (6.7)$$

$$\mathbf{B} = \mathbf{B}_0 + \delta\mathbf{B} \quad (6.8)$$

$$\mathbf{v} = 0 + \delta\mathbf{v} \quad (6.9)$$

where we assume that  $\mathbf{B}_0$  is uniform. When substituted into the ideal MHD equations, give the linearized ideal MHD equations

$$\frac{\partial\delta\rho}{\partial t} = -\rho_0\nabla\cdot\delta\mathbf{v} \quad (6.10)$$

$$\delta P = \frac{\gamma P_0}{\rho_0}\delta\rho \quad (6.11)$$

$$\rho_0\frac{\partial\delta\mathbf{v}}{\partial t} = -\nabla\delta P + \frac{1}{\mu_0}(\nabla\times\delta\mathbf{B})\times\mathbf{B}_0 \quad (6.12)$$

$$\frac{\partial\delta\mathbf{B}}{\partial t} = \nabla\times(\delta\mathbf{v}\times\mathbf{B}_0) \quad (6.13)$$

$$(6.14)$$

We assume that all perturbations are plane waves of the form  $\delta x = \hat{\delta}x \exp(i\mathbf{k}\cdot\mathbf{x} - i\omega t)$  with frequency  $\omega$  and wavenumber  $\mathbf{k}$ . To explore properties of the waves we transform the linearized MHD equations into the Fourier domain via the following relationships

$$\nabla_{\mathbf{x}} \rightarrow i\mathbf{k}, \quad \partial_t \rightarrow -i\omega \quad (6.15)$$

so that we obtain

$$\omega\delta\rho = \rho_0\mathbf{k}\cdot\delta\mathbf{v} \quad (6.16)$$

$$-\omega\rho_0\delta\mathbf{v} = -\frac{\gamma P_0}{\rho_0}\delta\rho\mathbf{k} + \frac{1}{\mu_0}(\mathbf{k}\times\delta\mathbf{B})\times\mathbf{B}_0 \quad (6.17)$$

$$-\omega\delta\mathbf{B} = \mathbf{k}\times(\delta\mathbf{v}\times\mathbf{B}_0) \quad (6.18)$$

$$\delta P = \frac{\gamma P_0}{\rho_0}\delta\rho \quad (6.19)$$

where  $\delta P$  from the energy equation has been substituted accordingly. Now, all variables correspond to the Fourier domain, ie  $\rho(\mathbf{x}, t) \rightarrow \rho(\omega, \mathbf{k})$ . If we choose the background magnetic field to be in the  $\hat{z}$  direction ( $\mathbf{B}_0 = B_0\hat{z}$ ), and the wavenumber to be of the form

$\mathbf{k} = k_{\perp}\hat{x} + k_{\parallel}\hat{z}$  without loss of generality, substituting into the above we obtain that

$$\delta\rho = \frac{\rho_0}{\omega}(k_{\perp}\delta v_x + k_{\parallel}\delta v_z) \quad (6.20)$$

$$\delta\mathbf{B} = -\omega^{-1}\mathbf{k} \times [\delta v_y B_0, -\delta v_x B_0, 0] \quad (6.21)$$

$$= -\omega^{-1}[k_{\parallel}\delta v_x B_0, k_{\parallel}\delta v_y B_0, -k_{\perp}\delta v_x B_0] \quad (6.22)$$

and the Fourier linearized Euler equation yields

$$\begin{bmatrix} \delta v_x \\ \delta v_y \\ \delta v_z \end{bmatrix} = \frac{c_s^2}{\omega^2}(k_{\perp}\delta v_x + k_{\parallel}\delta v_z) \begin{bmatrix} k_{\perp} \\ 0 \\ k_{\parallel} \end{bmatrix} + \frac{v_A^2}{\omega^2} \begin{bmatrix} \delta v_x(k_{\perp}^2 + k_{\parallel}^2) \\ \delta v_y k_{\parallel}^2 \\ 0 \end{bmatrix} \quad (6.23)$$

where  $v_A^2 = B_0^2/\mu_0\rho_0$  is the Alfvén speed, and  $c_s^2 = \frac{\gamma P_0}{\rho_0}$  is the sound speed. We can rearrange this equation into an eigenvalue problem  $\mathbf{A} \cdot \delta\mathbf{v} = 0$

$$\mathbf{A} \cdot \delta\mathbf{v} = \begin{bmatrix} \omega^2 - c_s^2 k_{\perp}^2 - v_A^2(k_{\perp}^2 + k_{\parallel}^2) & 0 & -c_s^2 k_{\perp} k_{\parallel} \\ 0 & \omega^2 - v_A^2 k_{\parallel}^2 & 0 \\ -c_s^2 k_{\perp} k_{\parallel} & 0 & \omega^2 - c_s^2 k_{\parallel}^2 \end{bmatrix} \begin{bmatrix} \delta v_x \\ \delta v_y \\ \delta v_z \end{bmatrix} = 0 \quad (6.24)$$

The solution to this eigenvalue problem is precisely when the determinant of  $\mathbf{A}$  is 0

$$\det(\mathbf{A}) = (\omega^2 - v_A^2 k_{\perp}^2)[(\omega^2 - v_A^2 k_{\parallel}^2 - (c_s^2 + v_A^2)k_{\perp}^2)(\omega^2 - c_s^2 k_{\parallel}^2) - c_s^4 k_{\perp}^2 k_{\parallel}^2] = 0 \quad (6.25)$$

### 6.1.1 Alfvén Waves

The first solution to Equation 6.25 is the Alfvén wave,

$$\omega^2 = v_A^2 k_{\perp}^2 \iff \omega = \pm \frac{\mathbf{k} \cdot \mathbf{B}_0}{\sqrt{\mu_0 \rho_0}} \quad (6.26)$$

These waves propagate with group velocity only in the direction of the background magnetic field, at the Alfvén speed. Casting back to Equation 6.24, the only velocity perturbation relevant in this case is  $\delta v_y$  and so velocity perturbations are transverse to the direction of propagation. The waves are therefore incompressible ( $\nabla \cdot \delta\mathbf{v} = i\mathbf{k} \cdot \delta\mathbf{v} = 0$ ). Applying this knowledge to the velocity perturbations in Equation 6.22, it follows that velocity perturbations are parallel to  $\delta v_y$  (and therefore also transverse to  $\mathbf{B}_0$ ). Alfvén waves are therefore kindred to *oscillating waves on a string*, which travel along magnetic field lines and drive perpendicular magnetic field oscillations.

### 6.1.2 Magnetosonic waves

The other two solutions of Equation 6.25, once rearranged, occur when

$$\omega^4 - c_f^2 k^2 \omega^2 + v_A^2 c_s^2 k^4 \cos^2 \theta = 0 \quad (6.27)$$

where  $c_f^2 = (c_s^2 + v_A^2)$ ,  $k^2 = k_{\parallel}^2 + k_{\perp}^2$  and  $\theta$  represents the angle between the wavevector  $\mathbf{k}$  and the background field direction  $\hat{z}$  such that  $k_{\parallel} = k \cos \theta$ .

If we divide Equation 6.27 through by  $k^4$  and treat as a quadratic in  $\omega^2/k^2$  we obtain the solution

$$\omega^2 = \frac{k^2}{2} c_f^2 \pm \frac{1}{2} \sqrt{c_f^4 - 4c_s^2 v_A^2 \cos^2 \theta} \quad (6.28)$$

The positive root corresponds to the fast mode and the negative root the slow mode. Both waves are compressible ( $\mathbf{k} \cdot \delta \mathbf{B} \neq 0$ ). Propagation speeds and directions can be determined by values of the angle  $\theta$ . If  $\theta = \pi/2$  (perpendicular to the magnetic field), there is no slow mode propagation. Conversely, the fast mode has the relation  $\omega^2 = (k^2/2)c_f^2$ , which is the maximal fast mode speed ( $c_f$ ) and propagates perpendicular to the background field. If  $\theta = 0$  (parallel to the background field) the two modes are given by

$$(Fast) \quad \omega^2 = k^2 v_A^2 \quad (6.29)$$

$$(Slow) \quad \omega^2 = k^2 c_s^2 \quad (6.30)$$

where the fast mode has the greater speed.

## 6.2 Field line resonances (FLRs) in a simple magnetic field box model

In the earlier derivation of MHD wave modes we considered a uniform plasma with infinite extent. In a uniform plasma we were able to decouple the Alfvén mode from the fast modes, with a phase speed (and frequency), dependent on the uniform background magnetic field and plasma density, that is constant and exists for any wave vector  $\mathbf{k}$ . In reality the magnetosphere is non-uniform. The variation of the plasma density, field line length and magnetic field strength all contribute to Alfvén frequencies varying with position (e.g. see

Wright et al. [1996]), known as the Alfvén continuum. In a non-uniform plasma fast mode energy can now couple to Alfvénic modes, via a mechanism known as a *field line resonance* (Southwood [1974]; Chen and Hasegawa [1974]).

For demonstration, consider another restriction on the ideal MHD equations of a *cold plasma approximation*, where plasma pressure gradients are negligible ( $\nabla p = 0$ ). Suppose we are interested in the plasma displacement  $\boldsymbol{\xi}$  ( $\partial_t \boldsymbol{\xi} = \mathbf{v}$ ), then the necessary linearized MHD equations are

$$\rho_0 \frac{\partial \delta \mathbf{v}}{\partial t} = \frac{1}{\mu_0} (\nabla \times \delta \mathbf{B}) \times \mathbf{B}_0 \quad (6.31)$$

$$\delta \mathbf{B} = \nabla \times (\boldsymbol{\xi} \times \mathbf{B}_0) \quad (6.32)$$

where the background plasma has  $\mathbf{j}_0 = \nabla \times \mathbf{B}_0 = 0$ . Expanding Equation 6.32 yields

$$\begin{bmatrix} \delta B_x \\ \delta B_y \\ \delta B_z \end{bmatrix} = B_0 \begin{bmatrix} \partial_z \xi_x \\ \partial_z \xi_y \\ -\partial_x \xi_x - \partial_y \xi_y \end{bmatrix} \quad (6.33)$$

which, when substituted into Equation 6.31 gives the set of equations for the displacement vector  $\boldsymbol{\xi}$

$$\frac{1}{v_A^2} \frac{\partial^2 \xi_x}{\partial t^2} - \frac{\partial^2 \xi_x}{\partial z^2} = -\frac{1}{B_0} \frac{\partial \delta B_z}{\partial x} \quad (6.34)$$

$$\frac{1}{v_A^2} \frac{\partial^2 \xi_y}{\partial t^2} - \frac{\partial^2 \xi_y}{\partial z^2} = -\frac{1}{B_0} \frac{\partial \delta B_z}{\partial y} \quad (6.35)$$

$$\delta B_z = -B_0 \left( \frac{\partial \xi_x}{\partial x} + \frac{\partial \xi_y}{\partial y} \right) \quad (6.36)$$

We observe that Alfvén waves create transverse (wrt the background field) displacements  $\xi_x, \xi_y$  which are driven by spatial gradients in  $b_z = \delta B_z$ .

We consider a plasma filled box as in Radoski [1971] and Southwood [1974], in a Cartesian geometry with uniform background magnetic field  $\mathbf{B}_0 = B_0 \hat{z}$  and radially varying density  $\rho = \rho(x)$  ( $\hat{x}$  denotes the radial coordinate in the box model). The boundaries in  $\hat{z}$  represent the ionospheres and are assumed to be perfectly reflecting, implying standing wave perturbations [ $\exp(ik_z z) \pm \exp(-ik_z z)$ ]. For  $\hat{y}$  we require periodic boundary conditions such that solutions vary as  $\exp(ik_y y)$ . Further, the outer boundary for  $\hat{x}$  is analogous

to the magnetopause. Fourier analysing Equations 6.34-6.36 with the subsequent relationships

$$\partial_t \rightarrow i\omega, \quad \partial_y \rightarrow ik_y, \quad \partial_z \rightarrow ik_z \quad (6.37)$$

and noting that  $v_A^2 = v_A^2(x)$ , the equations are reduced to a single second order ODE for  $b_z$  by eliminating  $\xi_x, \xi_y$

$$\frac{d^2 b_z}{dx^2} - \frac{dK^2/dx}{K^2 - k_z^2} \frac{db_z}{dx} + (K^2 - k_z^2 - k_y^2)b_z = 0 \quad (6.38)$$

where  $K^2 = \omega^2/v_A^2$  (Kivelson and Southwood [1985]).  $b_z$  represents the compressional fast mode perturbation which drives the Alfvénic modes in Equations 6.34 and 6.35. However, in Equation 6.38 we observe that there is a regular singularity at radial points  $x_{sing}$  wherein

$$\omega^2 = k_z^2 v_A(x_{sing})^2 \quad (6.39)$$

In other words, the fast compressional mode frequency and phase velocity matches that of the natural Alfvén eigenmode, we have a resonance, and energy from the fast mode is irreversibly transferred to the standing Alfvén mode along the field line.

Other radial (i.e., in the  $\hat{x}$  direction) points of interest known as *turning points* ( $x_{tp}$ ) correspond to the bracketed expression in the final term on Equation 6.38, namely, the square of the wavenumber in the  $\hat{x}$  direction,  $k_x^2$

$$\omega^2 = (k_y^2 + k_z^2)v_A(x_{tp})^2 \quad (6.40)$$

satisfied when  $k_x^2 = 0$ . At locations where Equation 6.40 holds, the fast mode  $b_z$  changes from an oscillatory to evanescent structure in  $\hat{x}$ . The resonance location and turning point are equal when the azimuthal wavenumber  $k_y = 0$ . If not equal, resonances will always occur in regions where  $(K^2 - k_z^2 - k_y^2) < 0$ .

Of course, a Cartesian box is a very simplified view of the magnetosphere. Early works also derived field line resonances in a dipole model (e.g. Chen and Hasegawa [1974]). Perturbations considered were of the form

$$\xi(\hat{\mu}, \hat{\phi}, \hat{\nu}, t) = e^{i\omega t} e^{im\hat{\phi}} \xi(\hat{\mu}, \hat{\nu}) \quad (6.41)$$

where coordinate  $\hat{\mu}$  is directed along the field line,  $\hat{\phi}$  in the azimuthal direction and  $\hat{\nu}$  normal to the field line and pointing towards Earth. We define the *poloidal* Alfvén mode

as that which corresponds to radial displacements of a field line ( $\xi_r$ , analogous to  $\xi_x$  in the box model) and *toroidal* to azimuthal displacements ( $\xi_\phi$ , analogous to  $\xi_y$  in the box model). Since the largest density variations (and therefore Alfvén speeds) occur with radius, natural Alfvén eigenfrequencies are most similar azimuthally along a single drift shell. Therefore, the magnetosphere better facilitates excitation of toroidal modes. Contrarily, eigenfrequency variations for radially separated field lines means that it is harder for poloidal modes to develop at discrete frequencies.

Southwood [1974] postulated that surface waves (with a radially evanescent structure) generated at the magnetopause via Kelvin-Helmholtz instabilities could drive FLRs where the fast mode frequency matches that of the local Alfvén eigenfrequency at some distance from the magnetopause boundary. Other mechanisms exist however which could excite magnetospheric FLRs. Kivelson and Southwood [1986] and Allan et al. [1986a,b] proposed that the preferential resonances correspond to global eigenmodes of the magnetospheric cavity which, when driven by solar wind perturbations, couple to FLRs with the same harmonic frequencies. Samson et al. [1992] also found a number of FLRs with preferred discrete frequencies (known as *magic* frequencies) more consistent with the magnetosphere acting as a waveguide rather than closed cavity.

### 6.3 FLRs in an arbitrary magnetic field

For illustrative purposes we derived FLRs in a heavily simplified magnetic field. Of course, the Earth’s magnetic field does not exist in a box and there has been extensive research to derive FLRs in more practical magnetic field geometries. We mentioned how FLRs for a stationary plasma in dipole coordinates and one-dimensional inhomogeneity perpendicular to  $\mathbf{B}$  (as in Southwood [1974]) were analytically derived in the early work of Chen and Hasegawa [1974]. This work was extended to include a more realistic dipole magnetic field in Chen and Cowley [1989] and more recent work has developed this further to include a moving plasma (Kozlov and Leonovich [2008]).

An axisymmetric dipole is also too simple to describe the magnetospheric magnetic field, and as seen when we investigated  $L^*$ , both analytic and empirical models for more

complex magnetic fields exist. FLRs in the most straightforward non-dipole field, that of a stretched (or compressed) locally axisymmetric magnetic field, were showcased by Rankin et al. [2000]. FLRs for more advanced models in the realm of *dipole-like* or *axisymmetric* fields have also been derived (Cheng [2003]; Cheng and Zaharia [2003]; Leonovich [2001]; Lui and Cheng [2001]; Proehl et al. [2002]), albeit they require external driving to excite the standing Alfvén waves which is computationally expensive.

In the case of empirical magnetic field models, where the magnetic field is significantly distorted, we face significant difficulty when modelling FLRs. It is not intuitive which coordinate system might be useful to adopt since the empirical models are non-orthogonal, which also exacerbates the clear separation of the poloidal and toroidal wave modes. FLR modelling in these instances has been enabled by Rankin et al. [2006], however, by defining the general, non-orthogonal coordinate systems by numerically solvable Euler potentials. These then be applied to any magnetic field model of choice their work - Rankin et al. [2006] applied this technique to the Tsyganenko [1995, 1996] magnetic field model. Indeed, field line resonances are clearly observed in MHD simulations with arbitrary magnetic field models (e.g. Claudepierre et al. [2016]; Degeling et al. [2010]; Proehl et al. [2002]; Waters and Sciffer [2008]). Allowance for arbitrary magnetic fields means that the properties of FLRs with  $L^*$  can be explored.

## 6.4 FLRs observed at the ground

We consider those externally driven ULF waves which can couple to local magnetic field line eigenfrequencies via FLRs (e.g. mediated waves within the solar wind, surface waves generated Kelvin-Helmholtz Instabilities (KHIs) and waves excited by waveguide modes in the magnetospheric cavity). We have already seen how the Alfvén frequencies vary with magnetic field strength and the radial profile of the plasma mass density in an axisymmetric, uniform magnetic field. In reality, we have a non-uniform magnetic field and it is more appropriate to model the magnetosphere as a waveguide which propagates dayside compressional energy down the magnetotail (Samson et al. [1992]; Walker et al. [1992]; Wright [1994]). In this setup, when there is a step change in the plasma density such as at the edge

of the plasmopause, there is a sharp decrease in the radial profile of the Alfvén velocity (the *Alfvén continuum*, see Waters et al. [2000] Figure 2) which allows standing waves to exist between the plasmasphere and ionosphere. Variations in the plasmopause location (Moldwin et al. [2002]) and plasmasphere population (and therefore density, Sheeley et al. [2001]) result in a variation of the Alfvén continuum and how the magnetosphere supports FLRs in time. It is worth noting that azimuthal variations of plasma density have also been considered, but they require numerical solutions as the theory is too complicated (Degeling et al. [2018]; Elsdén and Wright [2018]).

All descriptions discussed in Section 6.3 assume a perfectly reflecting ionosphere which binds the footprints of the field lines to support the standing waves induced by the FLR. This is not the strongest assumption as a perfectly reflective ionosphere would render ground observations unusable to detect ULF waves, but we know this to be untrue. Since magnetic field observations on the ground are not directly sampling the ionosphere, a relationship between the magnetic field at the ground to that of the ionosphere must be determined. Transmission of ULF waves through the ionosphere assumes a  $90^\circ$  rotation and attenuation of the wave magnetic field in a concept known as the *Hughes effect* (Hughes [1974]). This is true for those wave modes perpendicular to the ionosphere; other wave modes will be reflected. In a ground magnetometer, we therefore have the magnetic North-South (East-West) component relating to the toroidal (poloidal) component in the magnetosphere.

Across a latitudinal array of ground magnetometers FLRs exhibit a peaked amplitude profile with a  $180^\circ$  phase shift across the amplitude maximum (Walker et al. [1979]). An example of a clear FLR with these signatures across the CARISMA (then CANOPUS, Rostoker et al. [1995]) magnetometer chain (Mann et al. [2008]) during an event on 25 November 2001 has been adapted from Rae et al. [2005] in Figure 6.1. Ground-based magnetometer observations have received considerable attention over the years to determine the frequency and local time distribution of FLRs. A number of studies found the existence of persistent, discrete frequencies that occurred simultaneously, which have been referred to as *magic frequencies* (as mentioned in Section 6.2). These frequencies appear to be well explained by cavity/waveguide theory but values have local time dependence,

attributed to variations in the solar wind which drive the dimensions of the magnetospheric cavity and plasma density distributions (Archer et al. [2013]; Samson et al. [1992]; Ziesolleck et al. [1998]). In large statistical studies it was also found that the fundamental FLR frequencies decrease with increasing latitude and have an asymmetric local time distribution with preferential support in the morning sector (Baker et al. [2003]; Plaschke et al. [2008]). Importantly for radial diffusion, the ability to measure FLRs using ground magnetometers has enabled an analytic ground-ionosphere-equator coupling between the ground magnetic field and equatorial electric field in a dipole provided by Ozeke et al. [2009], which enables ground observed FLRs to remote sense the equatorial electric field radial diffusion coefficient (Fei et al. [2006]) in the case of poor and sparse satellite electric field observations. When used operationally, several assumptions about FLR characteristics are made for simplification. As a significant source of uncertainty in  $D_{LL}$  formulation, we consider this mapping and the global distribution of FLRs further in Section 6.5.

## 6.5 Analytic mapping

Recall that in Fei et al. [2006] it was assumed that there were no contributions of the induced electric field in the magnetic field perturbations, resulting in the separation of  $D_{LL}$  into purely magnetic and electric components,  $D_{LL}^B + D_{LL}^E$ , assumed to be uncorrelated. While erroneous (Lejosne [2019]), this separation is practical as it allows direct use of ULF magnetic and electric field power spectral density observations into their own equations. In the case of  $D_{LL}^E$ , azimuthal electric field perturbations at the magnetic equator are required to calculate the corresponding power spectral density. When using spacecraft for these measurements to infer  $D_{LL}$ , we are faced with a number of issues

- Spacecraft are not stationary which mixes spatial and temporal variations of the electric field
- Electric field measuring instruments are sensitive to error from a variety of sources, both in the low energy plasma environment and the spacecraft itself (e.g. Wygant et al. [2013], Section 4.2)

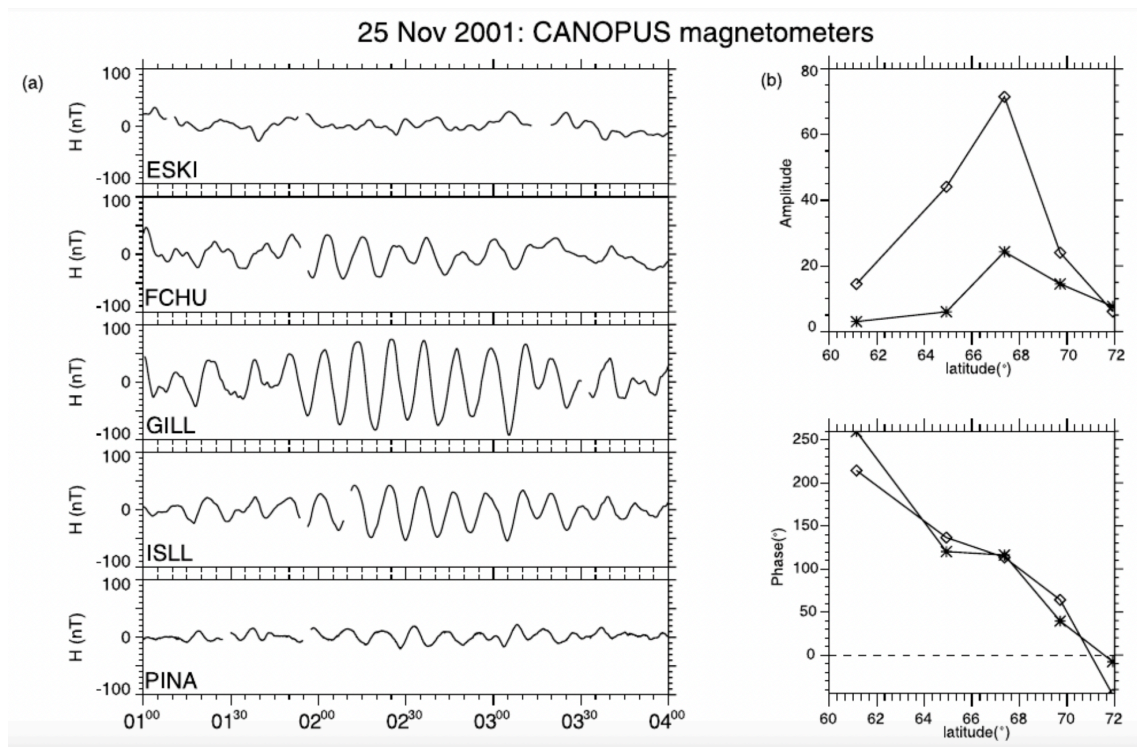


Figure 6.1: (a) Unfiltered H-component ground magnetograms from the CANOPUS Churchill magnetometer network between 0100 and 0400 UT on 25 November 2001. (b) Complex demodulation of the H- (diamonds) and D- (stars) components of the dominant spectral peak (i.e., 1.5 mHz), taken at 0235 UT of (top) the amplitude of, and (bottom) the phase difference between, the Churchill line magnetograms. Adapted from Rae et al. [2005]

- Even in the case of more accurate measurements, spacecraft observations are significantly spatially separated, while ULF wave power extends globally

For these reasons, the ability to remote sense the electric field (and the magnetosphere in general) using well-distributed ground instruments has a number of advantages over *in-situ* satellite measurements. Vast networks of ground instruments already exist at latitudes and MLT complementary to the Earth’s radiation belts with sufficient cadence to monitor ULF wave frequencies (for example, the CARISMA (Mann et al. [2008]) and IMAGE (Tanskanen [2009]) magnetometer arrays). Sufficient combinations of these ground instruments provide consistent global coverage when mapped out to the magnetosphere. Further, if better spatial coverage is desired, the cost and effort of installing new ground instruments is significantly less than that of satellites.

The ability to remote sense the electric field from ground instruments rests on being able to associate the waveforms observed at the ground with those occurring in space and map accordingly. For  $D_{LL}^E$  this is particularly important as the observed waves have to be those capable of driving radial diffusion. Fortunately, FLRs are capable of this and have a unique latitudinal and polarization structure across a latitudinal array of ground magnetometers. On the basis of an occurring FLR, Ozeke et al. [2009] developed a way to remote sense the equatorial electric field ( $E^{eq}$ ) through an analytic expression which couples it to the ground magnetic field ( $b^g$ ). Later work by Ozeke et al. [2012, 2014] proposed that ULF ground magnetic power relates to equatorial electric power via the relationship

$$\mathcal{P}_E^{eq} = \left( \frac{E^{eq}}{b^g} \right)^2 \mathcal{P}_b^g \quad (6.42)$$

and the mapping has gained a lot of traction to enable use of ground observations to infer  $D_{LL}^E$  (for example see studies by Murphy et al. [2014]; Drozdov et al. [2017]).

The Ozeke et al. [2009] mapping exploits the coupling of the magnetic and electric fields at various locations along the field line that an FLR has to travel through from the resonance location

$$\frac{E^{eq}}{b^g} = \frac{b^i}{b^g} \frac{E^i}{b^i} \frac{E^{eq}}{E^i} \quad (6.43)$$

where superscript  $i$  corresponds to the ionosphere. We provide a brief outline of each

component below. Note that a dipole field was assumed in the derivations.

### 6.5.1 Mapping $b^g$ to $b^i$

Assuming the ground is a perfect insulator, the relationship between the magnetic field amplitude at the top of the ionosphere to that on the ground is given by the relationship (Hughes and Southwood [1976])

$$\frac{b^i}{b^g} = \left( \frac{\Sigma_P}{\Sigma_H} \right) \exp(k_{\perp} h) \quad (6.44)$$

where  $\Sigma_P, \Sigma_H$  are the Pedersen and Hall conductivities,  $k_{\perp}^2$  is the wave vector at the ionosphere perpendicular to the ambient magnetic field and  $h$  is the height of the ionospheric E-region above the ground. The wave vector can also be written as the sum of the azimuthal and latitudinal wavenumbers

$$k_{\perp}^2 = k_{\phi}^2 + k_{\theta}^2 \quad (6.45)$$

$$= \frac{m^2 L}{R_E^2} + \frac{4\pi^2}{(R_E \Delta\theta)^2} \quad (6.46)$$

where  $m$  is the azimuthal wavenumber,  $L$  is the McIlwain [1961] L-Shell coordinate,  $R_E$  is the radius of the Earth and  $\Delta\theta$  is the full width half maxima of the latitudinal amplitude profile of the waves observed on the ground by a latitudinal array of magnetometers.

Combining we get the desired mapping

$$\frac{b^i}{b^g} = \left( \frac{\Sigma_P}{\Sigma_H} \right) \exp \left( \left[ m^2 L + \frac{4\pi^2}{(\Delta\theta)^2} \right]^{1/2} \frac{h}{R_E} \right) \quad (6.47)$$

### 6.5.2 Coupling $b_i$ to $E_i$

We couple the magnetic field amplitude to that of the electric field at the ionosphere through ionospheric boundary conditions. For the guided toroidal Alfvén wave we have (Allan and Knox [1979b])

$$b_{\phi}^i = \mu_0 \Sigma_P E_{\nu}^i \sin(\chi) \quad (6.48)$$

where  $\mu_0$  is the permeability of free space,  $\chi$  is the dipole dip angle of the field lines (Allan and Knox [1979b]) and  $\nu$  denotes the radial component.

Alternatively for the guided poloidal Alfvén wave, defined only for  $L \geq 4$  due to field lines assumed perpendicular to the ionosphere, we have (Ozeke and Mann [2004])

$$b_\nu^i = \mu_0 \Sigma_P E_\phi^i \quad (6.49)$$

### 6.5.3 Mapping $E^i$ to $E^{eq}$

These relationships were derived as solutions to the guided toroidal and poloidal wave equations in a dipole, assuming some field-aligned plasma density profile. Ozeke et al. [2009] presented the analytic solutions for a plasma density profile of  $\propto 1/r^6$  as demonstrated in Allan and Knox [1979a,b] and Ozeke and Mann [2004], however, to implement an arbitrary density profile the wave equations must be solved numerically. These are addressed in the next section.

### 6.5.4 Mapping $b^g$ to $E^{eq}$

Combining everything together Ozeke et al. [2009] map the magnetic field amplitude on the ground to the equatorial electric field amplitude via

$$\frac{E_{\{\phi,\nu\}}^{eq}}{b_{\{\phi,\nu\}}^g} = \frac{f_{ob}}{3mHz} \frac{E_{\{\phi,\nu\}}^i}{b_{\{\nu,\phi\}}^i} \left( \frac{\Sigma_P}{\Sigma_H} \right) \exp \left( \left[ m^2 L + \frac{4\pi^2}{(\Delta\theta \text{ radians})^2} \right]^{1/2} \frac{h \text{ km}}{R_E} \right) \quad (6.50)$$

where  $b_\phi^g$  and  $b_\nu^g$  at the ground correspond to the guided toroidal and poloidal modes, respectively, recalling that Alfvén waves are assumed to rotate by  $90^\circ$  as they transmit as they pass through the insulating atmosphere and anisotropically conducting ionosphere on their way to the ground (Hughes [1974]; Hughes and Southwood [1976]; Hughes [1983]). Further,  $f_{ob}$  is the frequency at the dominant spectral peak of the FLR and  $E_\phi^i/b_\nu^i, E_\nu^i/b_\phi^i$  are the numerical solutions to the guided poloidal and toroidal wave equations, respectively, which depend on the assumed plasma density profile. The  $E^i, b^i$  were solved for fundamental field-aligned wave frequency of 3 mHz at all L-shells in Ozeke et al. [2009] which is why the scaling with 3 mHz appears in the equation.

## 6.6 Uncertainty and limitations

There are a number of assumptions and simplifications made in the derivation of the Ozeke et al. [2009] mapping which induce uncertainties when used to construct  $D_{LL}^E$ . Fortunately we can attempt to quantify some of these with data already considered or through more sophisticated analysis, namely,

- Fourier-based signal processing
- Mapping using McIlwain [1961] L-shell rather than  $L^*$
- Assuming the resonance width at the ground, determined by the latitudinal amplitude profile full width half maximum  $\Delta\theta$ , is constant at  $4^\circ$

The remaining uncertainties are outwith the scope of this thesis, however, we outline them later as future work. We detail the uncertainties considered in this thesis below.

Our ability to successfully relate  $E^{eq}$  to  $b^q$ , and indeed our entire understanding of observed FLR characteristics, rests on the signal processing techniques used to isolate resonant frequency spectra. For example, the Ozeke et al. [2009] mapping was validated using *complex demodulation*, a Fourier-based signal processing technique which isolates frequency spectra in time and has been applied to ULF waves for decades (e.g. Myers and Orr [1995]). This technique is known to struggle with the correct decomposition of two or more superposed FLR phase structures within a narrow frequency band (Rae et al. [2007]; Plaschke et al. [2008]), and thus sustains measurement uncertainty. For test cases where the signal being analysed shows a clear long-lasting FLR which persists for the entirety of the window, measurements errors are likely to be negligible. When attempting to detect FLRs automatically for statistical analysis (e.g. Baker et al. [2003]; Plaschke et al. [2008]) when underlying signals are unknown, however, Fourier-based techniques have a number of important flaws

- *Spectral leakage*: When observed waveforms lasts for a non-integer number of periods

within a considered window the energy at the signal's frequencies leak to neighbouring bins in the Fourier domain.

- *False amplitude normalization for transient waveforms:* For transient signals that last for an integer number of periods (to neglect spectral leakage effects) but not for the duration of the window, this is analogous to the signal being *zero-padded* at times that it does not exist. Zero-padding does not add any new energy to the signal but only improves the discrete frequency resolution, so when the extent of zero-padding is known and you take the FFT you only have to normalize by the length of the original transient waveform. If however you have no knowledge about the length of the transient waveform relative to the window length, it is assumed that the wave lasts for the entirety of the window and the amplitude in the FFT will be over-normalized. This concept is illustrated in Figure 6.3. In previous statistical studies of Pc5 FLRs, events were identified (if not by eye (e.g. Hudson et al. [2004])) using power spectral density calculated over fixed window lengths, selecting frequencies with prominent power above a threshold in time (Plaschke et al. [2008]) or wave period (Baker et al. [2003]). Since wave period decays inversely proportional to frequency, desired high frequency FLRs in the ULF range are often transient compared to low frequency FLRs in a single window. Based on the reasoning above there is a likely risk of selection bias to low frequency FLRs in previous Fourier-based automated detection algorithms.

In Section 6.7 we present a novel FLR detection algorithm, which uses an advanced signal processing technique designed to extract all waveforms in time-frequency spectra and mitigate the bias to low frequency events. Our results are compared with previous studies to measure the extent of uncertainties in FLR characterisation due to Fourier-based analysis.

The clearest limitation of equation 6.50 is its restriction to a dipole magnetic field. The dipole approximation affects all components of equation 6.43, as the dipole solutions to the guided wave equations determine the ionospheric electric field, which the ionospheric boundary condition and the azimuthal magnetic wavelength are related to. As mentioned in Section 6.3, however, numerical solutions for the guided wave equations exist for arbitrary magnetic fields (Rankin et al. [2006]) and might allow for replacement of the dipole

approximation to provide a mapping. To do so requires describing a non-orthogonal, field-aligned coordinate systems using a covariant-contravariant formalism (as in general relativity) and solving the resulting linearized MHD wave equations on a particular field line (subject to respective metric coefficients). This could provide useful for individual observation mapping for *in situ*  $D_{LL}$ . Nevertheless, the Ozeke et al. [2009] approach can be applied globally and extrapolating the Rankin et al. [2006] equations globally whilst also considering temporal variations of empirical field models introduces computation expense. While re-deriving the mapping is beyond the scope of this thesis, we can investigate how the current mapping performs when substituting the McIlwain [1961] L-Shell for  $L^*$ . Although swapping these coordinates is somewhat arbitrary, any discrepancies with space-based electric  $\mathcal{P}$  distributions can provide probabilistic insight into errors (ie through some empirically determined scaling factor) that a future  $L^*$  based mapping might account for.

$\Delta\theta$  varies with MLT and has been suggested, in conjunction with azimuthal wave number  $m$ , to cause local time variations of ground-based ULF wave power (Glassmeier and Stellmacher [2000]) through the ionospheric screening effect (Hughes and Southwood [1976]). The default value used to construct the Ozeke et al. [2012, 2014]  $D_{LL}^E$  was  $\Delta\theta = 4$ , however, validation of the Ozeke et al. [2009] mapping against a FLR test case found  $\Delta\theta \approx 5.4^\circ$ . While discrepancies between these values is small it is important to remember that the units of  $\Delta\theta$  in equation 6.47 are *radians*, with  $\Delta\theta$  squared in the denominator of a term embedded in an exponential. Actual resonance widths narrower than the assumed  $4^\circ$  are therefore likely to grow the default mapping exponentially. Attenuation of wave amplitudes at the ionosphere is controlled by conductivity,  $m$  and  $\Delta\theta$ , of which all can be significantly variable (for an example of  $\Delta\theta$  variability based on empirical models of ionospheric screening, see Glassmeier and Stellmacher [2000] Figure 6).

It remains to be seen which of  $\Sigma_P, \Sigma_H, m, \Delta\theta$  most impact the  $E^{eq}/b_g$  mapping and consequently  $D_{LL}^E$  when realistic values are used. For illustration, however, Figure 6.2 highlights how the Ozeke et al. [2009] mapping scales across L-Shells when  $m$  and  $\Delta\theta$  diverge from their assumed default values. Since the impact of  $\Sigma_P$  variability is tied to the numerical solutions of the guided Alfvén wave equations, for which a pre-written solver is not readily available, mapping sensitivity to conductivity has not been considered. For

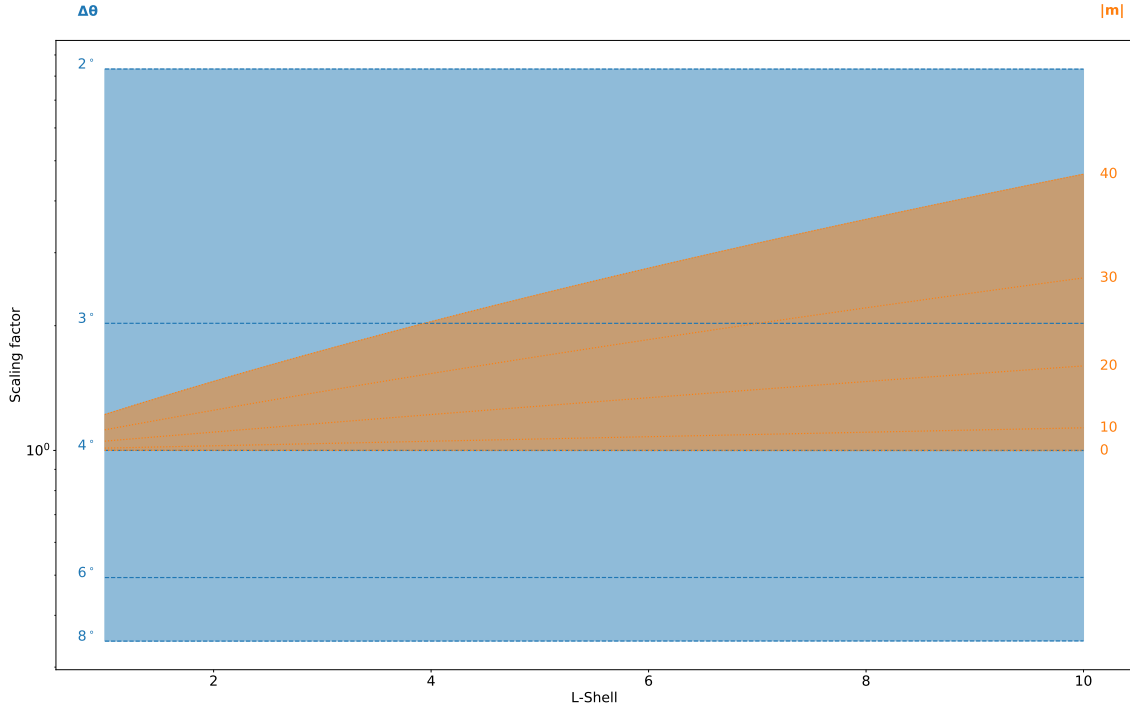


Figure 6.2: Sensitivity of the Ozeke et al. [2009]  $E^{eq}/b^g$  mapping (poloidal and toroidal) as a function of L-shell to variations of  $m$  and  $\Delta\theta$  from their assumed default values ( $m = 1, \Delta\theta = 4^\circ$ ). Sensitivity is given as the scaling factor found from dividing the varying mapping by the default. When varying a single parameter all others remain at their default values so that sensitivity is only attributed to a single parameter. The blue (orange) shaded region illustrates the mapping sensitivity space for varying  $\Delta\theta$  ( $m$ ), with blue (orange) dotted lines overplotted for the discrete values  $\Delta\theta = [2^\circ, 4^\circ, 6^\circ, 8^\circ]$  ( $m = [0, 10, 20, 30, 40]$ ).

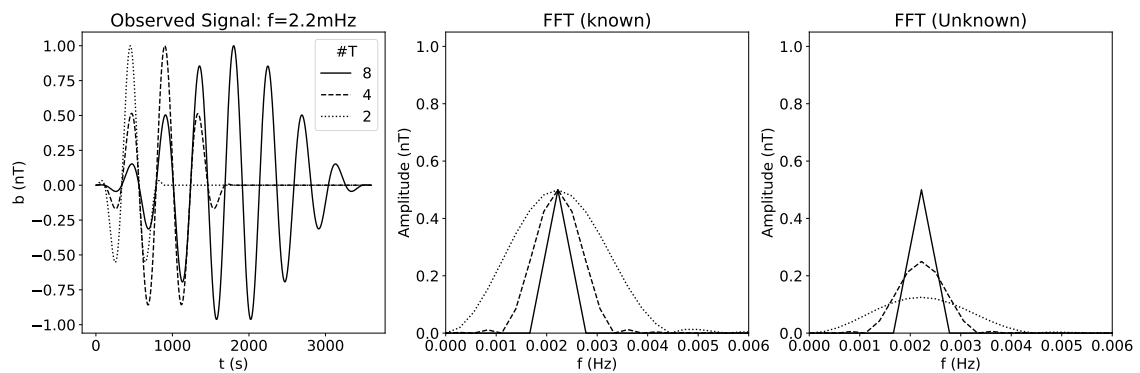


Figure 6.3: An illustration of the over-normalization of transient wave amplitudes that unknowingly persist for less than a considered window length. In all panels, we consider a  $f \sim 2.2\text{mHz}$  wave which lasts for (:) two periods, (-) four periods and (-) eight periods (which is the length of the window). (LEFT) The waves which are Hanning windowed (pulse-like), starting at time  $t = 0$  and zero-padded at other times they do not occur (if applicable). (CENTRE) The amplitudes of each wave as determined by the FFT and normalized appropriately when the length of each wave is known. (RIGHT) The amplitudes of each wave as determined by the FFT and normalized inappropriately when the length of each wave is unknown.

resonantly driven ULF waves observed on the ground ( $|m| \lesssim 10$ ), scaling of the default mapping is negligible across all L-Shells. Conversely the mapping is very sensitive to the resonance width. For the extrema, doubling the default resonance width dampens the mapping by  $\sim 0.65$ , whilst halving multiplies the mapping by  $\sim 7.5$ . Since we map ground-based ULF wave power in equation 6.42 using the square of the mapping, sufficient  $\Delta\theta$  variability implies potential  $P_E^{eq}$  (and subsequently  $D_{LL}^E$ ) that span orders of magnitude uncaptured by the assumed  $\Delta\theta = 4^\circ$ . It is already known that  $\Delta\theta$  varies with local time (Glassmeier and Stellmacher [2000]), but understanding the extent of its variability is necessary to constrain the uncertainty in  $D_{LL}^E$ .

## 6.7 Global frequency distribution of field line resonances in the inner magnetosphere

The following manuscript has been prepared for submission in the *Geophysical Research Letters*. The entirety of this manuscript, however, fits within the wider scope of this thesis and should be considered in this context.

1     **Global frequency distribution of field line resonances in**  
2                     **the inner magnetosphere**

3             **R. L. Thompson<sup>1</sup>, C. E. J. Watt<sup>2</sup>, P. D. Williams<sup>3</sup>, S. N. Bentley<sup>2</sup>**

4                             <sup>1</sup>Department of Mathematics and Statistics, University of Reading, UK

5   <sup>2</sup>Northumbria University, UK

6   <sup>3</sup>Department of Meteorology, University of Reading, UK

7             **Key Points:**

- 8             • A novel automatic field line resonance detection algorithm across a network of ground  
9             magnetometers is presented
- 10            • The spectral analysis used is unbiased to FLR frequency, amplitude or duration  
11            unlike previous studies which used the Fourier-Transform
- 12            • Multiple FLR populations overlooked by previous studies are uncovered and a well-  
13            informed distribution of FLR frequencies is demonstrated

---

Corresponding author: Rhys Thompson, [r.l.thompson@pgr.reading.ac.uk](mailto:r.l.thompson@pgr.reading.ac.uk)

**Abstract**

A number of statistical and event studies have postulated that the eigenmodes of Earth's magnetic field lines preferentially support certain discrete magnetospheric ultralow frequency (ULF) wave frequencies, named preferentially in the morning sector, to enable energy exchange through field line resonance (FLR) coupling. FLRs are detectable by a unique structure present in the ULF wave signal spectra, and all previous statistical studies using automated detection algorithms have used Fourier-based techniques for spectral analysis. ULF waves often manifest as transient 'pulse-like' waveforms in discrete signals and are prone to potentially severe over-normalization with Fourier analysis when the wave duration is smaller than the observation window. Time-frequency representations (TFRs) are powerful tools able to separate periodic components and their underlying properties within a signal when time localization is desired. In this study we present a novel algorithm to automatically extract FLRs using TFRs of magnetometer signals produced by the Synchrosqueezing Transform (SSQT), to uncover the frequency distribution of FLRs in the inner magnetosphere over 7 years of data across an array of magnetometers. Our algorithm is designed to be accurate at isolating FLR frequencies and is unbiased to waves of any particular duration or amplitude. We find the existence of preferential frequency bands which are compared with previous studies, and uncover multiple populations of FLRs in local time masked by the spectral analysis in previous statistical studies. Our results highlight the need for unbiased signal processing for FLR detection in the inner magnetosphere.

**Plain Language Summary**

When ultralow-frequency ( $\sim 1\text{-}20$  mHz), ULF) waves propagating through the magnetosphere have a discrete frequency matching that of the local magnetic field line, an irreversible energy exchange occurs from the ULF wave to Earth's magnetic field - known as a field line resonance (FLR). The theory of FLRs is rich and they have been observed numerous times in both ground and satellite data. For the former, using a network of ground magnetometers spanning multiple latitudes and aligned in longitude we can detect FLRs by a unique structure along the network's signal spectra. Previous statistical studies which have aimed to automatically identify FLRs in magnetometer networks have all based their spectral analysis on the Fourier Transform. Unfortunately many FLRs are short lived compared to the window length considered for Fourier analysis, leading to over-normalization of their amplitudes when using Fourier analysis. This means that previous studies are naturally biased to waves of smaller frequencies which have longer wave periods. In this study we present a novel algorithm for automatic FLR detection, using spectral analysis which does not discriminate between wave duration, amplitude or frequency. Applying our technique to 7 years of ground magnetometer we uncover the frequency distribution of FLRs in the inner magnetosphere and compare to previous studies. We find that our technique uncovers populations of FLRs overlooked by Fourier-based studies, and provides a similar yet alternative view regarding persistently observed FLR frequencies, highlighting the need for unbiased signal processing to uncover the full FLR distribution.

**1 Introduction**

The low frequency oscillations of the Earth's magnetic field, known as ultralow frequency (ULF) waves, have been observed at the ground as early as the Carrington event (Stewart, 1861). Previously known as "micropulsations" and formally classified by their frequency, continuity and irregularity by Jacobs et al. (1964), ULF waves are thought to play a key role in the energization and transport of trapped particles in the Earth's magnetosphere (D. N. Baker, Pulkkinen, Li, Kanekal, Ogilvie, et al., 1998; D. N. Baker, Pulkkinen, Li, Kanekal, Blake, et al., 1998; Mann et al., 2004). A prevailing theory to

64 explain the existence of ULF waves within ground observations is magnetospheric field  
65 line resonances (FLRs). This describes the coupling of fast compressional modes of prop-  
66 agating ULF waves to the natural Alfvén eigenmodes of Earth’s magnetic field lines at  
67 a particular location, causing an irreversible energy exchange directed along the field line.  
68 The study of FLRs in a rich variety of magnetic field configurations has developed across  
69 decades (Chen & Hasegawa, 1974; Elsden & Wright, 2017; Rankin et al., 2005; South-  
70 wood, 1974), and proven vital to drive certain physical processes in global models of the  
71 magnetosphere (e.g. Elsden & Wright, 2018, 2019; Degeling et al., 2010, 2018a; Lysak  
72 et al., 2020).

73 Ground-observed FLRs across latitudinal arrays of ground magnetometers have re-  
74 ceived considerable attention, with a well-known signature of a peaked amplitude pro-  
75 file at the resonant frequency and a  $180^\circ$  phase change across the resonance location (Allan  
76 et al., 1986; Samson et al., 1971; Walker et al., 1979; Rae et al., 2005). Since the arrays  
77 consistently sample the global magnetosphere, as opposed to sparsely located satellite  
78 observations, they are well positioned to remote sense the distribution of FLRs in the  
79 inner magnetosphere. Previous studies have investigated the statistical magnetospheric  
80 ULF resonance structure using the CANOPUS (now CARISMA, Mann et al. (2008)) ar-  
81 ray of ground magnetometers, finding typically that fundamental frequency decreases  
82 with increasing latitude and there is preferential FLR support in the morning sector (G. J. Baker  
83 et al., 2003; Plaschke et al., 2008). Such statistics can be used to explore phenomena found  
84 in other event studies, such as radar and satellite observed FLRs at persistent and local-  
85 time dependent frequencies, dubbed *magic* frequencies (Archer et al., 2013; Samson, Har-  
86 rold, et al., 1992; Ziesolleck et al., 1998).

87 Successful FLR identification is dependent on accurate approximations of signal  
88 spectra. In the previous statistical studies, FLRs were automatically identified across  
89 time series using Fourier Transform-based power spectral densities (PSDs), with prospec-  
90 tive events satisfying some length (Plaschke et al., 2008) or period (G. J. Baker et al.,  
91 2003) threshold. Applying the Fourier Transform to signals containing unknown wave-  
92 forms is potentially subject to substantial measurement uncertainty, however. Firstly,  
93 waves which persist for a non-integer number of periods in a considered signal succumb  
94 to *spectral-leakage*, where energy at the waves’ frequencies leak to neighbouring bins in  
95 the Fourier domain. Secondly, normalization of amplitude spectra is subject to the as-  
96 sumption that waves last the entirety of the signal. Transient waves existing for only a  
97 portion of signal should be normalized by their duration rather than the signal length  
98 (analogous to *zero-padding*), however for automatic detection nothing about the signal  
99 is known and transient events are likely to be over-normalized. Detection of transient  
100 FLRs lasting for comparable periods within the same signal will therefore be biased to  
101 those at lower frequencies. Indeed, high frequency FLRs were found to occur less and  
102 it remains to be seen whether this is physical or a consequence of measurement uncer-  
103 tainties.

104 In this paper we present a statistical study of ground-observed FLRs in the CARISMA  
105 array (Mann et al., 2008) using an algorithm which mitigates the biases imposed by Fourier  
106 approaches. Pulse-like wave-forms, irregardless of length, are found using a signal pro-  
107 cessing technique with high precision and localization in both the time and frequency  
108 domain. Events extracted from time-frequency representations of signal spectra allow  
109 for more refined descriptions of FLR characteristics, as Fourier-based power is averaged  
110 over multiple time instances. Wave-forms are extracted successfully using Hessian-based  
111 image feature detection, and prospective intervals which coincide across magnetometers  
112 are checked for FLR signatures. Our results are compared with previous observational  
113 and statistical studies to discern the impact of measurement uncertainty in FLR detec-  
114 tion.

115 The remainder of paper is as follows. A description of the array of magnetometers  
116 used in this study is given in Section 2, with the automatic detection algorithm detailed

117 in Section 3. Key results are presented in Section 4 and a comprehensive discussion com-  
118 parable to previous studies provided in Section 5.

## 119 2 Instrumentation and Data

### 120 2.1 Canadian Array for Realtime Investigations of Magnetic Activity 121 (CARISMA)

122 The CARISMA network (Mann et al., 2008) is an array of ground magnetometers  
123 in North America which measure disturbances in the Earth’s magnetic field. The net-  
124 work features a latitudinal chain of magnetometers located at approximately  $330^\circ\text{E}$  and  
125 spanning latitudes  $45.87^\circ\text{N}$ - $62.82^\circ\text{N}$ . The magnetometer stations used in this study are  
126 illustrated in Figure 1. We include stations at latitudes which typically cover a dipole-  
127 L range 3.6-10.9, generally containing the Van Allen Outer Radiation Belt (ORB) (see  
128 Table S2).

### 129 2.2 Pre-processing

130 In this study we use pre-processed magnetometer station data (see acknowledgments)  
131 throughout the period 2008-2014. The data were processed in an attempt to remove non-  
132 physical phenomena including step jumps, large outliers, spurious data spikes and con-  
133 stant values. We employ further that an individual station’s data contains sufficiently  
134 small amounts ( $<5$  minutes) of bad and/or missing data for consideration, with data in-  
135 terpolated if necessary. Time series are otherwise removed from analysis. A minimum  
136 of 4 stations are required for the both the wave extraction and FLR detection stages,  
137 since 3 might allow for false positives due to middle station bias. The algorithm stores  
138 an *identifier* for each station considered in a successfully detected FLR. Therefore, re-  
139 sults can be easily filtered for a desired level of confidence in the detected FLR (confi-  
140 dence increases with a higher number of stations considered).

## 141 3 Automated FLR detection

### 142 3.1 Wave extraction

143 We identify ULF wave signatures for a given magnetometer signal using the *Syn-*  
144 *chroqueezing Transform (SSQT)* on top of the *Continuous Wavelet Transform (CWT)*  
145 (see Supporting Information for a full mathematical description). The SSQT aims to re-  
146 cover the periodic components (*intrinsic mode functions*) which comprise a signal at their  
147 instantaneous frequencies, naturally having high-localization in both time and frequency.  
148 The robustness and high-performance of the SSQT has been found in an number of sci-  
149 entific fields, including cosmology, seismology, meteorology and paleontology (e.g. Thakur  
150 et al., 2013; Tary et al., 2018).

151 To automatically extract ULF waves present in the time-frequency representation,  
152 SSQT amplitude spectrograms are treated as images and *Hybrid-Hessian* filtered to en-  
153 hance localized wave structures, which are assumed to be vascular-like and binarized (equal  
154 to 1) relative to the noise (equal to 0). Connected structures can then be easily found  
155 in the SSQT coefficients and reconstructed accordingly. We require events to last for 4  
156 wave periods with a maximum amplitude more than 0.5nT to be considered for FLR de-  
157 tection. See Supporting Information for further details.

### 158 3.2 FLR detection

159 To detect FLRs across the latitudinal array of magnetometers, successfully extracted  
160 ULF wave spectra (amplitude and phase) in the time-frequency domain for each station  
161 are superposed, increasing with station latitude. Overlapping events which are shared

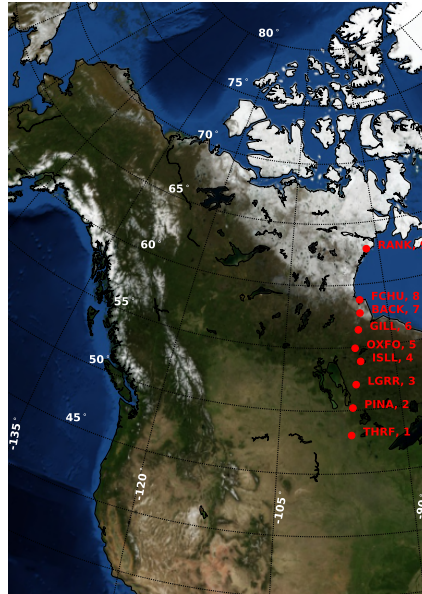


**Figure 1.** Geographical locations of latitudinal chain of ground magnetometers in the CARISMA network used in this study. Each stations identifier code and number (see Table S2) are given next to each location

162 by 4 or more stations are isolated and checked for the characteristic FLR amplitude pro-  
 163 file and phase change. With multiple instances of the satisfied criteria in a single event,  
 164 the dominant spectral peak is selected for parameter extraction (amplitude, full width  
 165 half maxima, etc). See Supporting Information for a full description, particularly the def-  
 166 inition for overlapping events which is relative to the mathematical representation of the  
 167 SSQT.

#### 168 4 Results

169 In some instances FLRs can co-exist at multiple frequencies for a single station due  
 170 to the following:

- 171 • By using a discrete number of stations to detect an FLR, the latitude correspond-  
 172 ing to the latitudinal peak need not be the true location of the FLR. Instead, this  
 173 location could exist anywhere in the region between the respective station and the  
 174 midpoints with respect to its neighbouring stations
- 175 • The wave extraction component of our detection algorithm does not discriminate  
 176 between any of the waves present in a signal. If both the fundamental and higher  
 177 order harmonic modes are present in the signal, which both have resonant char-  
 178 acteristics, our algorithm would identify each as a single event.

179 To avoid confounding results and to allow comparison with previous studies, when over-  
 180 lapping FLRs are detected at a particular station we select the event which has the max-  
 181 imum amplitude. We do this with knowledge that some real FLRs may be omitted from  
 182 the statistics, but since many studies have identified FLRs from peaks in ULF power spec-

183 tral density (e.g G. J. Baker et al., 2003; Plaschke et al., 2008; Samson, Harrold, et al.,  
 184 1992) we deem this the most appropriate choice. In addition to this we also filter results  
 185 by those events which have amplitude  $> 0.5nT$  in line with previous analysis (G. J. Baker  
 186 et al., 2003). This results 22585 and 32169 detected poloidal and toroidal FLRs, respec-  
 187 tively. For the readers' interest we have included figures corresponding to the global statis-  
 188 tics of a number of FLR parameters in the Supporting Information.

189 Figure 2 shows the distribution of FLR frequencies for all identified events, binned  
 190 by those given for an hourly time series sampled at 1 Hz for comparison. The frequen-  
 191 cies given in the wavelet discretization are indicated in rugs, as well as the magic frequen-  
 192 cies found by Samson, Harrold, et al. (1992) and Ziesolleck et al. (1998). Distribution  
 193 of FLR frequencies is near-identical for both the poloidal and toroidal ULF wave com-  
 194 ponents. We identify 2 persistent bands of frequencies rather than discrete frequencies,  
 195 which extend from  $\sim 1.25$ - $2.6$  mHz and  $\sim 2.9$ - $4$  mHz, respectively. The former band, which  
 196 cumulatively has the largest occurrence, was not observed in previous statistical stud-  
 197 ies due to limitations of the frequency discretization resulting from the length and cad-  
 198 ence of the time series considered. The second band aligns with previous findings, how-  
 199 ever. Most of the published magic frequencies appear to fall in these bands, with one at  
 200 1.4mHz aligned precisely where we see a peak in the distribution. Each band is charac-  
 201 terized by a decay in density from a peak at the leftmost frequencies. This is in contra-  
 202 diction to previous studies, which found that the occurrences of FLRs away from the global  
 203 frequency peak decay smoothly (G. J. Baker et al., 2003; Plaschke et al., 2008). In fact,  
 204 application of frequency-focused spectral analysis highlights a number of events at some  
 205 persistent, discrete higher frequencies likely to be obscured from classical Fourier-based  
 206 approaches. We do find as in previous studies, however, that FLRs generally do occur  
 207 less at higher frequencies.

208 In Figure 3 we illustrate the distribution of FLR frequencies across MLT, again in-  
 209 dicating the regions where particular magic frequencies were observed. Our predominant  
 210 frequency band which encloses most of the magic frequencies is supported globally, but  
 211 shows clear asymmetries with the poloidal component favouring the afternoon sector and  
 212 the toroidal component afternoon and nighttime. The second band exhibits an asym-  
 213 metry with maximal support in the afternoon for both components. This directly con-  
 214 tradicts previous statistical studies which found an asymmetry in FLR occurrence with  
 215 a peak around dawn for frequencies in this range. This asymmetry was initially observed  
 216 prominently at auroral latitudes by Chandra Gupta (1976), and has since been attributed  
 217 to peaks in Pc5 PSD distributions in the morning sector (Engebretson et al., 1998; Glass-  
 218 meier & Stellmacher, 2000). Since previous statistical studies identified FLRs from PSD  
 219 peaks it is therefore unsurprising that occurrence was biased to the morning. The asym-  
 220 metry is not clearly defined at all latitudes, however, with nighttime FLR occurrences  
 221 also notable and sometimes exceeding those of the morning (Chandra Gupta, 1976). These  
 222 cannot be explained by peaks in PSD distributions. Since our spectral analysis extracts  
 223 and treats each wave which comprises a signal independently, we believe we mitigate bi-  
 224 ases to PSD enhancements to reveal FLRs more difficult to detect, resulting in the oc-  
 225 currences with MLT highlighted in Figure 3. In addition to the bands of frequencies of  
 226 discussed, we also find that there appears to be no clear preferential support in MLT for  
 227 high frequency FLRs.

228 The distribution of FLR occurrences with MLT, as observed by individual stations,  
 229 are shown in Figure 4. We show distributions for PINA, ISLL, GILL and FCHU only  
 230 since BACK and OXFO (the other stations where FLRs were identified) had consider-  
 231 ably less data availability over the search period. Only PINA exhibits an MLT distri-  
 232 bution consistent with previous statistical studies with a peak in FLRs in the morning  
 233 sector, although the poloidal FLRs present another peak in the early-afternoon. The char-  
 234 acteristic frequencies of each FLR polarization at PINA are also significantly different,  
 235 with the poloidal and toroidal modes concentrated around  $\sim 1$ - $2$  and  $\sim 4$ - $6$  mHz, respec-

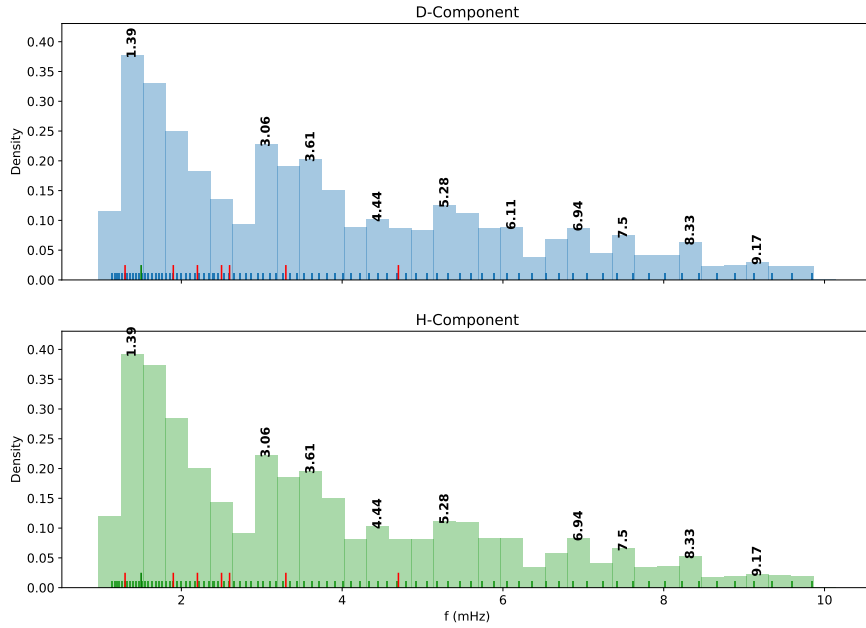


**Figure 2.** Global distribution of identified FLR frequencies for the (top) D and (bottom) H-components of the magnetic field perturbations, illustrated by a histogram with bins corresponding to those of an FFT for an hour long signal. These bins were chosen due to the logarithmic spacing between the SSQT frequencies (shown by the blue rugs) and to compare with previous studies. Magic frequencies identified by Samson, Harrold, et al. (1992) and Ziesolleck et al. (1998) are shown by red and green rugs, with a green rug indicating signifying an alignment with a peak (annotated throughout) in our frequency distribution.

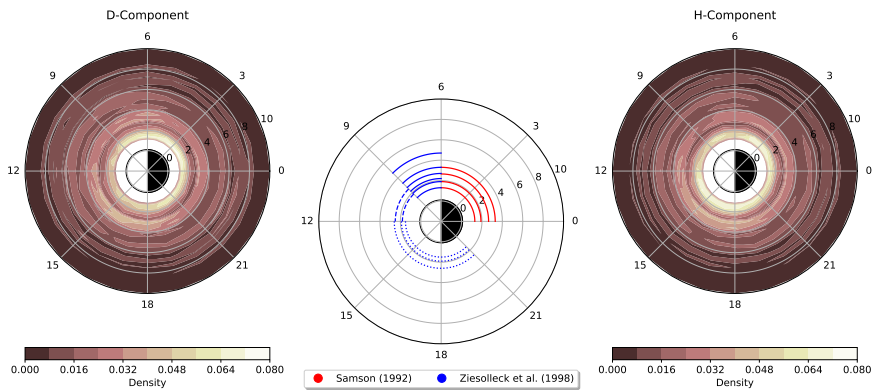


**Figure 3.** Contour of FLR frequency density with MLT for the (left) D and (right) H component of the magnetic field perturbations. MLT bins are hourly with frequency bins as in Figure 2. (Centre) The locations of magic frequencies identified by Samson, Harrold, et al. (1992) (red) and Ziesolleck et al. (1998) (blue) in the same domain.

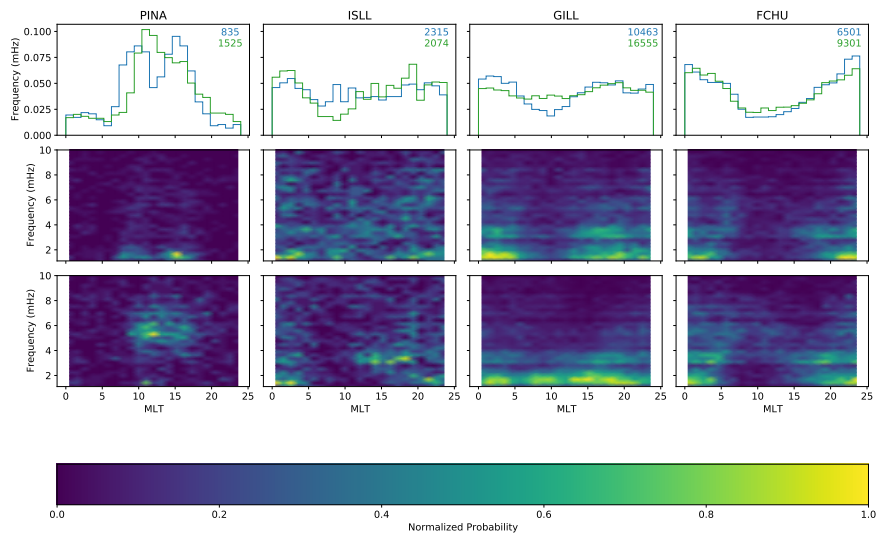


**Figure 4.** Distribution of FLR occurrences across MLT as a function of magnetometer station. (Top) D (blue) and H (green) component FLRs comprising all frequencies, where the number of FLRs identified for each component is also shown (in the same colour as the respective histogram). The distribution of (middle) D and (bottom) H-component FLRs at each station as a function of MLT and frequency are also provided, with frequency bins corresponding to those of an FFT for an hourly signal. In the frequency-MLT plots, densities have been normalized by the distribution maximum to enable comparison across stations.

236 tively. The remaining stations show a reversed relationship of an asymmetry favouring  
237 evening and nighttime, although this profile at GILL for the toroidal FLRs is much less  
238 pronounced and closer to equiprobability across MLT. In light of the number of FLRs  
239 identified at each station, we find that low-frequency FLRs at GILL account for the largest  
240 proportion of the dayside population. At this station, support for higher frequency events  
241 across all MLT decays smoothly. FCHU and ISLL show a clear preference to evening and  
242 nighttime at most frequencies, with a noticeable absence of dayside events, whilst FLRs  
243 at low-latitude PINA appear mostly confined around noon. Isolating the frequencies with  
244 the highest density, the classical behaviour of decreasing FLR frequency with latitude  
245 is generally satisfied, although all stations show profound FLR frequency variability across  
246 multiple MLT. Contrary to this, we observe a population of  $\sim 3$ -5mHz waves confined  
247 to the afternoon sector, more prevalent and deeper penetrating in for the toroidal mode  
248 FLRs.

## 249 5 Discussion

250 We have demonstrated further understanding of how the magnetosphere resonates,  
251 using spectral analysis specifically designed to detect FLR structure irrespective of the  
252 wave amplitude and duration. There is less evidence for discrete "magic frequencies",  
253 but rather separable bands of preferred frequencies which decay in occurrence with in-  
254 creasing frequency for any given band, as well in width with each successive band. The  
255 most prominent is that between  $\sim 1.4$ -2.5 mHz, which aligns with most of the magic fre-  
256 quencies found in previous literature (e.g. Archer et al., 2013; Samson, Harrold, et al.,  
257 1992; Ziesolleck et al., 1998). This globally supported band across MLT is consistent with  
258 the radially standing cavity/waveguide modes trapped between the boundaries of the  
259 magnetosphere (Kivelson & Southwood, 1985; Samson, Harrold, et al., 1992). The two  
260 most prominent bands displayed asymmetry with MLT, with favourable support in both  
261 the afternoon and nighttime sectors. This result is different to previous statistical stud-  
262 ies which found preferential support surrounding dawn (e.g. G. J. Baker et al., 2003; Plaschke  
263 et al., 2008) in agreement with FLRs driven by the Kelvin-Helmholtz instability (e.g. Rae  
264 et al., 2005, 2007). Considering the distribution of amplitude with both frequency (see  
265 Figure S6) and MLT (see Figure S5), it is clear that FLRs at the most prevalent frequen-  
266 cies in dawn tend to have larger amplitudes and therefore more easily detected by Fourier-  
267 based methods. Indeed, waves driven by external magnetopause perturbations tend to  
268 have larger power in the dawn sector (e.g. Bentley et al., 2020). By developing a tech-  
269 nique which does not discriminate against wave amplitude we are able to recover new  
270 populations of FLRs previously overlooked.

271 There is a clear population of FLRs confined to nighttime at high latitudes. These  
272 tend to be at lower frequencies which are compatible with FLRs on stretched field lines  
273 in a non-axisymmetric magnetic field (Allan & Wright, 1998; Mills & Wright, 2000; Rus-  
274 sell & Wright, 2010). Since high-latitude stations remote sense the magnetic field at a  
275 much greater distance than the compressed dayside (e.g. Thompson et al., 2020), we posit  
276 that these FLRs are connected to substorms in the magnetotail. The role of ULF waves  
277 with both large (Samson, Harrold, et al., 1992; Samson et al., 1996) and small (Rae et  
278 al., 2014) azimuthal structure has been previously hypothesised as a candidate trigger  
279 mechanism for substorm onset, due to the prominence of FLRs at the precise location  
280 of substorms prior to and following onset (e.g. Rae et al., 2014). Previous ground-based  
281 studies Samson, Lyons, et al. (1992) considered only toroidal (low-m) mode FLRs, as these  
282 are representative of classical resonance from fast mode wave coupling incoming from  
283 the magnetospheric boundary with standing Alfvén wave modes (O. Agapitov et al., 2009).  
284 Toroidal mode waves have also been found to be generated in some cases in energetic  
285 particle injections from substorms (James et al., 2013). Poloidal (high-m) mode waves,  
286 typically thought to originate in drift motions following substorm particle injections (A. V. Agapi-  
287 tov & Cherenmykh, 2011), should be more difficult to observe on the ground due to iono-

spheric screening effects (Hughes & Southwood, 1976). We find, however, that the distribution of nighttime FLRs is similar for both the poloidal and toroidal components. This may be caused by rotation errors of magnetometer signals into H and D using data-based declination resulting in toroidal mode pollution in the D-component, or perhaps that a toroidal-poloidal separation is problematic at high latitudes where the magnetic field is not very dipolar. Conversely, it may support the coupling of modes in realistic physical situations (e.g. Southwood & Hughes, 1983; Sinha et al., 2005). The coupling of modes may provide further insight a causal link between ground-based toroidal and space-based poloidal modes in substorm regions, such as the the transition of poloidal oscillations into toroidal over time controlled by the azimuthal wavenumber and Alfvén velocity profile (Mann & Wright, 1995; Mann et al., 1997) or dispersive effects along the geomagnetic field (Lu et al., 2003, 2007; Rae et al., 2014; Rankin et al., 2005).

We found that the mid-latitude support of low-frequency FLRs was limited completely to the toroidal wave component at Gillam station in the heart of the auroral oval. A number of case studies have suggested the auroral oval as a preferable latitude for magnetospheric resonator excitation (e.g. Bochev et al., 2009; Lam & Rostoker, 1978; Lepidi & Francia, n.d.; V. Pilipenko et al., 2001; Potemra et al., 1988; Simms et al., 2006), however, classical resonance theory implies that resonance location is determined entirely by the plasma mass density profile and magnetic field - not on ionospheric conductances or field aligned currents (V. A. Pilipenko et al., 2016). Reanalysing the linearized MHD equations with a fluctuating external current, V. Pilipenko et al. (2001) was able to derive the generation of toroidal Pc5 ULF waves with the same latitudinal and phase structure observed on the ground as for classical resonances. Since this is precisely the structure that our algorithm aims to detect, it is possible that this population of dayside FLRs in the auroral oval were generated by internally-generated fluctuating magnetospheric field-aligned-currents.

Our statistics presented a band of frequencies ranging from  $\sim 3$ -4mHz which persists in the afternoon sector at mid-high latitudes. While present in both the D and H statistics, this band penetrates deeper for the toroidal mode down to the Island Lake station at  $54^\circ$ . This range of frequencies is typical of the average peak frequencies observed at all latitudes for Pc5 toroidal and poloidal ULF waves in the dusk sector on board spacecraft (e.g. Liu et al., 2009, Figure 9). Typical frequencies in the dawn sector are larger than as dusk, which tend to have larger wave amplitudes (see Liu et al., 2009, Figure 8 and Supporting Information Figure S?), which may be why this dusk-side population was absent from previous statistical studies of ground-based FLRs. The existence of both poloidal and toroidal FLRs throughout dusk is not surprising, however, since the Kelvin-Helmholtz instability is expected to be strong on the dusk flank to drive toroidal FLRs, (Engebretson et al., 1998; Fujita et al., 1996; Pu & Kivelson, 1983), and dynamic pressure fluctuations in the noon sector can periodically move the magnetopause in and out to excite poloidal Pc5 ULF waves (Liu et al., 2009).

The lowest latitude station (Pinawa), where the decomposition into toroidal and poloidal modes is most sensible due to the dominance of the internal dipole-like magnetic field, showed the local time distribution of FLRs most aligned with previous studies but the largest differences between wave polarizations. We observe a peak of FLRs in the morning as found previously (e.g. G. J. Baker et al., 2003; Plaschke et al., 2008), although an additional peak for poloidal FLRs occurs in the afternoon. The presence of poloidal FLRs localized to the  $\sim 1$ -2mHz range suggests that we have identified poloidal FLRs at the numerical (Degeling et al., 2010; Rankin et al., 2006) fundamental frequencies (e.g. Zhang et al., 2019, Figure 6d). In order to be seen on the ground at such low latitudes near morning is consistent with giant pulsation events (Glassmeier et al., 1999; Rostoker et al., 1979; Takahashi et al., 2011; Wang et al., 2018). The isolated patch of toroidal FLRs between  $\sim 4$ -6mHz, with an asymmetric distribution about noon which favours the afternoon sector, is suggestive of controlled ULF wave access across the noon

meridian. The development of a plasmaspheric drainage plume in the afternoon sector during periods of storm activity and enhanced convection allows for ULF waves at our observed frequencies to access deeper into the inner magnetosphere (Degeling et al., 2018b), providing a possible source for the toroidal FLRs detected by our algorithm.

## 6 Conclusions

We have presented a novel FLR detection algorithm for latitudinal arrays of ground magnetometers, using the Synchrosqueezing Transform for signal spectra and techniques from image processing to extract agreeable FLR structures which does not discriminate between wave amplitudes. The Synchrosqueezing Transform was based on the continuous wavelet transform and accurately extracts the frequency and amplitudes of superposed transient ULF waveforms, with the inclusion of time-localization in the signal spectra circumventing any over-normalization incurred from Fourier-based techniques when the transient wave content of a signal is unknown.

Applying the algorithm to 7 years of magnetometer data in the CARISMA network, we were able to uncover poloidal and toroidal FLRs from a variety of sources found in previous studies. Our local time and frequency distributions differed from previous statistical studies of magnetospheric FLRs, which were based on events with peaks in the wave power spectrum, highlighting that our unbiased algorithm is successful in uncovering the types of FLRs that are overlooked by the Fourier Transform, as well as stressing the importance of spectral analysis which aims for accurate frequency identification.

## Acknowledgments

The authors thank I.R. Mann, D.K. Milling and the rest of the CARISMA team for data. CARISMA is operated by the University of Alberta, funded by the Canadian Space Agency.

## References

- Agapitov, A. V., & Cheremnykh, O. K. (2011, 6). Polarization of ULF waves in the earth's magnetosphere. *Kinematics and Physics of Celestial Bodies*, 27(3), 117–123. doi: 10.3103/S0884591311030020
- Agapitov, O., Glassmeier, K.-H., Plaschke, F., Auster, H.-U., Constantinescu, D., Angelopoulos, V., ... McFadden, J. P. (2009, 1). Surface waves and field line resonances: A THEMIS case study. *Journal of Geophysical Research: Space Physics*, 114(A1), 0–27. Retrieved from <https://agupubs.onlinelibrary.wiley.com/doi/full/10.1029/2008JA013553><https://agupubs.onlinelibrary.wiley.com/doi/abs/10.1029/2008JA013553> doi: 10.1029/2008JA013553
- Allan, W., White, S. P., & Poulter, E. M. (1986, 4). Impulse-excited hydromagnetic cavity and field-line resonances in the magnetosphere. *Planetary and Space Science*, 34(4), 371–385. doi: 10.1016/0032-0633(86)90144-3
- Allan, W., & Wright, A. N. (1998, 2). Hydromagnetic wave propagation and coupling in a magnetotail waveguide. *Journal of Geophysical Research: Space Physics*, 103(A2), 2359–2368. Retrieved from <https://agupubs.onlinelibrary.wiley.com/doi/full/10.1029/97JA02874><https://agupubs.onlinelibrary.wiley.com/doi/abs/10.1029/97JA02874><https://agupubs.onlinelibrary.wiley.com/doi/10.1029/97JA02874> doi: 10.1029/97JA02874
- Archer, M. O., Hartinger, M. D., & Horbury, T. S. (2013, 10). Magnetospheric "magic" frequencies as magnetopause surface eigenmodes. *Geophysical Research Letters*, 40(19), 5003–5008. Retrieved from <https://>

- 389 [agupubs.onlinelibrary.wiley.com/doi/full/10.1002/grl.50979](https://agupubs.onlinelibrary.wiley.com/doi/full/10.1002/grl.50979)[https://](https://agupubs.onlinelibrary.wiley.com/doi/abs/10.1002/grl.50979)  
390 [agupubs.onlinelibrary.wiley.com/doi/abs/10.1002/grl.50979](https://agupubs.onlinelibrary.wiley.com/doi/abs/10.1002/grl.50979)[https://](https://agupubs.onlinelibrary.wiley.com/doi/10.1002/grl.50979)  
391 [agupubs.onlinelibrary.wiley.com/doi/10.1002/grl.50979](https://agupubs.onlinelibrary.wiley.com/doi/10.1002/grl.50979) doi:  
392 10.1002/grl.50979
- 393 Baker, D. N., Pulkkinen, T. I., Li, X., Kanekal, S. G., Blake, J. B., Selesnick, R. S.,  
394 ... Rostoker, G. (1998, 8). Coronal mass ejections, magnetic clouds, and  
395 relativistic magnetospheric electron events: ISTP. *Journal of Geophysical*  
396 *Research: Space Physics*, 103(A8), 17279–17291. doi: 10.1029/97ja03329
- 397 Baker, D. N., Pulkkinen, T. I., Li, X., Kanekal, S. G., Ogilvie, K. W., Lepping,  
398 R. P., ... Reeves, G. D. (1998, 8). A strong CME-related magnetic cloud  
399 interaction with the Earth's magnetosphere: ISTP observations of rapid rela-  
400 tivistic electron acceleration on May 15, 1997. *Geophysical Research Letters*,  
401 25(15), 2975–2978. doi: 10.1029/98GL01134
- 402 Baker, G. J., Donovan, E. F., & Jackel, B. J. (2003, 10). A comprehensive survey of  
403 auroral latitude Pc5 pulsation characteristics. *Journal of Geophysical Research:*  
404 *Space Physics*, 108(A10), 1384. Retrieved from [http://doi.wiley.com/](http://doi.wiley.com/10.1029/2002JA009801)  
405 10.1029/2002JA009801 doi: 10.1029/2002JA009801
- 406 Bentley, S. N., Stout, J. R., Bloch, T. E., & Watt, C. E. J. (2020, 10). Ran-  
407 dom Forest Model of Ultralow-Frequency Magnetospheric Wave Power.  
408 *Earth and Space Science*, 7(10), e2020EA001274. Retrieved from  
409 [https://agupubs.onlinelibrary.wiley.com/doi/full/10.1029/](https://agupubs.onlinelibrary.wiley.com/doi/full/10.1029/2020EA001274)  
410 [2020EA001274](https://agupubs.onlinelibrary.wiley.com/doi/abs/10.1029/2020EA001274)[https://agupubs.onlinelibrary.wiley.com/doi/abs/](https://agupubs.onlinelibrary.wiley.com/doi/abs/10.1029/2020EA001274)  
411 [https://agupubs.onlinelibrary.wiley.com/doi/](https://agupubs.onlinelibrary.wiley.com/doi/abs/10.1029/2020EA001274)  
412 [abs/10.1029/2020EA001274](https://agupubs.onlinelibrary.wiley.com/doi/abs/10.1029/2020EA001274) doi: 10.1029/2020EA001274
- 413 Bochev, A. Z., Kudela, K., Dimitrova, I. A., Nenovski, P., Sinha, A. K., & Slivka, M.  
414 (2009, 12). Observations of PC5 pulsations near field-aligned current regions.  
415 *Studia Geophysica et Geodaetica 2009 53:4*, 53(4), 537–556. Retrieved from  
416 <https://link.springer.com/article/10.1007/s11200-009-0038-2> doi:  
417 10.1007/S11200-009-0038-2
- 418 Chandra Gupta, J. (1976). Some Characteristics of Large Amplitude Pc5 Pulsations.  
419 *Australian Journal of Physics*, 29(2), 67. doi: 10.1071/PH760067
- 420 Chen, L., & Hasegawa, A. (1974, 3). A theory of long-period magnetic pulsations:  
421 1. Steady state excitation of field line resonance. *Journal of Geophysical Re-*  
422 *search*, 79(7), 1024–1032. doi: 10.1029/ja079i007p01024
- 423 Degeling, A. W., Rae, I. J., Watt, C. E., Shi, Q. Q., Rankin, R., & Zong, Q. G.  
424 (2018a, 2). Control of ULF Wave Accessibility to the Inner Magnetosphere  
425 by the Convection of Plasma Density. *Journal of Geophysical Research: Space*  
426 *Physics*, 123(2), 1086–1099. Retrieved from [http://doi.wiley.com/10.1002/](http://doi.wiley.com/10.1002/2017JA024874)  
427 2017JA024874 doi: 10.1002/2017JA024874
- 428 Degeling, A. W., Rae, I. J., Watt, C. E. J., Shi, Q. Q., Rankin, R., & Zong,  
429 Q.-G. (2018b, 2). Control of ULF Wave Accessibility to the Inner  
430 Magnetosphere by the Convection of Plasma Density. *Journal of Geo-*  
431 *physical Research: Space Physics*, 123(2), 1086–1099. Retrieved from  
432 [https://agupubs.onlinelibrary.wiley.com/doi/full/10.1002/](https://agupubs.onlinelibrary.wiley.com/doi/full/10.1002/2017JA024874)  
433 [2017JA024874](https://agupubs.onlinelibrary.wiley.com/doi/abs/10.1002/2017JA024874)[https://agupubs.onlinelibrary.wiley.com/doi/abs/](https://agupubs.onlinelibrary.wiley.com/doi/abs/10.1002/2017JA024874)  
434 [10.1002/2017JA024874](https://agupubs.onlinelibrary.wiley.com/doi/abs/10.1002/2017JA024874)[https://agupubs.onlinelibrary.wiley.com/doi/](https://agupubs.onlinelibrary.wiley.com/doi/abs/10.1002/2017JA024874)  
435 [abs/10.1002/2017JA024874](https://agupubs.onlinelibrary.wiley.com/doi/abs/10.1002/2017JA024874) doi: 10.1002/2017JA024874
- 436 Degeling, A. W., Rankin, R., Kabin, K., Rae, I. J., & Fenrich, F. R. (2010,  
437 10). Modeling ULF waves in a compressed dipole magnetic field. *Jour-*  
438 *nal of Geophysical Research: Space Physics*, 115(10), 10212. Retrieved  
439 from [https://agupubs.onlinelibrary.wiley.com/doi/full/10.1029/](https://agupubs.onlinelibrary.wiley.com/doi/full/10.1029/2010JA015410)  
440 [2010JA015410](https://agupubs.onlinelibrary.wiley.com/doi/abs/10.1029/2010JA015410)[https://agupubs.onlinelibrary.wiley.com/doi/abs/](https://agupubs.onlinelibrary.wiley.com/doi/abs/10.1029/2010JA015410)  
441 [10.1029/2010JA015410](https://agupubs.onlinelibrary.wiley.com/doi/abs/10.1029/2010JA015410)[https://agupubs.onlinelibrary.wiley.com/doi/](https://agupubs.onlinelibrary.wiley.com/doi/abs/10.1029/2010JA015410)  
442 [abs/10.1029/2010JA015410](https://agupubs.onlinelibrary.wiley.com/doi/abs/10.1029/2010JA015410) doi: 10.1029/2010JA015410
- 443 Elsdén, T., & Wright, A. N. (2017, 3). The theoretical foundation of 3-D Alfvén

- 444 resonances: Time-dependent solutions. *Journal of Geophysical Research: Space*  
 445 *Physics*, 122(3), 3247–3261. Retrieved from [https://onlinelibrary.wiley](https://onlinelibrary.wiley.com/doi/abs/10.1002/2016JA023811)  
 446 [.com/doi/abs/10.1002/2016JA023811](https://onlinelibrary.wiley.com/doi/abs/10.1002/2016JA023811) doi: 10.1002/2016JA023811
- 447 Elsden, T., & Wright, A. N. (2018, 1). The Broadband Excitation of 3-D Alfvén  
 448 Resonances in a MHD Waveguide. *Journal of Geophysical Research: Space*  
 449 *Physics*, 123(1), 530–547. Retrieved from [http://doi.wiley.com/10.1002/](http://doi.wiley.com/10.1002/2017JA025018)  
 450 [2017JA025018](http://doi.wiley.com/10.1002/2017JA025018) doi: 10.1002/2017JA025018
- 451 Elsden, T., & Wright, A. N. (2019, 1). The Effect of Fast Normal Mode Struc-  
 452 ture and Magnetopause Forcing on FLRs in a 3-D Waveguide. *Journal of Geo-*  
 453 *physical Research: Space Physics*, 124(1), 178–196. Retrieved from [https://](https://onlinelibrary.wiley.com/doi/abs/10.1029/2018JA026222)  
 454 [onlinelibrary.wiley.com/doi/abs/10.1029/2018JA026222](https://onlinelibrary.wiley.com/doi/abs/10.1029/2018JA026222) doi: 10.1029/  
 455 [2018JA026222](https://onlinelibrary.wiley.com/doi/abs/10.1029/2018JA026222)
- 456 Engebretson, M., Glassmeier, K.-H., Stellmacher, M., Hughes, W. J., & Lühr,  
 457 H. (1998, 11). The dependence of high-latitude PcS wave power on solar  
 458 wind velocity and on the phase of high-speed solar wind streams. *Jour-*  
 459 *nal of Geophysical Research: Space Physics*, 103(A11), 26271–26283. doi:  
 460 [10.1029/97JA03143](https://doi.org/10.1029/97JA03143)
- 461 Fujita, S., Glassmeier, K.-H., & Kamide, K. (1996, 12). MHD waves generated by  
 462 the Kelvin-Helmholtz instability in a nonuniform magnetosphere. *Journal*  
 463 *of Geophysical Research: Space Physics*, 101(A12), 27317–27325. Retrieved  
 464 from [https://agupubs.onlinelibrary.wiley.com/doi/full/10.1029/](https://agupubs.onlinelibrary.wiley.com/doi/full/10.1029/96JA02676)  
 465 [96JA02676](https://agupubs.onlinelibrary.wiley.com/doi/full/10.1029/96JA02676)[https://agupubs.onlinelibrary.wiley.com/doi/abs/10.1029/](https://agupubs.onlinelibrary.wiley.com/doi/abs/10.1029/96JA02676)  
 466 [96JA02676](https://agupubs.onlinelibrary.wiley.com/doi/abs/10.1029/96JA02676)[https://agupubs.onlinelibrary.wiley.com/doi/10.1029/](https://agupubs.onlinelibrary.wiley.com/doi/10.1029/96JA02676)  
 467 [96JA02676](https://agupubs.onlinelibrary.wiley.com/doi/10.1029/96JA02676) doi: 10.1029/96JA02676
- 468 Glassmeier, K. H., Buchert, S., Motschmann, U., Korth, A., & Pedersen, A. (1999).  
 469 Concerning the generation of geomagnetic giant pulsations by drift-bounce  
 470 resonance ring current instabilities. *Annales Geophysicae*, 17(3), 338–350. doi:  
 471 [10.1007/S00585-999-0338-4](https://doi.org/10.1007/S00585-999-0338-4)
- 472 Glassmeier, K. H., & Stellmacher, M. (2000, 8). Concerning the local time asymme-  
 473 try of Pc5 wave power at the ground and field line resonance widths. *Journal*  
 474 *of Geophysical Research: Space Physics*, 105(A8), 18847–18855. doi: 10.1029/  
 475 [2000ja900037](https://doi.org/10.1029/2000ja900037)
- 476 Hughes, W. J., & Southwood, D. J. (1976, 7). SCREENING OF MICROPULSA-  
 477 TION SIGNALS BY THE ATMOSPHERE AND IONOSPHERE. *J Geophys*  
 478 *Res*, 81(19), 3234–3240. Retrieved from [http://doi.wiley.com/10.1029/](http://doi.wiley.com/10.1029/JA081i019p03234)  
 479 [JA081i019p03234](http://doi.wiley.com/10.1029/JA081i019p03234) doi: 10.1029/JA081i019p03234
- 480 Jacobs, J. A., Kato, Y., Matsushita, S., & Troitskaya, V. A. (1964, 1). Classification  
 481 of geomagnetic micropulsations. *Journal of Geophysical Research*, 69(1), 180–  
 482 181. doi: 10.1029/jz069i001p00180
- 483 James, M. K., Yeoman, T. K., Mager, P. N., & Klimushkin, D. Y. (2013, 4). The  
 484 spatio-temporal characteristics of ULF waves driven by substorm injected par-  
 485 ticles. *Journal of Geophysical Research: Space Physics*, 118(4), 1737–1749.  
 486 Retrieved from [https://agupubs.onlinelibrary.wiley.com/doi/full/](https://agupubs.onlinelibrary.wiley.com/doi/full/10.1002/jgra.50131)  
 487 [10.1002/jgra.50131](https://agupubs.onlinelibrary.wiley.com/doi/full/10.1002/jgra.50131)[https://agupubs.onlinelibrary.wiley.com/doi/](https://agupubs.onlinelibrary.wiley.com/doi/abs/10.1002/jgra.50131)  
 488 [abs/10.1002/jgra.50131](https://agupubs.onlinelibrary.wiley.com/doi/abs/10.1002/jgra.50131)[https://agupubs.onlinelibrary.wiley.com/doi/](https://agupubs.onlinelibrary.wiley.com/doi/10.1002/jgra.50131)  
 489 [10.1002/jgra.50131](https://agupubs.onlinelibrary.wiley.com/doi/10.1002/jgra.50131) doi: 10.1002/JGRA.50131
- 490 Kivelson, M. G., & Southwood, D. J. (1985, 1). Resonant ULF waves: A new inter-  
 491 pretation. *Geophysical Research Letters*, 12(1), 49–52. Retrieved from [http://](http://doi.wiley.com/10.1029/GL012i001p00049)  
 492 [doi.wiley.com/10.1029/GL012i001p00049](http://doi.wiley.com/10.1029/GL012i001p00049) doi: 10.1029/GL012i001p00049
- 493 Lam, K. L., & Rostoker, G. (1978, 5). The relationship of pc 5 micropulsation ac-  
 494 tivity in the morning sector to the auroral westward electrojet. *Planetary and*  
 495 *Space Science*, 26(5), 473–492. doi: 10.1016/0032-0633(78)90069-7
- 496 Lepidi, S., & Francia, P. (n.d.). Low-frequency (1-4 mHz) geomagnetic celd uctu-  
 497 ation power at diierent latitudes for a diagnosis of the auroral oval position.  
 498 *Mem. S.A.It*, 74, 762.

- 499 Liu, W., Sarris, T. E., Li, X., Elkington, S. R., Ergun, R., Angelopoulos, V.,  
500 ... Glassmeier, K. H. (2009, 12). Electric and magnetic field observa-  
501 tions of Pc4 and Pc5 pulsations in the inner magnetosphere: A statistical  
502 study. *Journal of Geophysical Research: Space Physics*, 114(12), n/a-n/a.  
503 Retrieved from <http://doi.wiley.com/10.1029/2009JA014243> doi:  
504 10.1029/2009JA014243
- 505 Lu, J. Y., Rankin, R., Marchand, R., Rae, I. J., Wang, W., Solomon, S. C., &  
506 Lei, J. (2007, 10). Electrodynamics of magnetosphere-ionosphere cou-  
507 pling and feedback on magnetospheric field line resonances. *Journal*  
508 *of Geophysical Research: Space Physics*, 112(A10), 10219. Retrieved  
509 from [https://agupubs.onlinelibrary.wiley.com/doi/full/10.1029/](https://agupubs.onlinelibrary.wiley.com/doi/full/10.1029/2006JA012195)  
510 [https://agupubs.onlinelibrary.wiley.com/doi/abs/](https://agupubs.onlinelibrary.wiley.com/doi/abs/10.1029/2006JA012195)  
511 [10.1029/2006JA012195](https://agupubs.onlinelibrary.wiley.com/doi/10.1029/2006JA012195) doi: 10.1029/2006JA012195
- 512 Lu, J. Y., Rankin, R., Marchand, R., & Tikhonchuk, V. T. (2003, 5). Nonlin-  
513 ear acceleration of dispersive effects in field line resonances. *Geophysical*  
514 *Research Letters*, 30(10). Retrieved from [https://agupubs.pericles-](https://agupubs.pericles-prod.literatumonline.com/doi/full/10.1029/2003GL016929)  
515 [-prod.literatumonline.com/doi/full/10.1029/2003GL016929](https://agupubs.pericles-prod.literatumonline.com/doi/full/10.1029/2003GL016929)[https://](https://agupubs.pericles-prod.literatumonline.com/doi/abs/10.1029/2003GL016929)  
516 [agupubs.pericles-prod.literatumonline.com/doi/abs/10.1029/](https://agupubs.pericles-prod.literatumonline.com/doi/abs/10.1029/2003GL016929)  
517 [2003GL016929](https://agupubs.pericles-prod.literatumonline.com/doi/abs/10.1029/2003GL016929)[https://agupubs.onlinelibrary.wiley.com/doi/10.1029/](https://agupubs.onlinelibrary.wiley.com/doi/10.1029/2003GL016929)  
518 [2003GL016929](https://agupubs.onlinelibrary.wiley.com/doi/10.1029/2003GL016929) doi: 10.1029/2003GL016929
- 519 Lysak, R. L., Song, Y., Waters, C. L., Sciffer, M. D., & Obana, Y. (2020, 7). Nu-  
520 merical Investigations of Interhemispheric Asymmetry due to Ionospheric  
521 Conductance. *Journal of Geophysical Research: Space Physics*, 125(7). doi:  
522 10.1029/2020JA027866
- 523 Mann, I. R., Milling, D. K., Rae, I. J., Ozeke, L. G., Kale, A., Kale, Z. C., ...  
524 Singer, H. J. (2008, 12). The upgraded CARISMA magnetometer ar-  
525 ray in the THEMIS era. *Space Science Reviews*, 141(1-4), 413–451. doi:  
526 10.1007/s11214-008-9457-6
- 527 Mann, I. R., O'Brien, T. P., & Milling, D. K. (2004, 1). Correlations between ULF  
528 wave power, solar wind speed, and relativistic electron flux in the magneto-  
529 sphere: Solar cycle dependence. *Journal of Atmospheric and Solar-Terrestrial*  
530 *Physics*, 66(2), 187–198. doi: 10.1016/j.jastp.2003.10.002
- 531 Mann, I. R., & Wright, A. N. (1995, 12). Finite lifetimes of ideal poloidal Alfvén  
532 waves. *Journal of Geophysical Research: Space Physics*, 100(A12), 23677–  
533 23686. Retrieved from [https://agupubs.pericles-prod.literatumonline](https://agupubs.pericles-prod.literatumonline.com/doi/full/10.1029/95JA02689)  
534 [.com/doi/full/10.1029/95JA02689](https://agupubs.pericles-prod.literatumonline.com/doi/full/10.1029/95JA02689)[https://agupubs](https://agupubs.pericles-prod.literatumonline.com/doi/abs/10.1029/95JA02689)  
535 [.pericles-prod](https://agupubs.pericles-prod.literatumonline.com/doi/abs/10.1029/95JA02689)  
536 [.literatumonline.com/doi/abs/10.1029/95JA02689](https://agupubs.pericles-prod.literatumonline.com/doi/abs/10.1029/95JA02689)[https://agupubs](https://agupubs.onlinelibrary.wiley.com/doi/10.1029/95JA02689)  
537 [.onlinelibrary.wiley.com/doi/10.1029/95JA02689](https://agupubs.onlinelibrary.wiley.com/doi/10.1029/95JA02689) doi: 10.1029/  
538 95JA02689
- 539 Mann, I. R., Wright, A. N., & Hood, A. W. (1997, 2). Multiple-timescales  
540 analysis of ideal poloidal Alfvén waves. *Journal of Geophysical Re-*  
541 *search: Space Physics*, 102(A2), 2381–2390. Retrieved from [https://](https://agupubs.pericles-prod.literatumonline.com/doi/full/10.1029/96JA03034)  
542 [agupubs.pericles-prod.literatumonline.com/doi/full/10.1029/](https://agupubs.pericles-prod.literatumonline.com/doi/full/10.1029/96JA03034)  
543 [96JA03034](https://agupubs.pericles-prod.literatumonline.com/doi/abs/10.1029/96JA03034)[https://agupubs.onlinelibrary.wiley.com/doi/](https://agupubs.onlinelibrary.wiley.com/doi/abs/10.1029/96JA03034)  
544 [abs/10.1029/96JA03034](https://agupubs.onlinelibrary.wiley.com/doi/abs/10.1029/96JA03034) doi: 10.1029/96JA03034
- 545 Mills, K. J., & Wright, A. N. (2000, 4). Trapping and excitation of modes in the  
546 magnetotail. *Physics of Plasmas*, 7(5), 1572. Retrieved from [https://aip](https://aip.scitation.org/doi/abs/10.1063/1.873977)  
547 [.scitation.org/doi/abs/10.1063/1.873977](https://aip.scitation.org/doi/abs/10.1063/1.873977) doi: 10.1063/1.873977
- 548 Pilipenko, V., Watermann, J., Popov, V., & Papitashvili, V. (2001, 9). Relation-  
549 ship between auroral electrojet and Pc5 ULF waves. *Journal of Atmospheric*  
550 *and Solar-Terrestrial Physics*, 63(14), 1545–1557. doi: 10.1016/S1364-6826(01)  
551 00031-1
- 552 Pilipenko, V. A., Yu. Klimushkin, D., Mager, P. N., Engebretson, M. J., &  
553

## CHAPTER 6. MAPPING ULF WAVE POWER FROM THE GROUND INTO SPACE

manuscript submitted to *Geophysical Research Letters*

- 554 Kozyreva, O. V. (2016, 2). Generation of resonant Alfvén waves in  
 555 the auroral oval. *Annales Geophysicae*, *34*(2), 241–248. doi: 10.5194/  
 556 ANGE0-34-241-2016
- 557 Plaschke, F., Glassmeier, K.-h., Constantinescu, O. D., Mann, I. R., Milling, D. K.,  
 558 Motschmann, U., & Rae, I. J. (2008). *Statistical analysis of ground based mag-*  
 559 *netic field measurements with the field line resonance detector* (Vol. 26; Tech.  
 560 Rep.). Retrieved from [www.ann-geophys.net/26/3477/2008/](http://www.ann-geophys.net/26/3477/2008/)
- 561 Potemra, T. A., Zanetti, L. J., Bythrow, P. F., Erlandson, R. E., Lundin, R.,  
 562 Marklund, G. T., ... Lindqvist, P.-A. (1988, 4). Resonant geomagnetic  
 563 field oscillations and Birkeland currents in the morning sector. *Journal*  
 564 *of Geophysical Research: Space Physics*, *93*(A4), 2661–2674. Retrieved  
 565 from [https://agupubs.onlinelibrary.wiley.com/doi/full/10.1029/](https://agupubs.onlinelibrary.wiley.com/doi/full/10.1029/JA093iA04p02661)  
 566 [https://agupubs.onlinelibrary.wiley.com/doi/abs/](https://agupubs.onlinelibrary.wiley.com/doi/abs/10.1029/JA093iA04p02661)  
 567 [https://agupubs.onlinelibrary.wiley.com/](https://agupubs.onlinelibrary.wiley.com/doi/10.1029/JA093iA04p02661)  
 568 [doi/10.1029/JA093iA04p02661](https://agupubs.onlinelibrary.wiley.com/doi/10.1029/JA093iA04p02661) doi: 10.1029/JA093iA04p02661
- 569 Pu, Z.-Y., & Kivelson, M. G. (1983, 2). Kelvin-Helmholtz instability at  
 570 the magnetopause: Solution for compressible plasmas. *Journal of Geo-*  
 571 *physical Research: Space Physics*, *88*(A2), 841–852. Retrieved from  
 572 [https://agupubs.onlinelibrary.wiley.com/doi/full/10.1029/](https://agupubs.onlinelibrary.wiley.com/doi/full/10.1029/JA088iA02p00841)  
 573 [https://agupubs.onlinelibrary.wiley.com/doi/abs/](https://agupubs.onlinelibrary.wiley.com/doi/abs/10.1029/JA088iA02p00841)  
 574 [https://agupubs.onlinelibrary.wiley.com/](https://agupubs.onlinelibrary.wiley.com/doi/10.1029/JA088iA02p00841)  
 575 [doi/10.1029/JA088iA02p00841](https://agupubs.onlinelibrary.wiley.com/doi/10.1029/JA088iA02p00841) doi: 10.1029/JA088iA02p00841
- 576 Rae, I. J., Donovan, E. F., Mann, I. R., Fenrich, F. R., Watt, C. E. J., Milling,  
 577 D. K., ... Balogh, A. (2005, 12). Evolution and characteristics of global Pc5  
 578 ULF waves during a high solar wind speed interval. *Journal of Geophysical Re-*  
 579 *search*, *110*(A12), A12211. Retrieved from [http://doi.wiley.com/10.1029/](http://doi.wiley.com/10.1029/2005JA011007)  
 580 [2005JA011007](http://doi.wiley.com/10.1029/2005JA011007) doi: 10.1029/2005JA011007
- 581 Rae, I. J., Mann, I. R., Dent, Z. C., Milling, D. K., Donovan, E. F., & Spanswick,  
 582 E. (2007, 4). Multiple field line resonances: Optical, magnetic and ab-  
 583 sorption signatures. *Planetary and Space Science*, *55*(6), 701–713. doi:  
 584 10.1016/j.pss.2006.02.009
- 585 Rae, I. J., Murphy, K. R., Watt, C. E. J., Rostoker, G., Rankin, R., Mann, I. R., ...  
 586 Forsyth, C. (2014, 7). Field line resonances as a trigger and a tracer for sub-  
 587 storm onset. *Journal of Geophysical Research: Space Physics*, *119*(7), 5343–  
 588 5363. Retrieved from [https://agupubs.onlinelibrary.wiley.com/doi/](https://agupubs.onlinelibrary.wiley.com/doi/full/10.1002/2013JA018889)  
 589 [https://agupubs.onlinelibrary.wiley.com/](https://agupubs.onlinelibrary.wiley.com/doi/abs/10.1002/2013JA018889)  
 590 [doi/abs/10.1002/2013JA018889](https://agupubs.onlinelibrary.wiley.com/doi/10.1002/2013JA018889)  
 591 [https://agupubs.onlinelibrary.wiley](https://agupubs.onlinelibrary.wiley.com/doi/10.1002/2013JA018889)  
 592 [.com/doi/10.1002/2013JA018889](https://agupubs.onlinelibrary.wiley.com/doi/10.1002/2013JA018889) doi: 10.1002/2013JA018889
- 593 Rankin, R., Kabin, K., Lu, J. Y., Mann, I. R., Marchand, R., Rae, I. J., ... Dono-  
 594 van, E. F. (2005, 10). Magnetospheric field-line resonances: Ground-based  
 595 observations and modeling. *Journal of Geophysical Research: Space Physics*,  
 596 *110*(A10), A10S09. Retrieved from [http://doi.wiley.com/10.1029/](http://doi.wiley.com/10.1029/2004JA010919)  
 597 [2004JA010919](http://doi.wiley.com/10.1029/2004JA010919) doi: 10.1029/2004JA010919
- 598 Rankin, R., Kabin, K., & Marchand, R. (2006, 1). Alfvénic field line resonances  
 599 in arbitrary magnetic field topology. *Advances in Space Research*, *38*(8), 1720–  
 600 1729. doi: 10.1016/j.asr.2005.09.034
- 601 Rostoker, G., Lam, H.-L., & Olson, J. V. (1979, 9). PC 4 giant pulsations  
 602 in the morning sector. *Journal of Geophysical Research: Space Physics*,  
 603 *84*(A9), 5153–5166. Retrieved from [https://agupubs.onlinelibrary](https://agupubs.onlinelibrary.wiley.com/doi/full/10.1029/JA084iA09p05153)  
 604 [.wiley.com/doi/full/10.1029/JA084iA09p05153](https://agupubs.onlinelibrary.wiley.com/doi/abs/10.1029/JA084iA09p05153)  
 605 [https://agupubs](https://agupubs.onlinelibrary.wiley.com/doi/abs/10.1029/JA084iA09p05153)  
 606 [.onlinelibrary.wiley.com/doi/abs/10.1029/JA084iA09p05153](https://agupubs.onlinelibrary.wiley.com/doi/10.1029/JA084iA09p05153)  
 607 [https://](https://agupubs.onlinelibrary.wiley.com/doi/10.1029/JA084iA09p05153)  
 608 [agupubs.onlinelibrary.wiley.com/doi/10.1029/JA084iA09p05153](https://agupubs.onlinelibrary.wiley.com/doi/10.1029/JA084iA09p05153) doi:  
 10.1029/JA084iA09p05153
- 607 Russell, A. J. B., & Wright, A. N. (2010, 2). Resonant absorption with 2D vari-  
 608 ation of field line eigenfrequencies. *Astronomy & Astrophysics*, *511*(2),

- 609 A17. Retrieved from [https://www.aanda.org/articles/aa/abs/2010/](https://www.aanda.org/articles/aa/abs/2010/03/aa12669-09/aa12669-09.html)  
610 [03/aa12669-09/aa12669-09.html](https://www.aanda.org/articles/aa/abs/2010/03/aa12669-09/aa12669-09.html) doi: 10.1051/0004-6361/200912669
- 611 Samson, J. C., Cogger, L. L., & Pao, Q. (1996, 8). Observations of field line  
612 resonances, auroral arcs, and auroral vortex structures. *Journal of Geo-*  
613 *physical Research: Space Physics*, 101(A8), 17373–17383. Retrieved from  
614 [https://agupubs.pericles-prod.literatumonline.com/doi/full/10](https://agupubs.pericles-prod.literatumonline.com/doi/full/10.1029/96JA01086)  
615 [.1029/96JA01086](https://agupubs.pericles-prod.literatumonline.com/doi/full/10.1029/96JA01086)[https://agupubs.pericles-prod.literatumonline.com/](https://agupubs.pericles-prod.literatumonline.com/doi/abs/10.1029/96JA01086)  
616 [doi/abs/10.1029/96JA01086](https://agupubs.pericles-prod.literatumonline.com/doi/abs/10.1029/96JA01086)[https://agupubs.onlinelibrary.wiley.com/](https://agupubs.onlinelibrary.wiley.com/doi/10.1029/96JA01086)  
617 [doi/10.1029/96JA01086](https://agupubs.onlinelibrary.wiley.com/doi/10.1029/96JA01086) doi: 10.1029/96JA01086
- 618 Samson, J. C., Harrold, B. G., Ruohoniemi, J. M., Greenwald, R. A., & Walker,  
619 A. D. (1992, 3). Field line resonances associated with MHD waveguides in the  
620 magnetosphere. *Geophysical Research Letters*, 19(5), 441–444. Retrieved from  
621 <http://doi.wiley.com/10.1029/92GL00116> doi: 10.1029/92GL00116
- 622 Samson, J. C., Jacobs, J. A., & Rostoker, G. (1971, 6). Latitude-dependent char-  
623 acteristics of long-period geomagnetic micropulsations. *Journal of Geophysical*  
624 *Research*, 76(16), 3675–3683. doi: 10.1029/ja076i016p03675
- 625 Samson, J. C., Lyons, L. R., Newell, P. T., Creutzberg, F., & Xu, B. (1992,  
626 11). Proton aurora and substorm intensifications. *Geophysical Research*  
627 *Letters*, 19(21), 2167–2170. Retrieved from [https://agupubs.pericles](https://agupubs.pericles-prod.literatumonline.com/doi/full/10.1029/92GL02184)  
628 [-prod.literatumonline.com/doi/full/10.1029/92GL02184](https://agupubs.pericles-prod.literatumonline.com/doi/full/10.1029/92GL02184)[https://](https://agupubs.pericles-prod.literatumonline.com/doi/abs/10.1029/92GL02184)  
629 [agupubs.pericles-prod.literatumonline.com/doi/abs/10.1029/](https://agupubs.pericles-prod.literatumonline.com/doi/abs/10.1029/92GL02184)  
630 [92GL02184](https://agupubs.pericles-prod.literatumonline.com/doi/abs/10.1029/92GL02184)[https://agupubs.onlinelibrary.wiley.com/doi/10.1029/](https://agupubs.onlinelibrary.wiley.com/doi/10.1029/92GL02184)  
631 [92GL02184](https://agupubs.onlinelibrary.wiley.com/doi/10.1029/92GL02184) doi: 10.1029/92GL02184
- 632 Simms, L. E., Engebretson, M. J., Posch, J. L., & Hughes, W. J. (2006, 10). Effects  
633 of the equatorward auroral boundary location and solar wind parameters on  
634 Pc5 activity at auroral zone stations: A multiple regression analysis. *Jour-*  
635 *nal of Geophysical Research: Space Physics*, 111(A10), 10217. Retrieved  
636 from [https://agupubs.onlinelibrary.wiley.com/doi/full/10.1029/](https://agupubs.onlinelibrary.wiley.com/doi/full/10.1029/2005JA011587)  
637 [2005JA011587](https://agupubs.onlinelibrary.wiley.com/doi/full/10.1029/2005JA011587)[https://agupubs.onlinelibrary.wiley.com/doi/abs/](https://agupubs.onlinelibrary.wiley.com/doi/abs/10.1029/2005JA011587)  
638 [10.1029/2005JA011587](https://agupubs.onlinelibrary.wiley.com/doi/abs/10.1029/2005JA011587)[https://agupubs.onlinelibrary.wiley.com/doi/](https://agupubs.onlinelibrary.wiley.com/doi/10.1029/2005JA011587)  
639 [10.1029/2005JA011587](https://agupubs.onlinelibrary.wiley.com/doi/10.1029/2005JA011587) doi: 10.1029/2005JA011587
- 640 Sinha, A. K., Yeoman, T. K., Wild, J. A., Wright, D. M., Cowley, S. W., & Balogh,  
641 A. (2005). Evidence of transverse magnetospheric field line oscillations as ob-  
642 served from Cluster and ground magnetometers. *Annales Geophysicae*, 23(3),  
643 919–929. doi: 10.5194/ANGE0-23-919-2005
- 644 Southwood, D. J. (1974, 3). Some features of field line resonances in the magne-  
645 tosphere. *Planetary and Space Science*, 22(3), 483–491. doi: 10.1016/0032-  
646 -0633(74)90078-6
- 647 Southwood, D. J., & Hughes, W. J. (1983, 8). Theory of hydromagnetic waves in  
648 the magnetosphere. *Space Science Reviews*, 35(4), 301–366. Retrieved from  
649 <https://link.springer.com/article/10.1007/BF00169231> doi: 10.1007/  
650 BF00169231
- 651 Stewart, B. (1861, 12). XXII. On the great magnetic disturbance which extended  
652 from August 28 to September 7, 1859, as recorded by photography at the Kew  
653 Observatory. *Philosophical Transactions of the Royal Society of London*, 151,  
654 423–430. doi: 10.1098/rstl.1861.0023
- 655 Takahashi, K., Glassmeier, K.-H., Angelopoulos, V., Bonnell, J., Nishimura, Y.,  
656 Singer, H. J., & Russell, C. T. (2011, 11). Multisatellite observations of a giant  
657 pulsation event. *Journal of Geophysical Research: Space Physics*, 116(A11),  
658 11223. Retrieved from [https://agupubs.onlinelibrary.wiley.com/doi/](https://agupubs.onlinelibrary.wiley.com/doi/full/10.1029/2011JA016955)  
659 [full/10.1029/2011JA016955](https://agupubs.onlinelibrary.wiley.com/doi/full/10.1029/2011JA016955)[https://agupubs.onlinelibrary.wiley.com/](https://agupubs.onlinelibrary.wiley.com/doi/abs/10.1029/2011JA016955)  
660 [doi/abs/10.1029/2011JA016955](https://agupubs.onlinelibrary.wiley.com/doi/abs/10.1029/2011JA016955)[https://agupubs.onlinelibrary.wiley](https://agupubs.onlinelibrary.wiley.com/doi/10.1029/2011JA016955)  
661 [.com/doi/10.1029/2011JA016955](https://agupubs.onlinelibrary.wiley.com/doi/10.1029/2011JA016955) doi: 10.1029/2011JA016955
- 662 Tary, J. B., Herrera, R. H., & Baan, M. v. d. (2018, 8). Analysis of time-  
663 varying signals using continuous wavelet and synchrosqueezed transforms.

- 664 *Philosophical Transactions of the Royal Society A: Mathematical, Physical*  
665 *and Engineering Sciences*, 376(2126), 20170254. Retrieved from  
666 <https://royalsocietypublishing.org/doi/abs/10.1098/rsta.2017.0254>  
667 doi: 10.1098/RSTA.2017.0254
- 668 Thakur, G., Brevdo, E., Fućkar, N. S., & Wu, H. T. (2013, 5). The Synchroqueez-  
669 ing algorithm for time-varying spectral analysis: Robustness properties and  
670 new paleoclimate applications. *Signal Processing*, 93(5), 1079–1094. doi:  
671 10.1016/J.SIGPRO.2012.11.029
- 672 Thompson, R. L., Morley, S. K., Watt, C. E. J., Bentley, S. N., & Williams, P. D.  
673 (2020, 12). Pro-L\* - A probabilistic L\* mapping tool for ground observa-  
674 tions. *Space Weather*. Retrieved from [https://agupubs.onlinelibrary](https://agupubs.onlinelibrary.wiley.com/doi/full/10.1029/2020SW002602)  
675 [.wiley.com/doi/full/10.1029/2020SW002602](https://agupubs.onlinelibrary.wiley.com/doi/full/10.1029/2020SW002602)<https://agupubs>  
676 [.onlinelibrary.wiley.com/doi/abs/10.1029/2020SW002602](https://agupubs.onlinelibrary.wiley.com/doi/abs/10.1029/2020SW002602)[https://](https://agupubs)  
677 [agupubs.onlinelibrary.wiley.com/doi/10.1029/2020SW002602](https://agupubs.onlinelibrary.wiley.com/doi/10.1029/2020SW002602) doi:  
678 10.1029/2020sw002602
- 679 Walker, A., Greenwald, R., Stuart, W., & Green, C. (1979). Stare auroral radar  
680 observations of Pc 5 geomagnetic pulsations. *Journal of Geophysical Research*,  
681 84(A7), 3373. doi: 10.1029/ja084ia07p03373
- 682 Wang, C., Rankin, R., Wang, Y., Zong, Q.-G., Zhou, X., Takahashi, K., ...  
683 Degeling, A. W. (2018, 6). Poloidal Mode Wave-Particle Interactions In-  
684 ferred From Van Allen Probes and CARISMA Ground-Based Observations.  
685 *Journal of Geophysical Research: Space Physics*, 123(6), 4652–4667. Retrieved  
686 from [https://agupubs.onlinelibrary.wiley.com/doi/full/10.1029/](https://agupubs.onlinelibrary.wiley.com/doi/full/10.1029/2017JA025123)  
687 [2017JA025123](https://agupubs.onlinelibrary.wiley.com/doi/abs/10.1029/2017JA025123)[https://agupubs.onlinelibrary.wiley.com/doi/abs/](https://agupubs.onlinelibrary.wiley.com/doi/abs/10.1029/2017JA025123)  
688 [10.1029/2017JA025123](https://agupubs.onlinelibrary.wiley.com/doi/10.1029/2017JA025123)[https://agupubs.onlinelibrary.wiley.com/doi/](https://agupubs.onlinelibrary.wiley.com/doi/10.1029/2017JA025123)  
689 [10.1029/2017JA025123](https://agupubs.onlinelibrary.wiley.com/doi/10.1029/2017JA025123) doi: 10.1029/2017JA025123
- 690 Zhang, S., Tian, A., Degeling, A. W., Shi, Q., Wang, M., Hao, Y., ... Bai, S. (2019,  
691 12). Pc4-5 Poloidal ULF Wave Observed in the Dawnside Plasmaspheric  
692 Plume. *Journal of Geophysical Research: Space Physics*, 124(12), 9986–9998.  
693 Retrieved from [https://onlinelibrary.wiley.com/doi/full/10.1029/](https://onlinelibrary.wiley.com/doi/full/10.1029/2019JA027319)  
694 [2019JA027319](https://onlinelibrary.wiley.com/doi/abs/10.1029/2019JA027319)[https://onlinelibrary.wiley.com/doi/abs/10.1029/](https://onlinelibrary.wiley.com/doi/abs/10.1029/2019JA027319)  
695 [2019JA027319](https://agupubs.onlinelibrary.wiley.com/doi/10.1029/2019JA027319)[https://agupubs.onlinelibrary.wiley.com/doi/10.1029/](https://agupubs.onlinelibrary.wiley.com/doi/10.1029/2019JA027319)  
696 [2019JA027319](https://agupubs.onlinelibrary.wiley.com/doi/10.1029/2019JA027319) doi: 10.1029/2019JA027319
- 697 Ziesolleck, C. W. S., Fenrich, F. R., Samson, J. C., & McDiarmid, D. R. (1998, 6).  
698 Pc5 field line resonance frequencies and structure observed by SuperDARN  
699 and CANOPUS. *Journal of Geophysical Research: Space Physics*, 103(A6),  
700 11771–11785. doi: 10.1029/98ja00590

### **6.7.1 Supporting Information**

The following document has been prepared for submission in the *Geophysical Research Letters*, as Supporting information for Section 6.7. The entirety of this document, however, fits within the wider scope of this thesis and should be considered in this context.

## Supporting Information for ”Global frequency distribution of field line resonances in the inner magnetosphere”

R. L. Thompson<sup>1</sup>, C. E. J. Watt<sup>2</sup>, P. D. Williams<sup>3</sup>, S. N. Bentley<sup>2</sup>

<sup>1</sup>Department of Mathematics and Statistics, University of Reading, UK

<sup>2</sup>Northumbria University, UK

<sup>3</sup>Department of Meteorology, University of Reading, UK

### Contents of this file

1. Extraction of transient waveforms using the Synchrosqueezing Transform (SSQT) and Hessian-based image feature detection
2. Automated field line resonance detection algorithm across magnetometers
3. Table of saved variables in FLR algorithm
4. Table of magnetometer station information
5. Supplementary Figures to main results in manuscript

### 1. Extraction of transient waveforms using the Synchrosqueezing Transform (SSQT) and Hessian-based image feature detection

Real signals are often comprised of multiple amplitude or frequency modulated (AM/FM) components plus some noise (not necessarily Gaussian)  $Z(t)$

$$f(t) = \sum_k f_k(t) + Z(t) \tag{1}$$

X - 2

$$f_k(t) = A_k(t) \cos(2\pi\phi_k(t)) \quad (2)$$

$$= \Re[A_k(t) \exp(2\pi i\phi_k(t))] \quad (3)$$

The goal is to recover the amplitudes  $\{A_k(t)\} \geq 0$  and *instantaneous frequencies* (IF)  $\{\phi'_k(t)\} \geq 0$ .

### 1.1. Continuous wavelet transform (CWT)

We consider wavelets  $\psi$  concentrated on the positive frequency axis:  $\Psi(\xi) = 0, \forall \xi < 0$  with  $\Psi$  the Fourier transform of  $\psi$ . If the mother wavelet satisfies the admissibility condition

$$\int_{-\infty}^{\infty} \psi(t) dt = 0 \quad (4)$$

we define the CWT of  $f$  at *scale*  $a$  and *time-shift*  $t$  by

$$W_f(a, t) = a^{-1/2} \int_{-\infty}^{\infty} f(u) \overline{\psi\left(\frac{u-t}{a}\right)} du \quad (5)$$

Here,  $(-)$  denotes the *complex-conjugate* operation.

Scales are determined by supplying a number of *octaves* and the *voices* within each octave. Defining the product of both of these as  $M$ , scales are given by

$$a_k = 2^{k/n_v} \quad (6)$$

where  $n_v$  is the number of voices and  $1 \leq k \leq M$ . Choice of  $M, n_v$  amounts to a trade-off between frequency resolution and computational cost.

### 1.2. Phase-transform

Suppose that we have a purely harmonic signal  $f(t) = A \cos(\Omega t)$ , then the CWT is given by

$$W_f(a, t) = a^{-1/2} \int_{-\infty}^{\infty} f(u) \overline{\psi\left(\frac{u-t}{a}\right)} du$$

$$= \frac{1}{2\pi} \int_{-\infty}^{\infty} F(\xi) a^{1/2} \overline{\Psi(a\xi)} e^{it\xi} d\xi \quad (7)$$

$$= \frac{A}{4\pi} \int_{-\infty}^{\infty} [\delta(\xi - \Omega) + \delta(\xi + \Omega)] a^{1/2} \overline{\Psi(a\xi)} e^{it\xi} d\xi \quad (8)$$

$$= \frac{A}{4\pi} a^{1/2} \overline{\Psi(a\Omega)} e^{it\Omega} \quad (9)$$

with  $F(\cdot)$  the Fourier transform of  $f$ .

It follows that if  $\Psi(\xi)$  is concentrated around  $\xi = \Omega_0$ , then the CWT  $W_f(a, t)$  will be concentrated around  $a = \Omega_0/\Omega$ . Redundancy in the CWT means that information is spread across the horizontal line  $a = \Omega_0/\Omega$  to other scales in the time-scale plane, however. Daubechies and Maes (2019) observed that contrary to the redundancy across scales, the oscillatory behaviour across time-shifts preserves the original frequency  $\Omega$ , regardless of any scale  $a$  considered.

We therefore define the *phase-transform* as a candidate IF for any  $(a, t)$  with  $W_f(a, t) \neq 0$

$$\omega(a, t) = \frac{1}{2\pi i W_f(a, t)} \partial_t W_f(a, t) \quad (10)$$

which follows immediately from the derivative of Equation 9 with respect to  $t$ .

Now,  $\omega$  is unstable when  $|W_f| \approx 0$  due to noise and other artifacts in a signal. Therefore, we set a hard threshold  $\gamma_W$  and disregard instances in the CWT where  $|W_f| \leq \gamma_W$  (Thakur et al., 2013). The default value in an ideal noiseless case is set to  $10^{-8}$  for double precision machines (Thakur et al., 2013). For real signals (where the level of noise is unknown), a sensible value for  $\gamma_W$  makes use of the finest scale of the wavelet decomposition and the *noise variance*  $\sigma_v^2$  (Donoho, 1995). This is defined as the median absolute deviation (MAD) of the first octave (Donoho, 1995; Herrera et al., 2014; Thakur

X - 4

et al., 2013)

$$\sigma_\nu = \text{median}(|W_f(a_{1:n_\nu}, b) - \text{median}(W_f(a_{1:n_\nu}, b))|)/0.6745 \quad (11)$$

with normalizing factor MAD from a Gaussian distribution. The threshold is then weighted by the signal length to be asymptotically optimal

$$\gamma_W = \sqrt{2 \log n} \sigma_\nu \quad (12)$$

### 1.3. Synchrosqueezing transform

We summarise the key results for the synchrosqueezing transform below. For a full mathematical description along with proofs please refer to Daubechies, Lu, and Wu (2009).

Following application of the CWT on a signal  $f(t)$  the resulting wavelet coefficients correspond to the time-scale plane. Using the candidate IFs in Equation 10, we can reassign the output of the CWT to map from  $(t, a) \rightarrow (t, \omega(a, t))$  space via a technique called *synchrosqueezing*. At a given  $t$ , wavelet coefficients at scales with equivalent phase-transform are reassigned via the following, which results in the synchrosqueezed transform (SSQ/T) in the time-frequency plane

$$T_f(\omega, t) = \int_{A(t)=\{a:W_f(a,t)\neq 0\}} W_f(a, t) a^{-3/2} \delta(\omega(a, t) - \omega) da \quad (13)$$

For discrete signals it is important to remember that our variables  $(a, \omega(a, t))$  are discretized rather than continuous. Denote the *scale-resolutions*  $(\Delta a)_k = a_k - a_{k-1}$  and *frequency-resolutions*  $\Delta\omega = \omega_l - \omega_{l-1}$  at indices  $k, l$  for which the CWT was computed. The SSQT is now determined by bins centred on frequency  $\omega_l$ ,  $[\omega_l - \Delta\omega/2, \omega_l + \Delta\omega/2]$ , as

$$T_f(\omega_l, t) = (\Delta\omega)^{-1} \sum_{a_k:|\omega(a_k,t)-\omega_l|\leq\Delta\omega/2} W_f(a_k, t) a_k^{-3/2} (\Delta a)_k \quad (14)$$

The SSQT retains the invertibility of the CWT, so that the signal  $f(t)$  can be reconstructed by

$$f(t) =_C \Re[C_\psi^{-1} \int_0^\infty W_f(a, t) a^{-3/2} da] =_D \Re[C_\psi^{-1} \sum_l T_f(\omega_l, t) \Delta\omega] \quad (15)$$

where  $C_\psi = 2 \int_0^\infty \overline{\Psi(\xi)} \frac{d\xi}{\xi}$  is the admissibility constant for the mother wavelet used, and subscripts  $C$  and  $D$  correspond to the continuous and discrete cases, respectively.

Note that the discretization of  $\omega$  above is assumed linear implicitly. In practice, we find log-discretization to be more appropriate. In this case we can express the frequency resolution as  $(\Delta\omega)_l = \omega_l - \omega_{l-1}$  and position inside the summation, or change the  $a$  exponent to  $-1/2$ .

The main result of the SSQT is as follows: If  $f(t)$  is a superposition of *intrinsic mode functions* (IMFs, of the form (3)) which are sufficiently *well-separated*, the SSQT is completely concentrated, in the  $(t, \omega)$ -plane, in narrow bands around the curves  $\omega = \phi_k(t)$ . Using this result, restriction of the SSQT to the  $k$ -th narrow band is therefore sufficient to reconstruct, with high precision, the  $k$ -th IMF component of  $f(t)$ . In the discrete case the  $k$ -th component is reconstructed via

$$f_k(t_m) = 2C_\psi^{-1} \Re\left( \sum_{l \in \mathcal{L}_k(t_m)} T_f(\omega_l, t_m) \right) \quad (16)$$

where  $l \in \mathcal{L}_k$  are the indices of the small frequency band around the curve of  $k$ -th component. A full demonstration of IMF reconstruction using the SSQT is given in Figure S1, where we consider a signal comprising three pure tones.

#### 1.4. Automatic IMF extraction for transient waveforms

In Figure S1 the SSQT clearly isolates the curves around the IMF frequencies. If we did not know anything about the underlying signal, any wave detection algorithm must be able to

1. Automatically detect the curves around the  $k$ -th IMF component of  $f(t)$  in the SSQT amplitudes (hereon denoted *ridge curves*)

2. Estimate the bandwidth of the curve (with regards to frequency bins)

Whilst the bandwidth value is typically an arbitrary choice by the user, locating appropriate ridge curves is not a trivial issue and there is no universal agreement on the most optimal method. Algorithms based on dynamic path optimization and fixed point iteration have proven effective on short windowed Fourier Transform (SWFT) and CWT TFRs, which include penalties for both frequency jumps and deviations from typical values of the component frequency and its derivative (Iatsenko et al., 2016). Whilst the primary goal of the algorithms is to find the *dominant* ridge curve, we can apply the algorithms iteratively for multiple ridge curve detection, provided we know the number of IMF curves in the signal and that they persist for the entirety of the signal.

In many real life applications we have an unknown number of IMFs which are often transient and can appear anywhere within an observed signal. Further, the aforementioned techniques work so efficiently for the SWFT and CWT because of their smoothness in the time-scale plane, with amplitudes which are universally proportional to those of the IMFs we seek. In the case of the SSQT, amplitudes at ridge curve peaks are not indicative of IMF amplitudes; this is instead spread across frequencies in the ridge curve band (which we can recover using Equation 16). As a result there are more spurious peaks in

neighbourhood of ridge curve peaks which causes issues for ridge extraction, particularly with regards to frequency jumping between ridge curves (Iatsenko et al., 2016).

In the following sections we develop on these ideas and describe our automatic transient IMF extractor, designed to:

1. Automatically isolate transient waveforms in the SSQT using Hessian-based feature detection
2. Calculate their ridge curves using the techniques described by Iatsenko et al. (2016)
3. Estimate the bandwidths for each ridge curve as a function of time
4. Reconstruct the IMFs at the appropriate temporal locations in the signal

Following description we assess the algorithm's performance on a number of use cases.

### 1.5. Hessian-based feature detection

When isolating IMF ridge curves across SSQT amplitudes we seek frequency bands around some dominant spectral peak which varies in time. Although the IMF amplitudes are spread across the frequency bands, each ridge curve appears as a region of local maxima in the SSQT amplitude. If we consider SSQT amplitudes in the time-frequency plane as a gray-scale image, that is, the value in each  $(t, \omega)$  cell signifies *intensity* only, the ridge curves manifest as bright regions in the image whilst we'd expect the brightness to change significantly immediately outside the edges of the frequency bands. In image processing, these are precisely the definitions of the ridges and edges of an image, respectively.

We adopt the Hybrid-Hessian filter detailed in Ng, Yap, Costen, and Li (2015). Local curvature in the SSQT image is highlighted using second derivatives of the  $(t, \omega)$  axes. As in image processing, we consider the scale-space representation of  $|SSQT(t, \omega)|$ , (where  $|\cdot|$  denotes the magnitude, in this case the amplitudes)  $L(t, \omega)$ , which is obtained via

convolution of  $|SSQT(t, \omega)|$  with a 2-d Gaussian kernel at scale  $\sigma$

$$g(t, \omega, \sigma) = \frac{1}{2\pi\sigma^2} e^{-(t^2 + \omega^2)/2\sigma^2} \quad (17)$$

When choosing  $\sigma$ ,  $\sigma = 0$  represents an impulse function ( $L(t, \omega) = |SSQT(t, \omega)|$ ), whilst increasing sigma decreases the level of detail that an image contains. Depending on the nature of localization expected from transient waveforms within a signal,  $\sigma$  must be an informed choice. The Gaussian filter is generally used as the canonical way to generate a linear scale-space, since it satisfies the *scale-space axioms* which require that the filter used must not introduce new features when transitioning from finer to coarser scales in the scale-space representation. While uniqueness of the Gaussian filter has been argued (e.g. Babaud et al., 1986), a number of other filters are also appropriate (e.g. Moons et al., 1995).

For second derivatives we define the *Hessian* matrix by

$$H(t, \omega, \sigma) = \begin{bmatrix} \frac{\partial^2 L(t, \omega)}{\partial L(t) \partial L(t)} & \frac{\partial^2 L(t, \omega)}{\partial L(\omega) \partial L(t)} \\ \frac{\partial^2 L(t, \omega)}{\partial L(t) \partial L(\omega)} & \frac{\partial^2 L(t, \omega)}{\partial L(\omega) \partial L(\omega)} \end{bmatrix} = \begin{bmatrix} \mathcal{H}_a & \mathcal{H}_b \\ \mathcal{H}_b & \mathcal{H}_c \end{bmatrix} \quad (18)$$

Using the property of convolution

$$\frac{d^2}{dx^2}(n(x) * m(x)) = n(x) * \frac{d^2 m(x)}{dx^2} \quad (19)$$

it follows that

$$\mathcal{H}_a(t, \omega, \sigma) = L(t, \omega) * g_1(\sigma) \quad (20)$$

$$\mathcal{H}_b(t, \omega, \sigma) = L(t, \omega) * g_2(\sigma) \quad (21)$$

$$\mathcal{H}_c = [\mathcal{H}_a]^T \quad (22)$$

where  $g_1, g_2$  are the second derivatives of the Gaussian kernel (17)

$$g_1(\sigma) = \frac{1}{2\pi\sigma^4} \left[ \frac{(\chi)^2}{\sigma^2} - 1 \right] e^{-\frac{(\chi^2 + \gamma^2)}{2\sigma^2}} \quad (23)$$

$$g_2(\sigma) = \frac{1}{2\pi\sigma^6}(\chi\gamma)e^{-\frac{(\chi^2+\gamma^2)}{2\sigma^2}} \quad (24)$$

with vertical and horizontal directions

$$\chi = \sum_{i=-3\sigma}^{3\sigma} \sum_{j=-3\sigma}^{3\sigma} i \quad (25)$$

$$\gamma = \sum_{i=-3\sigma}^{3\sigma} \sum_{j=-3\sigma}^{3\sigma} j \quad (26)$$

respectively. Kernel sizes of 3 times the standard deviation are generally used so as to encompass the whole Gaussian bell with edge weights asymptotically tending to 0.

Example  $\mathcal{H}_a, \mathcal{H}_b, \mathcal{H}_c$  for different values of  $\sigma$  are shown in Figure S2. The Hessian matrix has eigenvalues

$$\lambda_1 = \frac{1}{2}[\mathcal{H}_a + \mathcal{H}_c + \sqrt{(\mathcal{H}_a - \mathcal{H}_c)^2 + 4\mathcal{H}_b^2}] \quad (27)$$

$$\lambda_2 = \frac{1}{2}[\mathcal{H}_a + \mathcal{H}_c - \sqrt{(\mathcal{H}_a - \mathcal{H}_c)^2 + 4\mathcal{H}_b^2}] \quad (28)$$

and we define the *vessel likeness measure* as (Frangi, 2001)

$$\mathcal{E}(t, \omega, \sigma) = \begin{cases} 0 & \text{if } \lambda_2 < 0 \\ e^{-\frac{\mathcal{R}}{2\beta_1^2} [1 - e^{-\frac{\mathcal{S}}{2\beta_2^2}}]} & \text{otherwise} \end{cases} \quad (29)$$

Here,  $\mathcal{R} = \lambda_1/\lambda_2$  is the measure of *blobness* structure in a 2-D image,  $\mathcal{S} = \sqrt{\lambda_1^2 + \lambda_2^2}$  is the *second order structureness* measure which is low in the background where no structure is present, and  $\beta_1, \beta_2$  are thresholds pertaining to the two measures, respectively (we keep both fixed to 0.5). The idea behind (29) is to map the aforementioned measures into probability-like estimates of vessel-likeness based on criteria related to the Hessian-eigenvalues.

For the *Hybrid-Hessian filter* we analyse (29) at a range of different Gaussian scales,  $\sigma$ . The response of (29) will be maximum at the scale which most closely resembles the size of the vessel that we want to detect. We iterate (29) over different scales to obtain a final

approximation to the vessel-likeness (Frangi, 2001; Ng et al., 2015)

$$\mathcal{L}(t, \omega) = \max_{\sigma_{min} \leq \sigma \leq \sigma_{max}} \mathcal{E}(t, \omega, \sigma) \quad (30)$$

Note that the non-zero elements in (29) are given for dark curvilinear structures. For bright structures we can either reverse the condition on  $\lambda_2$  or invert the image. However, for the Hessian matrix we find that pixels are bright when  $\lambda_2 < 0$  or when  $\mathcal{E}$  is exactly zero. Following derivation of (30) which highlights dark structures with positive values, we can manipulate a mask for the bright structures by

$$\mathcal{B}(t, \omega) = \begin{cases} 0 & \text{if } \mathcal{L}(t, \omega) > 0 \\ 1 & \text{otherwise} \end{cases} \quad (31)$$

For our purposes the non-zero values (bright-structures) here denote ridges in the SSQT corresponding to local maxima. The edges can be found by repeating the process with an inverted SSQT (looking for dark structures) and extracting bands with the first non-zero values above and below the ridges.

It suffices that the only free parameters are the values of  $\sigma$  to consider. Larger  $\sigma$  corresponds to increased filtering of images, thereby increasingly removing more of the details that an image contains. Given that  $\sigma$  determines the size of the Gaussian kernel, we might base this decision on how much we might expect amplitudes to spread across frequency bins in the SSQT reconstruction bands, for example. Care must be taken however to ensure that the  $\sigma$  remove noise in the SSQT whilst preserving local frequency structures that remain *well-separated* in the SSQT, to avoid the beating effect (Wu et al., 2011).

On investigation we found that  $1 \leq \sigma \leq 6$  is a good range for isolating ULF wave structures. Having a smaller upper bound results in an overestimation of a signals du-

ration, while having a larger upper bound removes too much local structure. A rigorous testing of the  $\sigma$  range is a goal of future work. To illustrate the ability of the automated wave extraction we refer the reader back to Figure S1, for which we applied the algorithm to extract the reconstructed IMFs precisely. Since the goal of applying the SSQT is to detect transient ULF signals, Figure S3 shows our application to a signal comprised of three waveforms at discrete frequencies, each lasting for four-periods and overlapping. For the higher frequencies there is greater redundancy spread across neighbouring frequencies, which is a general property of the CWT, yet our algorithm manages to successfully extract the desired waveforms to a high degree of accuracy with relative to frequency. In Figure, we apply the algorithm to a real magnetometer signal. As expected from the continuous nature of ULF pulsations (known as Pc5, (Jacobs et al., 1964)), we can see that the signal is comprised of multiple superposed periodic components, which we extract accordingly.

## 2. Automated field line resonance detection algorithm across magnetometers

Field line resonances (FLRs) describe the transfer of energy from waves to field lines via resonant-mode coupling in a narrow region of space, and for ultralow frequency (ULF) waves in the range  $\sim 1 - 10mHz$  are thought to play a key role in the energization and transport of trapped particles in the Earth's magnetosphere (Baker et al., 1998; Mann et al., 2004). ULF wave driven FLRs manifest in ground magnetometer signals as Pc-5 pulsations (periods of  $\sim 150-600s$ , Jacobs et al. (1964)) observed simultaneously across a latitudinal array of stations, subject to the following conditions:

- A localized amplitude in latitude
- A  $180^\circ$  phase change across the peak station

For a latitudinal array of magnetometers, we identify events in the Pc-5 range (those with dominant spectral peak outside of Pc5 range are discarded). The SSQTs at the corresponding ridge curves and bandwidths are used to calculate the event amplitude and phase via:

$$S(t, \omega) = \frac{2}{C_\psi} SSQT(t, \omega) \quad (32)$$

$$A(t, \omega_p) = \sum_{\nu=\omega_t^l}^{\omega_t^u} |S(t, \nu)| \quad (33)$$

$$\phi(t, \omega_p) = \tan^{-1} \left( \frac{\mathcal{R}\{\sum_{\nu=\omega_t^l}^{\omega_t^u} S(t, \nu)\}}{\mathcal{I}\{\sum_{\nu=\omega_t^l}^{\omega_t^u} S(t, \nu)\}} \right) \quad (34)$$

where  $\omega_p$  is the dominant spectral peak frequency and  $\omega_t^l, \omega_t^u$  are the event lower and upper band frequencies at time  $t$ , respectively. Such an approach means that the 2-dimensional amplitude and frequency curves in the  $(t, \omega)$ -plane have the finest frequency resolution possible (no redundancy). Such a resolution is likely to lead to general misalignment of many events when comparing across magnetometer stations, even though slight offsets in frequency at a particular event actually belong to the same event. To mitigate this possibility, we project event amplitudes and phases across their respective reconstruction frequency bandwidths, which we denote as *edge-to-edge mapping*

$$A(t, \omega_t^l : \omega_t^u) = A(t, \omega_p) \quad (35)$$

$$\phi(t, \omega_t^l : \omega_t^u) = \phi(t, \omega_p) \quad (36)$$

Now, amplitude and phase spectra for the latitudinal array of ground magnetometers can be stacked with conjugate events identified as those with overlapping frequency bandwidths. It is easy to filter events on a desired latitudinal resolution by specifying the number of stations that an event must be observed. For overlapping events, latitudinal

amplitude peaks are located and the phase change across the peak characteristic of FLRs is confirmed, otherwise these instances are nulled. From the remaining times in the same event, the maximum of all amplitude peaks is considered the dominant spectral peak to be associated with the FLR and mapped back to its respective frequency prior to the edge-to-edge mapping. When possible, the full width half maximum of the FLR across latitude is also calculated.

### 3. Supplementary figures for manuscript

#### References

- Babaud, J., Witkin, A. P., Baudin, M., & Duda, R. O. (1986, 1). Uniqueness of the Gaussian Kernel for Scale-Space Filtering. *IEEE Transactions on Pattern Analysis and Machine Intelligence, PAMI-8*(1), 26–33. Retrieved from <http://ieeexplore.ieee.org/document/4767749/> doi: 10.1109/TPAMI.1986.4767749
- Baker, D. N., Li, X., Blake, J. B., & Kanekal, S. (1998). Strong electron acceleration in the Earth's magnetosphere. *Advances in Space Research, 21*(4), 609–613. Retrieved from <http://www.sciencedirect.com/science/article/pii/S0273117797009708> doi: [https://doi.org/10.1016/S0273-1177\(97\)00970-8](https://doi.org/10.1016/S0273-1177(97)00970-8)
- Daubechies, I., Lu, J., & Wu, H.-T. (2009). Synchrosqueezed Wavelet Transforms: a Tool for Empirical Mode Decomposition. Retrieved from <http://arxiv.org/abs/0912.2437>
- Daubechies, I., & Maes, S. (2019, 6). A Nonlinear Squeezing of the Continuous Wavelet Transform Based on Auditory Nerve Models. In *Wavelets in medicine and biology* (pp. 527–546). Routledge. Retrieved from <https://www.taylorfrancis.com/>

- chapters/nonlinear-squeezing-continuous-wavelet-transform-based  
-auditory-nerve-models-ingrid-daubechies-stphane-maes/e/10.1201/  
9780203734032-20 doi: 10.1201/9780203734032-20
- Donoho, D. L. (1995). De-Noising by Soft-Thresholding. *IEEE Transactions on Information Theory*, 41(3), 613–627. doi: 10.1109/18.382009
- Frangi, A. (2001). *Three-dimensional model-based analysis of vascular and cardiac images* (Tech. Rep.). Retrieved from <https://dspace.library.uu.nl/handle/1874/377>
- Herrera, R. H., Han, J., & Baan, M. v. d. (2014, 3). Applications of the synchrosqueezing transform in seismic time-frequency analysis. <http://dx.doi.org/10.1190/geo2013-0204.1>, 79(3), V55–V64. Retrieved from <https://library.seg.org/doi/abs/10.1190/geo2013-0204.1> doi: 10.1190/GEO2013-0204.1
- Iatsenko, D., McClintock, P. V., & Stefanovska, A. (2016). Extraction of instantaneous frequencies from ridges in time-frequency representations of signals. *Signal Processing*, 125, 290–303. doi: 10.1016/j.sigpro.2016.01.024
- Jacobs, J. A., Kato, Y., Matsushita, S., & Troitskaya, V. A. (1964, 1). Classification of geomagnetic micropulsations. *Journal of Geophysical Research*, 69(1), 180–181. doi: 10.1029/jz069i001p00180
- Mann, I. R., O’Brien, T. P., & Milling, D. K. (2004, 1). Correlations between ULF wave power, solar wind speed, and relativistic electron flux in the magnetosphere: Solar cycle dependence. *Journal of Atmospheric and Solar-Terrestrial Physics*, 66(2), 187–198. doi: 10.1016/j.jastp.2003.10.002
- Moons, T., Pauwels, E. J., Van Gool, L. J., & Fiddelaers, P. (1995, 7). An Extended Class of Scale-Invariant and Recursive Scale Space Filters. *IEEE Transactions on*

- Pattern Analysis and Machine Intelligence*, 17(7), 691–701. Retrieved from <http://ieeexplore.ieee.org/document/391411/> doi: 10.1109/34.391411
- Ng, C. C., Yap, M. H., Costen, N., & Li, B. (2015). Automatic wrinkle detection using hybrid Hessian filter. In *Lecture notes in computer science (including subseries lecture notes in artificial intelligence and lecture notes in bioinformatics)* (Vol. 9005, pp. 609–622). Springer Verlag. Retrieved from [https://link.springer.com/chapter/10.1007/978-3-319-16811-1\\_40](https://link.springer.com/chapter/10.1007/978-3-319-16811-1_40) doi: 10.1007/978-3-319-16811-1{\\\_}40
- Thakur, G., Brevdo, E., Fućkar, N. S., & Wu, H. T. (2013, 5). The Synchrosqueezing algorithm for time-varying spectral analysis: Robustness properties and new paleoclimate applications. *Signal Processing*, 93(5), 1079–1094. doi: 10.1016/J.SIGPRO.2012.11.029
- Wu, H. T., Flandrin, P., & Daubechies, I. (2011, 4). One or two frequencies? the synchrosqueezing answers. In *Advances in adaptive data analysis* (Vol. 3, pp. 29–39). Retrieved from <https://www.worldscientific.com/doi/abs/10.1142/S179353691100074X> doi: 10.1142/S179353691100074X

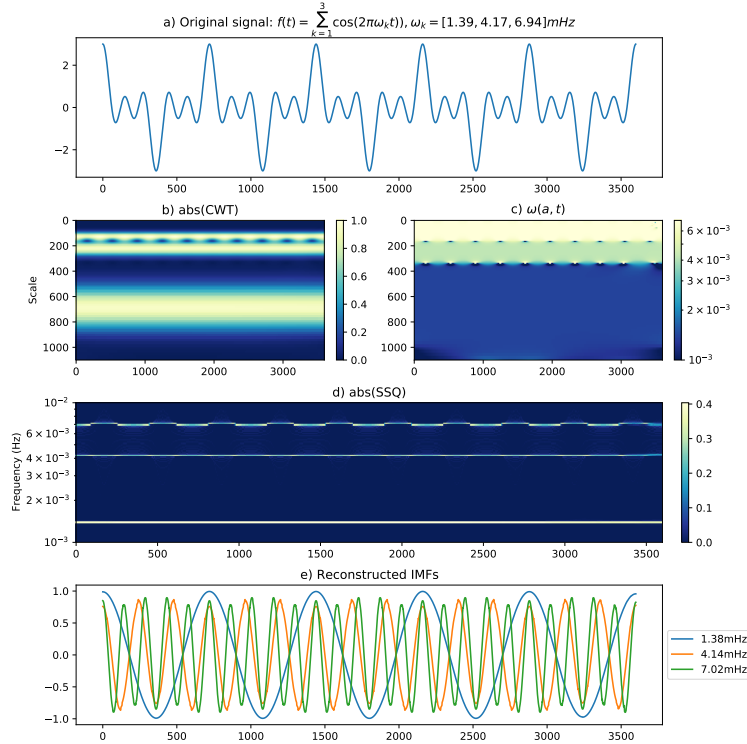


**Figure S1.** A full demonstration of the reconstruction of 3 pure-tone IMFs within a signal (a) using the SSQT. (b) Absolute values of the CWT coefficients in the time-scale plane. (c) Phase-transform (candidate frequency approximations) in the time-scale plane. (d) Absolute values of the SSQT coefficients in the time-frequency plane, following reassignment of the CWT coefficients using the phase-transform as in Equation 14. (e) Reconstructed IMFs found by inverting the SSQT coefficients in small bands around the curve of the relevant frequency component, as in Equation 16. Note that in this example the scales and frequencies are  $\log_2$  discretized. The reconstructed IMF frequencies are not exactly the frequencies of the pure-tones since the latter do not appear in the frequency resolution of the SSQT. They do, however, resemble the frequencies closest to the pure-tone frequencies in the SSQT frequency resolution.

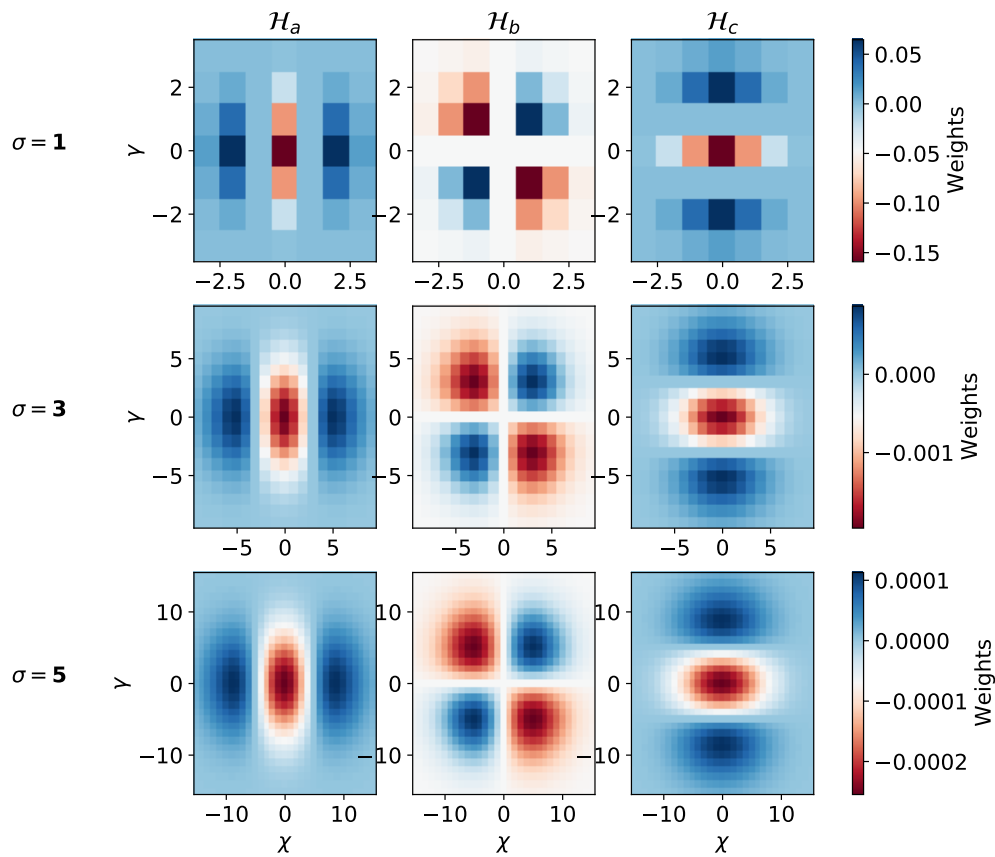


**Figure S2.** Example Gaussian kernels  $g(\sigma)$  for convolution with the scale-space  $L$  to determine the Hessian matrix components  $\mathcal{H}_a$ ,  $\mathcal{H}_b$  and  $\mathcal{H}_c$  (columns). Kernels are parameterized by the standard deviation  $\sigma$ . In all instances, the kernel sizes are  $3\sigma + 1$  across the  $\chi$  and  $\gamma$  domains.

X - 18

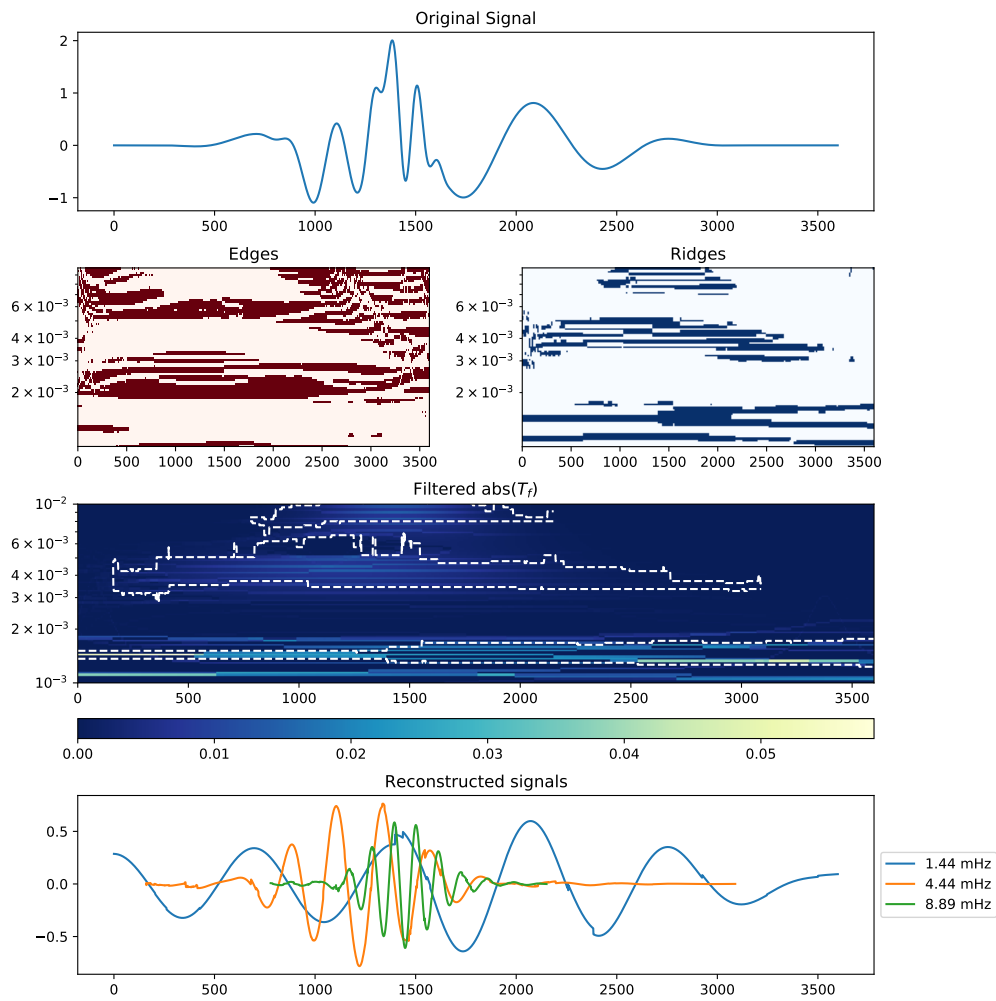


**Figure S3.** Automated wave extraction algorithm applied to a signal comprised of three hanning-windowed unit-amplitude waveforms (pulse-like) at discrete frequencies (1.4, 4.2 and 8.3mHz), which each last for four periods and have some overlap. From top to bottom are the original signal, edges and ridges following Hybrid-Hessian filtering of the SSQT ( $T_f$ ) amplitudes, qualifying events identified in the SSQT amplitudes enclosed by their IMF reconstruction bands (dashed white lines), and the resulting reconstructed IMFs at the determined frequencies.

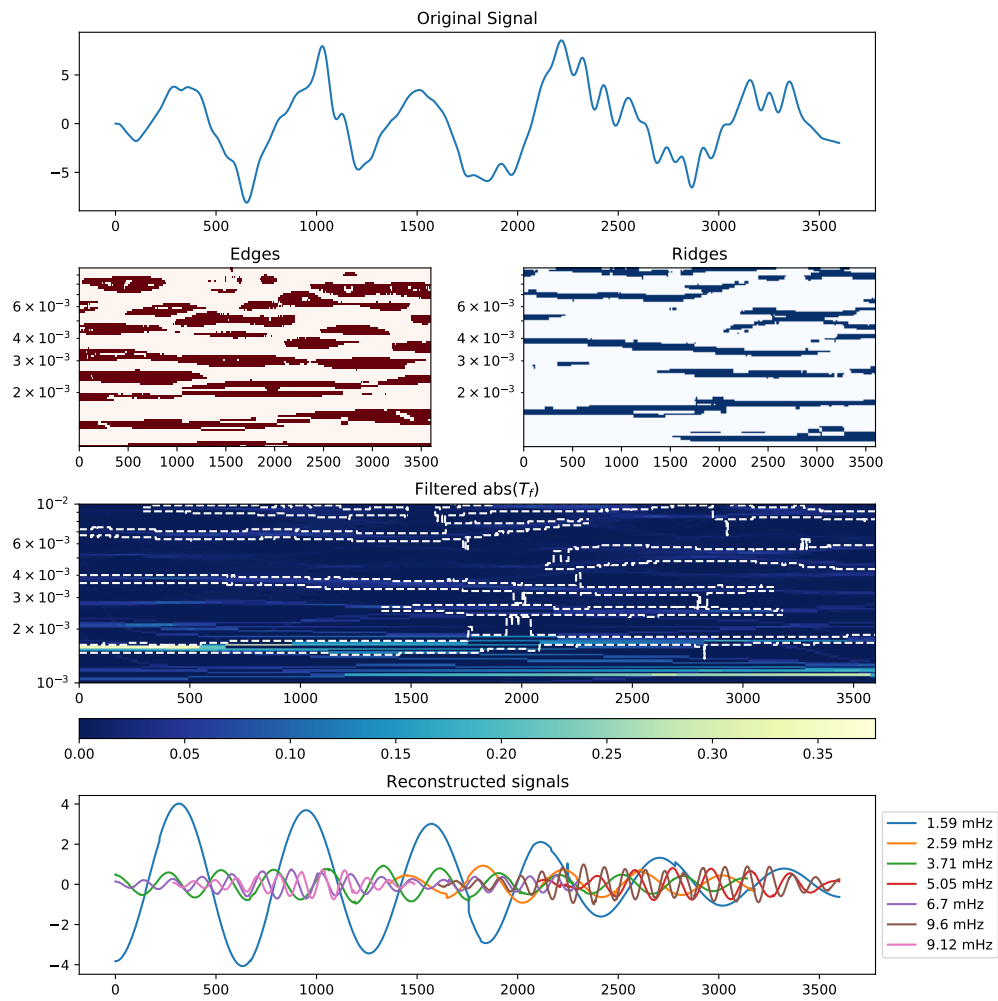


**Figure S4.** Automated wave extraction algorithm applied to a real magnetometer signal (Gillam station in the CARISMA chain). Format follows that of Figure S3.

Variable name	Description
<i>start</i>	Start time (UT) of FLR
<i>end</i>	End time (UT) of FLR
<i>peak_time</i>	Time during FLR with peak amplitude
<i>length</i>	Length of FLR (seconds)
<i>f</i>	Frequency (mHz) of the FLR
<i>fmin</i>	Lower bound frequency (mHz) in FLR SSQT reconstruction band
<i>fmax</i>	Upper bound frequency (mHz) in FLR SSQT reconstruction band
<i>amp</i>	Peak amplitude (nT) of FLR
<i>phase</i>	Latitudinal phase change ( $^{\circ}$ ) across FLR <i>mlat</i> . Here, considered phase changes must be monotonic either side of <i>mlat</i>
<i>station</i>	Corresponding CARISMA station at <i>mlat</i>
<i>mlat</i>	Magnetic latitude ( $^{\circ}$ ) of dominant spectral peak
<i>fwhm</i>	Latitudinal full-width half maximum ( $^{\circ}$ ) of FLR amplitude.
<i>fwhm_lbound</i>	Lower bound estimate of FWHM (if half amplitude crosses two latitudes either side of peak, else 0)
<i>fwhm_ubound</i>	Upper bound estimate of FWHM (if half amplitude crosses two latitudes either side of peak, else 0)
<i>identifier</i>	String containing stations considered for FLR detection (station identifiers are as in Table S2)
<i>mlt</i>	Magnetic local time

**Table S1.** Name and description of variables saved in the automated FLR detection algorithm

Name	Code	Identifier	Geodetic Latitude	Geodetic Longitude	L-Shell (2009)
Thief River Falls	THRF	1	48.027	263.635	3.58
Pinawa	PINA	2	50.199	263.960	4.06
Little Grand Rapids	LGRR	3	52.035	264.537	4.55
Island Lake	ISLL	4	53.856	265.340	5.15
Oxford House	OXFO	5	54.929	264.713	5.52
Gillam	GILL	6	56.376	265.360	6.15
Back Lake	BACK	7	57.707	265.794	6.83
Fort Churchill	FCHU	8	58.763	265.920	7.44
Rankin	RANK	9	62.824	267.890	10.89

**Table S2.** Name and description of magnetometer station codes, identifiers, location and L-Shell (as per 2009) relevant to the FLR statistical study.

X - 22

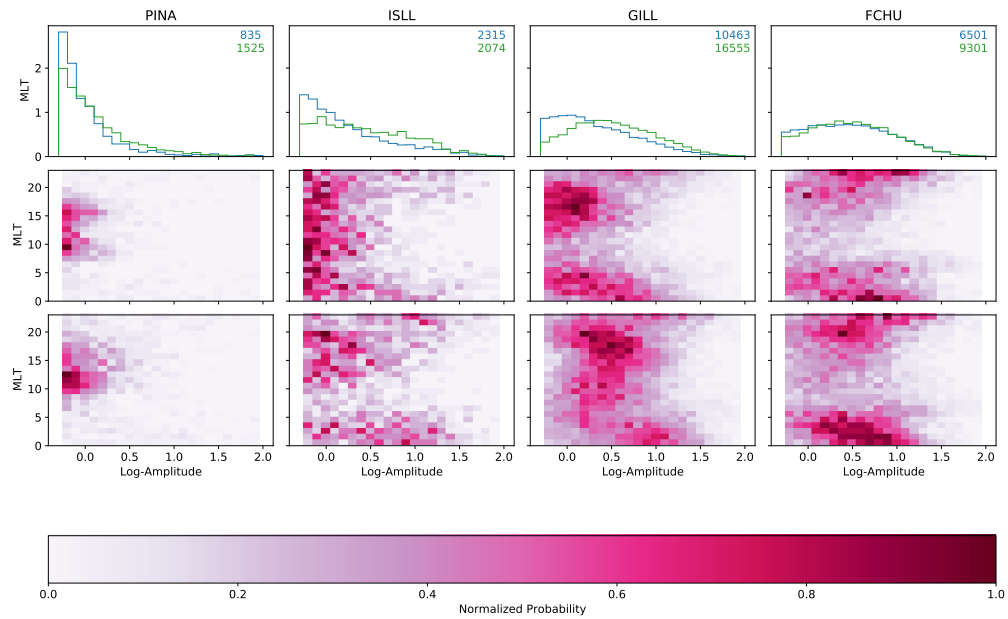


**Figure S5.** Distribution of observed FLR  $\log_{10}$ -amplitudes across MLT as a function of the magnetometer station (or latitude, columns). The top row illustrates the global amplitude distribution irrespective of MLT, where the blue and green histograms represent the poloidal and toroidal mode FLRs, respectively. The middle and bottom rows show the 2-dimensional histograms across amplitude and MLT for the poloidal and toroidal modes, respectively. Each 2-dimensional histogram has been normalized by its maximum value for comparison across magnetometer stations.

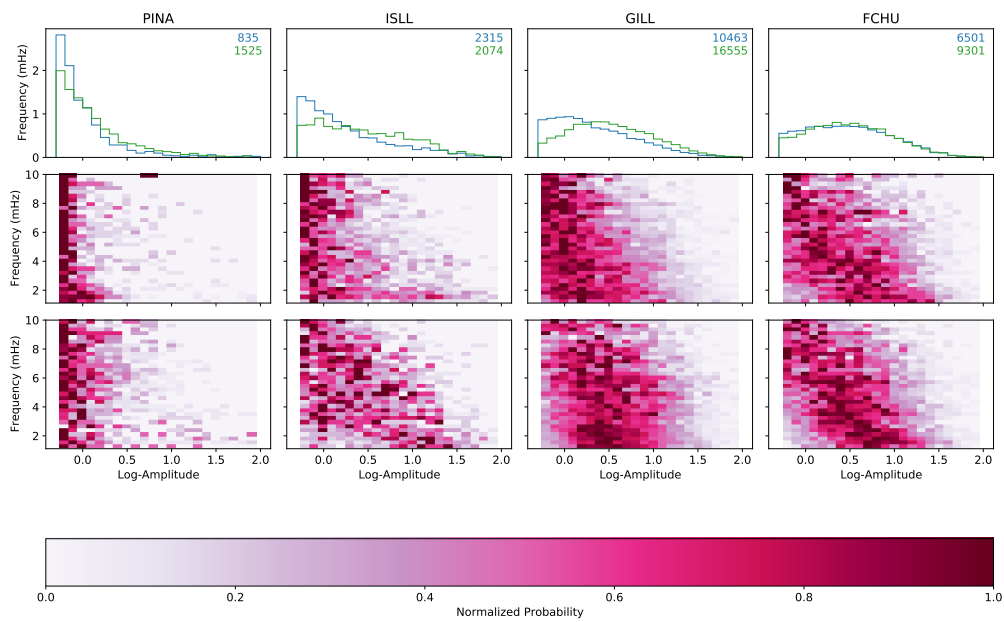


**Figure S6.** Distribution of observed FLR  $\log_{10}$ -amplitudes vs frequency (mHz) as a function of the magnetometer station (or latitude, columns). The top row illustrates the global amplitude distribution irrespective of frequency, where the blue and green histograms represent the poloidal and toroidal mode FLRs, respectively. The middle and bottom rows show the 2-dimensional histograms across amplitude and frequency for the poloidal and toroidal modes, respectively. Each 2-dimensional histogram has been normalized by the maximum value in each row to illustrate the relative distribution of amplitude across an FLR of a particular frequency.

X - 24

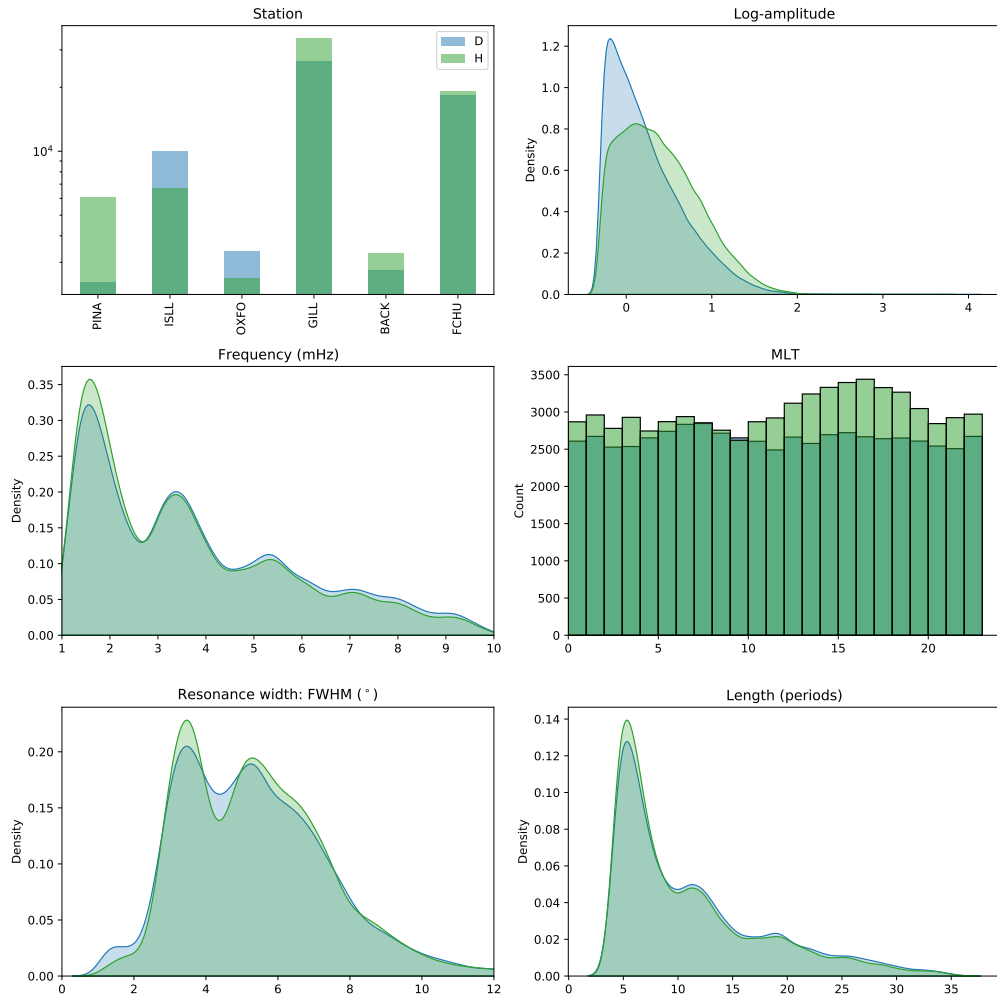


**Figure S7.** A glance at the global distributions of a number of observed FLR parameters, for both the poloidal (blue) and toroidal (green) modes. We illustrate a bar chart of counts for which magnetometer station an FLR is observed, kernel density estimates (approximations to the probability density function) for the FLR  $\log_{10}$ -amplitude, frequency, resonance width (described by the full-width-half-maximum (FWHM) at peak latitude) and FLR duration (in periods). We also provide a histogram with the counts of FLRs across MLT.

## 6.8 Towards a probabilistic mapping

When exploring the modern  $D_{LL}$  parameterizations in Chapter 2, we detailed the innovative approach by Ozeke et al. [2012, 2014] which mapped median ground-based D-component magnetic wave power to the equatorial azimuthal electric field, using the analytic Ozeke et al. [2009] mapping under the assumption of occurring field line resonances at each frequency with preordained azimuthal and latitudinal structure. Specifically, all FLRs had azimuthal wavenumber  $m = 1$  and latitudinal full-width-half-maximum (which determines the mean latitudinal wavelength in the ionosphere)  $\Delta\theta = 4^\circ$ . In Figure 6.2 it is clear that magnitudes of the Ozeke et al. [2009] mapping are highly sensitive to changes in  $\Delta\theta$  and  $m$ , and should therefore be explored probabilistically to see how realistic values might affect the resulting distribution of  $D_{LL}^E$  (azimuthal electric field radial diffusion coefficient in the Fei et al. [2006] framework).

### 6.8.1 Global distribution of resonance widths

Estimates of  $m$  (e.g. Murphy et al. [2018]; Sarris and Li [2017]) in space are difficult due to the necessity of multi-point spacecraft measurements which are often lacking, and therefore are frequently found using co-latitudinal ground magnetometers separated in azimuth. Contrarily, calculation of  $\Delta\theta$  was encoded in our FLR detection algorithm in Section 6.7 (note that successful calculation is dependent on both half-amplitude latitudes being within the highest and lowest latitudes of the ground magnetometers considered in a particular hour). Looking at the subset of FLRs with successful  $\Delta\theta$  calculation, we can explore the radial, spectral and azimuthal structure of resonance widths and how they relate to expected ULF wave power.

The global distribution of  $\Delta\theta$  across multiple dimensions is shown in Figure 6.4. If we consider all  $\Delta\theta$  as a collective we observe a clear bimodal probability density function, comprising a less-variable population of narrow FLRs with a typical width of  $\sim 3^\circ$  and another highly variable wide population with typical width  $\sim 5.5^\circ$ . In MLT, we see that the narrow-width population exists predominantly on the border regions of night-morning

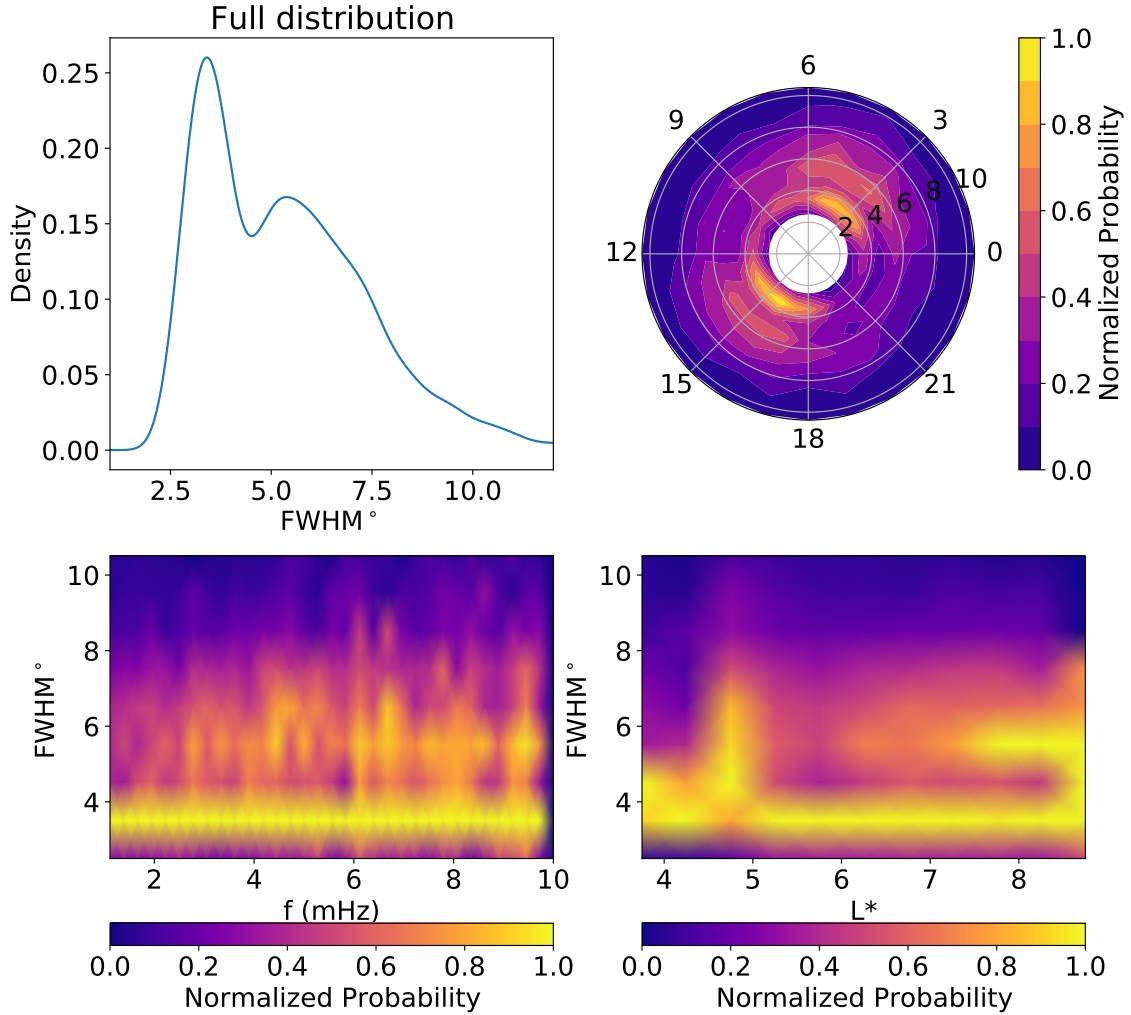


Figure 6.4: The global distribution of resonance widths, described by the full-width-half-maximum of the latitudinal amplitude profile,  $\Delta\theta$ , calculated at the FLR dominant spectral peak. (Top-left) Kernel density estimate of the probability density of all FLRs with successfully identified  $\Delta\theta$ . (Top-right) The maximum-normalized density of  $\Delta\theta$  in MLT. (Bottom-left) The density of  $\Delta\theta$  across FLR frequency, maximum-normalized over each frequency. (Bottom-right) The density of  $\Delta\theta$  across  $L^*$ , maximum-normalized over each drift-shell.

and noon-evening, whilst the wide population is prevalent at most MLT except late-morning and early-nighttime. Across frequency we find no particular preference for the narrow population, with each frequency exhibiting the highest region of density around  $\sim 3^\circ$ . For the wider population there are clear differences in peak-widths, modalities and variability as a function of frequency, although most do have significant density near  $\sim 5.5^\circ$ . Distributions are also not necessarily bimodal across  $L^*$ . FLRs which penetrate down to the lowest  $L^*$  tend to be narrow in width, but in the region of the plasmopause (approaching  $L^* = 5$ , e.g. Moldwin et al. [2002]) FLRs of all widths appear to have similar occurrence. It seems that abrupt changes in the plasma density mediate a larger variety of radial wave scale-lengths. Moving beyond the plasmopause the classic bimodal structure is evident.

The probabilistic nature of  $\Delta\theta$  is certainly a function of  $(L^*, f, MLT)$ , much like ULF power spectral density. It is clear that a constant assumption of  $\Delta\theta = 4^\circ$ , while central to the peaks in the bimodal distribution, masks much of the complex variability of magnetospheric FLR structure and subsequently  $D_{LL}^E$ . At face value, the typical values of the narrow and wide populations scale the mapping up and down by an approximate factor of 2, respectively, which becomes a factor of 4 when mapping the ground power into space (see Ozeke et al. [2012]). Possible amplitude dependencies of the separate populations will be explored in future work. Asymmetries in the MLT distribution also necessitate the full distribution of  $\Delta\theta$  to successfully remote sense azimuthal electric field wave power from the ground. It has been suggested that local time variations of resonance widths, caused by radial gradients of the plasma density changing in azimuth, induce variations in Pc5 ULF wave power measured on the ground due to the screening effect. Yet, distributions of space-measured wave power are more symmetric across azimuth (Glassmeier and Stellmacher [2000]; Hughes and Southwood [1976]). It is true that during most times the distributions of azimuthal electric field power across MLT are similar (see Figure 5.8). Fixing  $\Delta\theta = 4^\circ$  may lead to erroneous distributions of mapped power when, say, separating ground-power measurements into MLT sector to calculate drift-averaged wave power.

### 6.8.2 Inclusion of resonance widths in the Ozeke et al. [2009] mapping

We are now in a position to be able to quantify some of the uncertainty due to assumptions made by Ozeke et al. [2012, 2014] when mapping ground-based power to infer that of the azimuthal electric field. In the following analysis we assume that the Ozeke et al. [2009] equation is well-posed to reproduce the expected electric wave power when the correct parameter values are available. In reality, this may not be the case and a direct comparison of the mapping compared to conjugate ground and satellite power observations is required. Comparing our subset of FLRs (with successful  $\Delta\theta$  calculation) with the entirety of the Van Allen Probes mission we unfortunately found no conjugate observations to enable this analysis. However, a recent study has begun to explore the empirical relationship between  $b_g$  and  $E_\phi^{eq}$  finding considerable variability when compared to the Ozeke et al. [2009] expression (Warden et al. [2021]), which may provide useful for future analysis.

To remain consistent with previous analysis we also associate power observations with  $L^*$  determined by the Tsyganenko and Sitnov [2005] magnetic field model. We acknowledge that the applicability of the Ozeke et al. [2009] mapping to a distorted magnetic field via substitution of McIlwain [1961] L-Shell with  $L^*$  introduces uncertainties. Yet, with no other mapping accessible without the intensive solving of guided wave equations in an arbitrary magnetic field (Rankin et al. [2006]), we allow this substitution as the best available approach. Comparisons to data in future work may yield some correction factor to improve the accuracy of the mapping when applying to  $L^*$ . This would contain uncertainties from both a ground magnetometer's mapped adiabatic location and the guided wave equation solutions in an arbitrary magnetic field, which are difficult to decouple physically, so the correction factor would be purely for improving modelling accuracy rather than a physical quantity.

Inclusion of realistic values for  $\Delta\theta$  renders the mapping as considered by Ozeke et al. [2012, 2014] to be no longer constant as a function of frequency and drift-shell. Therefore, the distribution of equatorial azimuthal electric field wave power ( $\mathcal{P}_E^{eq}$ ) is dependent on whether averages are taken prior to or after mapping has taken place. Here we consider both to highlight any differences in the methods. We also explore the power distribu-

tions in azimuth to unpack information lost through non-inclusion of drift-averaged wave power. Since the FLRs in Section 6.7 were identified using the CARISMA array of ground magnetometers, we continue to use their magnetic field measurements (sampled at 1 Hz) for consistency. Specifically, we consider the PINA, ISLL, GILL and FCHU stations as these provided the most FLRs. We transform the geographic North (GN) and East (GE) components of the measured magnetic field perturbations into poloidal (H) and toroidal (D) via the following

$$H = GN \cos \theta + GE \sin \theta \quad (6.51)$$

$$D = -GN \sin \theta + GE \cos \theta \quad (6.52)$$

$$\theta = \overline{\arctan(GE/GN)} \quad (6.53)$$

where  $\theta$  is the declination angle calculated as a median ( $\bar{\cdot}$ ) over each month of data.

We map 9 years (2008-2016) of hourly ground magnetic power spectra, calculated using the multitaper method and provided by Dr Sarah Bentley (Bentley et al. [2018]; Percival and Walden [1993]; Thomson [1982]), using default values in the Ozeke et al. [2009] mapping:  $\Delta\theta = 4^\circ$ ,  $m = 1$ ,  $h = 150\text{km}$ , and a field-aligned plasma mass proportional to  $1/r^3$ . For times that align with our identified FLRs, we also map using the calculated  $\Delta\theta$  (if applicable) at the given frequency. Note that the spectral technique to calculate ULF wave power was not provided by Ozeke et al. [2012, 2014] and so differences in technique may lead to different estimations of power (see 6.7 for example). Further, assumptions in the mapping were made to facilitate the dayside magnetosphere which is most similar to a dipole. Indeed, only dayside power was mapped in Ozeke et al. [2012, 2014]. Extension to other MLT requires detailed knowledge about the ratio of Hall and Pedersen conductivities (e.g. Wallis and Budzinski [1981]), however, we map nightside power with dayside assumptions with the knowledge that some results may be erroneous.

Regression plots which highlight general differences between distributions of ground-power mapped with empirical  $\Delta\theta$  and  $\Delta\theta = 4^\circ$  are shown in Figure 6.5 as a function of  $L^*$  and Kp. The units of power were  $(\text{mV/m})^2 \text{ mHz}^{-1}$ . A general rule of thumb to perform regression requires a sample size of at least 10 (for each variable); we do not draw any

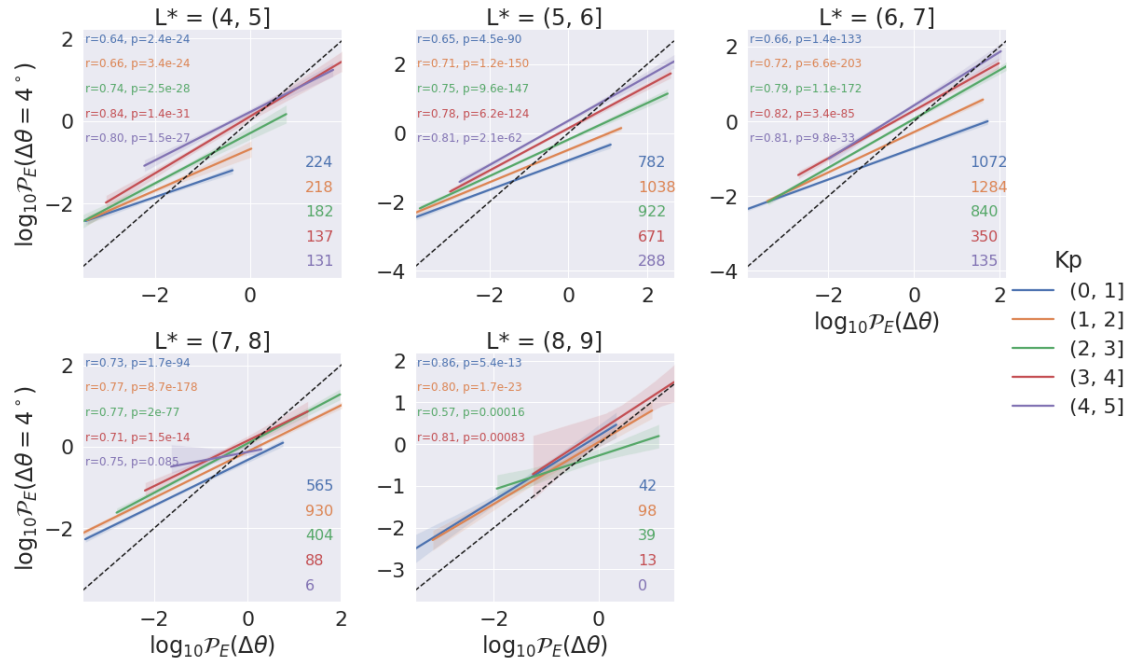


Figure 6.5: Regression plot for mapped  $\log_{10} \mathcal{P}_E$  with empirical  $\Delta\theta$  vs ground-power mapped with default  $\Delta\theta = 4^\circ$ , as a function of  $L^*$  and  $K_p$ . 95% confidence intervals are also shown for each regression plot, as well as unity lines (black-dashed). The number of samples in each  $K_p$  bin to perform the regression are also provided in the bottom-right of each plot, as well as the Pearson correlation coefficient (and corresponding p-value) in the top-left.

conclusions from curves in Figure 6.5 with a smaller sample than this. The regression parameter  $\beta$  (slope of the *best fit* line) was determined by *ordinary least squares (OLS)* which is a closed form expression that minimises the sum of squared residuals

$$\beta = (\mathbf{X}^T \mathbf{X})^{-1} \mathbf{X}^T \mathbf{y} \quad (6.54)$$

where  $\mathbf{X}, \mathbf{y}$  are the set of conjugate  $\log_{10} \mathcal{P}_E(\Delta\theta), \log_{10} \mathcal{P}_E(\Delta\theta = 4^\circ)$  vectors, respectively. Curves which are above/below the unity line indicate where the widths of resonant ULF waves are smaller/larger than the assumed  $4^\circ$ . We find that the distributions are typically more similar for both higher values of Kp and  $L^*$ , indicated by increasing Pearson correlation coefficients. The existence of non-unity regression curves introduces some power threshold whereby the Ozeke et al. [2009] default mapping transitions from over-estimating to underestimating mapped power compared to the empirical  $\Delta\theta$  distribution. This threshold increases with  $L^*$  for all Kp, suggesting that narrow resonance widths are increasingly confined to waves in the upper tail of the distribution for larger values of  $L^*$ . Since the tail values of  $D_{LL}^E$  significantly and irreversibly advance the electron population in the radial diffusion equation (Thompson et al. [2020b]), the default Ozeke et al. [2009] will fail to capture many of these instances.

Since the regression plots encapsulate power from all ULF frequencies it is useful to examine their distributions individually. Ideally we would explore the distribution of drift-averaged empirically-mapped power for more robust descriptions of  $D_{LL}^E$ , however, as shown in Figure 6.6 there are severe class imbalances of MLT sector across frequency,  $L^*$  and geomagnetic activity. We therefore limit ourselves to the azimuthally-independent distributions. The most simple way to characterize the distribution is through the median, however, with the inclusion of empirical  $\Delta\theta$  *when* averages are made becomes important. We illustrate this in figure 6.7, where we show median log-power for three different cases: (i) median empirical mapping x median ground power, (ii) median of empirically mapped ground power), and (iii) median of mapped ground power with  $\Delta\theta = 4^\circ$  (same as in Ozeke et al. [2012, 2014]). Median profiles are shown for each frequency as a function of geomagnetic activity (through Kp) and  $L^*$ . We find that both methods based on empirical  $\Delta\theta$  are vastly different from that with the default mapping, both in power magnitudes

CHAPTER 6. MAPPING ULF WAVE POWER FROM THE GROUND INTO SPACE



Figure 6.6: Occurrence of FLRs with calculable  $\Delta\theta$  in each MLT sector, as a function of  $(L^*, Kp, f)$ .

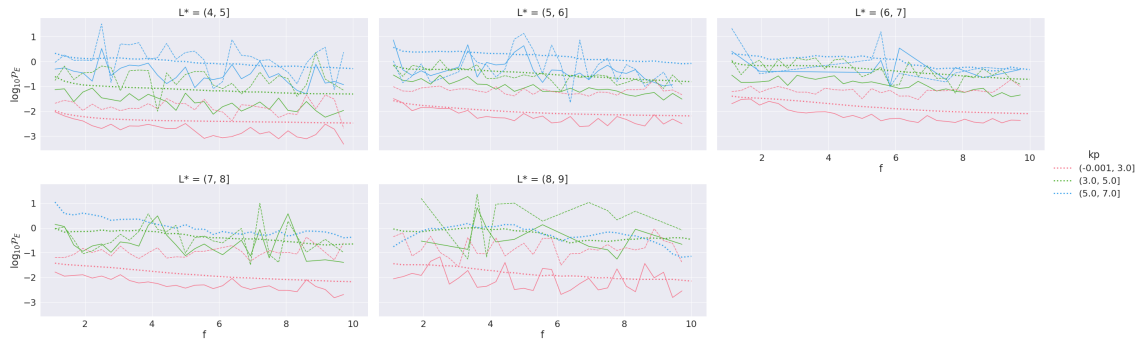


Figure 6.7: Median  $\log_{10} \mathcal{P}_E$  as a function of  $(f, L^*, Kp)$ , calculated from: (i) median empirical mapping x median ground power (solid), (ii) median of empirically mapped ground power (dashed), (iii) median of mapped ground power with  $\theta = 4^\circ$  (dotted).

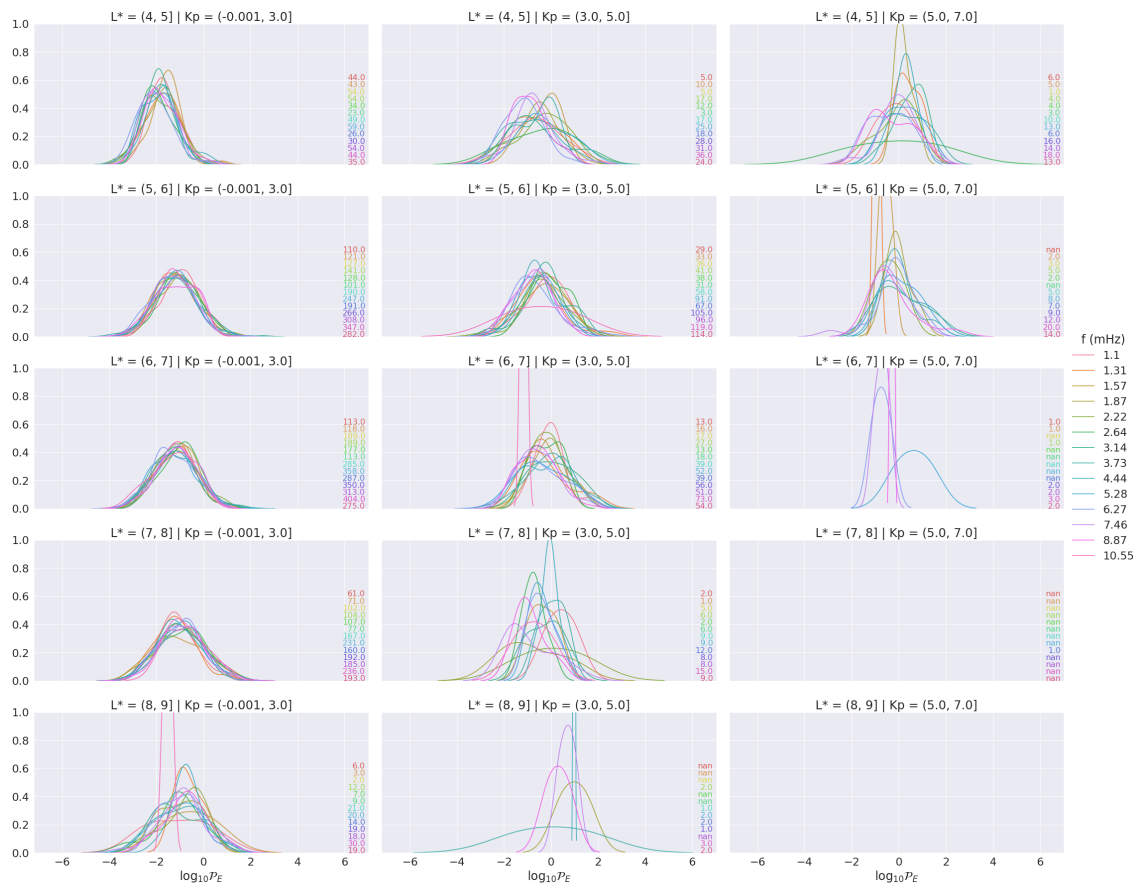


Figure 6.8: KDEs for the  $\log_{10} P_E$  probability density functions with empirical  $\Delta\theta$ , as a function of  $L^*$  and  $K_p$

and non-smooth variation across frequency. Ozeke et al. [2014] postulated that their median power profiles were invariant across frequency, removing any energy dependence from  $D_{LL}$ . However, we see that this is a consequence of too simplistic assumptions about the structure of observed ULF waves. Interestingly, the gradients of median power across frequencies are mostly in agreement, but it is rare for their magnitudes to align and can appear to differ up to one order of magnitude. Since the techniques result in different outcomes, a decision must be made as to which is most appropriate to reduce uncertainty. Provided that the Ozeke et al. [2009] mapping is accurate it is more intuitive to consider averages from the empirically mapped ground power rather than mapping from the medians. Using this approach we are also able to retain the full distribution of mapped power which is key for any probabilistic modelling.

To investigate the power distributions further we explore the probability densities in Figure 6.8. Note that the provided KDEs are reliable with higher numbers of samples and we generally consider those with more than 19 samples. We find that the majority of electric power distributions are log-symmetric, although some feature the bimodality respective of  $\Delta\theta$ . Generally, the structure of distributions across frequency does not align with those found in spacecraft calculated power (see Figure 5.2). We expect to see a well-ordered set of similar-shaped distributions which shift to the right (increasing power) with decreasing frequency. Instead, for "quiet" times (lowest Kp bin) all frequency distributions are aligned with no clear structure, whilst with more activity the distributions begin to diverge yet still with unexpected frequency structuring. Failure to align with *in situ* space-based power could be due to a number of reasons. Firstly, we have only considered once source of uncertainty in the mapping,  $\Delta\theta$ . Another great source of variability,  $m$  (e.g. Glassmeier and Stellmacher [2000], Figure 7) has been omitted due to complications of its calculation. Looking at the distributions in Figure 6.8 it could be possible to obtain the expected structure across frequency were there to generally be increasing wavenumbers with decreasing frequency, yet this is something that must be determined in future analysis since  $m$  is dependent on a number of things, including the driver of the ULF waves (Murphy et al. [2018]). The most obvious would be that accuracy of the analytic Ozeke et al. [2009] mapping is limited to magnetospheric states which align with the implicit assumptions that the mapping makes, ie a dayside global mode ULF wave with fixed radial structure in a

dipolar magnetic field. The ambiguity of applying to all waves in an empirical magnetic field might be too great, but this could be rectified by some numerical *correction factor* if conjugate measurements of ground and space observed FLRs were in abundance. A final reason is that FLRs observed by a latitudinal array of ground magnetometers make up only a certain amount of all ULF waves. Specifically these waves are discrete by nature, but broadband ULF waves are also prevalent in the inner magnetosphere and couple to the local plasma through wave-particle interactions. Both types of waves have different frequency, MLT and activity dependence (Murphy et al. [2020]) and could therefore possibly have dissimilar power probability density functions.

We have defined the efficacy of any probabilistic mapping to rest on its ability to reproduce the expected probability distribution of azimuthal electric field wave power as measured by spacecraft. Rather than determining this visually it is more effective to have some statistical measure of how similar the distributions are, such that successive improvements to the mapping (eg including realistic values for other uncertain parameters) will aim to increasingly improve this measure. One measure we can use is from *information theory* and named the *Kullback-Leibler Divergence* (or KL-Divergence), which calculates how much information is lost when we approximate one distribution with another. Mathematically we have

$$D_{KL}(p \parallel q) = \sum_{i=1}^N p(x_i) \log \frac{p(x_i)}{q(x_i)} \quad (6.55)$$

where  $p$  is the *true* target distribution and  $q$  is the approximating distribution. A perfect score of 0 suggests that no information is lost and the mapping, in our case, is a good approximation of the space-based power. KL divergences for both the empirical (ie including real  $\Delta\theta$ ) and default (Ozeke et al. [2009] with default values) mapped wave power are given in Figure 6.9. In almost all cases the empirical outperforms the default with KL scores very similar in the reverse case too. This suggests that the mapping improves almost universally when realistic values of  $\Delta\theta$  are used. There appears to be no performance bias towards certain ULF frequencies and mid-low  $L^*$ , and we also generally see worsening performance with Kp. Distributions from both mapping techniques become more similar with increasing  $L^*$ , although they both perform poorly when compared to

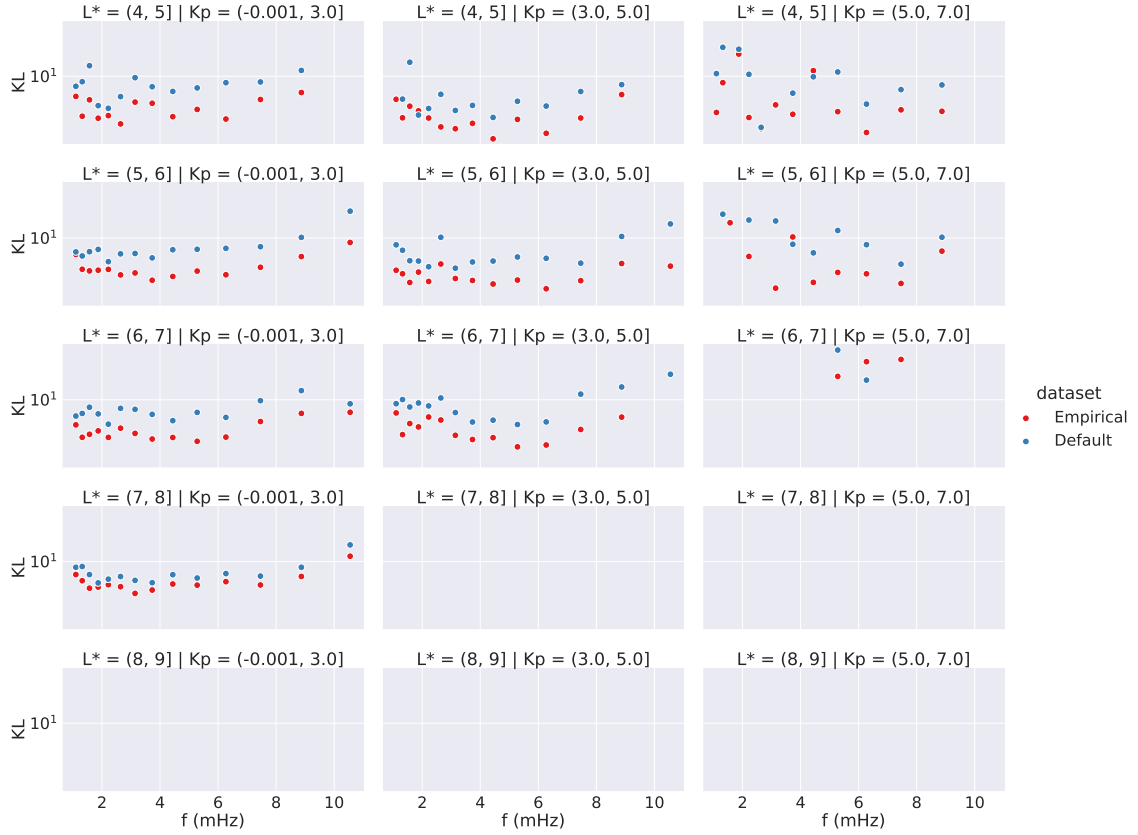


Figure 6.9: KL divergences for empirically (pink) and default (gold) mapped  $\log_{10} \mathcal{P}_E$  compared to the target spacecraft based wave power, as a function of  $(L^*, f, K_p)$ .

space-based power, implying that the radial scale-lengths (which map to latitudinal width on the ground) of ULF waves in the outer regions of the outer radiation belt are less important for describing ULF wave power magnitudes.

Even though mapping with empirical  $\Delta\theta$  better approximates the observed wave power it still fails to emulate the true underlying distribution. For general modelling of  $D_{LL}$  it is likely more useful to sample from space-based power distributions, assuming MLT independence as in Chapter 5 as well as some power structure across  $L^*$ , as opposed to those from empirically-mapped ground power. Contrarily for operational *in situ*  $D_{LL}^E$ , which is realistically available only across networks of ground magnetometers, current practices have profound limitations. Ensemble modelling of *in situ* ground power could mitigate some of the discrepancies when compared to space power, or a large statistical study of conjugate ground-space FLRs could quantify shortfall in the analytic Ozeke et al.

[2009] mapping. However, it should first be investigated whether possible improvements of the mapping could be made through inclusion of other variables previously assumed to be constant (with the ULF azimuthal mode structure most notable).

## 6.9 Chapter summary

In the previous Chapter, we discussed how limitations of point-based satellite observations to infer global ULF wave power distributions could be mitigated by using a global network of ground observations to remote sense power in the magnetosphere. Exploiting relationships between the ground magnetic and equatorial electric fields (Ozeke et al. [2009]), in this Chapter we investigated uncertainty in  $D_{LL}^E$  that were created from ULF wave power distributions mapped from the ground to the equatorial electric field (e.g. Ozeke et al. [2012, 2014]).

The mapping assumes that a field line resonance is occurring. Previous implementations of the mapping to construct  $D_{LL}^E$  assumed constant azimuthal wave structure and latitudinal width of the resonant ULF wave, as well as constant dayside-like ionospheric conductivity which introduces uncertainty in the resulting mapped power. To quantify the uncertainty in these assumptions we designed an automated FLR detection algorithm for use across a latitudinal array of ground magnetometers. The algorithm uses sophisticated signal and image processing techniques that circumvent biases in Fourier-based spectral analysis used in previous statistical FLR detection studies. We found that our algorithm was successful in uncovering populations of ULF waves found within case-studies but absent from prior statistical FLR studies.

Using the results from our algorithm we investigated the probabilistic distribution of ground-mapped power when realistic values for the latitudinal resonance width are considered.

- Generally there are two populations of resonant ULF waves, wide and narrow, which appear asymmetrically across MLT and are also functions of frequency and  $L^*$ .
- We found that mapping with constant resonance width (and all other variables

constant) fails to capture much of the narrow, high-power ULF waves in the tails of the power distributions which significantly drive the radial diffusion equation (see Thompson et al. [2020b]). This worsens further with increasing  $L^*$  and Kp.

- When using a probabilistic mapping our results showed that *when* the mapping is performed becomes important if considering median power to infer  $D_{LL}$ .
- The shapes of the probabilistically mapped ground-power are somewhat akin to those for space-based power, however, comparison of distributions using information theory (KL-divergence) yields that the distributions were not identical. Differences between distributions tend to be larger for increasing Kp and  $L^*$  also. Conversely, the distributions were more similar for empirical resonance width rather than constant, suggesting that inclusion of realistic values for other variables in the mapping may help alignment with space-based power distributions.

## 6.10 Future work

Future improvements to the mapping should account for other sources of uncertainty introduced by assumptions in Ozeke et al. [2009] which were unaddressed in this thesis. We detail these below.

To arrive at equation 6.50 itself simplifying assumptions were made which limit the mapping to the dayside. The guided poloidal and toroidal wave equations are dependent on  $\Sigma_P$  and a term proportional to the reciprocal of the Alfvén speed at the ionosphere ( $v_{A_i}^2$ ),  $\Sigma_P^C = 1/(\mu_0 v_{A_i}^2 \sin(\chi))$ . By solving the guided wave equations numerically assuming  $\Sigma_P = 10S$ , comparable to values observed on the dayside ionosphere,  $\Sigma_P \gg \Sigma_P^C$  and  $\Sigma_P^C$  can be neglected to produce a ratio  $E^{eq}/b^i$  which is linearly proportional to the observed wave frequency. Limiting to the dayside also implies the conductivity ratio  $\Sigma_H/\Sigma_P \approx 2$  (Wallis and Budzinski [1981]). The mapping is therefore limited by the informed, arbitrary choice for  $\Sigma_P$ . In fact, the distributions of  $\Sigma_P$  and  $\Sigma_H/\Sigma_P$  are considerably variable on the dayside and vary with the electric field itself (see Davies and Lester [1999], Figures 1 and 4, and Ieda et al. [2014], Figure 6d), so adopting single values to extend over the entire dayside induces uncertainty in the mapping. Neglecting the nightside and activity level

also limits the practicality of the mapping. Conductances can be calculated across all MLT, where we see distinct variations in typical values and a clear separation of distributions with respect to substorm progression (Carter et al. [2020]). A probabilistic mapping based on the distributions of conductances, with higher resolution in MLT and dependence of geomagnetic activity, might be a more intuitive approach for accurate mapping.

Subsequent uses of the mapping have made further assumptions about the free parameters in equation 6.50, for ease of application, which introduces further uncertainty. The ULF azimuthal wave number  $m$  is difficult to approximate as it typically requires two (or more) observations at the same latitude, with stringent azimuthal separation requirements, from which cross phase spectra at identifiable discrete ULF frequencies can be analysed. A number of studies have approximated  $m$  using closely separated satellite observations (Le et al. [2017]; Murphy et al. [2018]; Rae et al. [2005]; Sarris and Li [2017]). Another way to calculate  $m$  is via direct particle observations with sufficient energy, pitch angle resolution energy range (e.g. Claudepierre et al. [2013]; Min et al. [2017]; Ren et al. [2017]; Zhou et al. [2015]). Mapping  $E^{eq}/b^g$  requires ground-based ULF observations and approximating  $m$  using ground observations is also possible, but high- $m$  ULF waves with short azimuthal scale lengths are mostly screened by the ionosphere with only low- $m$  waves possible to detect at the ground (e.g. Sarris et al. [2013]). There are a class of ULF waves ( $|m| = 15 - 40$ ), however, that can overcome ionospheric screening such as the rarely occurring giant pulsations (Chisham et al. [1992]) and waves generated throughout geomagnetic storms (Pilipenko et al. [2001, 2002]). Due to the difficulties in resolving actual ULF wave mode structures globally it is often assumed that ULF waves originate only from  $m = 1$ . This is certainly the case for many interpretations of  $D_{LL}$  (Ali et al. [2016]; Brautigam et al. [2005]; Fei et al. [2006]; Ozeke et al. [2012, 2014]). From those  $m$  approximated *in situ* on the ground we have values in disagreement with  $m = 1$  (e.g. Sarris et al. [2013], Figure 2), and in general (ground and space) there are significant measurement errors when estimating  $m$ , with the overall distribution of  $m$ -values significantly variable in probability (see Murphy et al. [2018], Figures 5 and 6). Presuming  $m = 1$  at all times is therefore a flawed assumption.

One final uncertainty of note, which is a by-product of the mapping itself, stems from the necessity of amplitude and phase spectra across the array of magnetometers to locate the FLR at the dominant spectral peak and map accordingly. Validation of the Ozeke et al. [2009] mapping was performed for a long-lasting observed FLR (Rae et al. [2005]) at the dominant spectral peak. Since power spectral density is calculated over a window of observations, considering the dominant spectral peak is also the most intuitive approach when applying a single mapping value in equation 6.42 to map ground-based power and infer  $D_{LL}$ . There is no temporal dependence on the mapping equation, however, and it is not yet clear how the mapping performs at the resonant frequency for times outside of the dominant spectral peak. Having said that, a recent study by Warden et al. [2021] found that, for a number of test cases, the mapping underperformed when compared directly against conjugate  $E^{eq}, b^g$  amplitudes during an FLR event.

## CHAPTER 7

# PROBABILISTIC RADIAL DIFFUSION WITH STOCHASTIC PARAMETERIZATION OF $D_{LL}$

Throughout this thesis we have systematically investigated selected sources of large uncertainty in the radial diffusion coefficient - the underlying magnetic field which assigns observations of ULF wave power spectral density to  $L^*$  (drift shells), the subsequent natural variability of the wave power when limited to satellite observations, and the mapping of wave power from the ground into space for more informative, global analysis of azimuthal electric field wave power. Whilst this set of uncertainties is not exhaustive by any means (see Figure 2.2), they provide in unison some of the key ingredients to investigate the levels of expected diffusion when we account for natural variability in ULF wave driven radial diffusion models.

We are now able to revisit the study by Thompson et al. [2020b] (Chapter 3) with answers to some of the pivotal questions necessary for a probabilistic description of  $D_{LL}$ . Specifically, *"what are the distribution shapes and widths of the radial diffusion coefficient?"*. We revisit numerical experiments of radial diffusion, employing ensembles of  $D_{LL}$  that are now constrained by the probability distributions found throughout previous Chapters. Comparing to modern characterizations of  $D_{LL}$  detailed in Chapter 2, we hope to highlight the importance of variability inclusion and the shortfall of current practices.

Questions about the probabilistic nature of  $D_{LL}$  still remain however, namely the temporal and spatial variability of  $D_{LL}$ , and we will discuss combating these as a natural progression of this thesis.

## 7.1 Experiment set-up

The goal of these numerical experiments is not to imply that probabilistic descriptions of  $D_{LL}$  outperform deterministic models when compared to reanalysis data (e.g. Drozdov et al. [2021] for deterministic  $D_{LL}$ ). A full numerical treatment of the processes in the radiation belts that include other magnetospheric processes, and realistic initial and boundary conditions, is beyond the scope of this analysis. A probabilistic  $D_{LL}$  model is a more accurate description of what we do know, given that the model is constrained by the natural uncertainties of key components which formulate  $D_{LL}$  ( $L^*$ , the underlying ULF waves which drive radial diffusion, etc). Using a probabilistic model we can ask the following question:

*“What are the (many) possible things that could happen, based on the current state of the magnetosphere?”*

This is similar to an operational forecasting situation, where validation data is not available at any one given time and there is limited knowledge about the current (initial condition) and future states of the magnetosphere. In this setting we must employ the  $D_{LL}$  description we believe most likely to advance the electron population to a state aligned with observations, were they to be available. The problem with current parameterizations of  $D_{LL}$  is that they operate on describing the wave-particle interactions by what happens *most of the time* (i.e. averages). We postulate this as a possible reason we find discrepancies between diffusion models and observed electron densities (e.g. Glauert et al. [2018]; Kim et al. [2011]).

Approaching our modelling probabilistically, we hope to capture the resulting electron distribution somewhere within our predicted range. Indeed, deterministic  $D_{LL}$  which implicitly describe the behaviour of ULF waves in a systematic, structured way are just

one of these possible outcomes. Comparison to deterministic  $D_{LL}$  therefore acts as an indication of their limitation to express natural magnetospheric variability. Of course, we are still performing very idealised numerical experiments, with radial diffusion the only process being modelled in the absence of any sources or sinks. A full comparison between deterministic and probabilistic treatments of  $D_{LL}$  in more realistic circumstances with data-driven initial conditions is left for future work.

### 7.1.1 Modelling the radial diffusion equation

We consider again the Fokker-Planck radial diffusion equation defined for conserved  $(\mu, J)$  pairs (where \*'s have been dropped from  $L^*$  for convenience)

$$\left. \frac{\partial f}{\partial t} \right|_{(\mu, J)} = L^2 \left. \frac{\partial f}{\partial L} \left( \frac{D_{LL}}{L^2} \frac{\partial f}{\partial L} \right) \right|_{(\mu, J)} \quad (7.1)$$

We model radial diffusion over the domain  $L = 3.5 - 6.5$  (where the minimum has been set to avoid spectral leakage issues in the magnetic power distributions), with no electron phase space density (PSD) at the inner boundary ( $f = 0$  at  $L = 3.5$ , forcing a slot region) and no gradient at the outer boundary ( $\partial f / \partial L = 0$  at  $L = 6.5$ ). Whilst a realistic outer boundary is dynamic (e.g. Glauert et al. [2018]), we opt for this simplification to monitor differences due to changes in  $D_{LL}$  formulation only (Thompson et al. [2020b]). As in Thompson et al. [2020b], the initial PSD is analytic with a peak inside the computational domain and zero gradient at the outer boundary

$$f(M, J, \Phi; t = 0) = A \exp \left( - \frac{(L - \mu)^2}{2\sigma^2} \right) + \frac{1}{2} AB [erf(\gamma(L - \mu)) + 1] \quad (7.2)$$

where we have chosen  $A = 9 \times 10^4$ ,  $\mu = 4$ ,  $\sigma = 0.38$ ,  $B = 0.05$ ,  $\gamma = 5$  and  $erf$  is the error function. Such a profile is reasonable when compared to satellite observations (see Boyd et al. [2018], Figures 1 and 2).

Numerically we use a modified Crank-Nicolson second-order finite difference scheme

presented by Welling et al. [2012], which is semi implicit and unconditionally stable

$$\frac{f_j^{n+1} - f_j^n}{\Delta t} = \frac{L_j^2}{2} \left[ \frac{\bar{D}_{j+\frac{1}{2}}^{n+\frac{1}{2}}(f_{j+1}^n - f_j^n) - \bar{D}_{j-\frac{1}{2}}^{n+\frac{1}{2}}(f_j^n - f_{j-1}^n)}{(\Delta L)^2} + \frac{\bar{D}_{j+\frac{1}{2}}^{n+\frac{1}{2}}(f_{j+1}^{n+1} - f_j^{n+1}) - \bar{D}_{j-\frac{1}{2}}^{n+\frac{1}{2}}(f_j^{n+1} - f_{j-1}^{n+1})}{(\Delta L)^2} \right] \quad (7.3)$$

where  $L_j = 3.5 + j\Delta L$ ,  $t_n = n\Delta t$ ,  $f_j^n = f(L_j, t_n)$ ,  $\bar{D}_j^{n+\frac{1}{2}} = \bar{D}_{LL}(L_j, t_{n+\frac{1}{2}})$ , and  $\bar{D}_{LL} = \frac{D_{LL}}{L^2}$  for modeling simplicity. The chosen grid ( $\Delta L$ ) and time-step ( $\Delta t$ ) for our numerical experiments are 0.1L and 10s, respectively (see Thompson et al. [2020b] Supporting Information for numerical stability analysis).

### 7.1.2 Formalism for $D_{LL}$

For practicality we employ the framework by Fei et al. [2006], separating  $D_{LL}$  into the symmetric compressional magnetic and azimuthal (equatorial) electric field components, assumed to be uncorrelated

$$D_{LL}^B = \frac{\mu^2 L^4}{8q^2 \gamma^2 B_E^2 R_E^4} \sum_m m^2 P_m^B(m\omega_d) \quad (7.4)$$

$$D_{LL}^E = \frac{1}{8B_E^2 R_E^2} L^{*6} \sum_m P_m^E(m\omega_d) \quad (7.5)$$

where  $P_m^B(m\omega_d)$ ,  $P_m^E(m\omega_d)$  are the power spectra of the  $m$ th harmonic of the magnetic and electric field fluctuations, respectively,  $q$  is the electron charge,  $\gamma$  the relativistic correction factor,  $B_E$  is the equatorial magnetic field strength at the surface of the Earth and  $\omega_d$  is the bounce-averaged angular drift frequency of the electron satisfying the drift resonance condition  $m\omega_d = \omega$ , with  $\omega$  the observed ULF wave frequency.

### 7.1.3 Energy dependence

The drift frequency  $\omega_d$  is related to the first adiabatic invariant  $\mu$  in a dipole via the following

$$\omega_d = \frac{3\mu}{2\pi\hat{\gamma}qL^2R_E^2} \quad (7.6)$$

$$\hat{\gamma} = \sqrt{1 + \frac{B\mu}{W_{rest}}} \quad (7.7)$$

where  $W_{rest}$  is the electron rest energy and  $B$  the local magnetic field strength. It is the scaling factor  $2\pi$  which is relevant to a dipole magnetic field. For another magnetic field model the period function must be integrated along one complete drift orbit (Ali [2016]). Extension to a non-dipolar magnetic field involves computationally expensive probing of the magnetic field across physical space and azimuth to estimate the location of the magnetic equator,  $B$ , and  $L^*$ . Observation times also become important since the empirical magnetic field models are dependent on solar wind parameters and geomagnetic indices. For simplicity in the idealized experiments, which are not indicative of any true time period, we accept the above equations to determine energy dependence. We therefore have *approximate* energy dependence from which the local magnetic field strength is found through the dipole relationship  $B = B_E/L^3$ . Typically,  $\mu$  is given in units MeV/G. To retain this and obtain drift-frequencies in the correct units (Hz),  $\mu$  must be converted to SI units. As such, we use the following units and conversions to SI for each variable

- $\mu \rightarrow MeV/G = 1.602176634 \times 10^{-19} m^2 A$
- $B \rightarrow G = 10^{-4} kg/(As^2)$
- $W_{rest} \rightarrow MeV = 1.602176634 \times 10^{-13} kgm^2/s^2$
- $q \rightarrow Coulomb = A \cdot s$
- $R_E \rightarrow m$

for Ampere  $A$ , second  $s$ , kilogram  $kg$ , metre  $m$ , Gauss  $G$  and mega-electron-volt  $MeV$ . The resulting electron drift frequencies as a function of  $L^*$  can be seen in Figure 7.1.

For a drift resonance to occur the particle drift frequency must match the ULF wave frequency multiplied by its azimuthal wavenumber. Due to impossibility of calculating

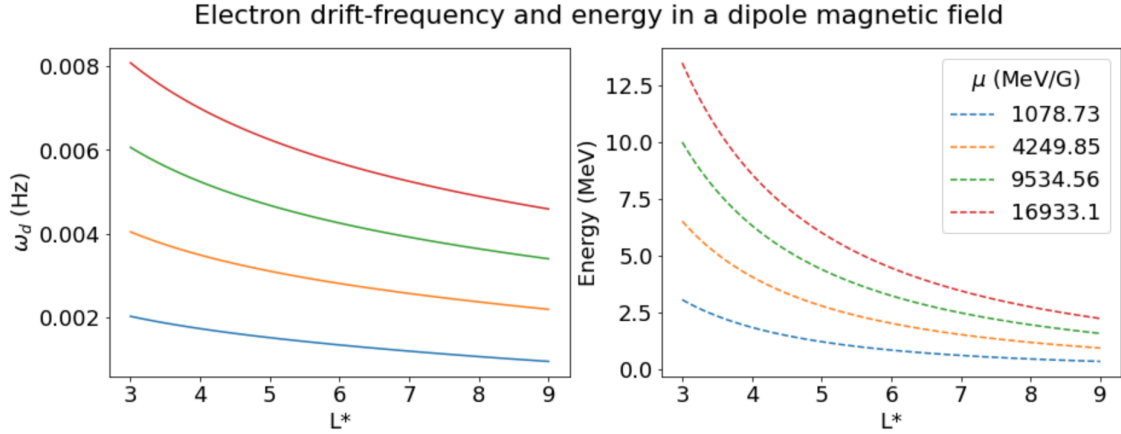


Figure 7.1: (Left) Bounce-averaged angular drift frequencies and (right) electron energies in a dipole magnetic field, as a function of  $L^*$  (in this case, L-Shell) and  $\mu$ .

$m$  directly from single-point observations (in azimuth), distributions of ULF wave power spectral density considered in this thesis are not separable by  $m$ . As a result we assume  $m = 1$  for all ULF waves for simplicity, which equates the wave and drift frequencies in the resonance condition. Indeed, an identical assumption was made for all of the modern  $D_{LL}$  parameterizations. It is then simple to extract specific electron energies using Equation 7.7. For the experiments we consider electrons with first invariant  $\mu = 500, 1000, 2500, 5000$  MeV/G.

#### 7.1.4 Construction of probabilistic $D_{LL}$

To construct a probabilistic  $D_{LL}$  in the numerical experiments we employ the Van Allen Probes ULF wave power ( $\mathcal{P}$ ) data considered in Chapter 5. The electric and magnetic  $\log_{10} \mathcal{P}$  data are segmented into  $(L^*, Kp)$  bins (relevant to each experiment), before fitting multivariate KDEs (see Chapter 5) to the subsequent power distributions which retain correlations across ULF frequencies. To form a probabilistic  $D_{LL}$  within a particular  $(L^*, Kp)$  bin at energy  $\mu$ , power spectra for  $\log_{10} \mathcal{P}_B$  and  $\log_{10} \mathcal{P}_E$  are randomly sampled independently from their relevant KDEs and the power from the frequency associated with the desired  $\mu$  can then be extracted. These are then exponentiated (base-10), input into the Fei et al. [2006] equations for  $D_{LL}^B$  and  $D_{LL}^E$ , before finally being summed to form  $D_{LL}$ . Note that we consider the MLT invariant power here for illustration, rather than

drift-averaged power, since covariances across MLT are currently unknown (see Chapter 5).

The experiments vary how the  $D_{LL}$  are selected, and what relationship they might have in time or space. For example, suppose that  $D_{LL}$  varies every 3 hours with  $0.5L^*$  variability, where there is no correlation between  $L^*$ -bins and Kp=3 for the entire 2 day period (as in Experiment 1, see Section 7.1.5). To create a probabilistic  $D_{LL}$  for the numerical experiment, bearing in mind that our time and space discretizations are  $\Delta t = 10s$  and  $\Delta L = 0.1$ , respectively:

1. Split the  $\log_{10} \mathcal{P}_E$  and  $\log_{10} \mathcal{P}_B$  data into  $(L^*, Kp)$  bins, where  $L^*$  bin edges have  $0.5L^*$  width beginning and ending at the domain endpoints, and Kp bins have width 1 centred at integers 0-9.
2. Fit multivariate KDEs to each data split that retains frequency correlations
3. At each sampling period (3 hours), sample  $\log_{10} \mathcal{P}_E$ ,  $\log_{10} \mathcal{P}_B$  power spectra once from each  $(L^*, Kp=3)$ -bin KDE independently and extract the frequency component associated with the desired  $\mu$
4. Base-10 exponentiate the extracted power sample for each  $(L^*, Kp=3)$ -bin, input into the Fei et al. [2006] equations and sum to form  $D_{LL}$
5. Spread each of these  $D_{LL}$ 's across the respective  $L^*$  bin (wrt  $\Delta L$ ), whilst also propagating  $D_{LL}$ 's in each  $L^*$  bin forward in time until the next sampling period (wrt  $\Delta t$ )

A resulting probabilistic  $D_{LL}$  for this example with  $\mu = 1000 MeV/G$  can be seen in panel 1 of Figure 7.2. See Thompson et al. [2020b]; Watt et al. [2021] for similar constructions of probabilistic diffusion coefficients.

### 7.1.5 Ensemble modelling of $D_{LL}$

For our numerical experiments we run an ensemble of probabilistic  $D_{LL}$  with 250 ensemble members. Each member comprises a possible realisation of  $D_{LL}$  over a 48-hour period,

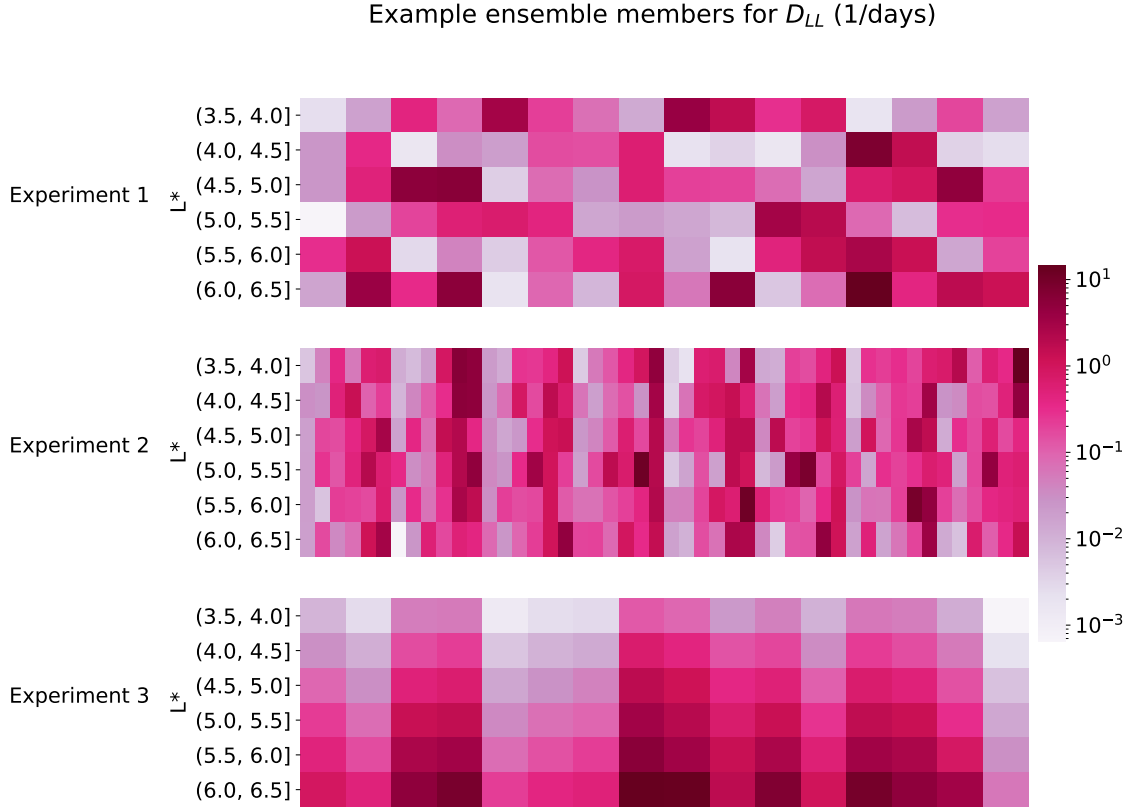


Figure 7.2: Example  $D_{LL}$  ensemble members for each of the numerical experiments over the 48-hour interval.

which varies probabilistically as a function of  $L^*$ , drift-frequency and geomagnetic activity. In this thesis we have considered ULF wave power variability with geomagnetic activity through the geomagnetic index  $K_p$ , as was the case for all modern  $D_{LL}$  descriptions. To compare to Thompson et al. [2020b] we keep  $K_p=3$  constant for the entire 48 hour period.

The efficacy of power (and subsequently  $D_{LL}$ ) distribution shapes and widths to drive radial diffusion is coupled to the temporal and spatial (with regards to  $L^*$ ) variability (Thompson et al. [2020b]). To test the sensitivity to the temporal and spatial variability we therefore consider a number of speculative numerical experiments (note that many other experiments could be designed, however, we choose those related to key results published in Thompson et al. [2020b]):

1.  $D_{LL}$  varies every 3 hours with  $0.5L^*$  variability, where there are no correlations between individual  $L^*$  bins. The three hour variability was chosen as this is the

temporal variability of Kp, and in Thompson et al. [2020b] it was found that the expected level of diffusion increases with smaller spatial scales of  $D_{LL}$  variability.  $0.5L^*$  variability is also consistent with the split of ULF wave power data in Chapter 5.

2.  $D_{LL}$  varies every hour with  $0.5L^*$  spatial variability, again with no correlations between individual  $L^*$  bins. We investigate a more rapidly varying (temporally)  $D_{LL}$  since the results of Chapter 3 (Thompson et al. [2020b]) showed radial diffusion dependence on variability timescale.
3.  $D_{LL}$  varies on 3 hour timescales with global spatial variability that scales with median  $D_{LL}$ . In this instance all  $(L^*, Kp)$  split ULF wave power are divided by (or subtracted by in log-space) the median at each frequency. The  $L^*$  dependence is then removed and a kernel density estimate is fit to the  $L^*$ -combined *noise distribution* for each Kp. When sampling we employ the median profile and scale it with a probabilistic sample from the noise distribution associated with the relevant Kp. We run this experiment since we showed in Chapter 3 (Thompson et al. [2020b]) that the coherence of  $D_{LL}$  across  $L^*$  was important.

Example ensemble members in each of the experiments for  $\mu = 1000MeV/G$  are illustrated in Figure 7.2.

## 7.2 Numerical experiment results

The results for each of the numerical experiments is shown in Figure 7.3. In all instances we see that accounting for the natural variability of  $D_{LL}$  typically results in more diffusion than that imposed by the deterministic models. In almost all panels of Figure 7.3, the median of the ensemble results (the black dashed line) lies below the solid coloured lines, indicating that the radial diffusion in the stochastic parameterization experiments has more significantly flattened the original condition than for the deterministic experiments. In experiments 1 and 2 which considered shorter spatial scale-lengths of  $D_{LL}$  variability, we find a decreasing spread of resulting ensemble PSDs with increasing  $\mu$ . In fact, the

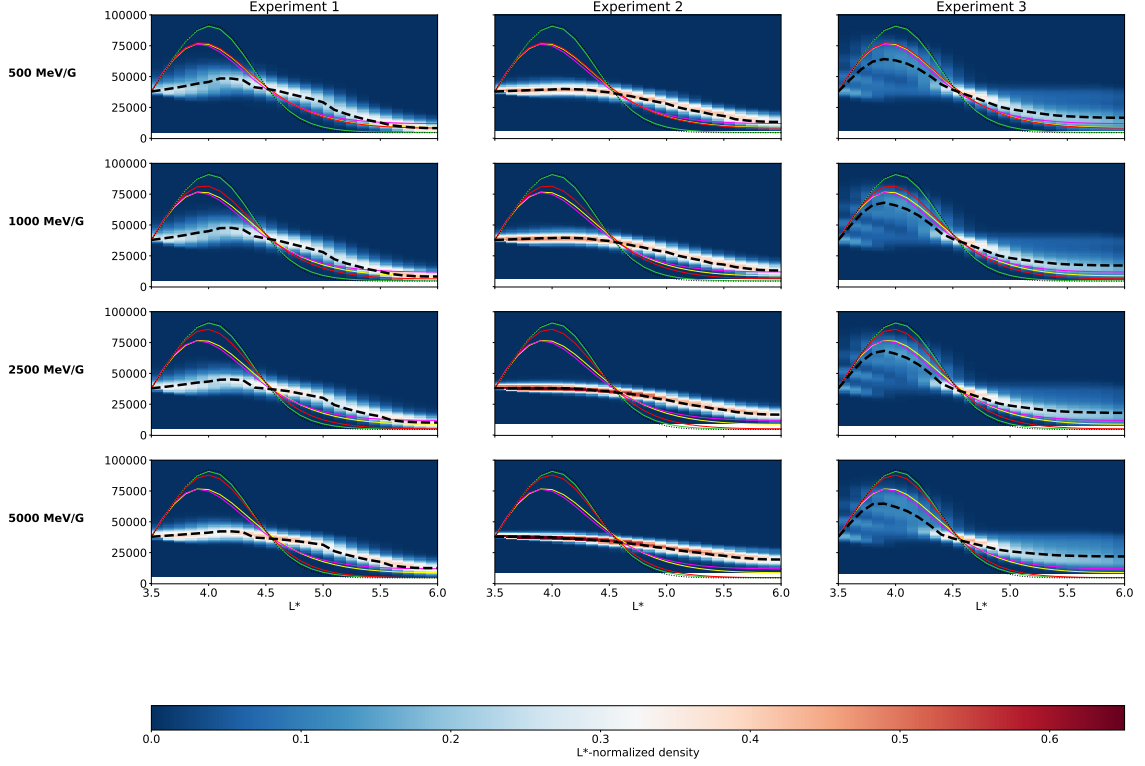


Figure 7.3: Results for each of the numerical experiments, where each row corresponds to a different  $\mu$ . In each Figure the  $L^*$  normalized kernel density estimate of the ensemble PSD is shown by the shaded regions. Over-plotted are the resulting PSD from the deterministic  $D_{LL}$ : Ozeke et al. [2014] (yellow), Brautigam and Albert [2000] (magenta), Ali et al. [2015, 2016] (green) and Liu et al. [2016] (red). Also shown are the initial PSD (black-dotted) and the ensemble median PSD (black-dashed). The units of PSD are  $(c/cm \text{ MeV})^{-1} \text{ sr}^{-1}$ .

variance of the ensemble for  $\mu = 5000 \text{ MeV/G}$  is small enough that the ensemble median is indicative of the entire distribution. The entire ensemble PSD distribution lies below all of the deterministic models, suggesting that radial diffusion is significantly driven by ULF wave power sampled from the tail of the distribution, and is not mediated by those instances of power smaller than the median which are sampled more frequently (due to the log-symmetric-like shapes of the ULF wave power distributions). The experiments with short spatial scale-lengths (experiments 1 and 2) also result in less smooth PSD profiles due to discontinuities in  $D_{LL}$  between  $L^*$  bins which act against each other in the smoothing of gradients.

If we compare results from experiment 1 to experiment 2 (column 1 and column 2 in Figure 7.3), we see that diffusion is clearly more effective when increasing the temporal variability of  $D_{LL}$  to hourly, enough so that the effect of diffusion coefficient discontinuities across  $L^*$  bins vanishes to result in smooth PSD across the spatial domain. Increased levels of diffusion are to be expected as more frequent sampling increases the chance of large ULF wave power appearing in  $D_{LL}$ . Again we see the importance of retaining energy dependence through the increasing levels of diffusion with  $\mu$ , wherein the ensemble median at all  $\mu$  is representative of the majority of the distribution. By including informed variability of ULF wave power quantified within *in situ* data, we observe more diffusion for the hourly variability than that of Thompson et al. [2020b]. In that study, the distribution of  $D_{LL}$  (implicitly through ULF wave power) was considered lognormal (e.g. Bentley et al. [2018]) and constrained by the interquartile range provided in Ozeke et al. [2014]. Our results highlight that characterizing the shape of the distribution is as important knowing its width, since the skewness in many of the log-wave-power distributions (see Chapter 5) drive diffusion beyond what we might expect from one assumed log-symmetric.

The largest spread of the ensemble appears when we assume there is spatial coherence to  $D_{LL}$ , and apply the same variability across all  $L^*$ , as in experiment 3 (3rd column of Figure 3). We also see the least amount of diffusion when compared to experiments 1 and 2. This is consistent with Thompson et al. [2020b] who found that expected diffusion decreases with increasing coherence of  $D_{LL}$  across  $L^*$ . It is only in this experiment that some of the deterministic models are comparable to members of the ensemble, specifically those by Brautigam and Albert [2000]; Ozeke et al. [2014] at all  $\mu$  and Liu et al. [2016] at the lower energies. While the ensemble median still shows more diffusion than the collection of deterministic models, the results of this experiment indicate that the effectiveness of current state-of-the-science models for  $D_{LL}$  is dependent on the spatial correlation structure of  $D_{LL}$  with  $L^*$ . If the monotonic, quadratic profile given by median  $D_{LL}$  is suggestive of all times we can expect a varied set of resulting PSD when we include natural variability (from the spread of the ensemble). However, only some noise distribution relative to the deterministic median  $D_{LL}$  may be necessary to reproduce the probabilistic outcomes. This could be through an equation of the form  $D_{LL} \approx \epsilon(Kp)D_{LL}^{Deterministic}(L, Kp)$ , where  $\epsilon$  is the noise distribution found by dividing the empirical  $D_{LL}$  distribution (which includes

measured ULF wave power) by the deterministic  $D_{LL}$  based on median wave power.

### 7.3 Chapter summary and Future work

We have performed idealized numerical ensemble experiments with a stochastically parameterized  $D_{LL}$  which contains the full distribution shape of ULF wave power. The distributions of wave power are respective of the entire drift-shell (ie MLT invariant) but vary with geomagnetic activity (Kp) and electron energy. Our main findings were:

- When accounting for the natural variability of  $D_{LL}$ , the majority of ensemble members exhibited more diffusion compared to all considered deterministic  $D_{LL}$  parameterizations, which are based on median ULF wave power.
- Ensembles also showed increased levels of diffusion with electron energy.
- We found that the radial diffusion equation is more sensitive to the inclusion of ULF wave power variability when  $D_{LL}$  also varies on shorter time and spatial scales.

These results are very similar to those found in Chapter 3 (Thompson et al. [2020b]), however, these were more speculative about the shape of the empirical ULF wave power distributions. By accounting for the natural variability of *in situ* wave power, we are able to constrain this key source of uncertainty and view more realistic results of radial diffusion driven by tail values in the power distribution. Our experiments also highlight the necessity of retaining energy dependence when modelling radial diffusion, which was not considered in Chapter 3, since this provides another notable source of uncertainty when omitted.

The solutions of the ensemble experiments depend not only on the empirical distribution of ULF wave power, as demonstrated in this Chapter, but also on the nature of the temporal variability of  $D_{LL}$  and its local spatial correlation structure across  $L^*$ . In order to help quantify both of these sources of variability we outline some future projects for consideration:

- **Auto-correlative properties of ULF wave power:** We have observed that modern parameterizations of  $D_{LL}$  place temporal variability on the geomagnetic index  $Kp$ , which is produced every three hours. However,  $Kp$  can also be nowcast in real time (e.g. Shprits et al. [2019]) which makes it more favourable for radiation belt modelling. Models of ULF wave power have also placed dependencies on solar wind variables (e.g. Bentley et al. [2018]). One might then think that changes in  $D_{LL}$  occur on timescales comparable to that of its parameterizing variable. To determine whether this is true for any particular physical variable or index, we can look at the auto-correlative properties of ULF wave power measurements. That is, how correlated are power measurements at a particular instance with those at previous time lags? If significant correlations occur up to a particular time then we may deem that a reasonable timescale to probabilistically sample  $D_{LL}$ .

This is not a simple task due to the nature of power spectral density itself, as well as the coordinate reference frame used for radial diffusion, which are somewhat coupled. From the time-frequency trade-off resulting from the *Heisenberg-Gabor* principle (Heisenberg [1985]), we must consider a sufficiently long window of magnetic and electric field perturbations in order to obtain an adequate ULF frequency resolution. This is a problem that exists for both Fourier and wavelet-based spectral analysis. Therefore, there is some minimum timescale that exists to efficiently calculate  $D_{LL}$ . If the most important temporal variability occurs on timescales less than this we can look at correlations between sliding windows of ULF wave power, but this comes at the expense of computing power and decoupling correlations of interest from those which stem from a sliding window sharing perturbation instances with its predecessor. Typically a window length of 1-hour is used to study ULF wave power (e.g. Ozeke et al. [2012, 2014]; Bentley et al. [2018]) from ground or space-based instruments. This is sensible for any drift-averaged  $D_{LL}$ , since instruments rotate with the Earth and remain in a region of interest for a limited amount of time. For a single point measurement we therefore have some maximum length of time to investigate autocorrelation of ULF wave power.

A full correlation study will need a continuous time series of power at fixed  $L^*$  and MLT. As we have discussed in this thesis, the limited number of satellites in opera-

tion are unable to provide such a comprehensive data set and we must look to ground instruments instead. Of course we are limited to azimuthal electric field perturbations only (and therefore  $D_{LL}^E$ ) through the Ozeke et al. [2009] mapping, subject to any improvements suggested in Chapter 6. Vast networks of ground magnetometers with global coverage are already in operation and suitable for this job, such as the SuperMAG array (Gjerloev [2012]). Power spectral density for the ground magnetic field, calculated from hundreds of stations, would have to be mapped to  $L^*$  and MLT and stitched to form cohesive time series for power correlation analysis. Such a big-data task will be very computationally expensive, and rapid models to map an observation into space are required, since the relationship between a location on the ground with its mapped location at the magnetic equator in both real and adiabatic space is non-trivial (see Thompson et al. [2020a] and Chapter 4). Sampling from empirical models fit to Pro- $L^*$  (Thompson et al. [2020a]) or employing algorithms from *machine learning* with Pro- $L^*$  as the training set may be good places to start for this. Using machine learning models to predict the ULF wave power at the ground rather than performing brute force calculations might also reduce the computational complexity (e.g. Bentley et al. [2020]).

With consistent power or electric-perturbation time-series at fixed MLT and  $L^*$ , one way to investigate auto-correlative properties is through (partial) autocorrelation functions. These are figures which indicate the correlation of values with previous lags (the partial autocorrelation function further removes any indirect correlations with observations at intervening time steps before a particular lag). Once autocorrelation timescales are known, more sophisticated models of  $D_{LL}$  may be sought, such as autoregressive moving average (ARMA) models. These can be used to create spatio-temporal series of the  $D_{LL}$  with the appropriate auto-correlative properties (Thompson et al. [2020b]).

- **Spatial correlation structure of  $D_{LL}$  across  $L^*$ :** All  $D_{LL}$  based on median ULF wave power exhibit a smooth, monotonically-increasing profile with  $L^*$ . As seen in Thompson et al. [2020a] and the numerical experiments above, application of a single variability to the monotonic curve generally results in less but smoother diffusion in the ensemble, when compared to probabilistic variability applied to  $L^*$  on smaller

spatial scales. So far our imposed local spatial structures of  $D_{LL}$  have been purely speculative - the true scale lengths of  $D_{LL}$  must be inferred from data. Again this requires a set of cotemporal power measurements spanning a number of drift-shells with the same local time, which is impossible to gain from the current satellite fleet. Fortunately, the ground-based power spectral densities from the CARISMA latitudinal chain of magnetometers considered in Chapter 6, or the global SuperMAG network mentioned above (Gjerloev [2012]), may provide further insight.

One of the key questions we want to answer is - if ULF wave power increases at a particular  $L^*$  (plus MLT if considering drift averaged power) does it also increase at all other  $L^*$ ? If not, what is the decorrelation range with other  $L^*$ ? A number of advances in the mathematics of two-dimensional spatial correlation structure have been developed in the fields of hydrology (Israelsson et al. [2020]) and climatology (Ricciardulli and Sardeshmukh [2002]), which can be adapted to our problem. The goal is to look at the response of magnetometer observations (either power or electric field perturbations) in particular locations to certain power intensity classes. A natural proxy for intensity class might be variable magnitudes related to Kp, another other geomagnetic index or discretized bands of a solar wind variable. Some initial work would be need to be completed to determine conjugate intensity classes for a set of stations as expected power (and therefore electric field perturbation) varies as a function of latitude and MLT. A simple approach to determine a threshold for an intensity class could be some percentage above the median power for that station relative to its  $L^*$ , MLT and proxy intensity index/variable.

For a particular time instance, we could then examine the probability of observing the same power intensity at nearby stations within some radius of a given origin station (e.g. binary-transform stations to 1/0 if they satisfy/do not satisfy the intensity class and look at the probability of stations with value 1 within some radius of the origin magnetometer). Similar methods also allow for dependence structures of co-occurring events between multiple intensity classes (Israelsson et al. [2020]), which could allow the inclusion of localized ULF wave structures in azimuth, for example. Understanding the 2-dimensional spatial structure of ULF wave power will provide key insight into the scale-lengths for which to sample the probabilistic

power distributions, and inform what levels of diffusion we might expect. Of course, successful application of this technique relies on an accurate mapping of power from the ground to the magnetic equator (see Ozeke et al. [2009]; Thompson et al. [2020a]).

Our work has focused on the uncertainty specifically within the radial diffusion coefficient  $D_{LL}$ .  $D_{LL}$  is not the only variable that drives the radial diffusion equation, however, and future work should investigate uncertainty in the dynamic boundary conditions. The radial boundary conditions play pivotal roles of sources and sinks, which in turn impact the distribution of PSD which simultaneously undergoes radial diffusion. Both the inner and outer radial boundary conditions are typically determined from electron flux data on board spacecraft (e.g. Drozdov et al. [2021]; Glauert et al. [2018]), but the limited availability of data, especially in the case of radiation belt modelling in present day, would make parameterized boundary conditions more desirable.

The inner radial boundary at the slot region has an energy dependence with electron energies above 894 keV essentially not present due to proton contamination (Fennell et al. [2015]), and the phase space density here has previously been parameterized by geomagnetic activity (Glauert et al. [2014a]). Fortunately, it has been found that variability in the inner radial boundary condition does not have too much of an impact in radiation belt simulations (Glauert et al. [2018]).

The outer radial boundary condition is a lot more complex. Where the inner boundary is relatively stable in physical space due to the dominance of the internal magnetic field at lower drift-shells, the outer boundary varies in time with radial distance. This means that flux measurements (or predictions) must be mapped to some fixed boundary  $L^*$  (e.g. Glauert et al. [2018]), or in the case of the last closed drift shell encroaching the simulation domain, must be updated each time-step (e.g. Drozdov et al. [2021]). Efficient modelling and parameterization of the radial outer boundary should therefore predict its radial position, map this location to  $L^*$  and sample from the electron flux probability distribution parameterized by some measure of geomagnetic activity. Recent studies have explored the statistical outer boundary of the outer radiation belt using sophisticated machine learning techniques (Bloch et al. [2021]) which could form the basis for a predictive model of the boundary's physical location as a function of geomagnetic activity. Our work in Chapter

4 and Thompson et al. [2020a] is useful to map these radial positions to  $L^*$ . Finally, we can sample from the electron flux data accordingly. Stochastic parameterizations of the outer boundary using such an approach allow for ensemble modelling as we did for  $D_{LL}$ . A pilot study examining the sensitivity of the radial diffusion equation to the outer boundary alone, as well as in conjunction with a probabilistic  $D_{LL}$ , would provide key insight into the diffusive response to key sources of natural variability and which sources might dominate.

## CHAPTER 8

## CONCLUSION

The goal of this thesis was to quantify key uncertainties in the formulation of the radial diffusion coefficient,  $D_{LL}$ , and explore the impact on radial diffusion when these uncertainties are accounted for via probabilistic modelling. Radial diffusion driven by ultralow frequency (ULF) waves is currently poorly described in outer radiation belt diffusion models (Horne et al. [2013]). In Chapter 2 we reviewed the prevailing theoretical descriptions for radial diffusion developed by Fälthammar [1965]; Fei et al. [2006], which formed the basis for many of the modern  $D_{LL}$  parameterizations used in operational models today. Many of the assumptions and simplifications used to form  $D_{LL}$  are inconsistent between each parameterization, resulting in deterministic radial diffusion coefficients that can vary by orders of magnitude to result in conflicting levels of radial diffusion (e.g. Drozdov et al. [2021]).

We wanted to challenge the current scientific state-of-the-art of a deterministic  $D_{LL}$ , which provides a single output per set of inputs and is typically a realisation of median ULF wave power (for which  $D_{LL}$  is proportional to in the theory) split by geomagnetic activity. Accounting for variability in  $D_{LL}$  should recover its full distribution when modelling the radial diffusion equation, however, the number of factors which contribute to uncertainties in the power distributions is immense (see the uncertainty tree diagram in Figure 2.2). We found in Chapter 3 (Thompson et al. [2020b]) through idealized ensemble modelling

of a stochastic  $D_{LL}$ , that radial diffusion is highly sensitive to a more rapidly varying  $D_{LL}$  in both time and space, as well as a wide and heavy-tailed distribution. The work in this thesis focuses mostly on the shape and width of  $D_{LL}$  distributions. The key sources of uncertainty that we considered to recover these were

1. The variability of  $L^*$  with an observation's location when assigning ULF wave power approximations to drift-shells
2. The variability of space-based ULF wave power
3. Uncertainties when mapping ground-based magnetic power to the equatorial electric field to infer  $D_{LL}$  (Ozeke et al. [2009, 2012, 2014])

Quantifying  $L^*$  variability is crucial as it underpins the entire construction of  $D_{LL}$ . By designing Pro- $L^*$  (Thompson et al. [2020a]) in Chapter 4, a probabilistic  $L^*$  mapping tool for ground-observations to the magnetic equator, we were able to quantify  $L^*$  variability which varied between magnetic field models, across real-space and with geomagnetic activity (in our case geomagnetic storms). On timescales relevant to radial diffusion, we found that too simplistic representations of the magnetic field (ie a dipole) do not accurately capture the response of  $L^*$  to variability in the magnetospheric topology. Generally, we expect  $L^*$  to be closer than expected when compared to analytic magnetic field models, with offsets increasing with both  $L^*$  and geomagnetic activity. Since many of the modern parameterizations of  $D_{LL}$  were based on dipole-like magnetic fields, a notable proportion of ULF wave power approximations would have been allocated to the wrong  $L^*$ . This aliasing must be accounted for to recover the full power distribution of  $D_{LL}$ . One important thing to note is that all models have imperfections that cannot be mitigated (see Brito and Morley [2017]) so that uncertainty will *always* be present in any  $D_{LL}$  we construct. Being conscious of these uncertainties across the magnetospheric domain allows us to make more informed decisions in our modelling, however.

In Chapter 5 we then investigated the distributions of space-based ULF wave power assigned to  $L^*$  using more a more realistic magnetic field model. Our main findings were:

- ULF wave power had clear dependencies with  $L^*$ , frequency, geomagnetic activity

(Kp) and MLT

- Many of the power distributions could be well approximated by theoretical distributions to be easy sampled in probabilistic modelling
- Although a large number of power distributions were log-symmetric as found in previous studies (e.g. Bentley et al. [2018]), a notable proportion were also log-skewed. This means that (i) median power is not a good indication for the region of highest density, and (ii) the skewed distributions are likely to sample the tail values of ULF wave power that considerably drive the radial diffusion equation (see Thompson et al. [2020b])
- Synthetic power data sets generated in each MLT sector (assumed independent and uncorrelated in time) highlighted that the distribution of drift-averaged power in local is characteristically different

While satellites have the benefit of approximating ULF wave power *in situ*, due to being point-based they cannot provide any information about the temporal and spatial structure of  $D_{LL}$  which requires cotemporal measurements across MLT and  $L^*$ . Global networks of ground observations which can remote sense  $D_{LL}$  are therefore desirable. The ability to remote sense is only possible for the azimuthal electric field  $D_{LL}$  component (see Fei et al. [2006]) and rests on a relationship between the ground-based compressional magnetic field and the equatorial azimuthal electric field (Ozeke et al. [2009]), dependent on the occurrence of a field line resonance (FLR). In Chapter 6 we explored uncertainties in  $D_{LL}$  resulting in the mapping of ground-based magnetic power to space-based electric power. By designing an automated FLR detection algorithm across a latitudinal array of ground magnetometers and running over 7 years of magnetometer data we were able to recover the probabilistic distribution of latitudinal resonance widths, a key parameter in the mapping generally assumed to be constant when constructing  $D_{LL}^E$  (see Ozeke et al. [2012]). Accounting for the distribution of resonance widths we were able to produce probabilistic mapped-power distributions more akin to those observed on board satellites, when compared to the constant width assumption. However, there was still a misalignment between the ground-mapped and space-based power distributions, suggesting that the probabilistic inclusion of other mapping variables (ULF wave azimuthal wavenumber,

ionospheric conductivity, non-dipolar magnetic field) are likely necessary to recover the space-based power distributions.

Although ground-mapped  $D_{LL}^E$  still needs considerable work before it can be used in probabilistic radial diffusion models, in Chapter 7 we revisited the space-based ULF wave power distributions to form stochastic  $D_{LL}$  and discern the impact on radial diffusion again through idealized numerical ensemble experiments. We found that accounting for the shape and width of  $D_{LL}$  distributions resulted in more diffusion than *all* deterministic  $D_{LL}$  parameterizations, with generally more diffusion observed for increasing electron energies. As in Thompson et al. [2020b], however, the efficacy of the shape of the  $D_{LL}$  distribution to significantly drive radial diffusion is coupled to the temporal and spatial variability of  $D_{LL}$ . We have outlined how future work could focus on these through large scale statistical studies and machine learning capabilities.

The work completed in this thesis as well as discussed future projects are those which we believe consider the largest sources of variability in the radial diffusion coefficient, but are by no means the only possible projects which should be completed. A stochastic parameterization of radial diffusion can only be complete once all sources of variability within the uncertainty tree diagram in Figure 2.2 are quantified. We hope that our work presented here will lead us towards becoming more certain about our uncertainties when modelling radial diffusion.

## APPENDIX A

APPENDIX A

### A.1 Fälthammar's description of radial diffusion

The derivations in the following sections are extensions of those provided in Fälthammar [1965]; Lejosne [2019].

#### A.1.1 Magnetic disturbances and electromagnetic radial diffusion

We consider a simple, linearized, perturbation superimposed on the background magnetic dipole field  $B_d$

$$\mathbf{B}_d = -\frac{B_E R_E^3}{r^3} \begin{bmatrix} 2 \cos \theta \\ \sin \theta \\ 0 \end{bmatrix} \quad (\text{A.1})$$

where  $B_E \sim 30,000\text{nT}$  is the magnitude of the equatorial magnetic field and  $R_E \sim 6400\text{km}$ . The small perturbation in spherical coordinates  $(\hat{r}, \hat{\theta}, \hat{\phi})$  is

$$\mathbf{b} = \begin{bmatrix} S(t) \cos \theta + A(t)r \sin 2\phi \\ -S(t) \sin \theta + A(t)r \cos 2\theta \cos \phi \\ -A(t)r \cos \theta \sin \phi \end{bmatrix} \quad (\text{A.2})$$

with the assumption that  $|b/B_d| \ll 1$ . The fluctuation has a symmetric part proportional to  $S(t)$  (independent of local time) and an asymmetric part proportional to  $A(t)$  (dependent on local time).

The perturbation is curl free by design:

$$\nabla \times \mathbf{b} = \begin{bmatrix} \frac{1}{r^2 \sin \theta} \hat{r} & \frac{1}{r \sin \theta} \hat{\theta} & \frac{1}{r} \hat{\phi} \\ \partial_r & \partial_\theta & \partial_\phi \\ b_r & r b_\theta & r \sin \theta b_\phi \end{bmatrix} \quad (\text{A.3})$$

$$= \frac{1}{r^2 \sin \theta} [-Ar^2 \sin \phi \underbrace{(-\sin^2 \theta + \cos^2 \theta)}_{\cos 2\theta} + Ar^2 \cos 2\theta \sin \phi] \hat{r} \quad (\text{A.4})$$

$$\begin{aligned} & - \frac{1}{r \sin \theta} [-A \underbrace{2r \sin \theta \cos \theta}_{r \sin 2\theta} \sin \phi + Ar \sin 2\theta \sin \phi] \hat{\theta} \\ & + \frac{1}{r} [-S \sin \theta + 2Ar \cos 2\theta \cos \phi - (-S \sin \theta + 2 \cos 2\theta Ar \cos \phi)] \hat{\phi} \\ & = 0 \end{aligned} \quad (\text{A.5})$$

We assume frozen-in-flux (ALFVÉN [1942]): In a fluid with infinite electric conductivity, the magnetic field is frozen into the flux and has to move with it.

The induced electric field associated with time variations of  $\mathbf{b}$  is

$$\mathbf{E}_{\text{ind}} = \begin{bmatrix} -\frac{r^2}{7} \frac{dA}{dt}(t) \sin \theta \sin \phi \\ \frac{2r^2}{7} \frac{dA}{dt}(t) \cos \theta \sin \phi \\ -\frac{r}{2} \frac{dS}{dt}(t) \sin \theta + \frac{2r^2}{21} \frac{dA}{dt}(t) (3 - 7 \sin^2 \theta) \cos \phi \end{bmatrix} \quad (\text{A.6})$$

It is straight forward to verify Faraday's law  $\nabla \times \mathbf{E}_{\text{ind}} = -\partial \mathbf{b} / \partial t$ :

$$\begin{aligned}
 \nabla \times \mathbf{E}_{\text{ind}} &= \frac{1}{r^2 \sin \theta} \left[ \left( -\frac{r^2}{2} \frac{dS}{dt} 2 \sin \theta \cos \theta + \frac{2r^3}{21} \frac{dA}{dt} \cos \phi (3 \cos \theta - 7(3 \sin^2 \theta \cos \theta)) - \frac{2r^3}{7} \frac{dA}{dt} \cos \theta \cos \phi \right) \hat{r} \right. \\
 &\quad - \frac{1}{r \sin \theta} \left[ \left( -r \frac{dS}{dt} \sin^2 \theta + \frac{6r^2}{21} \frac{dA}{dt} (3 - 7 \sin^2 \theta) \sin \theta \cos \phi \right) + \frac{r^2}{7} \frac{dA}{dt} \sin \theta \cos \phi \right] \hat{\theta} \\
 &\quad \left. + \frac{1}{r} \left[ \frac{6r^2}{7} \frac{dA}{dt} \cos \theta \sin \phi + \frac{r^2}{7} \frac{dA}{dt} \cos \theta \sin \phi \right] \hat{\phi} \right] \quad (\text{A.7})
 \end{aligned}$$

$$\begin{aligned}
 &= \left[ -\frac{dS}{dt} \cos \theta - \frac{dA}{dt} r \sin 2\theta \cos \phi \right] \hat{r} + \left[ \frac{dS}{dt} \sin \theta - \frac{dA}{dt} r \cos \phi (1 - 2 \sin^2 \theta) \right] \hat{\theta} + \frac{dA}{dt} r \cos \theta \sin \phi \hat{\phi} \\
 &\quad (\text{A.8})
 \end{aligned}$$

$$= -\partial \mathbf{b} / \partial t \quad (\text{A.9})$$

We consider the magnetic equator ( $\theta = \frac{\pi}{2}$ ) only. We have

$$\mathbf{B} = -\frac{B_E R_E^3}{r^3} \begin{bmatrix} 0 \\ 1 \\ 0 \end{bmatrix} + \begin{bmatrix} 0 \\ -S(t) - A(t)r \cos \phi \\ 0 \end{bmatrix} \quad (\text{A.10})$$

$$\mathbf{E}_{\text{ind}} = \begin{bmatrix} E_r \\ 0 \\ E_\phi \end{bmatrix} \quad (\text{A.11})$$

$$B = B_d + b, \quad \nabla B = \partial_r \hat{r} + \frac{1}{r} \partial_\theta \hat{\theta} + \frac{1}{r \sin \theta} \partial_\phi \hat{\phi} \quad (\text{A.12})$$

If we consider the equation of motion for non-relativistic particles normal to the magnetic field  $\mathbf{B}$  at the magnetic equator (Fälthammar [1965])

$$\mathbf{u}_\perp = -\frac{1}{eB^2} \mathbf{B} \times (e\mathbf{E} - \mu \nabla B) \quad (\text{A.13})$$

where  $\mu$  here is the magnetic moment,  $e = \frac{3\mu}{\Omega r^2}$ ,  $\Omega = \frac{3\mu}{\hat{\gamma} q r^2}$ ,  $\hat{\gamma}$  is the Lorentz factor. We obtain the following cross product

$$\begin{vmatrix} \hat{r} & \hat{\theta} & \hat{\phi} \\ 0 & -\frac{1}{eB} & 0 \\ eE_r - \mu \partial_r B & 0 & eE_\phi - \frac{\mu}{r} \partial_\phi B \end{vmatrix} \quad (\text{A.14})$$

From this we can extract the radial component of the drift velocity, reversing the signs since the Fälthammar [1965] notation has azimuthal angle positive eastwards

$$\frac{dr}{dt} = \frac{E_{ind,\phi}}{B} - \frac{\mu}{rBe} \frac{\partial b}{\partial \phi} \quad (\text{A.15})$$

$$= \frac{1}{B_d(1+b/B_d)} \left[ E_{ind,\phi} - \frac{\Omega r}{3B} \frac{\partial b}{\partial \phi} \right], \quad e = \frac{3\mu}{\Omega r^2} \quad (\text{A.16})$$

$$= \frac{1}{(1+b/B_d)} \left[ \frac{E_{ind,\phi}}{B} - \frac{\mu}{Bq\hat{\gamma}r} \frac{\partial b}{\partial \phi} \right], \quad \Omega = \frac{3\mu}{\hat{\gamma}qr^2} \quad (\text{A.17})$$

We can do the same for the azimuthal component of the drift velocity

$$r \frac{d\phi}{dt} = \frac{1}{eB} (eE_r - \mu \frac{\partial b}{\partial r}) \quad (\text{A.18})$$

$$= \frac{E_r}{B} + \frac{\mu}{eB} \left( \frac{3B_E R_E^3}{r^4} + \frac{\partial b}{\partial r} \right) \quad (\text{A.19})$$

$$= \frac{1}{(1+b/B_d)} \left[ \frac{E_r}{B_d} + \Omega r - \frac{\Omega r^2}{3B_d} \frac{\partial b}{\partial r} \right] \quad (\text{A.20})$$

Recall the earlier approximation  $|b/B_d| \ll 1$ . Further to this, the strength of the electric field disturbance is (from Equation A.13 look at terms containing  $E$  and normalize by distance, angular frequency and background magnetic field)

$$Q = |E/\Omega r B_d| \quad (\text{A.21})$$

We do not require  $Q$  to always be small, provided

$$\left| \Omega \int_{t_0}^{t_0+1/\Omega} Q dt \right| \leq \eta \ll 1 \quad (\text{A.22})$$

To zeroth order in  $r$ ,  $r = \text{constant} = r_0$  is the unperturbed value of the particle radial location and we therefore obtain the following

$$\frac{dr}{dt} = \frac{E_{ind,\phi}}{B_d} - \frac{\mu}{B_d q \gamma r_0} \frac{\partial b}{\partial \phi} \quad (\text{A.23})$$

where  $B_d = B_E R_E^3 / r_0^3$ . We reformulate the the drift phase  $\phi$  in terms of the angular drift velocity

$$\phi(t) = -\Omega t + \phi_0 \quad (\text{A.24})$$

If we substitute everything into the radial component of the drift velocity we get

$$\frac{dr}{dt} = -\frac{r_0}{2B_d} \frac{dS}{dt}(t) - \frac{8r_0^2}{21B_d} \frac{dA}{dt}(t) \cos(\Omega t - \phi_0) - \frac{r_0^2 \Omega}{3B_d} A(t) \sin(\Omega t - \phi_0) \quad (\text{A.25})$$

Partial integration of the first 2 terms ( $\int_a^b u(x)v'(x)dx = [u(x)v(x)]_a^b - \int_a^b u'(x)v(x)dx$ ) yields

$$\begin{aligned} r(t) - r_0 &= -\frac{r_0}{2B_d} (S(t) - S(0)) \\ &\quad - \frac{8r_0^2}{21B_d} [(A(t) \cos(\Omega t - \phi_0) - A(0) \cos(\phi_0)) + \Omega \int_0^t A(\psi) \sin(\Omega \psi - \phi_0) d\psi] \\ &\quad + \frac{r_0^2 \Omega}{3B_d} \int_0^t A(\psi) \sin(\Omega \psi - \phi_0) d\psi \end{aligned} \quad (\text{A.26})$$

Collecting everything together the total radial displacement of an equatorial particle after time  $t$  is

$$\begin{aligned} r(t) - r_0 &= -\frac{5}{7} \frac{r_0^2 \Omega}{B_d} \int_0^t A(\psi) \sin(\Omega \psi - \phi_0) d\psi - \frac{r_0}{2B_d} (S(t) - S(0)) \\ &\quad - \frac{8r_0^2}{21B_d} (A(t) \cos(\Omega t - \phi_0) - A(0) \cos(\phi_0)) \end{aligned} \quad (\text{A.27})$$

Recall Equation A.10 and the assumption  $|b/B_d| \ll 1$ . Both components of the disturbance  $\mathbf{b}$  must therefore be small

$$\implies S(t) - S(0) \ll B_d \quad (\text{A.28})$$

$$\implies r_0^2 (A(t) \cos(\Omega t - \phi_0) - A(0) \cos(\phi_0)) \ll B_d \quad (\text{A.29})$$

Therefore the only contribution that can potentially lead to large cumulative effects is

$$X(t) = -\frac{5}{7} \frac{r_0^2 \Omega}{B_d} \int_0^t A(\psi) \sin(\Omega \psi - \phi_0) d\psi \quad (\text{A.30})$$

Things to note about this integral:

- If the signal  $A$  has frequencies in the neighbourhood of the angular drift velocity  $\Omega$ , the integral  $X$  can increase with time, and the radial displacement can become significant.
- The integral  $X(t)$  only depends on the signal  $A$ , i.e., it only depends on the characteristics of the asymmetric perturbations of the magnetic field.
- The integral  $X(t)$  consists of the partial integration of two nearly equal contributions: (1) the induced electric field contributes  $8/21$  of the  $5/7$  factor in the radial displacement (i.e., about 55%), and (2) the magnetic disturbance contributes  $1/3$  of the  $5/7$  factor in the radial displacement (i.e., about 45%).

Fälthammar [1968] assumed  $A(t)$  are realizations of a stationary stochastic process (fluctuates randomly around zero mean, with time independent statistical properties). In that context, after a time  $t$  that is much longer than the autocorrelation time of the signal  $A$ , and much longer than the particle drift period, the expected value of the square displacement  $(r(t) - r_0)^2$  will grow linearly with time. Thus, over a long period of time  $t$ , the expected value of the square displacement per unit time will be constant. It is that constant rate of change value that determines the radial diffusion coefficient  $D_{LL}$ :

$$\frac{d}{dt}[(r(t) - r_0)^2] = \text{constant} = 2R_E^2 D_{LL} \quad (\text{A.31})$$

where  $[\cdot]$  denotes the expectation value (over all possible scenarios and possible initial drift phases  $\phi_0$ ). Suppose we begin with

$$x(t) = \int_0^t A(\xi) \sin(\Omega\xi + \phi_0) d\xi = \int_0^t u(\xi) d\xi \quad (\text{A.32})$$

Then

$$\frac{d}{dt}[x^2(t)] = [2x \frac{dx}{dt}] \quad (\text{A.33})$$

$$= 2[\int_0^t u(t)u(\xi)d\xi] \quad (\text{A.34})$$

$$= 2 \int_0^t [u(t)u(\xi)]d\xi \quad (\text{A.35})$$

$$= -2 \int_t^0 [u(t)u(t-\tau)]d\tau, \quad \xi = t - \tau \quad (\text{A.36})$$

$$= 2 \int_0^t [u(t)u(t-\tau)]d\tau \quad (\text{A.37})$$

If we expand out the  $u$  function we have

$$[u(t)u(t-\tau)] = [A(t)A(t-\tau)] \sin(\Omega t + \phi_0) \sin(\Omega t + \phi_0 - \Omega\tau) \quad (\text{A.38})$$

$$= [A(t)A(t+\tau)] \sin(\Omega t + \phi_0) \sin(\Omega t + \phi_0 - \Omega\tau), \quad (\text{Stationarity}) \quad (\text{A.39})$$

$$= [A(t)A(t+\tau)]\{\sin^2(\Omega t + \phi_0) \cos(\Omega\tau) - \sin(\Omega t + \phi_0) \cos(\Omega t + \phi_0) \sin(\Omega\tau)\} \quad (\text{A.40})$$

According to Equation A.37, using a simple integration

$$[x^2(t)] = \int_0^t 2 \int_0^\xi [u(\xi)u(\xi-\tau)]d\tau d\xi \quad (\text{A.41})$$

we can decompose the signal  $A$  into its mean and fluctuating part

$$A = [A] + \tilde{A} \quad (\text{A.42})$$

and the following holds

$$[A(t)A(t+\tau)] = [[A(t)] + \tilde{A}(t)][A(t+\tau)] + \tilde{A}(t+\tau)] \quad (\text{A.43})$$

$$= [[A(t)][A(t+\tau)] + [A(t)]\tilde{A}(t+\tau) + \tilde{A}(t)[A(t+\tau)] + \tilde{A}(t)\tilde{A}(t+\tau)] \quad (\text{A.44})$$

$$[\tilde{A}] = 0 \implies [A(t)][A(t+\tau)] + [\tilde{A}(t)\tilde{A}(t+\tau)] \quad (\text{A.45})$$

Due to the assumed stationarity of  $A$  we can also write the following

$$[A(t)] = [[A(t)] + \tilde{A}(t)] = [A(t+\tau)] = \bar{A} = \text{constant} \quad (\text{A.46})$$

Using all of these we have that

$$\int_0^t [u(t)u(t-\tau)]d\tau = \int_0^t ([A(t)][A(t+\tau)] + [\tilde{A}(t)\tilde{A}(t+\tau)])\{\sin^2(\Omega t + \phi_0) \cos(\Omega\tau) - \sin(\Omega t + \phi_0) \cos(\Omega t + \phi_0) \sin(\Omega\tau)\} \quad (\text{A.47})$$

$$\begin{aligned} &= \sin^2(\Omega t + \phi_0) \left\{ \frac{\bar{A}^2 \sin(\Omega t)}{\Omega} + \underbrace{\int_0^t [\tilde{A}(t)\tilde{A}(t+\tau)] \cos(\Omega\tau) d\tau}_{(\text{T})} \right\} \\ &+ \sin(\Omega t + \phi_0) \cos(\Omega t + \phi_0) \left\{ \frac{\bar{A}^2(\cos(\Omega t) - 1)}{\Omega} - \underbrace{\int_0^t [\tilde{A}(t)\tilde{A}(t+\tau)] \sin(\Omega\tau) d\tau}_{(\text{TT})} \right\} \end{aligned} \quad (\text{A.48})$$

We denote the following definite integrals

$$I_1 = \int_0^\infty [\tilde{A}(t)\tilde{A}(t+\tau)] \cos(\Omega\tau) d\tau \quad (\text{A.49})$$

$$I_2 = \int_0^\infty [\tilde{A}(t)\tilde{A}(t+\tau)] \sin(\Omega\tau) d\tau \quad (\text{A.50})$$

which exist in the sense that their indefinite counterparts **T**, **TT** are approximately independent of  $t$  when  $t$  exceeds a certain finite value  $t_1$ . Then, when  $t \gg t_1$ ,

$$[x^2(t)] = \int_0^t \underbrace{2\sin^2(\Omega t + \phi_0)}_{1 - \cos(2\Omega t + 2\phi_0)} \left\{ \frac{\bar{A}^2 \sin(\Omega t)}{\Omega} + I_1 \right\} dt + 2 \int_0^t \sin(\Omega t + \phi_0) \cos(\Omega t + \phi_0) \left\{ \frac{\bar{A}^2(\cos(\Omega t) - 1)}{\Omega} - I_2 \right\} dt \quad (\text{A.51})$$

$$\begin{aligned} &= 2 \left[ -\frac{\bar{A}^2}{\Omega^2} \cos(\Omega t - 1) + tI_1 + \frac{I_1}{3\Omega} (\sin^3(\Omega t + \phi_0) - \sin^3(\phi_0)) + \frac{\bar{A}^2}{\Omega} \int_0^t \cos^2(\Omega t + \phi_0) \sin(\Omega t) dt \right] \\ &+ \left[ \frac{I_2}{2\Omega} (\cos(2\Omega t + 2\phi_0) - \cos(2\phi_0)) + \frac{\bar{A}^2(\cos(\Omega t) - 1)}{\Omega} \int_0^t \sin(2\Omega t + 2\phi_0) \cos(\Omega t) dt \right] \end{aligned} \quad (\text{A.52})$$

To remove some of these terms we only consider times where  $t \gg 1/\Omega$ , and therefore  $tI_1$  dominates as long as  $I_1$  does not vanish. Further, recall the strength of the electric disturbance in Equation A.21 which we assume to be small

$$\implies \frac{\bar{A}}{\Omega B_d} \leq \eta r_0 \quad (\text{A.53})$$

Since we are interested in the accumulated displacements  $\gg \eta r_0$

$$[(r - r_0)^2] = \frac{c[x^2(t)]}{B_d} \gg (\eta r_0)^2 \quad (\text{A.54})$$

$$\implies [x^2(t)] \gg \left(\frac{\bar{A}}{\Omega}\right)^2 \quad (\text{A.55})$$

Since all that remains is  $[x^2(t)] = 2tI_1$  we therefore obtain the result

$$\frac{d}{dt}[x^2(t)] = \int_0^\infty [\tilde{A}(t)\tilde{A}(t + \xi)] \cos(\Omega\xi) d\xi \quad (\text{A.56})$$

It follows that we have

$$D_{LL,m,eq} = \frac{1}{2R_E^2} \frac{d}{dt}[X^2(t)] = \frac{1}{2} \left(\frac{5}{7}\right)^2 \left(\frac{r_0^2 \Omega}{R_E B_d}\right)^2 \int_0^\infty [\tilde{A}(t)\tilde{A}(t + \xi)] \cos(\Omega\xi) d\xi \quad (\text{A.57})$$

Using the Wiener–Khinchin theorem, we have that

$$P_A(\Omega) = \int_{-\infty}^\infty [\tilde{A}(t)\tilde{A}(t + \xi)] \cos(\Omega\xi) d\xi \quad (\text{A.58})$$

$$= 4 \int_0^\infty [\tilde{A}(t)\tilde{A}(t + \xi)] \cos(\Omega\xi) d\xi \quad (\text{A.59})$$

where  $P_A(\Omega)$  the power spectrum of the asymmetric field perturbation  $A$  evaluated at  $\Omega$ . Here we have assumed that  $A$  and  $[A(t)A(t + \xi)]$  satisfy the necessary conditions for Fourier inversion to be valid. The factor of 4 arises because the power spectral density for positive frequencies only is double that for all frequencies, which multiplies with the integral defined on  $[0, \infty]$  instead of  $[-\infty, \infty]$ .

We finally obtain the appropriate expression for the diffusion coefficient

$$D_{LL,m,eq} = \frac{1}{8} \left(\frac{5}{7}\right)^2 \left(\frac{r_0^2 \Omega}{R_E B_d}\right)^2 P_A(\Omega) \quad (\text{A.60})$$

$$= \frac{1}{8} \left(\frac{5}{7}\right)^2 \left(\frac{(LR_E)^2 \Omega}{R_E (B_E/L^3)}\right)^2 P_A(\Omega), \quad L = r_0/R_E, B_d = B_E/L^3 \quad (\text{A.61})$$

$$= \frac{1}{8} \left(\frac{5}{7}\right)^2 \frac{L^{10} R_E^2}{B_E^2} \Omega^2 P_A(\Omega), \quad L = r_0/R_E, B_d = B_E/L^3 \quad (\text{A.62})$$

where  $B_E$  is the equatorial magnetic field strength at the Earth's surface and  $L$  is the L-Shell parameter. In terms of the drift frequency  $\omega = \Omega/2\pi$  we have the following

$$D_{LL,m,eq} = \frac{\pi^2}{2} \left(\frac{5}{7}\right)^2 \frac{L^{10} R_E^2}{B_E^2} \omega^2 P_A(\omega) \quad (\text{A.63})$$

It is often discussed how the electromagnetic diffusion coefficient varies proportional to  $L^{10}$ . Theoretically this statement corresponds to 2 specific scenarios:

1.  $P_A \propto \omega^{-2}$ : Randomly occurring events with a very short rise time and a very long recovery time
2.  $P_A \propto \omega^{-n}$ : The variations of the radial diffusion coefficient with normalized equatorial radial distance,  $L$ , first adiabatic invariant,  $M$ , or kinetic energy,  $T$ , are the following

$$D_{LL,m,eq} \propto L^{6+2n} M^{2-n} \propto L^{12-n} T^{2-n} \quad (\text{A.64})$$

### A.1.2 Electric potential disturbances and electrostatic radial diffusion

We now consider electric potential fields such that

$$\nabla \times \mathbf{E} = 0 \quad (\text{A.65})$$

Recalling Equation A.23, in an electric potential field the magnetic component of the equation will average out over one  $1/\Omega$  period (since the integral of  $\cos$  or  $\sin$  over 1 period is zero) and we only retain the first term

$$\frac{dr}{dt} = \frac{E_\phi}{B_d} \quad (\text{A.66})$$

We can decompose the electric field term at any time  $t$ , on any circle  $r = r_0$ , into the Fourier series

$$E_\phi(r_0, \phi, t) = \sum_{n=1}^{\infty} E_{\phi n} \cos(n\phi + \gamma_n(r_0, t)) \quad (\text{A.67})$$

which we can approximate by

$$E_\phi(r_0, \phi, t) = \sum_{n=1}^N E_{\phi n} \cos(n\phi + \gamma_n(r_0, t)) \quad (\text{A.68})$$

As an idealized setup we assume that only the amplitudes  $E_{\phi_n}$  vary with time and not the phases ( $\gamma_n(r_0, t) = \gamma_n$ ). We follow the same process as for the electromagnetic diffusion coefficient. Integrating Equation A.66 we have (again using  $\phi = \Omega t + \phi_0$ )

$$r(t) - r_0 = \frac{1}{B_d} \sum_{n=1}^N \int_0^t E_{n\phi} \cos(n\Omega\xi + n\phi_0 + \gamma_n) d\xi = \frac{1}{B_d} y(t) \quad (\text{A.69})$$

As before we have  $y(t) = \int_0^t v(\xi) d\xi$  and

$$\frac{d}{dt}[y^2(t)] = 2 \int_0^t [v(t)v(t - \tau)] d\tau \quad (\text{A.70})$$

We assume that  $E_n$  are individually and jointly stationary stochastic processes which yields the following

$$[E_m(t - \tau)E_n(t)] = [E_m(t)E_n(t + \tau)], \quad \forall m = n, m \neq n \quad (\text{A.71})$$

$$[v(t)v(t - \tau)] = \left[ \sum_m \sum_n E_m(t - \tau) E_n(t) \cos(n\Omega t + \psi_n) \cos(m\Omega t + -m\Omega\tau + \psi_m) \right] \quad (\text{A.72})$$

$$(\text{Bring in averages}) = \sum_m \sum_n [E_m(t) E_n(t + \tau)] \cos(n\Omega t + \psi_n) \cos(m\Omega t + -m\Omega\tau + \psi_m) \quad (\text{A.73})$$

$$(\cos(A - B) \text{ identity}) = \sum_m \sum_n [E_m(t) E_n(t + \tau)] \{ \cos(n\Omega t + \psi_n) \cos(m\Omega t + \psi_m) \cos(m\Omega\tau) + \cos(n\Omega t + \psi_n) \sin(m\Omega t + \psi_m) \sin(m\Omega\tau) \} \quad (\text{A.74})$$

$$\begin{aligned} &= \sum_n [E_n(t) E_n(t + \tau)] \cos^2(n\Omega t + \psi_n) \cos(n\Omega\tau) \quad (\text{A.75}) \\ &+ \sum_n [E_n(t) E_n(t + \tau)] \cos(n\Omega t + \psi_n) \sin(n\Omega t + \psi_n) \sin(n\Omega\tau) \\ &+ \sum_{\substack{m \\ m \neq n}} \sum_n [E_m(t) E_n(t + \tau)] \cos(n\Omega t + \psi_n) \cos(m\Omega t + \psi_m) \cos(m\Omega\tau) \\ &+ \sum_{\substack{m \\ m \neq n}} \sum_n [E_m(t) E_n(t + \tau)] \cos(n\Omega t + \psi_n) \sin(m\Omega t + \psi_m) \sin(m\Omega\tau) \end{aligned}$$

From  $[y^2(t)] = \int_0^t 2 \int_0^\xi [v(\xi)v(\xi - \tau)] d\tau$  and the decomposition of  $E_n$  into its mean ( $[.]$ ) and fluctuating ( $\sim$ ) parts with the relations

$$[E_m(t) E_n(t + \tau)] = [E_m(t)][E_n(t + \tau)] + [\tilde{E}_m(t) \tilde{E}_n(t + \tau)] \quad (\text{A.76})$$

$$[E_n(t)] = [E_n(t + \tau)] = \bar{E} = \text{constant} \quad (\text{A.77})$$

we obtain

$$\begin{aligned}
 \int_0^t [v(t)v(t-\tau)]d\tau &= \sum_n \cos^2(n\Omega t + \psi_n) \left\{ \frac{\bar{E}^2}{n\Omega} \sin(n\Omega t) + \int_0^t [\tilde{E}_n(t)\tilde{E}_n(t+\tau)] \cos(n\Omega\tau) d\tau \right\} \\
 &+ \sum_n \cos(n\Omega t + \psi_n) \sin(n\Omega t + \psi_n) \left\{ \frac{\bar{E}^2}{n\Omega} (1 - \cos n\Omega t) + \int_0^t [\tilde{E}_n(t)\tilde{E}_n(t+\tau)] \sin(n\Omega\tau) d\tau \right\} \\
 &+ \sum_{\substack{m \\ m \neq n}} \sum_n \cos(n\Omega t + \psi_n) \cos(m\Omega t + \psi_m) \left\{ \frac{\bar{E}_m \bar{E}_n}{m\Omega} \sin(m\Omega t) \right. \\
 &+ \left. \int_0^t [\tilde{E}_m(t)\tilde{E}_n(t+\tau)] \cos(m\Omega\tau) d\tau \right\} \\
 &+ \sum_{\substack{m \\ m \neq n}} \sum_n \cos(n\Omega t + \psi_n) \sin(m\Omega t + \psi_m) \left\{ \frac{\bar{E}_m \bar{E}_n}{m\Omega} (1 - \cos m\Omega t) \right. \\
 &+ \left. \int_0^t [\tilde{E}_m(t)\tilde{E}_n(t+\tau)] \sin(m\Omega\tau) d\tau \right\} \tag{A.78}
 \end{aligned}$$

We now define the following definite integrals in the same way which we did for the electromagnetic case

$$I_{mn1} = \int_0^\infty [\tilde{E}_m(t)\tilde{E}_n(t+\tau)] \cos(m\Omega\tau) d\tau \tag{A.79}$$

$$I_{mn2} = \int_0^\infty [\tilde{E}_m(t)\tilde{E}_n(t+\tau)] \sin(m\Omega\tau) d\tau \tag{A.80}$$

Assuming  $t \gg t_1$  we get the following

$$[y^2(t)] = \sum_n 2 \int_0^t \cos^2(n\Omega t + \psi_n) \left\{ \frac{\bar{E}^2}{n\Omega} \sin(n\Omega t) + I_{nn1} \right\} dt \tag{A.81}$$

$$\begin{aligned}
 &+ \sum_n 2 \int_0^t \cos(n\Omega t + \psi_n) \sin(n\Omega t + \psi_n) \left\{ \frac{\bar{E}^2}{n\Omega} (1 - \cos n\Omega t) + I_{nn2} \right\} dt \\
 &+ \sum_{\substack{m \\ m \neq n}} \sum_n 2 \int_0^t \cos(n\Omega t + \psi_n) \cos(m\Omega t + \psi_m) \left\{ \frac{\bar{E}_m \bar{E}_n}{m\Omega} \sin(m\Omega t) + I_{mn1} \right\} dt \\
 &+ \sum_{\substack{m \\ m \neq n}} \sum_n 2 \int_0^t \cos(n\Omega t + \psi_n) \sin(m\Omega t + \psi_m) \left\{ \frac{\bar{E}_m \bar{E}_n}{m\Omega} (1 - \cos m\Omega t) + I_{mn2} \right\} dt
 \end{aligned} \tag{A.82}$$

Assuming again that  $t \gg 1/\Omega$  and Equation A.55 we obtain the result

$$\frac{d}{dt}[y^2(t)] = \sum_{n=1}^N \int_0^\infty [\tilde{E}_n(t)\tilde{E}_n(t+\xi)] \cos(n\Omega\xi) d\xi \quad (\text{A.83})$$

and the subsequent diffusion equation

$$D_{LL,e} = \frac{1}{2} \left( \frac{1}{R_E B_d} \right)^2 \sum_{n=1}^N \int_0^\infty [\tilde{E}_n(t)\tilde{E}_n(t+\xi)] \cos(n\Omega\xi) d\xi \quad (\text{A.84})$$

$$= \frac{L^6}{8R_E^2 B_E^2} \sum_{n=1}^N P_E(n\omega) \quad (\text{A.85})$$

## A.2 Fei's description of radial diffusion

The key difference between Fälthammar [1965] and Fei et al. [2006] is the treatment of magnetic and electric perturbations. In Fälthammar [1965] perturbations were separated into electric potential and magnetic disturbances, justified by the fact that they originate from different sources. Conversely in Fei et al. [2006] magnetic and electric disturbances were treated separately, inherently assuming that they are uncorrelated. When magnetic and electric disturbances are uncorrelated (which was justified using a misinterpretation of the work by Brizard and Chan [2001b]) Faraday's Law is not satisfied. By omitting the relationship between electric and magnetic field perturbations, the Fei et al. [2006] description underestimates the total radial diffusion (Lejosne and Kollmann [2020]). However, treating the field perturbations separately is very practical. Separating the induced and electrostatic contributions from electric field perturbation measurements is very difficult, which makes the application of Fälthammar [1965] to ground and satellite measurements unviable without further simplifying assumptions (e.g. Brautigam et al. [2005]). By using the Fei et al. [2006] description this issue is avoided.

We start with a background magnetic field model as a superposition of a dipole field and time-stationary asymmetric disturbance in the equatorial plane. This magnetic field

model has magnitude

$$B_0(r, \phi) = B_d + \Delta B(r) \cos \phi \quad (\text{A.86})$$

$$= \frac{B_E R_E^3}{r^3} + \Delta B(r) \cos \phi \quad (\text{A.87})$$

An unperturbed equatorial electron drifting adiabatically in the magnetic field will move such that the guiding centre drifts along contours of constant magnetic field. Suppose we have initial  $r_0, \Delta B(r_0) = 0$ , then

$$\frac{B_E R_E^3}{r^3} + \Delta B \cos \phi = \frac{B_E R_E^3}{r_0^3} \quad (\text{A.88})$$

$$\implies r^3 \left[ \frac{B_E R_E^3}{r_0^3} - \Delta B \cos \phi \right] = B_E R_E^3 \quad (\text{A.89})$$

$$\implies r^3 \left[ \frac{R_E^3}{r_0^3} - \frac{\Delta B}{B_E} \cos \phi \right] = R_E^3 \quad (\text{A.90})$$

Let  $L^* = r_0/R_E$  be the drift shell of an equatorial particle initially at  $r_0, \phi_0$ ,

$$\implies r = R_E \left( L^{*-3} - \frac{\Delta B}{B_E} \cos \phi \right)^{-1/3} \quad (\text{A.91})$$

$$= R_E L^* \left( 1 - L^{*3} \frac{\Delta B}{B_E} \cos \phi \right)^{-1/3} \quad (\text{A.92})$$

$$= r_0 \left( 1 - \frac{\Delta B}{B_d} \cos \phi \right)^{-1/3}, \quad B_d = B_E / L^{*3} \quad (\text{A.93})$$

$$\sim r_0 \left( 1 + \frac{\Delta B}{3B_d} \cos \phi \right), \quad (\text{Binomial expansion 1st order}) \quad (\text{A.94})$$

Using the definition of  $L^*$  we have the following

$$\frac{dL^*}{dr} = \frac{1}{R_E} \frac{dr_0}{dr} \quad (\text{A.95})$$

$$= \frac{1}{R_E} \frac{d}{dr} \left[ r \left( 1 + \frac{\Delta B}{3B_d} \cos \phi \right)^{-1} \right] \quad (\text{A.96})$$

$$\sim \frac{1}{R_E} \frac{d}{dr} \left[ r \left( 1 - \frac{\Delta B}{3B_d} \cos \phi \right) \right], \quad (\text{Binomial expansion 1st order in } \Delta B) \quad (\text{A.97})$$

$$= \frac{1}{R_E} \frac{d}{dr} \left[ r \left( 1 - \frac{\Delta B r^3}{3B_E R_E} \cos \phi \right) \right] \quad (\text{A.98})$$

$$\sim \frac{1}{R_E} \left( 1 - \frac{4}{3} \frac{\Delta B}{B_d} \cos \phi \right), \quad (\text{1st order in } \Delta B) \quad (\text{A.99})$$

We therefore have a relation between the displacement of an equatorial particle away from the initial drift contour  $dr/dt$  and  $L^*$

$$\frac{dL^*}{dt} = \frac{dL^*}{dr} \frac{dr}{dt} \quad (\text{A.100})$$

The two drivers considered for radial diffusion are magnetic field and electric field disturbances (assumed to be uncorrelated).

### A.2.1 Magnetic disturbances and magnetic diffusion

Unlike in Fälthammar [1965, 1968], Fei et al. [2006] considers magnetic field fluctuations only in the direction of the background magnetic field (compressional perturbations). They are described by a Fourier sum around  $r_0$

$$\delta B(r, \phi, t) = \sum_{n=1} \delta B_n(t) \cos(n\phi) \quad (\text{A.101})$$

Since there are no contributions from the induced electric field, the radial component of the drift velocity is given by

$$\frac{dr}{dt} = -\frac{\mu}{q\gamma B_d r_0} \frac{\partial(\delta B)}{\partial \phi} \quad (\text{A.102})$$

It follows that the time variation of  $L^*$  is given by

$$\frac{dL^*}{dt} = \frac{1}{R_E} \left( 1 - \frac{4}{3} \frac{\Delta B}{B_d} \cos \phi \right) \left( \frac{\mu}{q\gamma B_d r_0} \sum_{n=1} n \delta B_n(t) \sin(n\phi) \right) \quad (\text{A.103})$$

$$= \frac{\mu}{q\gamma B_d r_0 R_E} \sum_{n=1} n \delta B_n(t) \sin(n\phi) - \frac{4}{3} \frac{\Delta B}{B_d} \frac{\mu}{q\gamma B_d r_0 R_E} \cos \phi \sum_{n=1} n \delta B_n(t) \sin(n\phi) \quad (\text{A.104})$$

$$= \frac{\mu L^{*2}}{q\gamma B_E R_E^2} \sum_{n=1} n \delta B_n(t) \sin(n\phi) - \frac{4}{3} \frac{\mu L^{*5}}{q\gamma B_E R_E^2} \frac{\Delta B}{B_E} \sum_{n=1} n \delta B_n(t) \cos \phi \sin(n\phi) \quad (\text{A.105})$$

If we acknowledge the following identities

$$\sin(\phi + n\phi) = \sin(\phi) \cos(n\phi) + \cos(\phi) \sin(n\phi) \quad (\text{A.106})$$

$$\sin(\phi - n\phi) = \sin(\phi) \cos(n\phi) - \cos(\phi) \sin(n\phi) \quad (\text{A.107})$$

$$\implies \cos(\phi) \sin(n\phi) = \frac{1}{2} [\sin(\phi(n+1)) + \sin(\phi(n-1))] \quad (\text{A.108})$$

we have that

$$\begin{aligned} \frac{dL^*}{dt} &= \frac{\mu L^{*2}}{q\gamma B_E R_E^2} \sum_{n=1} n \delta B_n(t) \sin(n\phi) \\ &\quad - \frac{2}{3} \frac{\mu L^{*5}}{q\gamma B_E R_E^2} \frac{\Delta B}{B_E} \sum_{n=1} n \delta B_n(t) \sin(\phi(n+1)) \\ &\quad - \frac{2}{3} \frac{\mu L^{*5}}{q\gamma B_E R_E^2} \frac{\Delta B}{B_E} \sum_{n=1} n \delta B_n(t) \sin(\phi(n-1)) \end{aligned} \quad (\text{A.109})$$

(**NB:** In Fei et al. [2006] the asymmetric terms were given as positive with no justification).

Let each of the terms in the previous equation equal  $u_1, u_2, u_3$  respectively, so that

$$\frac{dL^*}{dt} = u_1 - u_2 - u_3 \quad (\text{A.110})$$

It is easy to see with standard differentiation and the product rule that

$$\begin{aligned} \frac{d}{dt} [(L - L_0)^2] &= 2 \int [u_1(t)u_1(\xi)] d\xi + 2 \int [u_2(t)u_2(\xi)] d\xi + 2 \int [u_3(t)u_3(\xi)] d\xi \\ &\quad - 2 \int [u_1(t)u_2(\xi)] d\xi - 2 \int [u_2(t)u_1(\xi)] d\xi - 2 \int [u_1(t)u_3(\xi)] d\xi \\ &\quad - 2 \int [u_3(t)u_1(\xi)] d\xi + 2 \int [u_2(t)u_3(\xi)] d\xi + 2 \int [u_3(t)u_2(\xi)] d\xi \end{aligned} \quad (\text{A.111})$$

The diffusion coefficient is given by the following

$$D_{LL} = \frac{[(L - L_0)^2]}{2t} = \frac{1}{2t} \int_0^t \frac{d[(L - L_0)^2]}{dt} d\tau \quad (\text{A.112})$$

Now that the equations are in a form similar to Fälthammar [1965] we can simply derive the relevant diffusion coefficients using the same methodology as before. The symmetric and asymmetric components of the magnetic diffusion coefficient are given by

$$D_{LL}^{B,Sym} = \frac{1}{2t} \int_0^t 2 \int [u_1(t)u_1(t-\tau)]d\tau \quad (\text{A.113})$$

$$= \frac{1}{2t} \frac{\mu^2 L^{*4}}{q^2 \gamma^2 B_E^2 R_E^4} t \sum_n \int_0^\infty n^2 [\delta \tilde{B}_n(t) \delta \tilde{B}_n(t+\xi)] \cos(n\omega) \quad (\text{A.114})$$

$$= \frac{\mu^2 L^{*4}}{8q^2 \gamma^2 B_E^2 R_E^4} \sum_n n^2 P_n^B(n\omega) \quad (\text{A.115})$$

$$D_{LL}^{B,Asym} = \frac{1}{2t} \int_0^t 2 \int [u_2(t)u_2(t-\tau)]d\tau + \frac{1}{2t} \int_0^t 2 \int [u_3(t)u_3(t-\tau)]d\tau \quad (\text{A.116})$$

$$= \frac{1}{2t} \frac{4\mu^2 L^{*10}}{9q^2 \gamma^2 B_E^2 R_E^4} \left(\frac{\Delta B}{B_E}\right)^2 t \sum_n \int_0^\infty n^2 [\delta \tilde{B}_n(t) \delta \tilde{B}_n(t+\xi)] \cos((n+1)\omega) \quad (\text{A.117})$$

$$+ \frac{1}{2t} \frac{4\mu^2 L^{*10}}{9q^2 \gamma^2 B_E^2 R_E^4} \left(\frac{\Delta B}{B_E}\right)^2 t \sum_n \int_0^\infty n^2 [\delta \tilde{B}_n(t) \delta \tilde{B}_n(t+\xi)] \cos((n-1)\omega)$$

$$= \frac{2\mu^2 L^{*10}}{9q^2 \gamma^2 B_E^2 R_E^4} \left(\frac{\Delta B}{B_E}\right)^2 \sum_n n^2 \{P_n^B((n+1)\omega) + P_n^B((n-1)\omega)\} \quad (\text{A.118})$$

where  $P_n^B(n\omega)$  is the power spectrum of the nth harmonic of the magnetic field fluctuation  $\delta B$ .

### A.2.2 Electric disturbances and electric diffusion

The electric field disturbance is assumed to be in the azimuthal direction. They are also described by a Fourier sum around  $r_0$

$$\delta E_\phi(r, \phi, t) = \sum_{n=1} \delta E_{\phi n}(t) \cos(n\phi) \quad (\text{A.119})$$

The radial component of the drift velocity driven by electric field fluctuations is

$$\frac{dr}{dt} = \frac{\delta E_\phi}{B_d} \quad (\text{A.120})$$

The rate of change of  $L^*$  is therefore

$$\frac{dL^*}{dt} = \frac{1}{R_E} \left( 1 - \frac{4}{3} \frac{\Delta B}{B_d} \cos \phi \right) \left( \frac{\sum_{n=1} \delta E_{\phi n}(t) \cos(n\phi)}{B_d} \right) \quad (\text{A.121})$$

$$= \frac{1}{R_E B_d} \sum_{n=1} \delta E_{\phi n}(t) \cos(n\phi) - \frac{4}{3} \frac{\Delta B}{R_E B_d^2} \sum_{n=1} \delta E_{\phi n}(t) \cos(n\phi) \cos(\phi) \quad (\text{A.122})$$

$$= \frac{1}{R_E B_d} \sum_{n=1} \delta E_{\phi n}(t) \cos(n\phi) - \frac{2}{3} \frac{\Delta B}{R_E B_d^2} \sum_{n=1} \delta E_{\phi n}(t) \cos(\phi(n+1)) - \frac{2}{3} \frac{\Delta B}{R_E B_d^2} \sum_{n=1} \delta E_{\phi n}(t) \cos(\phi(n-1)) \quad (\text{A.123})$$

using the compound angle formulae

$$\cos(\phi + n\phi) = \cos(\phi) \cos(n\phi) - \sin(\phi) \sin(n\phi) \quad (\text{A.124})$$

$$\cos(\phi - n\phi) = \cos(\phi) \cos(n\phi) + \sin(\phi) \sin(n\phi) \quad (\text{A.125})$$

$$\implies \cos(\phi) \sin(n\phi) = \frac{1}{2} [\cos(\phi(n+1)) + \cos(\phi(n-1))] \quad (\text{A.126})$$

Repeating the previous methodology as for the magnetic diffusion coefficient,

$$\frac{dL^*}{dt} = v_1 - v_2 - v_3 \quad (\text{A.127})$$

and the symmetric and asymmetric electric diffusion coefficients follow (with null cross terms)

$$D_{LL}^{E,Sym} = \frac{1}{2t} \int_0^t 2 \int [v_1(t)v_1(t-\tau)] d\tau \quad (\text{A.128})$$

$$= \frac{1}{2t} \frac{L^{*6}}{R_E^2 B_E^2} t \sum_n \int_0^\infty [\delta \tilde{E}_{\phi n}(t) \delta \tilde{E}_{\phi n}(t+\xi)] \cos(n\omega) \quad (\text{A.129})$$

$$= \frac{1}{8B_E^2 R_E^2} L^{*6} \sum_n P_n^E(n\omega) \quad (\text{A.130})$$

$$D_{LL}^{E,Asym} = \frac{1}{2t} \int_0^t 2 \int [v_2(t)v_2(t-\tau)] d\tau + \frac{1}{2t} \int_0^t 2 \int [v_3(t)v_3(t-\tau)] d\tau \quad (\text{A.131})$$

$$= \frac{1}{2t} \frac{4}{9} \left( \frac{\Delta B}{B_E} \right)^2 \frac{L^{*12}}{R_E^2 B_E^2} \quad (\text{A.132})$$

---

## BIBLIOGRAPHY

- Abbo, L., Ofman, L., Antiochos, S. K., Hansteen, V. H., Harra, L., Ko, Y. K., Lapenta, G., Li, B., Riley, P., Strachan, L., von Steiger, R., Wang, Y. M., Abbo, L., Ofman, L., Antiochos, S. K., Hansteen, V. H., Harra, L., Ko, Y. K., Lapenta, G., Li, B., Riley, P., Strachan, L., von Steiger, R., and Wang, Y. M. (2016). Slow Solar Wind: Observations and Modeling. *SSRv*, 201(1-4):55–108.
- Albert, J. M., Selesnick, R. S., Morley, S. K., Henderson, M. G., and Kellerman, A. C. (2018). Calculation of Last Closed Drift Shells for the 2013 GEM Radiation Belt Challenge Events. *Journal of Geophysical Research: Space Physics*, 123(11):9597–9611.
- ALFVÉN, H. (1942). Existence of Electromagnetic-Hydrodynamic Waves. *Nature* 1942 150:3805, 150(3805):405–406.
- Ali, A. F. (2016). ULF Waves and Diffusive Radial Transport of Charged Particles. *PhDT (Faculty of the Graduate School of the University of Colorado)*, pages –undefined.
- Ali, A. F., Elkington, S. R., Tu, W., Ozeke, L. G., Chan, A. A., and Friedel, R. H. (2015). Magnetic field power spectra and magnetic radial diffusion coefficients using CRRES magnetometer data. *Journal of Geophysical Research: Space Physics*, 120(2):973–995.
- Ali, A. F., Malaspina, D. M., Elkington, S. R., Jaynes, A. N., Chan, A. A., Wygant, J., and Kletzing, C. A. (2016). Electric and magnetic radial diffusion coefficients using the Van Allen probes data. *Journal of Geophysical Research: Space Physics*, 121(10):9586–9607.

## BIBLIOGRAPHY

---

- Allan, W. and Knox, F. B. (1979a). A dipole field model for axisymmetric alfvén waves with finite ionosphere conductivities. *Planetary and Space Science*, 27(1):79–85.
- Allan, W. and Knox, F. B. (1979b). The effect of finite ionosphere conductivities on axisymmetric toroidal Alfvén wave resonances. *Planetary and Space Science*, 27(7):939–950.
- Allan, W., Poulter, E. M., and White, S. P. (1986a). Hydromagnetic wave coupling in the magnetosphere-Plasmapause effects on impulse-excited resonances. *Planetary and Space Science*, 34(12):1189–1200.
- Allan, W., White, S. P., and Poulter, E. M. (1986b). Impulse-excited hydromagnetic cavity and field-line resonances in the magnetosphere. *Planetary and Space Science*, 34(4):371–385.
- Anagnostopoulos, G., Rigas, V., and Vassiliadis, E. (2010). Radiation belt electron precipitation in the upper ionosphere at middle latitudes before strong earthquakes.
- Archer, M. O., Hartinger, M. D., and Horbury, T. S. (2013). Magnetospheric "magic" frequencies as magnetopause surface eigenmodes. *Geophysical Research Letters*, 40(19):5003–5008.
- Baker, D. N., Kanekal, S. G., Hoxie, V. C., Henderson, M. G., Li, X., Spence, H. E., Elkington, S. R., Friedel, R. H. W., Goldstein, J., Hudson, M. K., Reeves, G. D., Thorne, R. M., Kletzing, C. A., and Claudepierre, S. G. (2013). A Long-Lived Relativistic Electron Storage Ring Embedded in Earth's Outer Van Allen Belt. *Science*, 340(6129):186–190.
- Baker, D. N. and Lanzerotti, L. J. (2016). Resource Letter SW1: Space Weather. *American Journal of Physics*, 84(3):166.
- Baker, D. N., Li, X., Blake, J. B., and Kanekal, S. (1998). Strong electron acceleration in the Earth's magnetosphere. *Advances in Space Research*, 21(4):609–613.
- Baker, G. J., Donovan, E. F., and Jackel, B. J. (2003). A comprehensive survey of auroral latitude Pc5 pulsation characteristics. *Journal of Geophysical Research: Space Physics*, 108(A10):1384.

## BIBLIOGRAPHY

---

- Bartels, J., Heck, N. H., and Johnston, H. F. (1939). The three-hour-range index measuring geomagnetic activity. *Terrestrial Magnetism and Atmospheric Electricity*, 44(4):411–454.
- Baumjohann, W. W. and Treumann, R. A. (2012). Basic space plasma physics. page 479.
- Bentley, S. N., Stout, J. R., Bloch, T. E., and Watt, C. E. J. (2020). Random Forest Model of Ultralow-Frequency Magnetospheric Wave Power. *Earth and Space Science*, 7(10):e2020EA001274.
- Bentley, S. N., Watt, C. E. J., Owens, M. J., and Rae, I. J. (2018). ULF Wave Activity in the Magnetosphere: Resolving Solar Wind Interdependencies to Identify Driving Mechanisms. *Journal of Geophysical Research: Space Physics*, 123(4):2745–2771.
- Bentley, S. N., Watt, C. E. J., Rae, I. J., Owens, M. J., Murphy, K., Lockwood, M., and Sandhu, J. K. (2019). Capturing Uncertainty in Magnetospheric Ultralow Frequency Wave Models. *Space Weather*, 17(4):599–618.
- Bernacchia, A. and Pigolotti, S. (2011). Self-consistent method for density estimation. *Journal of the Royal Statistical Society: Series B (Statistical Methodology)*, 73(3):407–422.
- Berner, J., Achatz, U., Batté, L., Bengtsson, L., Cámara, A. d. l., Christensen, H. M., Colangeli, M., Coleman, D. R. B., Crommelin, D., Dolaptchiev, S. I., Franzke, C. L. E., Friederichs, P., Imkeller, P., Järvinen, H., Juricke, S., Kitsios, V., Lott, F., Lucarini, V., Mahajan, S., Palmer, T. N., Penland, C., Sakradzija, M., von Storch, J.-S., Weisheimer, A., Weniger, M., Williams, P. D., and Yano, J.-I. (2017). Stochastic Parameterization: Toward a New View of Weather and Climate Models. *Bulletin of the American Meteorological Society*, 98(3):565–588.
- Bloch, T., Watt, C. E. J., Owens, M. J., Thompson, R. L., and Agiwal, O. (2021). Constraining the Location of the Outer Boundary of Earth’s Outer Radiation Belt. *Earth and Space Science*, 8(6):e2020EA001610.
- Boyd, A. J., Turner, D. L., Reeves, G. D., Spence, H. E., Baker, D. N., and Blake, J. B. (2018). What Causes Radiation Belt Enhancements: A Survey of the Van Allen Probes Era. *Geophysical Research Letters*, 45(11):5253–5259.

## BIBLIOGRAPHY

---

- Brautigam, D. H. and Albert, J. M. (2000). Radial diffusion analysis of outer radiation belt electrons during the October 9, 1990, magnetic storm. *Journal of Geophysical Research: Space Physics*, 105(A1):291–309.
- Brautigam, D. H., Ginet, G. P., Albert, J. M., Wygant, J. R., Rowland, D. E., Ling, A., and Bass, J. (2005). CRRES electric field power spectra and radial diffusion coefficients. *Journal of Geophysical Research: Space Physics*, 110(A2).
- Brito, T. V. and Morley, S. K. (2017). Improving Empirical Magnetic Field Models by Fitting to In Situ Data Using an Optimized Parameter Approach. *Space Weather*, 15(12):1628–1648.
- Brizard, A. J. and Chan, A. A. (2001a). Relativistic bounce-averaged quasilinear diffusion equation for low-frequency electromagnetic fluctuations. *Physics of Plasmas*, 8(11):4762–4771.
- Brizard, A. J. and Chan, A. A. (2001b). Relativistic bounce-averaged quasilinear diffusion equation for low-frequency electromagnetic fluctuations. *Physics of Plasmas*, 8(11):4762–4771.
- Camporeale, E., Wilkie, G. J., Drozdov, A., and Bortnik, J. (2021). Machine-learning based discovery of missing physical processes in radiation belt modeling.
- Carter, J. A., Milan, S. E., Paxton, L. J., Anderson, B. J., and Gjerloev, J. (2020). Height-Integrated Ionospheric Conductances Parameterized By Interplanetary Magnetic Field and Substorm Phase. *Journal of Geophysical Research: Space Physics*, 125(10).
- Chapman, S. (1962). *Geomagnetism. v.2.*
- Chen, L. and Cowley, S. C. (1989). On field line resonances of hydromagnetic Alfvén waves in dipole magnetic field. *Geophysical Research Letters*, 16(8):895–897.
- Chen, L. and Hasegawa, A. (1974). A theory of long-period magnetic pulsations: 1. Steady state excitation of field line resonance. *Journal of Geophysical Research*, 79(7):1024–1032.
- Chen, Y., Friedel, R. H., Henderson, M. G., Claudepierre, S. G., Morley, S. K., and Spence, H. E. (2014). REPAD: An empirical model of pitch angle distributions for

## BIBLIOGRAPHY

---

- energetic electrons in the Earth's outer radiation belt. *Journal of Geophysical Research: Space Physics*, 119(3):1693–1708.
- Cheng, C. Z. (2003). MHD field line resonances and global modes in three-dimensional magnetic fields. *Journal of Geophysical Research: Space Physics*, 108(A1):1002.
- Cheng, C. Z. and Zaharia, S. (2003). Field line resonances in quiet and disturbed time three-dimensional magnetospheres. *Journal of Geophysical Research: Space Physics*, 108(A1):1001.
- Chisham, G., Orr, D., and Yeoman, T. K. (1992). Observations of a giant pulsation across an extended array of ground magnetometers and on auroral radar. *Planetary and Space Science*, 40(7):953–964.
- Claudepierre, S. G., Elkington, S. R., and Wiltberger, M. (2008). Solar wind driving of magnetospheric ULF waves: Pulsations driven by velocity shear at the magnetopause. *Journal of Geophysical Research: Space Physics*, 113(A5):5218.
- Claudepierre, S. G., Mann, I. R., Takahashi, K., Fennell, J. F., Hudson, M. K., Blake, J. B., Roeder, J. L., Clemmons, J. H., Spence, H. E., Reeves, G. D., Baker, D. N., Funsten, H. O., W. Friedel, R. H., Henderson, M. G., Kletzing, C. A., Kurth, W. S., Macdowall, R. J., Smith, C. W., and Wygant, J. R. (2013). Van Allen Probes observation of localized drift resonance between poloidal mode ultra-low frequency waves and 60 keV electrons. *Geophysical Research Letters*, 40(17):4491–4497.
- Claudepierre, S. G., Toffoletto, F. R., and Wiltberger, M. (2016). Global MHD modeling of resonant ULF waves: Simulations with and without a plasmasphere. *Journal of Geophysical Research A: Space Physics*, 121(1):227–244.
- Claudepierre, S. G., Wiltberger, M., Elkington, S. R., Lotko, W., and Hudson, M. K. (2009). Magnetospheric cavity modes driven by solar wind dynamic pressure fluctuations. *Geophysical Research Letters*, 36(13).
- Cornwall, J. M. (1968). Diffusion Processes Influenced by Conjugate-Point Wave Phenomena. *Radio Science*, 3(7):740–744.

## BIBLIOGRAPHY

---

- Davies, J. A. and Lester, M. (1999). The relationship between electric fields, conductances and currents in the high-latitude ionosphere: a statistical study using EISCAT data. The relationship between electric fields, conductances and currents in the high-latitude ionosphere: a statistical study using EISCAT data. Technical Report 1.
- Degeling, A. W., Rae, I. J., Watt, C. E., Shi, Q. Q., Rankin, R., and Zong, Q. G. (2018). Control of ULF Wave Accessibility to the Inner Magnetosphere by the Convection of Plasma Density. *Journal of Geophysical Research: Space Physics*, 123(2):1086–1099.
- Degeling, A. W., Rankin, R., Kabin, K., Marchand, R., and Mann, I. R. (2007). The effect of ULF compressional modes and field line resonances on relativistic electron dynamics. *Planetary and Space Science*, 55(6):731–742.
- Degeling, A. W., Rankin, R., Kabin, K., Rae, I. J., and Fenrich, F. R. (2010). Modeling ULF waves in a compressed dipole magnetic field. *Journal of Geophysical Research: Space Physics*, 115(10):10212.
- Drozдов, A., Allison, H., Shprits, Y., Aseev, N., Drozдов, A., Allison, H., Shprits, Y., and Aseev, N. (2020). A Comparison of Radial Diffusion Coefficients in 1-D and 3-D Long-Term Radiation Belt Simulations. *EGUGA*, page 17757.
- Drozдов, A. Y., Allison, H. J., Shprits, Y. Y., Elkington, S., and Aseev, N. (2021). A Comparison of Radial Diffusion Coefficients in 1-D and 3-D Long-Term Radiation Belt Simulations. *Journal of Geophysical Research: Space Physics*, page e2020JA028707.
- Drozдов, A. Y., Shprits, Y. Y., Aseev, N. A., Kellerman, A. C., and Reeves, G. D. (2017). Dependence of radiation belt simulations to assumed radial diffusion rates tested for two empirical models of radial transport. *Space Weather*, 15(1):150–162.
- Dungey, J. W. (1961). Interplanetary Magnetic Field and the Auroral Zones. *Physical Review Letters*, 6(2):47.
- Eastwood, J. P., Hietala, H., Toth, G., Phan, T. D., and Fujimoto, M. (2014). What Controls the Structure and Dynamics of Earth’s Magnetosphere? *Space Science Reviews* 2014 188:1, 188(1):251–286.

## BIBLIOGRAPHY

---

- Elkington, S. R., Hudson, M. K., and Chan, A. A. (1999). Acceleration of relativistic electrons via drift-resonant interaction with toroidal-mode Pc-5 ULF oscillations. *Geophysical Research Letters*, 26(21):3273–3276.
- Elkington, S. R., Hudson, M. K., and Chan, A. A. (2003). Resonant acceleration and diffusion of outer zone electrons in an asymmetric geomagnetic field. *Journal of Geophysical Research: Space Physics*, 108(A3).
- Elkington, S. R., Hudson, M. K., Chan, A. A., Elkington, S. R., Hudson, M. K., and Chan, A. A. (2001). Enhanced Radial Diffusion of Outer Zone Electrons in an Asymmetric Geomagnetic Field. *AGUSM*, 2001:SM32C–04.
- Elsden, T. and Wright, A. N. (2017). The theoretical foundation of 3-D Alfvén resonances: Time-dependent solutions. *Journal of Geophysical Research: Space Physics*, 122(3):3247–3261.
- Elsden, T. and Wright, A. N. (2018). The Broadband Excitation of 3-D Alfvén Resonances in a MHD Waveguide. *Journal of Geophysical Research: Space Physics*, 123(1):530–547.
- Elsden, T. and Wright, A. N. (2019). The Effect of Fast Normal Mode Structure and Magnetopause Forcing on FLRs in a 3-D Waveguide. *Journal of Geophysical Research: Space Physics*, 124(1):178–196.
- Fälthammar, C.-G. (1965). Effects of time-dependent electric fields on geomagnetically trapped radiation. *Journal of Geophysical Research*, 70(11):2503–2516.
- Fälthammar, C.-G. (1968). Radial Diffusion by Violation of the Third Adiabatic Invariant. In McCormac, B. M., editor, *Earth’s Particles and Fields*, page 157.
- Fei, Y., Chan, A. A., Elkington, S. R., and Wiltberger, M. J. (2006). Radial diffusion and MHD particle simulations of relativistic electron transport by ULF waves in the September 1998 storm. *Journal of Geophysical Research: Space Physics*, 111(A12).
- Fennell, J. F., Claudepierre, S. G., Blake, J. B., O’Brien, T. P., Clemmons, J. H., Baker, D. N., Spence, H. E., and Reeves, G. D. (2015). Van Allen Probes show that the inner radiation zone contains no MeV electrons: ECT/MagEIS data. *Geophysical Research Letters*, 42(5):1283–1289.

## BIBLIOGRAPHY

---

- Fick, A. (1855). Ueber Diffusion. *Annalen der Physik*, 170(1):59–86.
- Fok, M.-C., Horne, R. B., Meredith, N. P., and Glauert, S. A. (2008). Radiation Belt Environment model: Application to space weather nowcasting. *J. Geophys. Res.*, 113:3–08.
- Geiss, J., Gloeckler, G., and Von Steiger, R. (1995). Origin of the solar wind from composition data. *Space Science Reviews 1995 72:1*, 72(1):49–60.
- Gjerloev, J. W. (2012). The SuperMAG data processing technique. *Journal of Geophysical Research: Space Physics*, 117(A9):n/a–n/a.
- Glassmeier, K. H. and Stellmacher, M. (2000). Concerning the local time asymmetry of Pc5 wave power at the ground and field line resonance widths. *Journal of Geophysical Research: Space Physics*, 105(A8):18847–18855.
- Glauert, S. A., Horne, R. B., and Meredith, N. P. (2014a). Simulating the Earth’s radiation belts: Internal acceleration and continuous losses to the magnetopause. *Journal of Geophysical Research: Space Physics*, 119(9):7444–7463.
- Glauert, S. A., Horne, R. B., and Meredith, N. P. (2014b). Simulating the Earth’s radiation belts: Internal acceleration and continuous losses to the magnetopause. *Journal of Geophysical Research: Space Physics*, 119(9):7444–7463.
- Glauert, S. A., Horne, R. B., and Meredith, N. P. (2018). A 30-Year Simulation of the Outer Electron Radiation Belt. *Space Weather*, 0(0).
- Heisenberg, W. (1985). Über den anschaulichen Inhalt der quantentheoretischen Kinematik und Mechanik. In *Original Scientific Papers Wissenschaftliche Originalarbeiten*, pages 478–504. Springer Berlin Heidelberg.
- Holzworth, R. H. and Mozer, F. S. (1979). Direct evaluation of the radial diffusion coefficient near L=6 due to electric field fluctuations. *Journal of Geophysical Research*, 84(A6):2559.
- Horne, R. B., Glauert, S. A., Meredith, N. P., Boscher, D., Maget, V., Heynderickx, D., and Pitchford, D. (2013). Space weather impacts on satellites and forecasting the Earth’s electron radiation belts with SPACECAST. *Space Weather*, 11(4):169–186.

## BIBLIOGRAPHY

---

- Horne, R. B., Meredith, N. P., Thorne, R. M., Heynderickx, D., Iles, R. H., and Anderson, R. R. (2003). Evolution of energetic electron pitch angle distributions during storm time electron acceleration to megaelectronvolt energies. *Journal of Geophysical Research: Space Physics*, 108(A1).
- Horne, R. B. and Thorne, R. M. (1998). Potential waves for relativistic electron scattering and stochastic acceleration during magnetic storms. *Geophysical Research Letters*, 25(15):3011–3014.
- Horne, R. B., Thorne, R. M., Shprits, Y. Y., Meredith, N. P., Glauert, S. A., Smith, A. J., Kanekal, S. G., Baker, D. N., Engebretson, M. J., Posch, J. L., Spasojevic, M., Inan, U. S., Pickett, J. S., and Decreau, P. M. E. (2005). Wave acceleration of electrons in the Van Allen radiation belts. *Nature*, 437:227.
- Horwitz, J. L., Horwitz, and L., J. (1982). The Ionosphere as a Source for Magnetospheric Ions (Paper 2R1093). *RvGSP*, 20(4):929.
- Huang, C.-L., Spence, H. E., Hudson, M. K., and Elkington, S. R. (2010a). Modeling radiation belt radial diffusion in ULF wave fields: 2. Estimating rates of radial diffusion using combined MHD and particle codes. *Journal of Geophysical Research: Space Physics*, 115(A6).
- Huang, C. L., Spence, H. E., Hudson, M. K., and Elkington, S. R. (2010b). Modeling radiation belt radial diffusion in ULF wave fields: 2. Estimating rates of radial diffusion using combined MHD and particle codes. *Journal of Geophysical Research: Space Physics*, 115(6).
- Huang, C.-L. L., Spence, H. E., Singer, H. J., Tsyganenko, N. A., Huang, C.-L., Spence, H. E., Huang, C.-L., Singer, H. J., and Tsyganenko, N. A. (2008). A quantitative assessment of empirical magnetic field models at geosynchronous orbit during magnetic storms Recommended Citation A quantitative assessment of empirical magnetic field models at geosynchronous orbit during magnetic storms. *J. Geophys. Res*, 113:4208.
- Hudson, M. K., Denton, R. E., Lessard, M. R., Miftakhova, E. G., and Anderson, R. R. (2004). A study of Pc-5 ULF oscillations. Technical report.

## BIBLIOGRAPHY

---

- Hughes, W. J. (1974). The effect of the atmosphere and ionosphere on long period magnetospheric micropulsations. *Planetary and Space Science*, 22(8):1157–1172.
- Hughes, W. J. (1983). *Hydromagnetic Waves in the Magnetosphere*. pages 453–477. Springer, Dordrecht.
- Hughes, W. J. and Southwood, D. J. (1976). SCREENING OF MICROPULSATION SIGNALS BY THE ATMOSPHERE AND IONOSPHERE. *J Geophys Res*, 81(19):3234–3240.
- Hynönen, R., Tanskanen, E. I., and Francia, P. (2020). Solar cycle evolution of ULF wave power in solar wind and on ground. *Journal of Space Weather and Space Climate*, 10:43.
- Ieda, A., Oyama, S., Vanhamäki, H., Fujii, R., Nakamizo, A., Amm, O., Hori, T., Takeda, M., Ueno, G., Yoshikawa, A., Redmon, R. J., Denig, W. F., Kamide, Y., and Nishitani, N. (2014). Approximate forms of daytime ionospheric conductance. *Journal of Geophysical Research: Space Physics*, 119(12):397–10.
- Israelsson, J., Black, E., Neves, C., Torgbor, F. F., Greatrex, H., Tanu, M., and Lamptey, P. N. L. (2020). The spatial correlation structure of rainfall at the local scale over southern Ghana. *Journal of Hydrology: Regional Studies*, 31:100720.
- Jacobs, J. A., Kato, Y., Matsushita, S., and Troitskaya, V. A. (1964). Classification of geomagnetic micropulsations. *Journal of Geophysical Research*, 69(1):180–181.
- Jaynes, A. N., Ali, A. F., Elkington, S. R., Malaspina, D. M., Baker, D. N., Li, X., Kanekal, S. G., Henderson, M. G., Kletzing, C. A., and Wygant, J. R. (2018a). Fast Diffusion of Ultrarelativistic Electrons in the Outer Radiation Belt: 17 March 2015 Storm Event. *Geophysical Research Letters*, 45(20):874–10.
- Jaynes, A. N., Malaspina, D., Chan, A. A., Elkington, S. R., Ali, A., Bruff, M., Zhao, H., Baker, D. N., Li, X., Kanekal, S. G., Jaynes, A. N., Malaspina, D., Chan, A. A., Elkington, S. R., Ali, A., Bruff, M., Zhao, H., Baker, D. N., Li, X., and Kanekal, S. G. (2018b). Battle Royale: VLF-driven local acceleration vs. ULF-driven radial transport. *AGUFM*, 2018:SM11B–01.

## BIBLIOGRAPHY

---

- Jursa, A. S. (1985). HANDBOOK OF GEOPHYSICS AND THE SPACE ENVIRONMENT SCIENTIFIC EDITOR.
- Keiling, A., Lee, D. H., and Nakariakov, V. (2016). *Low-Frequency Waves in Space Plasmas*, volume 182. Wiley Blackwell.
- Kepko, L. and Spence, H. E. (2003). Observations of discrete, global magnetospheric oscillations directly driven by solar wind density variations. *Journal of Geophysical Research: Space Physics*, 108(A6):1257.
- Kepko, L., Spence, H. E., and Singer, H. J. (2002). ULF waves in the solar wind as direct drivers of magnetospheric pulsations. *Geophysical Research Letters*, 29(8):39–1.
- Kersten, T., Horne, R. B., Glauert, S. A., Meredith, N. P., Fraser, B. J., and Grew, R. S. (2014). Electron losses from the radiation belts caused by EMIC waves. *Journal of Geophysical Research: Space Physics*, 119(11):8820–8837.
- Kim, K.-C., Lee, D.-Y., Shprits, Y., Kim, H.-J., and Lee, E. (2011). Electron flux changes in the outer radiation belt by radial diffusion during the storm recovery phase in comparison with the fully adiabatic evolution. *Journal of Geophysical Research: Space Physics*, 116(A9):9229.
- Kivelson, M. G. and Southwood, D. J. (1985). Resonant ULF waves: A new interpretation. *Geophysical Research Letters*, 12(1):49–52.
- Kivelson, M. G. and Southwood, D. J. (1986). Coupling of global magnetospheric MHD eigenmodes to field line resonances. *Journal of Geophysical Research*, 91(A4):4345.
- Kivelson, M. G. M. G. and Russell, C. T. C. T. (1995). Introduction to space physics. page 568.
- Kletzing, C. A., Kurth, W. S., Acuna, M., MacDowall, R. J., Torbert, R. B., Averkamp, T., Bodet, D., Bounds, S. R., Chutter, M., Connerney, J., Crawford, D., Dolan, J. S., Dvorsky, R., Hospodarsky, G. B., Howard, J., Jordanova, V., Johnson, R. A., Kirchner, D. L., Mokrzycki, B., Needell, G., Odom, J., Mark, D., Pfaff, R., Phillips, J. R., Piker, C. W., Remington, S. L., Rowland, D., Santolik, O., Schnurr, R., Sheppard, D., Smith,

## BIBLIOGRAPHY

---

- C. W., Thorne, R. M., and Tyler, J. (2013). The electric and magnetic field instrument suite and integrated science (EMFISIS) on RBSP.
- Kozlov, D. A. and Leonovich, A. S. (2008). The structure of field line resonances in a dipole magnetosphere with moving plasma. *Annales Geophysicae*, 26(3):689–698.
- Lanzerotti, L. J. and Morgan, C. G. (1973). ULF geomagnetic power near  $L = 4$ : 2. Temporal variation of the radial diffusion coefficient for relativistic electrons. *Journal of Geophysical Research*, 78(22):4600–4610.
- Lanzerotti, L. J., Webb, D. C., and Arthur, C. W. (1978). Geomagnetic field fluctuations at synchronous orbit 2. Radial diffusion. *Journal of Geophysical Research: Space Physics*, 83(A8):3866–3870.
- Le, G., Chi, P. J., Strangeway, R. J., Russell, C. T., Slavin, J. A., Takahashi, K., Singer, H. J., Anderson, B. J., Bromund, K., Fischer, D., Kepko, E. L., Magnes, W., Nakamura, R., Plaschke, F., and Torbert, R. B. (2017). Global observations of magnetospheric high-m poloidal waves during the 22 June 2015 magnetic storm. *Geophysical Research Letters*, 44(8):3456–3464.
- Lejosne, S. (2019). Analytic Expressions for Radial Diffusion. *Journal of Geophysical Research: Space Physics*, 124(6):4278–4294.
- Lejosne, S. and Kollmann, P. (2020). Radiation Belt Radial Diffusion at Earth and Beyond. *Space Science Reviews 2020 216:1*, 216(1):1–78.
- Leonovich, A. S. (2001). A theory of field line resonance in a dipole-like axisymmetric magnetosphere. *Journal of Geophysical Research: Space Physics*, 106(A11):25803–25812.
- Li, W. and Hudson, M. (2019). Earth’s Van Allen Radiation Belts: From Discovery to the Van Allen Probes Era. *Journal of Geophysical Research: Space Physics*, 124(11):8319–8351.
- Li, X., Baker, D. N., Temerin, M., Cayton, T. E., Reeves, E. G. D., Christensen, R. A., Blake, J. B., Looper, M. D., Nakamura, R., and Kanekal, S. G. (1997). Multisatellite observations of the outer zone electron variation during the November 3–4, 1993, magnetic storm. *Journal of Geophysical Research: Space Physics*, 102(A7):14123–14140.

## BIBLIOGRAPHY

---

- Li, Z., Hudson, M., Patel, M., Wiltberger, M., Boyd, A., and Turner, D. (2017). ULF wave analysis and radial diffusion calculation using a global MHD model for the 17 March 2013 and 2015 storms. *Journal of Geophysical Research: Space Physics*, 122(7):7353–7363.
- Liu, W., Tu, W., Li, X., Sarris, T., Khotyaintsev, Y., Fu, H., Zhang, H., and Shi, Q. (2016). On the calculation of electric diffusion coefficient of radiation belt electrons with in situ electric field measurements by THEMIS. *Geophysical Research Letters*, 43(3):1023–1030.
- Lui, A. T. and Cheng, C. Z. (2001). Resonance frequency of stretched magnetic field lines based on a self-consistent equilibrium magnetosphere model. *Journal of Geophysical Research: Space Physics*, 106(A11):25793–25802.
- Lyons, L. R. and Thorne, R. M. (1973). Equilibrium structure of radiation belt electrons. *Journal of Geophysical Research*, 78(13):2142–2149.
- Lysak, R. L., Song, Y., Waters, C. L., Sciffer, M. D., and Obana, Y. (2020). Numerical Investigations of Interhemispheric Asymmetry due to Ionospheric Conductance. *Journal of Geophysical Research: Space Physics*, 125(7).
- Maget, V., Sicard-Piet, A., Bourdarie, S., Lazaro, D., Turner, D. L., Daglis, I. A., and Sandberg, I. (2015). Improved outer boundary conditions for outer radiation belt data assimilation using THEMIS-SST data and the Salammbó-EnKF code. *Journal of Geophysical Research: Space Physics*, 120(7):5608–5622.
- Mann, I. R., Lee, E. A., Claudepierre, S. G., Fennell, J. F., Degeling, A., Rae, I. J., Baker, D. N., Reeves, G. D., Spence, H. E., Ozeke, L. G., Rankin, R., Milling, D. K., Kale, A., Friedel, R. H. W., and Honary, F. (2013). Discovery of the action of a geophysical synchrotron in the Earth’s Van Allen radiation belts. *Nature Communications*, 4:2795.
- Mann, I. R., Milling, D. K., Rae, I. J., Ozeke, L. G., Kale, A., Kale, Z. C., Murphy, K. R., Parent, A., Usanova, M., Pahud, D. M., Lee, E. A., Amalraj, V., Wallis, D. D., Angelopoulos, V., Glassmeier, K. H., Russell, C. T., Auster, H. U., and Singer, H. J. (2008). The upgraded CARISMA magnetometer array in the THEMIS era. *Space Science Reviews*, 141(1-4):413–451.

## BIBLIOGRAPHY

---

- Mann, I. R., Ozeke, L. G., Murphy, K. R., Claudepierre, S. G., Turner, D. L., Baker, D. N., Rae, I. J., Kale, A., Milling, D. K., Boyd, A. J., Spence, H. E., Reeves, G. D., Singer, H. J., Dimitrakoudis, S., Daglis, I. A., and Honary, F. (2016). Explaining the dynamics of the ultra-relativistic third Van Allen radiation belt. *Nature Physics*, 12:978.
- Mathie, R. A. and Mann, I. R. (2001). On the solar wind control of Pc5 ULF pulsation power at mid-latitudes: Implications for MeV electron acceleration in the outer radiation belt. *Journal of Geophysical Research: Space Physics*, 106(A12):29783–29796.
- Mauk, B. H., Fox, N. J., Kanekal, S. G., Kessel, R. L., Sibeck, D. G., and Ukhorskiy, A. (2013). Science objectives and rationale for the radiation belt storm probes mission.
- McIlwain, C. E. (1961). Coordinates for mapping the distribution of magnetically trapped particles. *Journal of Geophysical Research*, 66(11):3681–3691.
- McPherron, R. L. (2005). Magnetic pulsations: Their sources and relation to solar wind and geomagnetic activity. *Surveys in Geophysics*, 26(5):545–592.
- Meredith, N. P., Horne, R. B., Glauert, S. A., and Anderson, R. R. (2007). Slot region electron loss timescales due to plasmaspheric hiss and lightning-generated whistlers. *Journal of Geophysical Research: Space Physics*, 112(A8):n/a–n/a.
- Min, K., Takahashi, K., Ukhorskiy, A. Y., Manweiler, J. W., Spence, H. E., Singer, H. J., Claudepierre, S. G., Larsen, B. A., Soto-Chavez, A. R., and Cohen, R. J. (2017). Second harmonic poloidal waves observed by Van Allen Probes in the dusk-midnight sector. *Journal of Geophysical Research: Space Physics*, 122(3):3013–3039.
- Mishin, V. V. (1993). Accelerated motions of the magnetopause as a trigger of the Kelvin-Helmholtz instability. *Journal of Geophysical Research: Space Physics*, 98(A12):21365–21371.
- Moldwin, M. B., Downward, L., Rassoul, H. K., Amin, R., and Anderson, R. R. (2002). A new model of the location of the plasmopause: CRRES results. *Journal of Geophysical Research: Space Physics*, 107(A11):2–1.
- Murphy, K. R., Inglis, A. R., Sibeck, D. G., Watt, C. E. J., and Rae, I. J. (2020). Inner Magnetospheric ULF Waves: The Occurrence and Distribution of Broadband

## BIBLIOGRAPHY

---

- and Discrete Wave Activity. *Journal of Geophysical Research: Space Physics*, 125(9):e2020JA027887.
- Murphy, K. R., Mann, I. R., and Ozeke, L. G. (2014). A ULF wave driver of ring current energization. *Geophysical Research Letters*, 41(19):6595–6602.
- Murphy, K. R., Mann, I. R., and Sibeck, D. G. (2015). On the dependence of storm time ULF wave power on magnetopause location: Impacts for ULF wave radial diffusion. *Geophysical Research Letters*, 42(22):9676–9684.
- Murphy, K. R., Rae, I. J., Mann, I. R., and Milling, D. K. (2011). On the nature of ULF wave power during nightside auroral activations and substorms: 1. Spatial distribution. *Journal of Geophysical Research: Space Physics*, 116(A5):0–21.
- Murphy, K. R., Watt, C. E. J., Mann, I. R., Jonathan Rae, I., Sibeck, D. G., Boyd, A. J., Forsyth, C. F., Turner, D. L., Claudepierre, S. G., Baker, D. N., Spence, H. E., Reeves, G. D., Blake, J. B., and Fennell, J. (2018). The Global Statistical Response of the Outer Radiation Belt During Geomagnetic Storms. *Geophysical Research Letters*, 45(9):3783–3792.
- Myers, A. P. and Orr, D. (1995). ULF Wave Analysis and Complex Demodulation. *ESASP*, 371:23.
- Ness, N. F., Scarce, C. S., and Seek, J. B. (1964). Initial results of the imp 1 magnetic field experiment. *Journal of Geophysical Research*, 69(17):3531–3569.
- Northrop, T. G. (1963). Adiabatic charged-particle motion. *Reviews of Geophysics*, 1(3):283–304.
- O’Brien, T. A., Kashinath, K., Cavanaugh, N. R., Collins, W. D., and O’Brien, J. P. (2016). A fast and objective multidimensional kernel density estimation method: fastKDE. *Computational Statistics & Data Analysis*, 101:148–160.
- O’Brien, T. P. (2014). Breaking all the invariants: Anomalous electron radiation belt diffusion by pitch angle scattering in the presence of split magnetic drift shells. *Geophysical Research Letters*, 41(2):216–222.

## BIBLIOGRAPHY

---

- O'Brien, T. P., McPherron, R. L., Sornette, D., Reeves, G. D., Friedel, R., and Singer, H. J. (2001). Which magnetic storms produce relativistic electrons at geosynchronous orbit? *Journal of Geophysical Research: Space Physics*, 106(A8):15533–15544.
- Olson, W. P. and Pfitzer, K. A. (1974). A quantitative model of the magnetospheric magnetic field. *Journal of Geophysical Research*, 79(25):3739–3748.
- Olson, W. P. and Pfitzer, K. A. (1982). A dynamic model of the magnetospheric magnetic and electric fields for July 29, 1977. *Journal of Geophysical Research*, 87(A8):5943.
- Owens, M. J. and Forsyth, R. J. (2013). The Heliospheric Magnetic Field. *Living Reviews in Solar Physics 2013 10:1*, 10(1):1–52.
- Ozeke, L. G. and Mann, I. R. (2004). Modeling the properties of guided poloidal Alfvén waves with finite asymmetric ionospheric conductivities in a dipole field. *Journal of Geophysical Research: Space Physics*, 109(A5):5205.
- Ozeke, L. G., Mann, I. R., Murphy, K. R., Degeling, A. W., Claudepierre, S. G., and Spence, H. E. (2018). Explaining the apparent impenetrable barrier to ultra-relativistic electrons in the outer Van Allen belt. *Nature Communications*, 9(1):1844.
- Ozeke, L. G., Mann, I. R., Murphy, K. R., Jonathan Rae, I., and Milling, D. K. (2014). Analytic expressions for ULF wave radiation belt radial diffusion coefficients. *Journal of Geophysical Research: Space Physics*, 119(3):1587–1605.
- Ozeke, L. G., Mann, I. R., Murphy, K. R., Rae, I. J., Milling, D. K., Elkington, S. R., Chan, A. A., and Singer, H. J. (2012). ULF wave derived radiation belt radial diffusion coefficients. *Journal of Geophysical Research: Space Physics*, 117(A4).
- Ozeke, L. G., Mann, I. R., Murphy, K. R., Sibeck, D. G., and Baker, D. N. (2017). Ultra-relativistic radiation belt extinction and ULF wave radial diffusion: Modeling the September 2014 extended dropout event. *Geophysical Research Letters*, 44(6):2624–2633.
- Ozeke, L. G., Mann, I. R., and Rae, I. J. (2009). Mapping guided Alfvén wave magnetic field amplitudes observed on the ground to equatorial electric field amplitudes in space. *Journal of Geophysical Research: Space Physics*, 114(A1).

## BIBLIOGRAPHY

---

- Pahud, D. M., Rae, I. J., Mann, I. R., Murphy, K. R., and Amalraj, V. (2009). Ground-based Pc5 ULF wave power: Solar wind speed and MLT dependence. *Journal of Atmospheric and Solar-Terrestrial Physics*, 71(10):1082–1092.
- Parker, E. N. (1960). Geomagnetic fluctuations and the form of the outer zone of the Van Allen radiation belt. *Journal of Geophysical Research*, 65(10):3117–3130.
- Percival, D. B. and Walden, A. T. (1993). Spectral Analysis for Physical Applications. *Spectral Analysis for Physical Applications*.
- Perry, K. L., Hudson, M. K., and Elkington, S. R. (2005). Incorporating spectral characteristics of Pc5 waves into three-dimensional radiation belt modeling and the diffusion of relativistic electrons. *Journal of Geophysical Research: Space Physics*, 110(A3):3215.
- Pilipenko, V., Kleimenova, N., Kozyreva, O., Engebretson, M., and Rasmussen, O. (2001). Long-period magnetic activity during the May 15, 1997 storm. *Journal of Atmospheric and Solar-Terrestrial Physics*, 63(5):489–501.
- Pilipenko, V. A., Kozyreva, O. V., Engebretson, M. J., Detrick, D. L., and Samsonov, S. N. (2002). Dynamics of long-period magnetic activity and energetic particle precipitation during the May 15, 1997 storm. *Journal of Atmospheric and Solar-Terrestrial Physics*, 64(7):831–843.
- Plaschke, F., Glassmeier, K.-h., Constantinescu, O. D., Mann, I. R., Milling, D. K., Motschmann, U., and Rae, I. J. (2008). Statistical analysis of ground based magnetic field measurements with the field line resonance detector. Technical report.
- Proehl, J. A., Lotko, W., Kouznetsov, I., and Geimer, S. D. (2002). Ultralow-frequency magnetohydrodynamics in boundary-constrained geomagnetic flux coordinates. *Journal of Geophysical Research: Space Physics*, 107(A9):1–1.
- Radoski, H. R. (1971). A note on the problem of hydromagnetic resonances in the magnetosphere. *Planetary and Space Science*, 19(8):1012–1013.
- Rae, I. J., Donovan, E. F., Mann, I. R., Fenrich, F. R., Watt, C. E. J., Milling, D. K., Lester, M., Lavraud, B., Wild, J. A., Singer, H. J., Rème, H., and Balogh, A. (2005).

## BIBLIOGRAPHY

---

- Evolution and characteristics of global Pc5 ULF waves during a high solar wind speed interval. *Journal of Geophysical Research*, 110(A12):A12211.
- Rae, I. J., Mann, I. R., Dent, Z. C., Milling, D. K., Donovan, E. F., and Spanswick, E. (2007). Multiple field line resonances: Optical, magnetic and absorption signatures. *Planetary and Space Science*, 55(6):701–713.
- Rae, I. J., Mann, I. R., Murphy, K. R., Ozeke, L. G., Milling, D. K., Chan, A. A., Elkington, S. R., and Honary, F. (2012). Ground-based magnetometer determination of in situ Pc4–5 ULF electric field wave spectra as a function of solar wind speed. *Journal of Geophysical Research: Space Physics*, 117(A4):4221.
- Rae, I. J., Murphy, K. R., Watt, C. E. J., and Mann, I. R. (2011). On the nature of ULF wave power during nightside auroral activations and substorms: 2. Temporal evolution. *Journal of Geophysical Research: Space Physics*, 116(A5):0–22.
- Rankin, R., Fenrich, F., and Tikhonchuk, V. T. (2000). Shear Alfvén waves on stretched magnetic field lines near midnight in Earth’s magnetosphere. *Geophysical Research Letters*, 27(20):3265–3268.
- Rankin, R., Kabin, K., and Marchand, R. (2006). Alfvénic field line resonances in arbitrary magnetic field topology. *Advances in Space Research*, 38(8):1720–1729.
- Ren, J., Zong, Q. G., Miyoshi, Y., Zhou, X. Z., Wang, Y. F., Rankin, R., Yue, C., Spence, H. E., Funsten, H. O., Wygant, J. R., and Kletzing, C. A. (2017). Low-Energy (<200 eV) Electron Acceleration by ULF Waves in the Plasmaspheric Boundary Layer: Van Allen Probes Observation. *Journal of Geophysical Research: Space Physics*, 122(10):9969–9982.
- Ricciardulli, L. and Sardeshmukh, P. D. (2002). Local Time- and Space Scales of Organized Tropical Deep Convection. *Journal of Climate*, 15(19):2775 – 2790.
- Roberts, P. H. (2007). Alfvén’s Theorem and the Frozen Flux Approximation. *Encyclopedia of Geomagnetism and Paleomagnetism*, pages 7–11.
- Roederer, J. G. (1970). *Dynamics of geomagnetically trapped radiation / J.G. Roederer*. Springer-Verlag Berlin.

## BIBLIOGRAPHY

---

- Roederer, J. G. and Lejosne, S. (2018a). Coordinates for Representing Radiation Belt Particle Flux. *Journal of Geophysical Research: Space Physics*, 123(2):1381–1387.
- Roederer, J. G. and Lejosne, S. (2018b). Coordinates for Representing Radiation Belt Particle Flux. *Journal of Geophysical Research: Space Physics*, 123(2):1381–1387.
- Roederer, J. G. and Zhang, H. (2014). *Dynamics of Magnetically Trapped Particles*, volume 403 of *Astrophysics and Space Science Library*. Springer Berlin Heidelberg, Berlin, Heidelberg.
- Rostoker, G., Samson, J. C., Creutzberg, F., Hughes, T. J., McDiarmid, D. R., McNamara, A. G., Jones, A. V., Wallis, D. D., and Cogger, L. L. (1995). Canopus - A ground-based instrument array for remote sensing the high latitude ionosphere during the ISTP/GGS program. *Space Science Reviews*, 71(1-4):743–760.
- Rostoker, G., Skone, S., and Baker, D. N. (1998). On the origin of relativistic electrons in the magnetosphere associated with some geomagnetic storms. *Geophysical Research Letters*, 25(19):3701–3704.
- Samson, J. C., Harrold, B. G., Ruohoniemi, J. M., Greenwald, R. A., and Walker, A. D. (1992). Field line resonances associated with MHD waveguides in the magnetosphere. *Geophysical Research Letters*, 19(5):441–444.
- Sandhu, J. K., Rae, I. J., Wygant, J. R., Breneman, A. W., Tian, S., Watt, C. E., Horne, R. B., Ozeke, L. G., Georgiou, M., and Walach, M. T. (2021). ULF Wave Driven Radial Diffusion During Geomagnetic Storms: A Statistical Analysis of Van Allen Probes Observations. *Journal of Geophysical Research: Space Physics*, 126(4):e2020JA029024.
- Sarris, T. E. and Li, X. (2017). Geomagnetic activity and local time dependence of the distribution of ultra low-frequency wave power in azimuthal wavenumbers, m. *Annales Geophysicae*, 35(3):629–638.
- Sarris, T. E., Li, X., Liu, W., Argyriadis, E., Boudouridis, A., and Ergun, R. (2013). Mode number calculations of ULF field-line resonances using ground magnetometers and THEMIS measurements. *Journal of Geophysical Research: Space Physics*, 118(11):6986–6997.

## BIBLIOGRAPHY

---

- Schulz, M. and Lanzerotti, L. (1974). *Particle diffusion in the radiation belts / [by] M. Schulz [and] L. J. Lanzerotti*. Springer-Verlag Berlin.
- Schwabe, S. H. (1843). Die Sonne. *Astronomische Nachrichten*, 20(17):283–286.
- Scott, D. W. (1992). Multivariate Density Estimation.
- Sheeley, B. W., Moldwin, M. B., Rassoul, H. K., and Anderson, R. R. (2001). An empirical plasmasphere and trough density model: CRRES observations. *Journal of Geophysical Research: Space Physics*, 106(A11):25631–25641.
- Shprits, Y. Y., Elkington, S. R., Meredith, N. P., and Subbotin, D. A. (2008a). Review of modeling of losses and sources of relativistic electrons in the outer radiation belt I: Radial transport. *Journal of Atmospheric and Solar-Terrestrial Physics*, 70(14):1679–1693.
- Shprits, Y. Y., Subbotin, D. A., Meredith, N. P., and Elkington, S. R. (2008b). Review of modeling of losses and sources of relativistic electrons in the outer radiation belt II: Local acceleration and loss. *Journal of Atmospheric and Solar-Terrestrial Physics*, 70(14):1694–1713.
- Shprits, Y. Y. and Thorne, R. M. (2004). Time dependent radial diffusion modeling of relativistic electrons with realistic loss rates. *Geophysical Research Letters*, 31(8).
- Shprits, Y. Y., Thorne, R. M., Friedel, R., Reeves, G. D., Fennell, J., Baker, D. N., and Kanekal, S. G. (2006). Outward radial diffusion driven by losses at magnetopause. *Journal of Geophysical Research: Space Physics*, 111(A11).
- Shprits, Y. Y., Vasile, R., and Zhelavskaya, I. S. (2019). Nowcasting and Predicting the Kp Index Using Historical Values and Real-Time Observations. *Space Weather*, 17(8):1219–1229.
- Silverman, B. W. (2018). Density Estimation for Statistics and Data Analysis. *Density Estimation: For Statistics and Data Analysis*, pages 1–175.
- Smirnov, A. G., Berrendorf, M., Shprits, Y. Y., Kronberg, E. A., Allison, H. J., Aseev, N. A., Zhelavskaya, I. S., Morley, S. K., Reeves, G. D., Carver, M. R., and Effenberger,

## BIBLIOGRAPHY

---

- F. (2020). Medium Energy Electron Flux in Earth's Outer Radiation Belt (MERLIN): A Machine Learning Model. *Space Weather*, 18(11):e2020SW002532.
- Southwood, D. J. (1968). The hydromagnetic stability of the magnetospheric boundary. *Planetary and Space Science*, 16(5):587–605.
- Southwood, D. J. (1974). Some features of field line resonances in the magnetosphere. *Planetary and Space Science*, 22(3):483–491.
- Stephenson, F. R. and Willis, D. M. (1999). The earliest drawing of sunspots. *Astronomy & Geophysics*, 40(6):21–6.
- Stewart, B. (1861). XXII. On the great magnetic disturbance which extended from August 28 to September 7, 1859, as recorded by photography at the Kew Observatory. *Philosophical Transactions of the Royal Society of London*, 151:423–430.
- Su, Z., Gao, Z., Zhu, H., Li, W., Zheng, H., Wang, Y., Wang, S., Spence, H. E., Reeves, G. D., Baker, D. N., Blake, J. B., Funsten, H. O., and Wygant, J. R. (2016). Non-storm time dropout of radiation belt electron fluxes on 24 September 2013. *Journal of Geophysical Research: Space Physics*, 121(7):6400–6416.
- Syun-Ichi, A. (2018). A Review of the Current Understanding in the Study of Geomagnetic Storms. *International Journal of Earth Science and Geophysics*, 4(1).
- Takahashi, K. and Ukhorskiy, A. Y. (2007). Solar wind control of Pc5 pulsation power at geosynchronous orbit. *Journal of Geophysical Research: Space Physics*, 112(11):11205.
- Takahashi, K. and Ukhorskiy, A. Y. (2008). Timing analysis of the relationship between solar wind parameters and geosynchronous Pc5 amplitude. *Journal of Geophysical Research: Space Physics*, 113(12):n/a–n/a.
- Tanskanen, E. I. (2009). A comprehensive high-throughput analysis of substorms observed by IMAGE magnetometer network: Years 1993-2003 examined. *Journal of Geophysical Research: Space Physics*, 114(5):5204.
- Thébault, E., Finlay, C. C., Beggan, C. D., Alken, P., Aubert, J., Barrois, O., Bertrand, F., Bondar, T., Boness, A., Brocco, L., Canet, E., Chambodut, A., Chulliat, A., Coisson, P.,

## BIBLIOGRAPHY

---

- Civet, F., Du, A., Fournier, A., Fratter, I., Gillet, N., Hamilton, B., Hamoudi, M., Hulot, G., Jager, T., Korte, M., Kuang, W., Lalanne, X., Langlais, B., Léger, J.-M., Lesur, V., Lowes, F. J., Macmillan, S., Manda, M., Manoj, C., Maus, S., Olsen, N., Petrov, V., Ridley, V., Rother, M., Sabaka, T. J., Saturnino, D., Schachtschneider, R., Sirol, O., Tangborn, A., Thomson, A., Tøffner-Clausen, L., Vigneron, P., Wardinski, I., and Zvereva, T. (2015). International Geomagnetic Reference Field: the 12th generation. *Earth, Planets and Space*, 67(1):79.
- Thompson, R. L., Morley, S. K., Watt, C. E. J., Bentley, S. N., and Williams, P. D. (2020a). Pro-L\* - A probabilistic L\* mapping tool for ground observations. *Space Weather*.
- Thompson, R. L., Watt, C. E. J., and Williams, P. D. (2020b). Accounting for variability in ULF wave radial diffusion models. *Journal of Geophysical Research: Space Physics*.
- Thomson, D. J. (1982). Spectrum Estimation and Harmonic Analysis. *Proceedings of the IEEE*, 70(9):1055–1096.
- Thorne, R. M., Li, W., Ni, B., Ma, Q., Bortnik, J., Chen, L., Baker, D. N., Spence, H. E., Reeves, G. D., Henderson, M. G., Kletzing, C. A., Kurth, W. S., Hospodarsky, G. B., Blake, J. B., Fennell, J. F., Claudepierre, S. G., and Kanekal, S. G. (2013). Rapid local acceleration of relativistic radiation-belt electrons by magnetospheric chorus. *Nature*, 504:411.
- Tsyganenko, N. A. (1989). A magnetospheric magnetic field model with a warped tail current sheet. *Planetary and Space Science*, 37(1):5–20.
- Tsyganenko, N. A. (1995). Modeling the Earth's magnetospheric magnetic field confined within a realistic magnetopause. *Journal of Geophysical Research*, 100(A4):5599.
- Tsyganenko, N. A. (1996). Effects of the solar wind conditions on the global magnetospheric configuration as deduced from data-based field models.
- Tsyganenko, N. A., Singer, H. J., and Kasper, J. C. (2003). Storm-time distortion of the inner magnetosphere: How severe can it get? *Journal of Geophysical Research: Space Physics*, 108(A5).

## BIBLIOGRAPHY

---

- Tsyganenko, N. A. and Sitnov, M. I. (2005). Modeling the dynamics of the inner magnetosphere during strong geomagnetic storms. *Journal of Geophysical Research*, 110(A3):A03208.
- Tu, W., Elkington, S. R., Li, X., Liu, W., and Bonnell, J. (2012). Quantifying radial diffusion coefficients of radiation belt electrons based on global MHD simulation and spacecraft measurements. *Journal of Geophysical Research: Space Physics*, 117(A10).
- Turner, D. L., Shprits, Y., Hartinger, M., and Angelopoulos, V. (2012). Explaining sudden losses of outer radiation belt electrons during geomagnetic storms. *Nature Physics*, 8(3):208–212.
- Ukhorskiy, A. Y., Anderson, B. J., Takahashi, K., and Tsyganenko, N. A. (2006). Impact of ULF oscillations in solar wind dynamic pressure on the outer radiation belt electrons. *Geophysical Research Letters*, 33(6).
- Ukhorskiy, A. Y., Sitnov, M. I., Takahashi, K., and Anderson, B. J. (2009). Radial transport of radiation belt electrons due to stormtime Pc5 waves. *Annales Geophysicae*, 27(5):2173–2181.
- Van Allen, J. A. and Frank, L. A. (1959). Radiation around the earth to a radial distance of 107,400 km. *Nature*, 183(4659):430–434.
- Walach, M. and Grocott, A. (2019). SuperDARN Observations During Geomagnetic Storms, Geomagnetically Active Times, and Enhanced Solar Wind Driving. *Journal of Geophysical Research: Space Physics*, 124(7):5828–5847.
- Walker, A., Greenwald, R., Stuart, W., and Green, C. (1979). Stare auroral radar observations of Pc 5 geomagnetic pulsations. *Journal of Geophysical Research*, 84(A7):3373.
- Walker, A. D. M., Ruohoniemi, J. M., Baker, K. B., Greenwald, R. A., and Samson, J. C. (1992). Spatial and temporal behavior of ULF pulsations observed by the Goose Bay HF Radar. *Journal of Geophysical Research*, 97(A8):12187.
- Wallis, D. D. and Budzinski, E. E. (1981). Empirical models of height integrated conductivities. *Journal of Geophysical Research*, 86(A1):125.
- Wand, M. P. and Jones, M. C. (1994). Kernel smoothing. page 224.

## BIBLIOGRAPHY

---

- Warden, L. J., Waters, C. L., Sciffer, M. D., and Hull, A. J. (2021). On the estimation of the ratio of ULF wave electric fields in space and the magnetic fields at the ground. *Journal of Geophysical Research: Space Physics*.
- Waters, C. L., Harrold, B. G., Menk, F. W., Samson, J. C., and Fraser, B. J. (2000). Field line resonances and waveguide modes at low latitudes 2. A model. *Journal of Geophysical Research: Space Physics*, 105(A4):7763–7774.
- Waters, C. L. and Sciffer, M. D. (2008). Field line resonant frequencies and ionospheric conductance: Results from a 2-D MHD model. *Journal of Geophysical Research: Space Physics*, 113(A5):5219.
- Watt, C. E. J., Allison, H. J., Meredith, N. P., Thompson, R. L., Bentley, S. N., Rae, I. J., Glauert, S. A., and Horne, R. B. (2019). Variability of Quasilinear Diffusion Coefficients for Plasmaspheric Hiss. *Journal of Geophysical Research: Space Physics*, 124(11):8488–8506.
- Watt, C. E. J., Allison, H. J., Thompson, R. L., Bentley, S. N., Meredith, N. P., Glauert, S. A., Horne, R. B., and Rae, I. J. (2021). The Implications of Temporal Variability in Wave-Particle Interactions in Earth’s Radiation Belts. *Geophysical Research Letters*, 48(1):e2020GL089962.
- Welling, D. T., Koller, J., and Camporeale, E. (2012). Verification of SpacePy’s radial diffusion radiation belt model. *Geoscientific Model Development*, 5(2):277–287.
- William, H. P., Brian, P. F., Saul, A. T., and William, T. V. (1989). Numerical recipes: The art of scientific computing (Fortran version). pages 550–560.
- Wright, A. N. (1994). Dispersion and wave coupling in inhomogeneous MHD waveguides. *Journal of Geophysical Research*, 99(A1):159.
- Wright, A. N., Allan, W., Wright, A. N., and Allan, W. (1996). Structure, phase motion, and heating within Alfvén resonances. *JGR*, 101(A8):17399–17408.
- Wygant, J. R., Bonnell, J. W., Goetz, K., Ergun, R. E., Mozer, F. S., Bale, S. D., Ludlam, M., Turin, P., Harvey, P. R., Hochmann, R., Harps, K., Dalton, G., McCauley, J., Rachelson, W., Gordon, D., Donakowski, B., Shultz, C., Smith, C., Diaz-Aguado,

## BIBLIOGRAPHY

---

- M., Fischer, J., Heavner, S., Berg, P., Malsapina, D. M., Bolton, M. K., Hudson, M., Strangeway, R. J., Baker, D. N., Li, X., Albert, J., Foster, J. C., Chaston, C. C., Mann, I., Donovan, E., Cully, C. M., Cattell, C. A., Krasnoselskikh, V., Kersten, K., Brenneman, A., and Tao, J. B. (2013). The electric field and waves instruments on the radiation belt storm probes mission.
- Yu, Y., Koller, J., and Morley, S. K. (2013). Quantifying the effect of magnetopause shadowing on electron radiation belt dropouts. *Annales Geophysicae*, 31(11):1929–1939.
- Zhou, X. Z., Wang, Z. H., Zong, Q. G., Claudepierre, S. G., Mann, I. R., Kivelson, M. G., Angelopoulos, V., Hao, Y. X., Wang, Y. F., and Pu, Z. Y. (2015). Imprints of impulse-excited hydromagnetic waves on electrons in the Van Allen radiation belts. *Geophysical Research Letters*, 42(15):6199–6204.
- Ziesolleck, C. W. S., Fenrich, F. R., Samson, J. C., and McDiarmid, D. R. (1998). Pc5 field line resonance frequencies and structure observed by SuperDARN and CANOPUS. *Journal of Geophysical Research: Space Physics*, 103(A6):11771–11785.
- Zirker, J. B. (1977). Coronal holes and high-speed wind streams. *Reviews of Geophysics*, 15(3):257–269.